NUCLEAR DOUBLE RESONANCE STUDY OF KH_2PO_4

Per-Erik Nordal
(Ph.D. Thesis)

May 1973

Prepared for the U. S. Atomic Energy Commission
under Contract W-7405-ENG-48

DISCLAIMER

NUCLEAR DOUBLE RESONANCE STUDY OF KH_2PO_4

Contents

NUCLEAR DOUBLE RESONANCE STUDY OF KH_2PO_4

Per-Erik Nordal

Inorganic Materials Research Division, Lawrence Berkeley Laboratory
and Department of Physics; University of California
Berkeley, California

ABSTRACT

NMR pulse methods are used to study NMR/NQR spectra and relaxation phenomena in single crystals of KH_2PO_4 (KDP). The main emphasis is on elucidating the lattice dynamics at the ferroelectric phase transition via the temperature dependence of the ferroelectric-mode induced spin-lattice relaxation of K^{39}. K^{39} spin-lattice relaxation time measurements are performed with a new high-sensitivity muclear double resonance method which employs an unmodulated radio-frequency (r.f.) field at the "rare spin" frequency. The method is developed and evaluated theoretically, and verified experimentally on K^{39}. In addition to being applicable in cases with very short spin-lattice relaxation times, the method yields double resonance lineshapes with structure which depends critically on spin reservoir parameters. Instead of exhibiting an increasing line depth as the line center is approached, there are typically 2 line depth maxima symmetrically located about the line center, with a minimum line depth exactly on resonance.

The K^{39} relaxation rate is found to increase rapidly with the temperature above approximately 200°K, and a strong increase in the relaxation rate is also detected as the Curie temperature T_c is approached. The increased relaxation rate at T_c is attributed to spin-phonon coupling to the ferroelectric mode, and in a temperature range extending from the Curie point to approximately 155°K the ferroelectric-mode induced relaxation

rate can be described well by a ferroelectric-mode response function of diffusive or heavily damped harmonic-oscillator type. The data tend to favor a logarithmic singularity in the relaxation-rate in this temperature range, indicating strong anisotropy in the ferroelectric quasi-dipole interaction.

The proton relaxation time following adiabatic demagnetization in the rotating frame (ADRF) is measured as a function of temperature. Above 250°K, H_2PO_4 rotations about a single axis are observed, characterized by an activation energy of 0.5 eV and a correlation time of approximately 1 sec at 250°K. In the region 100°K to 250°K the relaxation rate remains essentially constant, but has a slight increase in the vicinity of the Curie point. Proton relaxation measurements in the laboratory frame do not exhibit this anomaly, which may be linked to proton motion.

Conventional ADRF double resonance methods were used to study the spectra of K^{39} and K^{41} and their temperature dependence. The results agree with those of other authors. Double resonance data on other spin species in KDP are also presented.

Expressions for the effective gyromagnetic ratio in the rotating frame are derived for spin 3/2 particles in a strong, resonant r.f. field. For the first time, this problem is treated with no restrictions on the relative magnitudes of the quadrupole and Zeeman interactions in the laboratory frame, in the case where the static field H_o is perpendicular to the e.f.g. tensor principal axis. The results are verified for K^{39} in KDP. At a given temperature, the numerical values of the effective gyromagnetic ratios corresponding to the allowed laboratory frame transitions are found to vary by an order of magnitude; depending on which transition is excited.

Theoretical expressions for quadrupolar spin-lattice relaxation times in the spin-lock state are derived for the case of spin 3/2 particles with laboratory frame quadrupole and Zeeman interactions which may be of the same order of magnitude. The results are applied to the general problem of ferroelectric-mode induced spin-lattice relaxation.

I. INTRODUCTION

Phase transitions are of fundamental importance in nature, and one class of phase transitions that is currently being intensively and successfully studied by NMR methods is the transition in ferroelectrics between the unpolarized (para-) and the spontaneously polarized (ferro-) phase.

Early descriptions of ferroelectric phase transitions were formulated in terms of equilibrium thermodynamics.[1,2] During the last few years, however, it has been realized that an adequate description of microscopic and macroscopic aspects of the phase transition can be obtained by dynamic models involving the elementary excitations in the crystal lattice. Several theoretical works on different types of ferroelectrics have been published, and reviews are found in references 3, 4, and 5. Using a slightly simplified picture, the ferroelectric transition can be described in terms of lattice dynamics by a specific vibration mode, the "ferroelectric" or "soft" mode, whose characteristic frequency approaches zero as the transition temperature T_c is approached. At T_c, the mode becomes unstable, and in the ferroelectric phase below T_c an atomic displacement pattern is "frozen in" with a symmetry equal to that of the ferroelectric mode above T_c. In contrast to the thermodynamic treatment of the phase transition, the description in terms of the ferroelectric mode allows studies on the relationship between microscopic parameters of the ferroelectric solid and macroscopic ferroelectric properties.

Experimental studies on the nature of the ferroelectric mode in the vicinity of the Curie point have been reported for a variety of

of solids, using Raman- and Brillouin-scattering, neutron scattering, ultrasonics and NMR methods. The total amount of experimental data in this field is still relatively small, however. A main objective of this thesis has been to exploit the advantages of a high-sensitivity nuclear double resonance method to obtain experimental data on the ferroelectric mode in KH_2PO_4 (common abbreviation: KDP) which are not obtainable by direct NMR methods. To achieve this goal it was necessary to derive new theoretical results and develop experimental procedures which should be of more general interest in NMR.

Traditionally, NMR/NQR techniques used to study lattice dynamics and structural changes in solids include measurements of linewidths and of the temperature dependence of quadrupole coupling parameters. Recently, it has been demonstrated that it is possible to extract qualitative and quantitative information pertaining to the ferroelectric mode from measurements of the nuclear spin-lattice relaxation rate in a temperature interval around the Curie point. The basic argument can be summarized as follows: The spectral density of the stationary random fluctuations in the electric field gradient tensor components, due to lattice vibrations in a ferroelectric at thermodynamic equilibrium, can be related analytically to the imaginary part of the generalized dielectric susceptibility by means of the fluctuation dissipation theorem.[6] Close to the Curie point the dominant contribution to this susceptibility will come from the ferroelectric mode, which is strongly excited as the temperature T approaches T_c. Thus, by the Kramers-Kronig relations, the total ferroelectric mode response function (susceptibility) in the temperature region around T_c can be related to the spin-lattice relaxation

time T_1, if the functional form of T_1 in terms of spectral densities of the e.f.g. tensor fluctuations is known. One finds that the ferroelectric-mode induced spin-lattic relaxation rate should exhibit a sharp maximum at T_c, with diminishing magnitude as $|T - T_c|$ increases. This temperature dependence around T_c is expected to depend sensitively on the ferroelectric mode response function and on the nature of the interactions in the ferroelectric which precipitate the transition. In practice, the relaxation rate that is measured contains contributions from sources such as spin diffusion to paramagnetic impurities and migration of nuclei in the lattice, in addition to the ferrelectric-mode contribution of interest. Since the ferroelectric-mode induced relaxation rate diminishes as $|T - T_c|$ increases, it will ultimately be masked completely by the other relaxation contributions. Therefore, the spin-phonon coupling must be sufficiently strong such that the ferroelectric-mode induced spin-lattice relaxation rate can be extracted from the total relaxation rate with small relative error in a temperature range around T_c large enough to allow reliable determination of the temperature dependence. The strength of the spin-phonon coupling may vary greatly for different nuclear species in the same ferroelectric. Nuclei prossessing a quadrupole moment can interact strongly with the lattice vibrations through the coupling to the local electric field gradient, while spin 1/2 nuclei and other purely magnetic nuclei (protons, f.ex.) generally experience much weaker spin-phonon coupling via magnetic dipole interaction with the local magnetic field from paramagnets or local charge transport in the crystal.

The work reported here is a geared primarily towards determination

of the ferroelectric-mode induced spin-lattice relaxation rate of K^{39} in KDP as a function of temperature, and analysis of these data in terms of ferroelectric-mode response functions. In light of what was written above it is now apparent why K^{39} nuclei, which are unobservable by conventional NMR, are more interesting as microscopic probes than the easily detected H^1 or P^{31}: K^{39} has a nonzero quadrupole coupling constant, while H^1 and P^{31} are spin 1/2 particles with zero quadrupole coupling. The consequences of this for the ferroelectric-mode induced spin-lattice relaxation rates are quite dramatic and will be shown later.

KDP is representative of a family of hydrogen-bonded ferroelectrics. The following list is from Landolt-Börnstein tables:[7]

Table I.1. KDP isomorphs (deuterated analogs in parentheses).

Substance	T_c[°K]	Ferro-/Antiferroelectric
KH_2PO_4 (KD_2PO_4)	123 (213)	Ferroelectric
RbH_2PO_4 (RbD_2PO_4)	147 (218)	"
CsH_2PO_4	159	"
KH_2AsO_4 (KD_2AsO_4)	97 (161-159)	"
RbH_2AsO_4 (RbD_2AsO_4)	110 (173)	"
CsH_2AsO_4 (CsD_2AsO_4	260 (212)	"
$NH_4H_2PO_4$ ($ND_4D_2AsO_4$)	148 (242)	Antiferroelectric
$NH_4H_2AsO_4$ ($ND_4D_2AsO_4$)	216 (304)	"

The crystal structure of KDP in the paraelectric phase is shown on Fig. I-1. Paraelectric KDP belongs to the tetragonal space group $I\bar{4}2d$. The PO_4 groups are connected by a network of O-H . . .O hydrogen bonds such that the two oxygen atoms on the upper edge of each oxygen

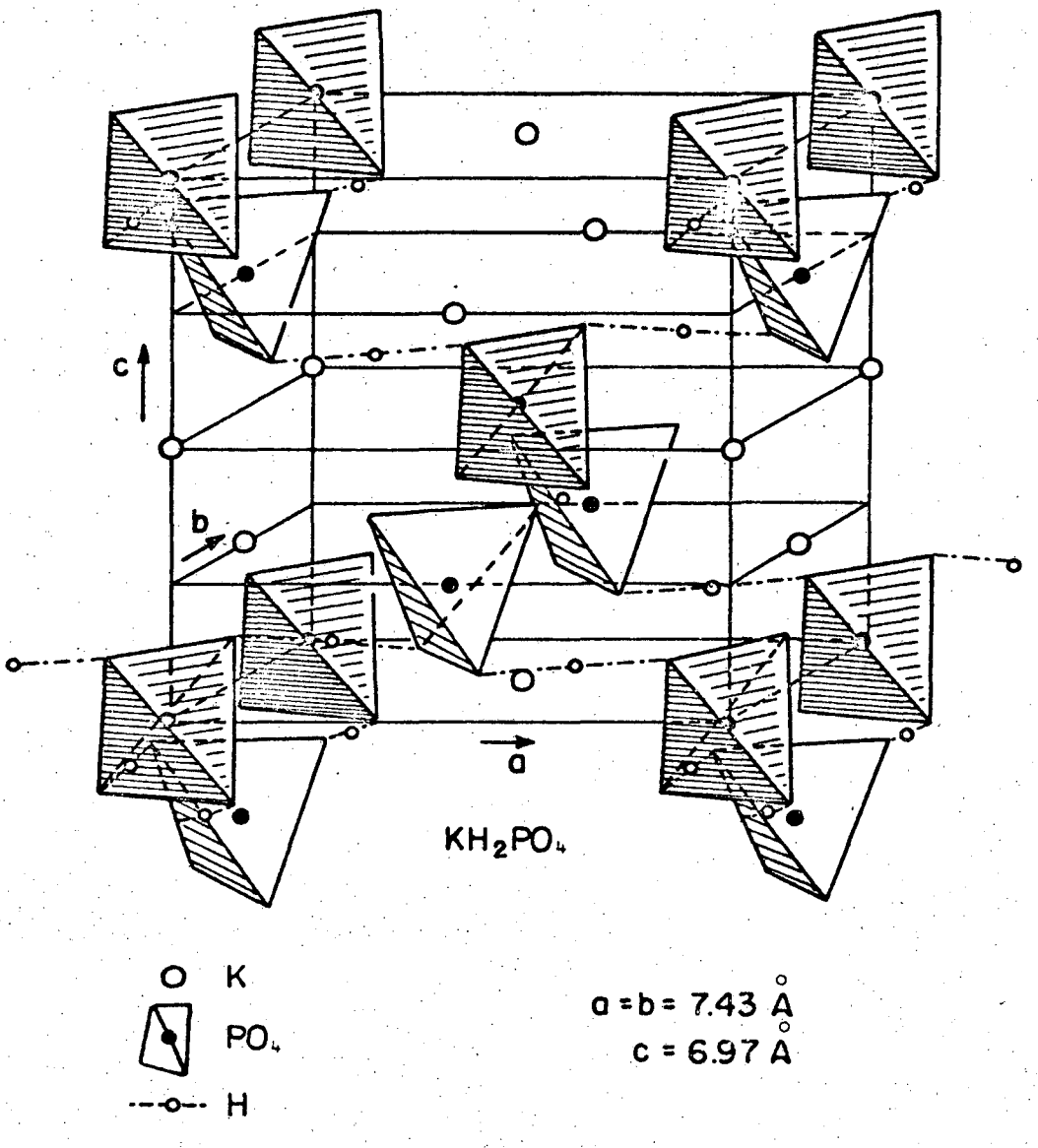

Fig. I.1. Structure of KH_2PO_4 in the paraelectric phase (after J. West[98]).

tetrahedron are linked to two oxygen atoms on the lower edge of two separate neighboring PO_4 groups. "Up" and "down" are the directions parallel and antiparallel to the c-axis. The hydrogen bonds are within 1/2 degree of being perpendicular to the c-axis and are mutually parallel or perpendicular. Potassium atoms and PO_4 groups alternate along lines parallel to the c-axis. In the ferroelectric phase, the crystal structure is orthorhombic Fdd2. Relative to their positions in the paraelectric phase, the potassium atoms and PO_4 groups are translated in opposite directions along the c-axis. Neutron scattering studies of KDP in the paraelectric phase reveal a proton distribution smeared out along the bond, symmetrically about the bond center. In the ferroelectric phase, the protons become localized toward one end of the bond, such that each phosphate group has protons adjacent to it on the two upper bonds and distant from it on the two lower ones, or vice versa, depending on the direction of polarization. Substitution of protons by deuterons not only increases the transition temperature, but also changes other ferroelectric parameters.

In principle, NMR methods should be especially well suited to the study of KOP, since there are paramagnetic isotopes at all nuclear sites:

Table I.2. Magnetic nuclei in KDP of natural isotopic composition.

Isotope	Abundance %	Larmour Frequency (MHz/10K Gauss)	Spin I Mult. of $\hbar$	Quad. Moment Q $e \cdot 10^{-24}$ cm^2
H^1	$1.19 \cdot 10^{-2}$	42.576	1/2	---
H^2	$1.56 \cdot 10^{-2}$	6.536	1	$2.77 \cdot 10^{-3}$
K^{39}	93.08	1.987	3/2	.07
K^{40}	$1.19 \cdot 10^{-2}$	2.470	4	---
K^{41}	6.91	1.092	3/2	---
O^{17}	$3.7 \cdot 10^{-2}$	5.772	5/2	$-4 \cdot 10^{-3}$
P^{31}	100	17.236	1/2	---

In practice, experimental sensitivity problems limit the isotopes observable by conventional NMR to ^{1}H and ^{31}P. Despite high abundance, ^{39}K requires high-sensitivity detection methods due to its low gyromagnetic ratio and moderate quadrupole coupling to the local electric field gradient. Because of this, the only spin-lattice relaxation studies on the ferroelectric mode in KDP reported so far[8] have been done on P^{31} in KDP. Due to weak spin-phonon coupling, and proton inter- and intrabond jumping, P^{31} and H^{1} are poorly suited for this application. Some KDP isomorphs do contain quadrupole coupled nuclei that are observable by direct methods, and data on the temperature dependence of the spin-lattice relaxation in the vicinity of the transition point have been published recently for D^{2}, As^{75}, Rb^{87} and Cs^{133} in some isomorphs (cfr. Chapter XI). Data obtained on isomorphs do not necessarily apply to KDP however. Deuteration alters the intrinsic ferroelectric properties greatly, and different masses and coupling strengths of nuclei at K and P sites may lead to qualitative differences in lattice dynamics. It is therefore of interest to obtain spin-lattice relaxation data on each isomorph separately and then compare results. At present, KDP is by far the most extensively studied of the isomorphs, and this provides richer material for comparison of data on the ferroelectric mode obtained by different methods.

The concepts and experimental procedures involved in high-sensitivity nuclear double resonance are reviewed in Chapters II and III. Nuclear double resonance should in principle make it possible to do spectroscopy on all magnetic isotopes in KDP listed above. As far as studies of ferroelectric properties are concerned, considerable information on

lattice dynamics and structural changes can be gathered from spectroscopy on quadrupole-coupled nuclei like K^{39} at various temperatures. Such data for K^{39} and K^{41} are presented in Chapter X. As will be described in Chapters II through V, double resonance methods have a wide range of applications in addition to pure spectroscopy, and in certain cases it is possible to measure the spin-lattice relaxation times of nuclei that require high-sensitivity methods for detection. For K^{39} in KDP, however, the spin-lattice relaxation time was so short that no method existed that was capable of measuring it, and a new method was devised.[9] The method involves a very simple form of double resonance which has not previously been analyzed carefully or exploited experimentally. The analysis is presented in Chapter IV, and it is shown how spin-lattice relaxation times can be determined experimentally for nuclei like K^{39} in KDP. According to results in Chapter IV, the double resonance method also yields an unusual double resonance lineshape and can give information on parameters of general interest in double resonance (thermal reservoir heat capacity ratios and cross relaxation rates). The analytical results of Chapter IV are compared with experimental data on K^{39} in Chapter IX, and good agreement is found, both qualitatively and quantitatively. This has been taken as sufficient justification for using the method to determine the K^{39} spin-lattice relaxation times at various temperatures.

In order to obtain sufficient information for analysis, it was necessary to measure the K^{39} spin-lattice relaxation rate throughout a large temperature range. A potentially important parameter, the strength of the r.f. field at the K^{39} transition frequency, was monitored by audio resonance[10,11] (rotary saturation) so as to obtain the necessary

consistency between data at all points throughout the temperature range. Here one encounters the problem that the only studies on the relationship between the audio resonance frequency and the r.f. field strength (expressed in terms of the "effective gyromagnetic ratio") have been made for the two limiting cases where the nucleus has either zero quadrupole or zero Zeeman interaction. The measurements reported here were performed on a nuclear species (K^{39}) with quadrupole and Zeeman interactions of the same order of magnitude, and with the quadrupole interaction dependent on the sample temperature. In Section V.A, the effective gyromagnetic ratio is computed for the general case of spin 3/2 particles with quadrupole and Zeeman interactions of arbitrary relative magnitudes, since the analysis might be of interest beyond the present application. The somewhat surprising results were verified experimentally on K^{39} in KDP, as described in Section IX-B.

Before the spin-lattice relaxation data can be used to study the ferroelectric-mode response function, it is necessary to obtain an analytic expression for the spin-lattice relaxation rate in terms of spectral densities of the lattice vibrations; or, more specifically, of the fluctuations in the different electric field gradient tensor components. No such expressions applicable to the present case of K^{39} in KDP is to be found in the literature. This problem is therefore treated in some detail in Section V-B, for the case of a spin 3/2 particle with quadrupole and Zeeman interactions of arbitrary relative magnitude. Expressions for the quadrupole spin-lattice relaxation rate in the spin-lock state (i.e. in a strong resonant field) are derived.

All the necessary theoretical foundations and experimental procedures

have thus been established, and the experimental results on the K^{39} spin-lattice relaxation rates are presented and analyzed in Sections XI-A and XI-B. The final results on the ferroelectric mode are compared with data from neutron, Raman and Brillouin scattering studies.

It is expected that other, more conventional nuclear double resonance methods could be helpful in the study of structural changes and microscopic motion in KDP, and preliminary work on double resonance spectroscopy and transient oscillations in the (K^{39}) rotating frame[11] is presented in Chapters X and XII. Of special interest is spectroscopy on ^{17}O and ^{2}H, since both are quadrupole coupled to their local electric field gradients and thus provide information on static and dynamic changes in their local environments. The double resonance sensitivity for detection of deuterium provided to be much poorer than expected, except for double quantum transitions. A similar effect has previously been observed in gypsum,[12] and measurements on KDP enriched in deuterium were performed to determine whether a mechanism like the "spin quenching" described by Gabriel, et al.[13] is responsible. Suggestions for further work are made at the end of Chapter XII.

The preparation of the samples used is described in Chapter VII. Since KDP is piezoelectric, special care had to be taken to suppress mechanical ringing after the strong r.f. pulses.

In Chapter VI the experimental apparatus is reviewed briefly. Of greatest interest here is possibly the NMR r.f. equipment, which was of the single-coil, pulsed type, with r.f. power at two generally quite different frequencies alternately being applied to the same coil. The system offered a wide choice of r.f. pulse sequences and field

modulation (phase and amplitude), and pulsed audio fields could also be applied from a second coil. The transient signal from the r.f. coil was amplified, phase sensitively detected, and captured by a boxcar integrator. Special problems arose due to the finite time required for the receiver to recover from the strong transmitter pulse. A brief description is given of measures taken to protect the receiver and reduce the recovery time, including a transmission line arrangement with cables of specific lengths in relation to the r.f. wavelength.

II. SOME CONCEPTS AND TECHNIQUES IN PULSED NMR

Below is a short review of subjects of specific pertinence to the present work. In this chapter, emphasis is on a single spin species, while coupling between different spin species is considered in more detail in the next chapter.

II-A. Spin Temperature

The concept of spin temperatures distinct from the lattice temperature is essential in the present work, and accounts for much of the success achieved in applications of pulsed NMR. Consider f.ex. a spin system characterized by the hamiltonian

$$\mathcal{H} = \mathcal{H}_o + \mathcal{H}_1$$

where $\mathcal{H}_o$ represents a sum of Zeeman and quadrupole interactions, either of which can be zero, and $\mathcal{H}_1$ represents magnetic dipole-dipole interactions between the spins. R.f. fields are assumed absent. In solids, motional narrowing is generally not capable of causing large reductions in the local fields, and in many important experimental applications, situations arise where $\langle \mathcal{H}_o \rangle \lesssim \langle \mathcal{H}_1 \rangle$. A quantum mechanical description of the coupled spin system then represents a many-body problem of great complexity, but it lends itself ideally to treatment by thermodynamics and statistical mechanics, which does not depend on a detailed knowledge of the structure of the system.

An extensive literature exists on the subject of spin temperatures, and in addition to references given in this chapter, discussion will be found in the article by Jeener[14] and in Goldman's book.[15]

Single nuclear species in high field: $\langle \mathcal{H}_o \rangle \gg \langle \mathcal{H}_1 \rangle$

In high fields, the spin system can be viewed as individual spins with energy levels defined by $\mathcal{H}_o$, while $\mathcal{H}_1$ causes the spin system to come into internal equilibrium. The spin-lattice relaxation time T_1 will be assumed along compared to the spin-spin relaxation time T_2. In thermal equilibrium with the lattice, the macroscopic observables of the system can be computed by the density matrix

$$\rho(T_L) \propto \exp(-\mathcal{H}_o/kT_L)$$

where T_L is the lattice temperature. Populations of the $\mathcal{H}_o$ eigenstates with energies E_i will be, f.ex.:

$$P_i(T_L) \propto \exp(-E_i/kT_L)$$

If the spin system is irradiated by a CW r.f. field causing transitions between energy levels E_i, the system is still describable by a spin temperature if the energy levels are equidistant,[16,17,18] and the new density matrix is

$$\rho(T_S) \propto \exp(-\mathcal{H}_o/kT_s) \qquad \text{(II-1)}$$

where T_S is different from T_L, and can be interpreted as the temperature of a spin system in internal equilibrium, weakly coupled to the lattice. The process of energy transport within the spin system (spin diffusion) is reviewed by Abragam.[18] Equation (II-1) also applies when strong r.f. pulses are applied to the sample, after the spin system has been allowed to attain internal equilibrium. Population inversions, caused by a π pulse, f.ex., are described by negative spin temperatures, which stand on the same footing as positive spin temperatures in this

formalism.[17] Equidistance of energy levels is not sufficient for the spin temperature concept to be meaningful during r.f. irradiation, and one must also require that off-diagonal elements of ρ be zero. This follows from the time independence of macroscopic observables in thermal equilibrium. The spin temperature concept does not apply, therefore, during free induction decay following a $\pi/2$ pulse, when a rapidly decaying transverse magnetization exists.

In an analysis of the spin temperature concept, Abragam and Proctor[16] concluded that it is convenient but dispensable in the high-field case with equidistant energy levels. If energy levels are non-equidistant due to quadrupole interaction, mutual spin flips are restricted from taking place due to energy conservation requirements, and the spin system can in general not reach internal equilibrium describable by a spin temperature different from that of the lattice, if originally in a non-equilibrium state. In low fields, however, the spin temperature approach yields results that are definitely non-trivial and not attainable by alternative methods.

Single nuclear species in low field $\langle \mathcal{H}_o \rangle \lesssim \langle \mathcal{H}_1 \rangle$

Assume for simplicity that $\mathcal{H}_o$ includes only magnetic interaction with a magnetic field which is lowered towards zero. When the external field approaches the local dipolar fields in magnitude, the simple Maxwell-Boltzmann approximation of coupled spins with individually defined energy levels breaks down. In low and zero applied field the Gibbs description in terms of eigenstates and energy levels of the whole spin system must be used, and although the formal description in terms of spin temperature is unchanged, the correctness of the spin

temperature assumption is not self evident. Abragam[18] has reviewed experiments which demonstrate clearly the inadequacy of the Maxwell-Boltzmann description at low fields, and also the viability of the spin temperature concept down to zero applied field. He discusses these results in terms of the ergodic theorem.

Analogies with the low-field results in the laboratory frame can be drawn in the cases of low effective fields in coordinate systems rotating in synchronium with the precessing spins, cfr. below.

Spin temperatures in the rotating coordinate system

Redfield[10] found that the BPP theory[19] does not apply when the rotating r.f. field component H_1 applied at the spin resonance frequency is so strong that the transition is saturated (i.e., $\gamma^2 H_1^2 T_1 T_2 \gg 1$). He showed that his results were consistent with the assumption of a spin temperature in the rotating frame (i.e., the coordinate system where the r.f. field vector rotating in the same sense as spin precession is stationary). In support of this assumption, he argued that the spin system will evolve towards the most probable state, which is characterized by a Boltzmann distribution between energy levels in the rotating frame. Abundant experimental support for his hypothesis has since been accumulated, and Goldburg[20] and Slichter and Holton[21] have extended his results to apply in cases where r.f. field amplitudes are considerably lower than the local fields. In adiabatic demagnetization experiments in the rotating frame, Anderson and Hartmann[22] have shown that the spin temperature assumption applies even in zero applied r.f. field. Since the applied static field H_o disappears in the rotating frame on resonance,[23] the only remaining fields in the latter case

are the local dipole fields, and the rotating frame temperature is defined by the state of the dipole-dipole system, in analogy with the zero field case in the laboratory frame. Thus, in high fields and with no r.f. irradiation, the total spin system can be described by two spin temperatures which may be quite different, one pertaining to the Zeeman and one to the dipole-dipole subsystem. This aspect has been studied in detail by several authors,[24-27] who also treat the case of several spin species with weak mutual interaction. In strong r.f. fields one can similarly define two Zeeman subsystems, and in the spin lock state described below one may have a lab frame Zeeman subsystem at infinite temperature and a rotating frame Zeeman subsystem at very low temperature.

After all this, it is somewhat alarming that Waugh, et al. recently have performed experiments[28] which demonstrate violation of the spin temperature concept. Their experiments exploit microreversibility in the spin system, however, corresponding to fine grain averaging in phase space, whereas the double resonance applications in this work and all other experiments quoted above depend on coarse grain averaging.

So far, only mutually isolated or weakly interacting spin species have been treated. The important case of strongly coupled spin species will be discussed separately in connection with double resonance applications (cfr. Section III-B).

II-B. Spin Locking and Adiabatic Demagnetization in the Rotating Frame (ADRF)

The procedures of spin locking and ADRF are used extensively in obtaining the low spin temperatures in the rotating frame which are necessary in high-sensitivity nuclear double resonance and in studies of ultraslow motion by the ADRF technique described below.

The spin-lock state can be produced several ways, and will depend on whether the laboratory frame spin hamiltonian is Zeeman or quadrupolar Consider for simplicity pulsed spin locking in the pure Zeeman case ($I = 1/2$ or cubic crystal), which is of specific interest here. Only a qualitative description will be given, but a quantitative analysis of spin locking and adiabatic demagnetization in this case will be found in the paper by Anderson and Hartmann:[22]

The procedure is most easily understood when viewed in the rotating frame shown in Fig. II-1. Starting out with a thermal equilibrium magnetization M_o along the laboratory frame magnetic field $H_o \parallel Z$, an r.f. field is applied on resonance at time $t = 0$. In the rotating frame, the r.f. field vector H_1 is stationary along the z-axis and will be assumed much larger than the local fields H_L. (A more stringent definition of H_L will be given later.) M_o will precess about H_1, and after a time $t_w = \frac{\pi}{2\gamma H_1}$ it will point along the y-axis. γ is the effective gyromagnetic moment in the rotating frame, which is equal to the one in the laboratory frame when the laboratory frame hamiltonian is purely Zeeman. At time $t = t_w$, the phase of the r.f. field is switched by 90°, and H_1 becomes parallel with M_o. If the r.f. is left on, the magnetization will decay only slowly (time constant $\approx T_1$), and one may

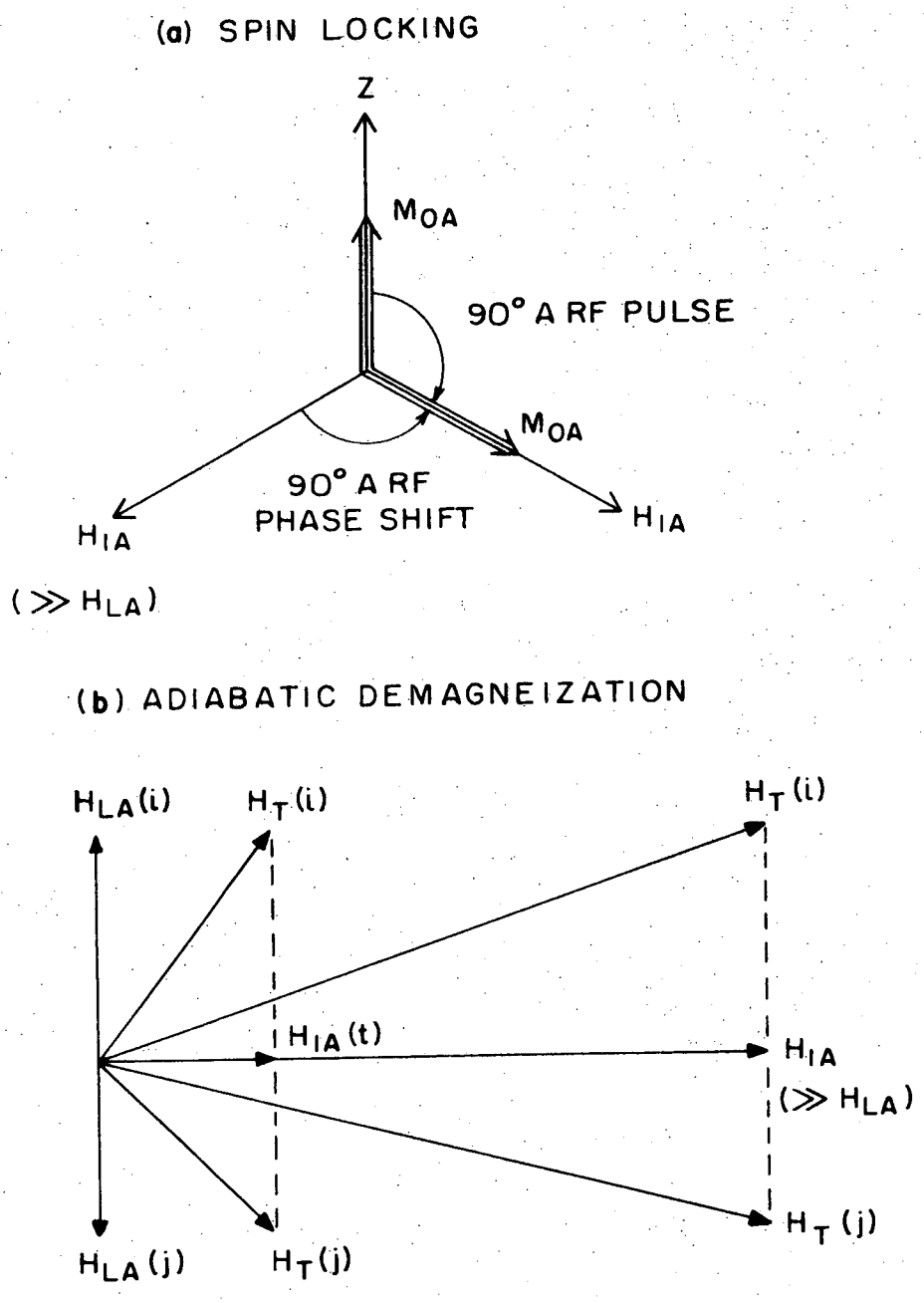

XBL 676-4150

Fig. II-1. ADRF process viewed from a frame rotating at the A spin Larmor frequench (after D. A. McArthur[12]).

say that the magnetization is "locked" to H_1. Since H_o and $H_1 \gg H_L$, the initial magnetization in the spin-lock state will differ only little from the original laboratory frame magnetization, and the process is essentially isentropic. The initial spin temperature in the spin lock state is then:

$$T_S(t_w) = T_L \cdot \frac{H_1}{H_o} \ll T_L \qquad \text{(II-2)}$$

and a cooling has been effected. Suddenly turning off the r.f. results in a free induction decay, since the spins then are free to dephase. The free induction signal amplitude will be $\propto T_s^{-1}$.

Adiabatic demagnetization in the rotating frame, or ADRF, proceeds exactly as described above, but instead of suddenly cutting off the r.f. power after the spin-lock state has been obtained, the amplitude is smoothly reduced to zero in a time much longer than T_2. Thermal equilibrium within the spin system is then maintained during demagnetization, which is isentropic, and the spin temperature will be proportional to the instantaneous effective field in the rotating frame:[22]

$$T_S = T_L \left(\frac{H_1^2 + H_L^2}{H_o^2 + H_L^2} \right)^{1/2} \qquad \text{(II-3)}$$

After demagnetization, the temperature is ($H_o \gg H_L$):

$$T_S \cong T_L \cdot \frac{H_L}{H_o} \gg T_L \qquad \text{(II-4)}$$

The explicit form of H_L follows from the quantitative treatment leading to Eq. (II-3):

$$H_L^2 = \mathrm{Tr}\{\mathcal{H}_d'^2\}/\mathrm{Tr}\{M_z^2\} \qquad \text{(II-5)}$$

Here $\mathcal{H}_d$ is the usual two-particle dipole-dipole coupling hamiltonian, and the dash indicates that only secular terms are to be included (due to their rapid time dependence in the rotating frame, the nonsecular terms effectively average to zero). In Eq. (II-5), one also has:

$$M_z \equiv \gamma I_z$$

The demagnetization process is shown in Fig. IIb: Due to the finite linewidth, individual spins experience off-resonance fields in the rotating frame, and in Fig. IIb are shown examples of spins with resonance frequencies slightly higher or lower than the center frequency. During demagnetization preferential alignment along $H_1 (\gg H_L)$ is thus converted to preferential alignment of individual spins along their local fields (corresponding to the secular parts of the dipole interaction). Since the local fields are random, the net magnetization is zero even though this "dipolar" state is highly ordered. The initial dipolar order after ADRF will decay slowly, and one can define a dipolar spin lattice relaxation time T_{1dip} which is distinct from the spin lattice relaxation times in the spin-lock state, $T_{1S.L.}$ and in the laboratory frame: T_1.

The spin temperature in the dipolar state can be sampled by:

1) Adiabatic remagnetization to an r.f. field $H_1 \gg H_L$, followed by suddenly cutting off the r.f. field. A free induction signal ensues, in analogy with the sampling of the spin-lock state temperature. The maximum signal amplitude is $\propto T_S^{-1}$.

2) Application of an r.f. θ pulse, where $\pi/4 < \theta < \pi/2$, cfr. Anderson and Hartmann.[22] The θ pulse stimulates a free induction signal

which starts from zero immediately following the θ pulse, grows to a maximum, and decays. This "dipolar signal" lasts a time $\approx T_2$, and the maximum signal amplitude is $\propto T_S^{-1}$. The qualitative shape of the dipolar signal and its phase relationship to the applied r.f. follow from simple physical arguments, but space does not allow further discussion of this subject.

A common feature of the free induction decays derived from the spin-lock and dipolar states is that the precessing magnetization is in phase with the r.f. that precedes the free induction decay. This is in contrast to the free induction decay following a $\pi/2$ pulse applied to a spin system in thermal equilibrium in the laboratory frame ("Zeeman signal"), where the magnetization is in exact quadrature. This feature allows discrimination between "Zeeman" and "dipolar" signals by using phase sensitive detection.

Finally, it should be mentioned that alternative methods of spin locking and ADRF have been demonstrated,[29] based on adiabatic fast passage. A spin system in a strong resonant field can also be brought into a spin lock state by exchanging energy with another spin system which is at low temperature. An example of this is the double resonance method outlined in Chapter IV. The pulse procedures described above have also been applied to pure quadrupole systems: $\mathcal{H} = \mathcal{H}_Q + \mathcal{H}_1$, $(\langle \mathcal{H}_Q \rangle \gg \langle \mathcal{H}_1 \rangle)$. $\mathcal{H}_Q$ represents the quadrupolar interaction of the nucleus with the local electric field gradient, while $\mathcal{H}_1$ represents the coupling between spins (e.g., dipole-dipole). Spin locking in the pure quadrupole and pure Zeeman cases differ in some respects. In the quadrupole case with $I = 3/2$, $\eta = 0$, f.ex., the effective gyromagnetic

ratio in the rotating frame is $\sqrt{3}\,\gamma$, where γ is the gyromagnetic ratio in the laboratory frame. This implies that the 90° pulse duration will be

$$t_w = \frac{\pi}{2\sqrt{3}\,\gamma\,H_1}$$

In the spin-lock state, there will be 2 counter-rotating frames, with a magnetization in each that couples to the r.f. field component that is stationary in each frame. Such differences have no import on practical applications, however, and as has been shown explicitly[30] for spin 1 and 3/2, the procedures apply equally well to Zeeman or quadrupole systems.

II-C. Detection of Ultraslow Atomic Motion

Motion of nuclei or groups of nuclei leads to two types of detectable effects in NMR, which have been used to great advantage in the study of microscopic dynamics in liquids and solids:

First, rapid motion leads to an effective averaging of local dipolar fields, and the linewidth is reduced to

$$\Delta\omega = (\Delta\omega_o)^2 \cdot \tau \qquad \text{(II-6)}$$

where $(\Delta\omega_o)$ is the rigid lattice linewidth and τ is the correlation line for the motion ("time between jumps"). Narrowing becomes effective when $\tau \ll (\Delta\omega_o)^{-1} = (T_2)_{R.L.}$, where $(T_2)_{R.L.}$ is the rigid lattice spin-spin relaxation time (typically ≈100 μsec).

Second, fluctuations in the local field seen by the moving nuclei leads to spin-lattice relaxation, as described by the following expression due to Bloembergen, Purcell and Pound[19] (BPP):

$$(T_1)^{-1}_{motion} \propto \frac{\Delta\omega_o \cdot \tau}{(1 + \omega_o^2 \cdot \tau^2)} \qquad \text{(II-7)}$$

where $(T_1)^{-1}_{motion}$ is the motional contribution to the total spin-lattice relaxation rate $(T_1)^{-1}$, and ω_o is the Larmour frequency (Zeeman systems). The temperature dependence of τ can be inferred from Eq. (II-7) by measuring T_1 as a function of temperature, if the rate $(T_1)^{-1}_{motion}$ is the dominant contribution to the relaxation:

$$(T_1)^{-1} = (T_1)^{-1}_{motion} + (T_1)^{-1}_{other}$$
$$(T_1)^{-1}_{motion} \gg (T_1)^{-1}_{other} \qquad \text{(II-8)}$$

From Eq. (II-7), the maximum relaxation rate occurs when $\tau \approx 1/\omega_o$, which is 10^{-7} - 10^{-8} sec in usual NMR applications.

Thus, conventional NMR methods can be used to detect motion with $\tau \lesssim 10^{-4}$ sec. In contrast, ultraslow motion techniques allow detection of motion where $\tau \lesssim T_1$, where T_1 may be minutes or hours. Below is given a qualitative introduction to the physical principles behind the ultraslow motion methods. For a recent review of this subject, the reader is referred to the article by Ailion.[31]

The trick used in all ultraslow motion techniques is to reduce the spin transition frequency ω_o in Eq. (II-7) to very low values. As ω_o decreases, the maximum in $(T_1)^{-1}_{motion}$ will shift to longer τ's, and contributions from slow motion will be more pronounced.

To date, all ultraslow motion experiments have been performed in the rotating frame: In pulsed spin-lattice relaxation measurements, one starts out with a spin system which is far from thermal equilibrium with the lattice. Since low fields are necessary in the ultraslow motion measurements, spin system cooling by adiabatic demagnetization is indicated. This is more quickly and efficiently performed in the

rotating frame, where very low effective fields can be obtained (cfr. Section II-B). At the same time, one retains good detectability of NMR signals due to the high laboratory frame transition frequencies.

The BPP expression (Eq. (II-7)) was derived under the assumption of high-field conditions ($\omega_o \gg \Delta\omega_o$). When $\omega_o \to \Delta\omega_o$, the description of the spin system in terms of coupled individual spins with well-defined energy levels breaks down and the relevant eigenstates will be those of the entire coupled spin system. A more correct description is then obtained by replacing ω_o with $\Delta\omega_o$ in Eq. (II-7). Combining Eqs. (II-7) and (II-8), one then finds that the relaxation rate contribution due to motion will dominate the other contributions if

$$\tau < \left(\frac{\Delta\omega_o}{\omega_o}\right)^2 (T_1)_{other} \simeq (T_1)_{other} \qquad \text{(II-9)}$$

in the slow motion limit ($\omega_o\tau \gg 1$). This is the fundamental condition for the applicability of ultraslow motion methods.

Some reservations must be made on results derived from the BPP expression (Eq. II-7), however. Not only was Eq. (II-7) derived for the high-field case, but it also describes a situation where perturbations due to the motion are inefficient in relaxing the spins, such that many jumps are required for complete loss of order ("weak collisions"). The weak collision theory applies when $\tau \ll T_2$, both in high and low fields. In situations where $\tau \gg T_2$ and $\omega_o \simeq \Delta\omega_o$, however, few jumps are sufficient in destroying spin order, since the dipole-dipole interaction no longer can be considered as a perturbation term in the total hamiltonian of the spin system ("strong collisions"). It follows that in the limits of weak or strong collisions, one will have $\tau \ll (T_1)_{motion}$ and $\tau \simeq (T_1)_{motion}$ respectively.

A strong collision theory for ultraslow motion in weak fields was first proposed by Slichter and Ailion,[32] who applied their theory to vacancy diffusion and molecular reorientation. (Later theories involving weak and strong collisions are reviewed in the article by Ailion[31].) Slichter and Ailion used an approach leaning heavily on the spin temperature concept in the rotating frame. The requirement of thermal equilibrium within the spin system between each jump then limits the region of validity of their results to $\tau \gg T_2$. They also assumed that the jumping time is much less than a Larmour period, which means that spins retain their original orientation during jumps ("sudden approximation"). In practice, jumping times are of the order of 10^{-12} sec. Slichter and Ailion found that in the case of molecular reorientation, the spin-lattice relaxation rate due to motion can be written

$$(T_1)^{-1}_{\text{motion}} = \frac{1 - p}{\tau} \qquad \text{(II-10)}$$

where p is a measure of the change of local field seen by a spin in a single jump, i.e., of the "strength" of the collision. If the field after the jump is completely random compared to the original field, $p = 0$ and $(T_1)_{\text{motion}} \simeq \tau$.

Several experimental methods can be used to detect ultraslow motion,[31] and two procedures that are much used are spin locking and ADRF, which create low temperature spin states in weak fields (cfr. Section II-B): Slow motion and other mechanisms, such as spin diffusion to paramagnetic impurities, cause irreversible loss of order in the spin lock and dipolar states. This leads to a gradual increase in the

rotating frame spin temperatures, which are easily sampled (in relative units) by one of the methods outlined in Section II-B. The rate of change of the spin temperatures defines the spin lock and dipolar state spin-lattice relaxation times, which can be measured by repeating the spin lock or ADRF cycle with different time spans between preparation and sampling of the spin system order in the rotating frame.

Since slow motion contributions to the relaxation in low fields are strongly dependent on low-frequency perturbations, discrimination between relaxation rate contributions due to slow motion and other mechanisms can be achieved via the dependence of the relaxation rate on the transition frequency. The transition frequency can be varied by adjusting the r.f. field strength H_1 in the spin lock state. Alternatively, one can compare rotating frame and laboratory frame relaxation rates as a function of temperature, cfr. Section VIII-C. Strictly speaking, one must know how the two relaxation rates depend on the relaxation perturbations in the latter case. In cases where the classical spectral density analysis applies,[33] however, fluctuation frequency components at low frequencies ($\approx\Delta\omega_o$ or γH) are effective in causing relaxation in the rotating frame only, while perturbations with flat fluctuation spectra at NMR frequencies cause relaxation in both laboratory and rotating frames (see f.ex., the article by Leppelmeier and Hahn[34]).

III. NUCLEAR DOUBLE RESONANCE

Many elements have isotopes which possess a nonzero nuclear magnetic moment and thus are potential candidates for NMR studies. Due to low isotopic abundance or low transition frequencies (weak quadrupole interaction or low gyromagnetic ratio), however, many such isotopes cannot be detected by standard NMR techniques. NMR spectra or relaxation characteristics of such hard-to-detect nuclear species may often yield information which is unobtainable from studies on more easily detectable nuclei in the sample under study, and considerable effort has been spent on schemes to enhance NMR sensitivity.

One standard approach for detection of nuclear species with weak NMR signals is to use coherent signal averaging by electronic means, in conjunction with pulsed (Fourier transform) or CW spectroscopy. Here one will review an entirely different method, namely high-sensitivity nuclear double resonance, which represents one of the most striking and elegant applications of the spin temperature and spin subsystem concepts introduced in the previous chapter. In addition to yielding high detection sensitivity, double resonance makes possible a wide variety of studies on spin dynamics in solids.

In this chapter, emphasis will be on qualitative physical understanding of the phenomena involved. Lack of rigor or completeness is sought compensated for by the literature references. A general description of basic principles in nuclear double resonance is given in Section III-A. In Section III-B, attention is focused on the specific double resonance method used in this work (double resonance after adiabatic demagnetization in the rotating frame). A transient double resonance phenomenon of interest

in a later chapter (cfr. Section X-C), is reviewed in Section III-C.

III-A. General

The theory of high-sensitivity nuclear double resonance was first developed and verified experimentally a decade ago by Hartmann and Hahn,[35] and many nuclear double resonance methods based on the same fundamental principles have been developed since. In its simplest form, nuclear double resonance involves two spin species in a given sample:

An abundant spin species which is easily observed by standard NMR techniques, henceforth called "A" spin species.

The spin species to be studied, which is undetectable by conventional methods. Henceforth called "B" spin species.

The basic principle in nuclear double resonance is to study the B spin species indirectly, by monitoring their effect on the easily observable A spins when the sample is irradiated near a B spin transition frequency. Resonantly absorbed energy in the B spin system must be transferred to the A spin system, and the necessary A-B coupling is obtained by proper adjustment of external radio frequency (r.f.) and DC magnetic field parameters.

The double resonance analysis of Hartmann and Hahn was based on the assumption that the A and B spin species can be treated as separate thermal reservoirs with well defined temperatures, also during A-B energy transfer. This assumption is not trivial, in light of the non-equilibrium nature of the problem and possible low B spin diffusion rates, but it has proved valid in all double resonance investigations to date, and the thermal reservoir model will be used extensively in the following. In Fig. III-1, the A and B spin species are represented

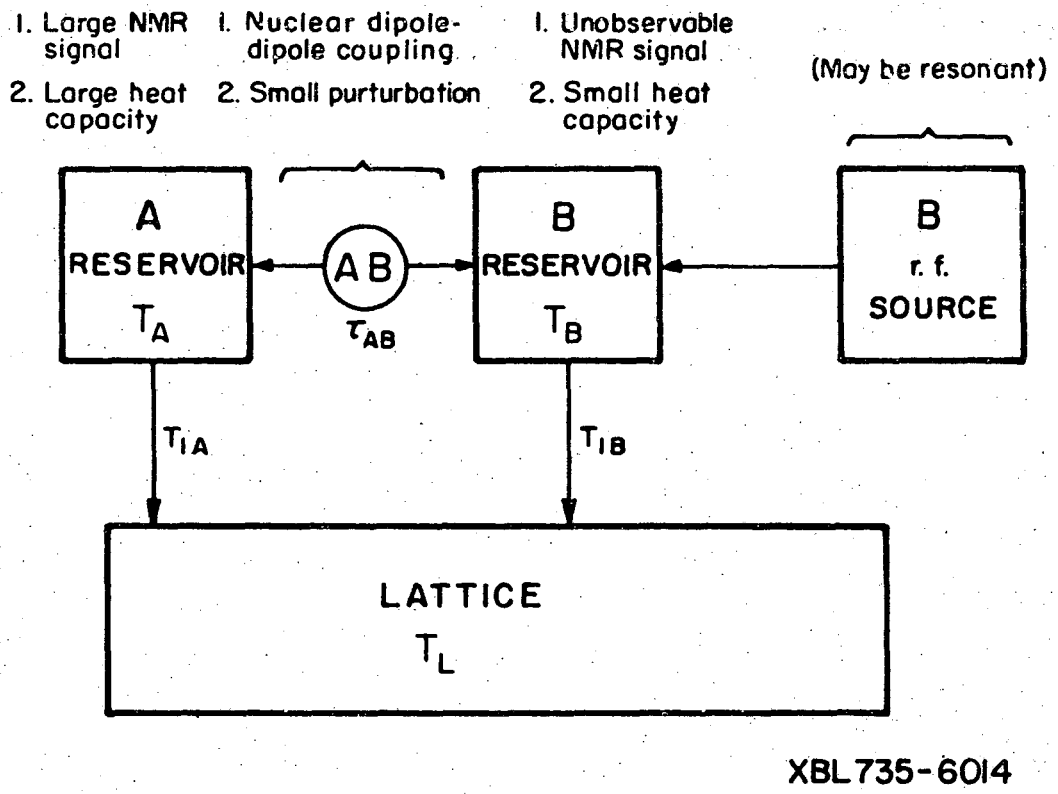

Fig. III-1. Thermal reservoir model of the double resonance process.

by thermal reservoirs with temperatures T_A and T_B. The thermal links to the lattice represent A and B spin-lattice relaxation, and the thermal link between the A and B reservoirs can be opened or closed at the discretion of the experimenter (by adjustment of external field parameters such that A-B spin flip-flops induced by magnetic dipolar coupling terms of the type $S_{A+} \cdot S_{B-}$ conserve enegy).

A double resonance cycle starts by adiabatic demagnetization of the A spins, which brings the A reservoir to a low temperature (a few mdeg K). In the absence of coupling to other spin reservoirs, T_A will approach the lattice temperature with a time constant T_{1A}, the A spin-lattice relaxation time. In spin calorimetry, the lattice can be considered a thermal reservoir of infinite heat capacity, and the lattice temperature will remain constant. While the A reservoir is still at low temperature, the thermal switch between the A and B reservoirs is closed, and a strong, oscillating magnetic field is applied to the sample. If the frequency is well separated from the A transition frequencies, but matches a B transition frequency, energy will be absorbed in the B reservoir and transferred to the A reservoir via the A-B coupling. A more rapid rise in the A reservoir temperature T_A results, as long as the B reservoir is kept "hot". T_A can easily be sampled (cfr. specific examples given in Chapter II), and the B spin resonance can be detected by monitoring T_A at a fixed time t_b after initiation of each double resonance cycle. When the B search field is far off resonance, no B reservoir heating will take place, and T_A will be the same at the

moment of temperature sampling ($t = t_b$) whether the B search field is on or off.

Instead of continuous B reservoir heating during the double resonance process, the B reservoir may be repeatedly be heated and brought in contact with the A reservoir. Due to the low B spin abundance and/or transition frequencies, the B reservoir heat capacity is usually much less than that of the A reservoir, and the increase in T_A will be small during each A-B contact. In practice, a large number (10^3-10^4) of thermal contacts with B reservoir re-heating can be made during each double resonance cycle, and a detectable heating effect on the A reservoir results.

Nuclear double resonance owes its high sensitivity to the integration effect obtained by the gradual transfer of energy from the B to the A system, with accumulation in the A system. One important parameter for the obtainable sensitivity is obviously the maximum length of time that can be allowed for B-A energy transfer, which is of order T_{1A}, the A spin-lattice relaxation time. (If sampling of T_A is made at a time $t_b \gg T_{1A}$, spin-lattice relaxation will have brought T_A close to the lattice temperature, which is very high in this context. Consequently the A spin signal $S_A \propto T_A^{-1}$ will be very small or unobservable.) Clearly, very long T_{1A}'s are desired for high double resonance sensitivity. On the other hand, the preparation of the low A spin temperature at the beginning of each double resonance cycle then becomes very time consuming, since one must allow the A spins to polarize before the adiabatic demagnetization process. A spin cooling can be speeded up f.ex. by using a superconducting polarizing magnet or by cross-relaxation between the A reservoir and a third, pre-cooled reservoir. Hartmann and Hahn[35]

have estimated the detection sensitivity that can be achieved by nuclear double resonance. Using typical parameter values for solids, they find an ultimate sensitivity capable of detecting spins in concentrations down to approximately $2 \cdot 10^{13}$ μ_B/cm^3. In practice, sensitivities of 10^{14}-10^{16} $\mu B/cm^3$ have been achieved, representing improvements of 3 to 5 orders of magnitude over conventional NMR.

Compared to alternative methods, double resonance suffers certain drawbacks: It requires the presence in the sample of a nuclear species with a strong NMR signal. Also, interpretation of the double resonance lineshape is complicated, and it may under certain circumstances be impossible to establish the A-B coupling, due to so-called "spin quenching".[13,36] When the method does apply, however, it offers specific advantages:

The information gathering rates in rare spin spectroscopy can be several orders of magnitude higher than those obtainable by signal averaging.

Low-field double resonance methods have been developed which are capable of measuring weak quadrupoles couplings in amorphous or powdered samples. Sensitivity-enhancement by the high fields obtainable in superconducting magnets cannot be used in such cases.

Double resonance methods can be used to obtain information about rare and abundant spin species in solids extending far beyond their spectra. Examples are measurements of B spin transverse and longitudinal relaxation times, T_{2B} and T_{1B}, and fluctuation spectra of the A-B dipolar coupling hamiltonian (cfr. Ref. 11).

The proliferation of double resonance methods has been more than matched by a proliferation of acronyms; a few of those most commonly

encountered are listed:

SEDR: Spin Echo Double Resonance. A precursor of the Hartmann and Hahn method. Essentially different in principle from methods reviewed in this chapter, and not as sensitive in solids.

SLDR: Spin Lock Double Resonance. The original Hartmann and Hahn method.

ADRF-DR: Double Resonance after Adiabatic Demagnetization in the Rotating Frame (cfr. Section III-B).

LOWDOR: Low Field Double Resonance. A-B coupling is established in low or zero external magnetic field and zero electric field gradient. Encompasses LNDRF (Low Field Nuclear Double Resonance via Rotational Frames) and LNDLF (Low Field Double Resonance via Laboratory Frame).

In connection with SLDR, ADRF-DR and LOWDOR, one may encounter RSDR (Rotary Saturation Double Resonance), which is usually termed audio resonance in this work, and the general RFDR (Rotating Frame Double Resonance).

III-B. Nuclear Double Resonance Following Adiabatic Demagnetization in the Rotating Frame (ADRF-DR)

The ADRF-DR method was used extensively in this thesis. Much of the discussion below also applies to SLDR and LOWDOR.

The ADRF-DR pulse sequence in one double resonance cycle is shown in Fig. III-2: First, the A reservoir is brought to a low temperature through ADRF. While the A reservoir is still at low temperature, a search radio-frequency (r.f.) field is applied to the B system, and finally the A spin temperature is sampled by the application of a θ pulse. For a double resonance heating of the A reservoir to take place, one can list the following requirements which will be treated

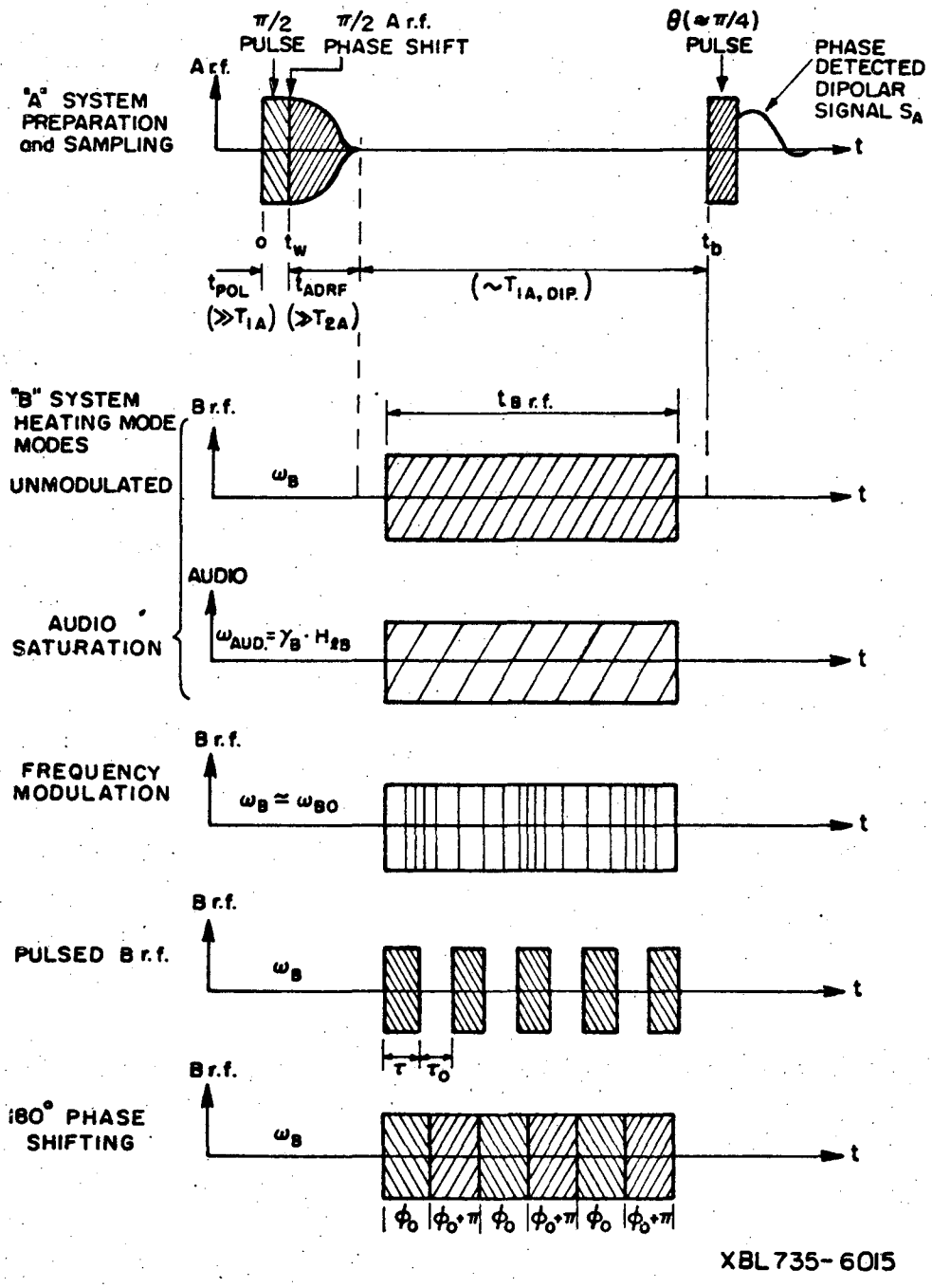

Fig. III-2. ADRF double resonance pulse combinations.

separately below: a) Energy must be conserved during the A-B spin flip-flop which constitutes the A-B cross-coupling mechanism. b) A nonzero time averaged coupling must exist between the A and B spin system. c) The B spin system must be kept disordered ("hot") during the double resonance process.

a. A-B Energy Conservation

In spin flip processes where one A and one B spin is involved, one must create A and B spin system states with common transition frequencies, so that net energy absorption in a flip-flop is zero. This is easily achieved in the rotating frames by adjusting the strengths of the applied resonant r.f. fields. In the A rotating frame after ADRF the A system will have a spectrum of transition frequencies determined by local magnetic dipole fields. The spectral width can be described by the local dipolar field H_{LA}, which was defined in Eq. (II-5). In the B rotating frame, the B transition frequency is (assuming the B r.f. field applied on resonance $\omega_B = \omega_{Bo}$):

$$\omega_{B,\text{rot. frame}} = \gamma_{\text{eff},B} \cdot H_{1B}$$

where $\gamma_{\text{eff},B}$ is the effective gyromagnetic ratio in the rotating frame (cfr. Section V-A), and H_{1B} is the strength of the B r.f. field component, which is stationary in the B rotating frame. Thus, by adjusting the magnitude of H_{1B}, one can satisfy the matching condition (Hahn condition):

$$\gamma_A H_{LA} \simeq \gamma_{\text{eff},B} \cdot H_{1B} \quad . \tag{III-1}$$

If the B r.f. is applied off resonance, H_{1B} must be substituted by the effective field

$$H_{eB} = [(\omega_{Bo} - \omega_B)^2/\gamma^2_{eff,B} + H^2_{1B}]^{1/2} \qquad \text{(III-2)}$$

b. Strength of A-B Coupling

A and B spins couple by magnetic dipole-dipole interaction. Since the coupling process takes place in the A and B rotating frames, it is necessary to transform the dipolar interaction hamiltonian into the proper interaction representation and there determine the effect of those A-B coupling terms which do not average to zero. The following is a brief outline of McArthur's[12] treatment of the cross-relaxation problem.

Assume for simplicity that the A and B spin species possess no quadrupole moment, and neglect A and B spin-lattice relaxation. The high temperature approximation

$$\gamma_A H_o \ll kT_A$$

will always apply in the following.

In the laboratory frame, the total hamiltonian during the application of the B r.f. search field is:

$$\mathcal{H}_{lAB} = \mathcal{H}^A_z + \mathcal{H}^B_z + \mathcal{H}^{AA}_{dd} + \mathcal{H}^{AB}_{dd} + \mathcal{H}^B_{B\ r.f.} \qquad \text{(III-3)}$$

where $\mathcal{H}^A_z$ and $\mathcal{H}^B_z$ are the A and B spin system interactions with the static magnetic field H_o. $\mathcal{H}^{AA}_{dd}$ and $\mathcal{H}^{AB}_{dd}$ are the magnetic dipolar A-A and A-B interactions (in high-sensitivity nuclear double resonance, B-B interactions can be neglected), and $\mathcal{H}^B_{B\ r.f.}$ is the interaction of the B spin system with the applied r.f. field, assumed near the B transition frequencies. R.f. interaction with the A system will be negligible, since A and B laboratory frame transition frequencies are assumed widely different.

The standard technique[11,35] is to transform the laboratory frame density matrix ρ_{LAB} into the double rotating-frame representation, which is accomplished with the operator

$$T(t) = \exp[i(\mathcal{H}_z^A - \omega_B S_B)t] \qquad \text{(III-4)}$$

where ω_B is the angular frequency of the B r.f. In the following, I and S will be A and B spin operators, respectively. The new density matrix in the rotating frame will then evolve as determined by the approximate Liouville equation:

$$\frac{d\rho'_R}{dt} \cong -i[\mathcal{H}'_R , \rho'_R] \qquad \text{(III-5)}$$

The approximation involved is that only the secular parts of the transformed hamiltonian

$$\mathcal{H}'_R = T(t)\, \mathcal{H}_{LAB}\, T(t)^{-1} - (\mathcal{H}_z^A - \omega_B S_Z)$$

have been included. The discarded parts have a rapid time dependence, and their effect averages to zero (here assuming slowly varying spin temperatures). One finds

$$\mathcal{H}'_R = \mathcal{H}_z^{B'} + \mathcal{H}_{B\ r.f.}^{B'} + \mathcal{H}_{dd}^{AA}(s) + \mathcal{H}_{dd}^{AB}(s) \qquad \text{(III-6)}$$

where the s in parentheses indicate secular parts. $\mathcal{H}_B^{B'}$ and $\mathcal{H}'_{B\ r.f.}$ represent the B spin interaction with the effective magnetic field in the B rotating frame, and $\mathcal{H}_{dd}^{AA}(s)$ and $\mathcal{H}_{dd}^{AB}(s)$ are the secular parts of the A-A and A-B magnetic dipolar interactions. Equation (III-6) can be simplified further by applying the rotation $R(\theta) = \exp(-i\theta Sy)$, which tilts the coordinate system in the B rotating frame such that the new z-axis coincides with the effective magnetic field vector

$\bar{H}_{eB}$ (cfr. Fig. III-3). In this new coordinate system one finally has:

$$\frac{d\rho_R}{dt} = -i[\mathcal{H}_R , \rho_R]$$

where

$$\mathcal{H}_R = \mathcal{H}_d^A(s) + \mathcal{H}_{dz}^{AB} + \mathcal{H}_{dx}^{AB} + \mathcal{H}_e^B$$

with (III-7)

$$\mathcal{H}_{dz}^{AB} = -\left(\sum_{i,k} A_{ik}^{AB} I_{zi} S_{zk}\right) \cos\theta = \cos\theta \, \mathcal{H}_{lz}$$

$$\mathcal{H}_{dx}^{AB} = -\left(\sum_{i,k} A_{ik}^{AB} I_{zi} S_{xk}\right) \sin\theta = -\sin\theta \, \mathcal{H}_{lx}$$

$$\mathcal{H}_e^B = -\omega_{eB} S_z = -\gamma_{eff,B} \cdot H_{eB} \cdot S_z$$

The A_{ik}^{AB} are standard A-B dipolar coupling coefficients.

In Eq. (III-7), $\mathcal{H}_d^A(s)$ represents the A dipolar reservoir, the temperature of which is monitored to detect double resonance, and $\mathcal{H}_e^B$ represents the B Zeeman reservoir in the B rotating frame. $\mathcal{H}_{dz}^{AB}$ and $\mathcal{H}_{dx}^{AB}$ are obvious candidates for providing A-B coupling, but $\mathcal{H}_{dz}^{AB}$ commutes with $\mathcal{H}_e^B$. One finds that AB coupling is provided by $\mathcal{H}_{dx}^{AB}$, while $\mathcal{H}_{dz}^{AB}$ is coupled to the A dipolar reservoir only, and can be lumped with it in a single dipole-dipole reservoir with spin temperature T_{ss} and hamiltonian

$$\mathcal{H}_{ss} \equiv \mathcal{H}_d^A(s) + \mathcal{H}_{dz}^{AB} \qquad \text{(III-8)}$$

As discussed by McArthur,[37] it is reasonable to assume that the B system is describable by a spin temperature T_B during cross-relaxation, at least when the B r.f. is applied on resonance ($\omega_B = \omega_{Bo}$), and the density matrix for the ensemble of A and B spins can be approximated by

$$\rho_R(t) = \exp[-\hbar(\mathcal{H}_{ss}\beta_{ss}(t) + \mathcal{H}_{eB} \cdot \beta_B(t))]/Tr\ \{1\}$$

where

$$\beta_{ss}(t) = \frac{1}{K\,T_{ss}(t)} \quad ; \quad \beta_B(t) = \frac{1}{K \cdot T_B(t)}$$

In order to calculate the effect of the cross relaxation term $\mathcal{H}_{dx}^{AB}$ on the dipolar reservoir temperature T_{ss}, it is convenient to transform into a new interaction representation by applying

$$T_I(t) = \exp[i(\mathcal{H}_{ss} + \mathcal{H}_{eB})t]$$

The new density matrix will then have the equation of motion

$$\frac{d\rho^*}{dt} = -i[\mathcal{H}^*(t)\ ,\ \rho^*] \qquad \text{(III-9)}$$

where

$$\mathcal{H}^*(t) = -\sin\theta \sum_{i,k} A_{ik}^{AB}\, I_{zi}(t)(S_{xk}\cos\omega_{eB}t + S_{yk}\sin\omega_{eB}t) \qquad \text{(III-10)}$$

and

$$I_{zi}(t) = e^{i\mathcal{H}_{ss}t}\, I_{zi}\, e^{-i\mathcal{H}_{ss}t} \qquad \text{(III-11)}$$

The time evolution of T_{ss} is linked to that of $\rho^*(t) = \rho_R(t)$. From Eq. (III-9) it is apparent that $\mathcal{H}^*(t)$ must be static or slowly varying in order to cause a slowly varying $\rho^*(t)$. This is possible if $I_{zi}(t)$ (which represents the fluctuating dipolar fields at the B spin sites, due to the A spins) has Fourier frequency components at ω_{eB}.

Using the master equation and second order perturbation theory, it can be shown that:[37]

$$\frac{d}{dt}\langle \mathcal{H}_{ss} \rangle \cong - \frac{1}{Tr\{1\}} \int_0^\infty d\tau \; Tr \left\{ \mathcal{H}_{ss} \left[\mathcal{H}^*(0), \left[\mathcal{H}^*(-\tau) \; , - \frac{\hbar \mathcal{H}_{ss}}{kT_{ss}} - \frac{\hbar \mathcal{H}_e^B}{kT_B} \right] \right] \right\}$$

This can be related to the rate of change of T_{ss}:

$$\frac{d}{dt}\langle \hbar \mathcal{H}_{ss} \rangle = - \frac{\hbar}{kTr\{1\}} Tr\{\mathcal{H}_{ss}^2\} \frac{d}{dt} (T_{ss}^{-1})$$

to yield the AB cross-relaxation time τ_{AB} in terms of the correlation function (for definition of $\mathcal{H}_{1x}$, See Eq. (III-7):

$$g_x(\tau) = Tr\{\mathcal{H}_{1x} \mathcal{H}_{1x}(\tau)\} \qquad \text{(III-12)}$$

τ_{AB} is defined by

$$\frac{d}{dt} (T_{ss}^{-1}) = - \frac{\varepsilon}{\tau_{AB}} (T_{ss}^{-1} - T_B^{-1}) \qquad \text{(III-13)}$$

where ε is the ratio of the B and A reservoir heat capacities:

$$\varepsilon = \frac{C_B H_{eB}^2}{C_A \cdot H_{LA}^2} \qquad \text{(III-14)}$$

C_A and C_B are the nuclear Curie constants.

McArthur, Hahn and Walsted[11] found for Ca-F in CaF_2 that a $g_x(\tau)$ proportional to the Lorentzian

$$f(\tau) = (1 + \tau^2/\tau_c^2)^{-1} \qquad \text{(III-15)}$$

gave a very good fit to the experimental data, and similar results have since been reported[38] for the Li-F coupling in LiF. With the form (Eq. (III-15)), the cross relaxation rate becomes:

$$\tau_{AB}^{-1} = \frac{\pi}{2} \sin^2\theta \, \langle \Delta\omega_B^2 \rangle_{BA} \, \tau_c(\theta) \, e^{-\omega_{eB}\tau_c(\theta)} \qquad \text{(III-16)}$$

where θ is the angle between $\vec{H}_{eB}$ and the laboratory z-axis (cfr. Fig. III-3) and $\langle \Delta\omega_B^2 \rangle_{BA}$ is the VanVleck second moment due to AB-coupling.

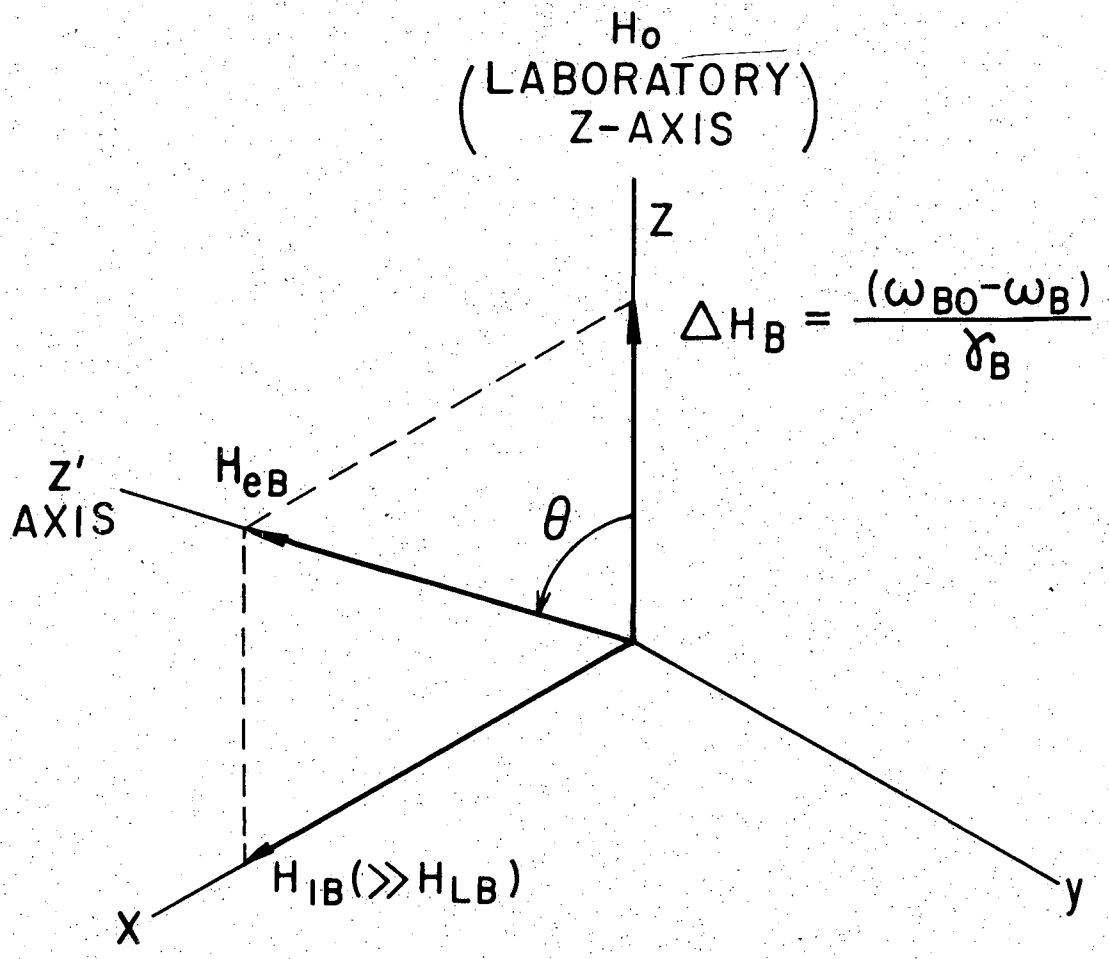

XBL 676-4154

Fig. III-3. Definition of the B spin effective field in the rotating frame, H_{eB}, viewed from a frame rotating at the B r.f. frequency ω_B; the z' axis is the frame in which the zero-order B Hamiltonian is diagonal (after D. A. McArthur[12]).

c. Heating of the B Reservoir

Imagine that a "cold" A dipolar reservoir and a "hot" B Zeeman reservoir (in the rotating frames) are brought in thermal contact. During A-B cross relaxation, order which originally resided in the alignment of A spins along their local dipolar fields will be transferred into the B system, and the B spins will be preferentially aligned along the effective magnetic field vector $\bar{H}_{eB}$ in the B rotating frame. Thus a low temperature B spin lock state results, and if the B r.f. is sustained CW, the low B spin temperature will persist for a time of order $T_{1S.L.}$ which is comparable to the high-field B spin-lattice relaxation time. This was discussed in Section II-B. Although B system heating via B spin-lattice relaxation can be used to advantage in certain applications (cfr. Chapters IV and XI), a much higher heating rate is required to obtain optimal double resonance sensitivity.

B reservoir heating is achieved by saturation of the B rotating frame Zeeman transitions. This can be done by sudden application of the B r.f., or by one of several resonant methods, as described below. The corresponding pulse sequences are shown in Fig. III-2.

Audio resonance (rotary saturation): This method was first demonstrated by Redfield[10] and has been analyzed in detail by McArthur, Hahn and Walstedt.[11] An oscillating magnetic field $H_{1Audio}(t)$ is applied to the sample at the B rotating frame transition frequency ω_{eB} (typically 0-20 kHz). The configuration of static and oscillating magnetic fields (H_o, $H_{1B}(t)$, $H_{1Audio}(t)$) is chosen such that nonzero audio field perturbation matrix elements exist between the B rotating frame (B interaction representation) eigenstates. Usually, one has

the linearly polarized fields

$$\bar{H}_{1Audio}(t) \perp H_{1B}(t) \; ; \; \bar{H}_{1Audio}(t) \parallel \bar{H}_o \parallel Z \qquad \text{(III-17)}$$

In ADRF-DR, the audio field does not destroy the A dipolar order directly when the A spin species has a purely Zeeman laboratory frame hamiltonian. With the configuration (Eq. (III-17)), the A spin interaction with $\bar{H}_{1Audio}(t)$ is still directly proportional to I_z when transformed into the A rotating frame, where one has

$$[\mathcal{H}_{ss}(\theta) \; , \; I_z] = 0$$

A qualitative definition of $\mathcal{H}_{ss}(\theta)$ was given above. Accidental audio field components along the x- and y-directions will not affect the A dipolar reservoir, since only high-frequency (i.e. $\gg \gamma_A H_{LA}$) field components result after transformation into the A rotating frame.

Audio saturation is inapplicable or poorly suited in SLDR and LOWDOR, however, since direct destruction of A dipolar order is possible in those cases. To get around this problem, the method of frequency modulation was devised:

Frequency modulation:[39] This method is similar to audio saturation in many respects. If the B r.f. frequency ω_B differs from the B laboratory frame transition frequency ω_{Bo}, there will be an off-resonance field

$$\Delta H_B = (\omega_{Bo} - \omega_B)/\gamma_{eff,B}$$

in the coordinate system rotating at ω_{Bo}. If ω_B is modulated sinusodially:

$$\omega_B = \omega_{Bo} + \Delta\omega_B \cdot \cos\omega_{eB}t$$

where ω_{eB} is the rotating frame transition frequency, then ΔH will oscillate along the z axis in the rotating frame (cfr. Fig. III-3) at

the frequency ω_{eB}. $\Delta\omega_B$ can be chosen large enough such that saturation of the B rotating frame Zeeman levels then results, in analogy with audio resonance saturation. This naïve picture is verified by formal transformation into the B interaction representation.[30] Obviously, selective B reservoir heating is possible with this scheme, if the A and B laboratory frame transition frequencies are widely separated (frequency separation $\gg$ A dipolar linewidth).

Pulsed B r.f.: Consider for simplicity the case where the B r.f. field is applied on resonance ($\omega_B = \omega_{Bo}$) at a moment when no phase memory from previous r.f. pulses exists in the B system. If the B r.f. is turned on in a time much shorter than the B precession period $2\pi/\omega_{Bo}$, the net magnetization along H_{1B} in the B rotating frame will initially be zero, corresponding to an infinite B reservoir temperature. If conditions for double resonance are met, A-B thermal equilibration will take place in a time of order τ_{AB}, leaving the B reservoir at a low temperature. Re-heating of the B reservoir is accomplished by suddenly turning off the B r.f., allowing the B spins to lose phase coherence (i.e., waiting a few B spin-spin relaxation times T_{2B}), and then suddenly turning the B r.f. on again. Apart from the slightly increased A reservoir temperature, the situation is then analogous to that at the start of the previous B r.f. pulse. The B heating/A-B thermal contact/B spin de-phasing can be repeated a large number of times ($\sim 10^3$-10^4) in a single double resonance cycle by applying a string of B r.f. pulses to the sample, and a cumulative heating of the A reservoir results.

Phase shifting:[35] After the initial A-B thermal equilibration has taken plase, the B Zeeman system in the rotating frame is a state of low

spin temperature, manifested by the net magnetization

$$\bar{M}_B = C_B \bar{H}_{1B}/T_B$$

where C_B and T_B are the B system nuclear Curie constant and spin temperature, respectively. If the B r.f. is suddenly phase shifted by 180°, the vector $\bar{H}_{1B}$ will be inverted in the rotating frame. The magnetization $\bar{M}_B$ cannot follow, however, if the phase shifting is fast (i.e., in a time $\ll 1/\omega_{Bo}$), and a negative spin temperature T_B results immediately after the phase shift. If phase shifting is repeated at intervals $\leq \tau_{AB}$, which is roughly the build-up time for M_B, the B reservoir temperature will fluctuate through infinity between high positive and negative values, yielding high double resonance sensitivity. Phase shifted B r.f. is not as well suited as pulsed B r.f. for quantitative measurements (of τ_{AB}, T_{2B}, etc), however.

III-C. Transient Oscillations in the Rotating Frame

When strong B r.f. pulses are applied in double resonance, the energy associated with the A-B dipolar coupling $\mathcal{H}_{AB}$ will oscillate for a time of order T_{2A}, the A spin-spin relaxation time, and the effect can be picked up by nuclear double resonance with pulsed B r.f. As shown in Ref. 11, the effect is due to transient oscillations of the B spin magnetization M_B in the rotating frame, with associated oscillations in the A-B dipolar coupling energy represented by the hamiltonian $\mathcal{H}_d^{AB}(s)$ in Section II-B.

A qualitative understanding of the transient oscillations is most easily obtained by considering separate B spins in the reference frame rotating at the B resonance frequency ω_{Bo} (cfr. Fig. III-4): In the

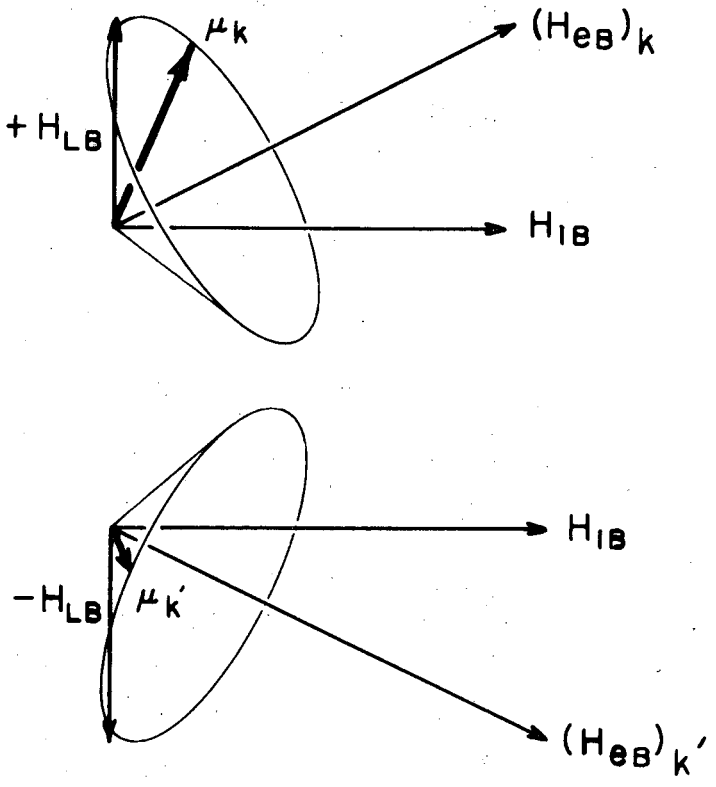

XBL 676-4156

Fig. III-4. Precession of two different B spins in their instantaneous effective fields, at beginning of the B r.f. pulse ($\Delta\omega_B = 0$) (after D. A. McArthur[12]).

absence of applied r.f. fields, A-B and A-A dipolar couplings will quickly (in a time of order T_{2A}) lead to a situation where B spins are preferentially aligned along their local fields H_{LB}, which by hypothesis are chiefly of A dipolar origin. If a strong B r.f. field is suddenly applied on or near the B frequency ω_{Bo} ($\Delta\omega_B = \omega_{Bo} - \omega_B \simeq 0$), the effective field for each spin K in the B rotating frame will be the vector sum of the applied field H_{1B} and the dipolar field component $(H_{LB})_K$. Each spin K will then precess about the local effective field $(H_{eB})_K$, as shown on Fig. III-4. No macroscopic B magnetization exists, however, due to the random distribution of the H_{LB}.

If the precession frequency $(\omega_{eB})_K = (\gamma_{eff,B} \cdot H_{eB})_K$ is $\lesssim T_{2A}^{-1}$, then $(H_{LA})_K$ will change little during a precession period, and the total A-B dipolar coupling energy will be modulated at the frequency ω_{eB}.

Detection: The A-B dipolar reservoir is strongly coupled to the A dipolar reservoir (cfr. Section II-B):

$$[\mathcal{H}_d^A(s) \ , \mathcal{H}_d^{AB}(s)] \neq 0.$$

If the B r.f. is suddenly cut off, the total coupled reservoir represented by

$$\mathcal{H}_{ss} = \mathcal{H}_d^A(s) + \mathcal{H}_d^{AB}(s)$$

can be described by a common spin temperature T_{ss} after a time of order T_{2A}. T_{ss} will depend in part on the energy $\langle \mathcal{H}_d^{AB}(s) \rangle$ at the moment when the B r.f. was cut off, and by varying the length τ of the B r.f. pulse and monitoring the A reservoir temperature T_{ss}, one could map out the oscillations in principle. Since $\langle \mathcal{H}_d^{AB}(s) \rangle / \langle \mathcal{H}_d^A \rangle \ll 1$, a string of

identical B r.f. pulses, spaced by a time $\gg T_{2A}$, T_{2B}, is required in practice to yield an observable effect on the A reservoir temperature.

In their theory of transient oscillations in the rotating frame, McArthur, Hahn and Walsted[11] calculated the quantity $\delta(\tau)$, defined by

$$e^{-\delta(\tau)} = \frac{S_A(n)}{S_A(n-1)} \tag{III-18}$$

where $S_A(n)$ is the A signal strength obtained if the A reservoir temperature is sampled after n B r.f. pulses (sampling time t_b fixed), and τ is the length of each B r.f. pulse. If the A signal strength with no B r.f. applied is normalized to one, Eq. (III-18) yields:

$$\delta(\tau) \simeq \frac{1}{N} \cdot \ln S_A(n) \tag{III-19}$$

where N is the total number of pulses applied. The experimentally obtained $\delta(\tau)$ as determined by Eq. (III-19) can be fitted with the theoretical expression:

$$\delta(\tau) = \frac{N_B \, \mathrm{Tr}\{\mathcal{H}_{ss}^2\}}{\mathrm{Tr}\{\mathcal{H}_d^A(s)^2\}} \, (1 - F(\tau)) \tag{III-20}$$

where N_B is the B spin concentration and

$$F(\tau) = g(\tau)\cos(\omega_{1B}\tau) - 2\int_0^\tau dt' \cos(\omega_{1B}t')\frac{dg(t')}{dt'} + \int_0^\tau dt' \int_0^{t'} dt'' \cos(\omega_{1B}t'')\frac{d^2g(t'')}{dt''} \tag{III-21}$$

Here, $g(\tau)$ is the A-B dipolar coupling correlation function introduced in Section III-B.

IV. NUCLEAR DOUBLE RESONANCE WITH A SINGLE, UNMODULATED B r.f. PULSE

In this chapter, it will be assumed that the B spin species has high abundance, but requires double resonance methods for detection because of low gyromagnetic ratio and small quadrupole coupling constant. As will be shown, it is then possible to create a B spin reservoir with sufficiently large heat capacity so that a single heat contact between the "cold" A system and a "hot" B system, with no reheating of the B system, produces an observable change in the A spin temperature. Since this double resonance method yields much information in addition to the B spin transition frequencies, it will be treated in detail below.

IV-A. Thermal Reservoir Model for the Double Resonance Process With No B Spin Saturation in the Rotating Frame

The r.f. pulse sequence is shown in Fig. III-2: The time scale is chosen so that the B r.f. pulse starts at t=0, stops at $t=t_{B\ r.f.}$, and the A r.f. θ-pulse is applied at $t=t_b$.

Immediately after low A spin temperature has been obtained through ADRF, an unmodulated square B r.f. pulse is applied, not necessarily on exact resonance. The final A spin temperature is measured by sampling the remaining A-spin dipolar order with a $\theta(=\pi/4)$ pulse.

In the following, we will assume that the A spin system, B spin system, and lattice can be described by separate, uniform temperatures T_A, T_B and $T_{lattice}$ (spin temperatures were discussed in II-A) and that there is thermal contact between the three systems. The lattice heat capacity will be assumed infinite.

The problem can then be treated as a simple example of calorimetry, cfr Fig. III-1.

The A and B spin systems and the lattice are thermal reservoirs characterized by their heat capacities and temperatures. If the temperatures are not all equal, heat will flow between the lattice and the A (B) reservoir at a rate proportional to the thermal coupling constants $1/T_{1A}$ ($1/T_{1B}$). A similar heat transfer at a rate proportional to $1/\tau_{AB}$ will take place between the A and B reservoirs when the thermal switch between them is closed, i.e. when the B r.f. pulse is on. Actually, the B reservoir in the form treated here exists only when the B r.f. field is applied, but this will not affect the following analysis. The heat capacity of the A reservoir can be defined by

$$C_A(T_A) = dE_A(T_A)/dT_A \qquad \text{(IV-1)}$$

where $E_A(T_A)$ is the thermal energy in the reservior. $C_B(T_B)$ can be defined analogously.

The parameters in this model must be properly identified and described in terms of spin resonance language. As described in Chapters II and III, the thermal reservoir model for coupled spin systems has been extensively analyzed in connection with studies on double resonance dynamics, and the results carry over as follows in the present case:

1) E_A and E_B are the A and B spin system energies in the interaction representation: For the A spins after ADRF this is the dipolar energy, for the B spins it is the Zeeman energy in the B rotating frame. Even at the lowest spin temperatures obtained following ADRF, the high temperature Curie expressions for the energies are valid ($\hbar\omega = kT$ for $\omega/2\pi$ = 100 kHz, $T = 4 \times 10^{-4}$ °K) :

$$E_A = - \frac{N_A \hbar^2 \gamma_A^2 \, I(I+1)}{3kT_A} H_{LA}^2$$

$$E_B = - \frac{N_B \hbar^2 \gamma_B^2 \, S(S+1)}{3kT_B} H_{eB}^2 \qquad \text{(IV-2)}$$

Here, N_A and N_B are the number of spins per unit volume; γ_A and γ_B are the A and B spin gyromagnetic ratios in the A and B rotating frames, respectively; I and S are the A and B spin quantum numbers; T_A and T_B are the spin temperatures in the A and B interaction representations. H_{LA} is the local field at A-sites: $H_{LA}^2 = Tr\{H_d^A(s)^2\}/Tr\{M_x^{A^2}\}$. H_{eB} is the effective field in the reference frame rotating at the B r.f. frequency ω_B, which may differ from the B resonance frequency ω_{BO}. In this rotating frame, the applied B r.f. field corresponds to a static magnetic field H_{1B}, and H_{eB} is the vector sum of H_{1B} and the off-resonance field $\Delta H_B = \frac{\omega_{Bo} - \omega_B}{\gamma_B}$, (cfr. Fig. III-3): $H_{eB} = \sqrt{H_{1B} + (\Delta H_B)^2}$. Throughout this chapter, it will be assumed that H_{1B} is much stronger than the local dipolar fields at the B spin sites.

With E_A and E_B defined as in Eq. (IV-2), it is apparent that the heat capacities $C_A(T_A)$ and $C_B(T_B)$ may be strongly temperature dependent. Also, with these definitions, infinite spin temperature corresponds to zero energy, while low spin temp. corresponds to a large, negative energy.

2) T_{1A} and T_{1B} are the rotating frame spin-lattice relaxation times for A and B spins, and are generally different from the laboratory spin-lattice times. This definition of the thermal coupling constants $1/T_{1A}$ and $1/T_{1B}$ applies to the rate equations for the spin energies in the case where the thermal coupling between the A and B systems is zero ($1/\tau_{AB} = 0$):

$$dE_A/dt = -(1/T_{1A})E_A \quad ; \quad dE_B/dt = -(1/T_{1B})E_B \qquad \text{(IV-3)}$$

Here, E_A and E_B relax toward zero. Strictly speaking, E_B will relax toward zero only when the B r.f. pulse is exactly on resonance: $\omega_B = \omega_{Bo}$. For off-resonance pulses T_B will approach a value $T_{lattice}$ or higher, depending on ω_B. Since E_B ($T_{lattice}$) is negligible in this context and the lattice heat capacity is vastly larger than C_A and C_B, it will lead only to insignificant errors to assume in the following that the lattice has constant and infinite temperature during the relaxation process.

3) τ_{AB} is the cross-coupling time constant for energy transfer between the A and B systems during double resonance. It is defined by:

$$\text{(Heat flow between A and B reservoirs)} = -\frac{1}{\tau_{AB}}\left(E_B(T_B) - E_B(T_A)\right); \qquad \text{(IV-4)}$$

Thus the B reservoir energy relaxes toward $E_B(T_A)$, the energy it would have had at the instantaneous A reservoir temperature, with a rate constant $1/\tau_{AB}$. Here and in the following it is assumed that the reservoir temperatures are the only parameters in Eq. (IV-2) that change during cross-relaxation. From one pulse cycle to the next, however, H_{LA} and H_{eB} may change if the sample temperature varies, and H_{eB} will also depend on the B r.f. field strength. These and related effects will be treated in the next section.

One can now proceed to set up the thermodynamic equations for the system in Fig. III-1. The A and B reserviors gain or lose energy in two ways: First, if one disregards the cross-coupling, ($1/\tau_{AB} = 0$), spin-lattice relaxation will generate heat flows as given by Eq. (IV -3)

between each reservoir and the lattice. Second, if the A and B reserviors are assumed decoupled from the lattice, $(1/T_{1A} = 1/T_{1B} = 0)$, cross relaxation creates an exchange of energy between the reservoirs. Then, by Eq. (IV-4):

$$\dot{E}_B(T_B) = -\frac{1}{\tau_{AB}}\left(E_B(T_B) - E_B(T_A)\right)$$

which can be rewritten:

$$\dot{E}_B(T_B) = -\frac{1}{\tau_{AB}}\left(E_B(T_B) - \varepsilon\, E_A(T_A)\right) \qquad \text{(IV-5)}$$

where

$$\varepsilon = \frac{E_B(T_A)}{E_A(T_A)} = \frac{C_B(T_A)}{C_A(T_A)}$$

ε is the ratio of the heat capacities of the B and A reserviors at the instantaneous temperature T_A. In the present case:

$$\varepsilon = \frac{N_B S(S+1)\,\omega_{eB}^2}{N_A I(I+1)\,\omega_{LA}^2} \qquad \text{(IV-6)}$$

and ε is therefore independent of the instantaneous temperature T_A during cross-relaxation. However, a change in the sample temperature or B r.f. field strength will alter ε through its dependence on ω_{eB} and ω_{LA}. In double resonance work on rare spin species, ε is usually very small (typically 10^{-2} to 10^{-4}). In order to make use of the results derived in this chapter for quantitative measurements, one typically needs $\varepsilon \gtrsim 0.1$ corresponding to an A spin signal to noise ratio of ~50. A lower signal to noise ratio would require a proportionately larger ε for the same application. Since $S(S+1)$ and $I(I+1)$ are of approximately the same magnitude and $\omega_{eB}^2 \simeq \omega_{LA}^2$ (cross relaxation condition),

$\varepsilon \gtrsim 0.1$ will correspond to $N_B \gtrsim 0.1\ N_A$. Therefore, the B spin species must be fairly abundant, and the methods of this chapter apply to B spins species that require double resonance methods for detection due to low gyromagnetic ratio and/or weak quadrupole interaction with the lattice. If no energy exhange with the lattice takes place during the A-B cross relaxation, one has by energy conservation: $\dot{E}_A(T_A) = -\dot{E}_B(T_B)$, and $\dot{E}_A(T_A)$ is immediately given by Eq. (IV-5).

One can now combine the contributions of energy flows into each reservoir. After the thermal switch between the A and B reserviors has been closed, the A and B reservior energies will evolve as described by the following homogeneous differential equation system:

$$\frac{dE_A}{dt} = -C_1 E_A + C_2 E_B$$

$$\frac{dE_B}{dt} = C_3 E_A - C_4 E_B \qquad \text{(IV-7)}$$

where

$$C_1 = \frac{\varepsilon}{\tau_{AB}} + \frac{1}{T_{1A}} \qquad C_2 = \frac{1}{\tau_{AB}}$$

$$C_3 = \frac{\varepsilon}{\tau_{AB}} \qquad C_4 = \frac{1}{\tau_{AB}} + \frac{1}{T_{1B}} \qquad \text{(IV-8)}$$

The temperatures in the arguments of $E_A(t)$ and $E_B(t)$ have been omitted, since they, from now on, are always the instantaneous temperatures of the A and B reserviors respectively: $E_A(T_A,t) \equiv E_A(t)$, $E_B(T_B,t) \equiv E_B(t)$.

The general solutions of Eq. (IV-A-7) are of the form,

$$E_A(t) = E_A(+)\ e^{-\lambda_+ t} + E_A(-)\ e^{-\lambda_- t} \qquad \text{(IV-9)}$$

$$E_B(t) = E_B(+)\ e^{-\lambda_+ t} + E_B(-)\ e^{-\lambda_- t} \qquad \text{(IV-10)}$$

where

$$\lambda_\pm = 1/2\ (C_1 + C_4)\left(1 \pm \sqrt{1 - \frac{4(C_1C_4 - C_2C_3)}{(C_1 + C_4)^2}}\right) \qquad \text{(IV-11)}$$

The constants $E_A(\pm)$ and $E_B(\pm)$ are determined by the initial conditions. The time reference is as shown in Fig. (III-2): At t=0 the B r.f. is turned on, and the A and B spin reservoir energies are $E_A(0) = E_{Ao}$ and $E_B(0) = E_{Bo}$, respectively. The set of Eqs. (IV-7), (IV-9) and (IV-10) then yields,

$$E_A(+) = \frac{(C_1 - \lambda_-)E_{Ao} - C_2E_{Bo}}{\lambda_+ - \lambda_-} \quad ; \quad E_A(-) = \frac{(\lambda_+ - C_1)E_{Ao} + C_2E_{Bo}}{\lambda_+ - \lambda_-}$$

$$E_B(+) = \frac{-C_3E_{Ao} + (C_4 - \lambda_-)E_{Bo}}{\lambda_+ - \lambda_-} \quad ; \quad E_B(-) = \frac{C_3E_{Ao} + (\lambda_+ - C_4)E_{Bo}}{\lambda_+ - \lambda_-} \qquad \text{(IV-12)}$$

Immediately after ADRF, the A spin temperature is very low, and therefore E_{Ao} is large. The B spin temperature immediately after the B r.f. is turned on, will generally be high, and depends on the frequency ω_B of the applied field. This problem is discussed in Appendix B, under the assumption that the B r.f. field is turned on so rapidly that the B spin quantum states at the beginning of the B r.f. pulse are identical to those immediately preceding it (sudden approximation). In the remainder of this section, it will be assumed that the B r.f. is exactly on resonance, while the off-resonance case is discussed in Section IV-B. On resonance, $E_{Bo} = 0$ or $T_{Bo} = \infty$, according to Appendix B, and the general solution for $E_A(t)$ simplifies to:

$$E_A(\omega_B=\omega_{Bo};t_{B\ r.f.}) = E_{Ao}\left(\frac{\lambda_+-C_1}{\lambda_+-\lambda_-}\,e^{-\lambda_- t_{B\ r.f.}} + \frac{C_1-\lambda_-}{\lambda_+-\lambda_-}\,e^{-\lambda_+ t_{B\ r.f.}}\right)$$

at $t = t_{B\ r.f.}$; i.e., at the end of the B r.f. pulse.

We are interested in the value of E_A at the time $t = t_b$ when the A system order is sampled (cfr. Fig. III-2). After the B r.f. pulse is turned off, the A and B systems are decoupled and the A spins undergo spin-lattice relaxation at the rate $1/T_{1A}$ during the time from $t = t_{B\ r.f.}$ to $t = t_b$. Thus one can write:

$E_A(\omega_B=\omega_{Bo};t_b) \simeq$ (IV-13)

$$E_{Ao}\,e^{-t_b/T_{1A}}\cdot\frac{\lambda_+-C_1}{\lambda_+-\lambda_-}\cdot e^{-(\lambda_- -1/T_{1A})\,t_{B\ r.f.}}\left(1 + \frac{C_1-\lambda_-}{\lambda_+-C_1}\,e^{-(\lambda_+-\lambda_-)\,t_{B\ r.f.}}\right)$$

The reason for arranging the expression for $E_A(t_b)$ in this fashion will become apparent after we analyze the physical significance and the relative magnitudes of the quantities involved. Substituting for the C's in $\lambda_\pm$, one obtains:

(IV-14)

$$\lambda_\pm = \frac{1}{2}\left(\frac{\varepsilon+1}{\tau_{AB}} + \frac{1}{T_{1A}} + \frac{1}{T_{1B}}\right)\times \left(1 \pm \sqrt{1 - \frac{4\left(\frac{\varepsilon}{\tau_{AB}T_{1B}} + \frac{1}{\tau_{AB}T_{1A}} + \frac{1}{T_{1A}T_{1B}}\right)}{\left(\frac{\varepsilon+1}{\tau_{AB}} + \frac{1}{T_{1A}} + \frac{1}{T_{1B}}\right)^2}}\right)$$

So far, no approximations have been made.

The expression simplifies considerably if

$$\tau_{AB} \ll T_{1A}\ ,\ T_{1B}\ . \qquad \text{(IV-15)}$$

Then, Eq. (IV-14) yields the approximate expressions:

$$\lambda_+ \simeq \frac{\varepsilon + 1}{\tau_{AB}}$$

$$\lambda_- \simeq \frac{1}{\varepsilon + 1}\left(\frac{\varepsilon}{T_{1B}} + \frac{1}{T_{1A}}\right) \qquad \text{(IV-16)}$$

$$\lambda_+ - \lambda_- \simeq \lambda_+ \simeq \frac{\varepsilon + 1}{\tau_{AB}}$$

The relationships Eq. (IV-16) are exact for $\tau_{AB}/T_{1A} = \tau_{AB}/T_{1B} = 0$.

In what follows, it will be assumed that the approximate expressions, Eq. (IV-16), are valid. One can now go back to the expression, Eq. (IV-13), for the A reservoir energy $E_A(t_{B\ r.f.})$ at the end of the B r.f. pulse. The second term in the parenthesis has a time dependence essentially governed by λ_+, since $\lambda_+ - \lambda_- \simeq \lambda_+ \simeq \frac{\varepsilon + 1}{\tau_{AB}}$. This time dependence reflects the strength of the A-B coupling through τ_{AB}, and also describes a relatively rapid (compared to T_{1A}, T_{1B}) transient, since the term disappears for $t_{B\ r.f.} \gg \frac{\tau_{AB}}{1 + \varepsilon}$. Physically, this describes the initial equilibration of T_A and T_B as the A and B reservoirs are brought into thermal contact with each other. If no heat exchange with the lattice takes place during this process, (T_{1A}; $T_{1B} \gg \tau_{AB}$), the A reservoir energy after complete equilibration ($t_{B\ r.f.} \gg \frac{\tau_{AB}}{1 + \varepsilon}$) will be determined solely by ε, given the initial conditions on E_A and E_B. This result is given by the term

$$\frac{\lambda_+ - C_1}{\lambda_+ - \lambda_-} \simeq \frac{\frac{\varepsilon + 1}{\tau_{AB}} - \frac{\varepsilon}{\tau_{AB}} - \frac{1}{T_{1A}}}{\frac{\varepsilon + 1}{\tau_{AB}}} \approx \frac{1}{\varepsilon + 1}$$

for

$$\frac{\tau_{AB}}{T_{1A}} \ll 1 \quad .$$

The other variation with $t_{B\ r.f.}$ comes from the factor $e^{-\lambda_- \cdot t_{B\ r.f.}}$, and is much slower, since $\lambda_+ \gg \lambda_-$ (cfr. Eq. (IV-16)). λ_- in Eq. (IV-16) depends on ε, T_{1A} and T_{1B}, and the factor $e^{-\lambda_- \cdot t_{B\ r.f.}}$ reflects the transfer of heat from the lattice to the A system by two routes: Direct A-spin-lattice relaxation; and B-spin-lattice relaxation with transfer of energy from the B to the A system. For $t_{B\ r.f.} \gg \frac{\tau_{AB}}{1+\varepsilon}$ and with assumptions on τ_{AB}, T_{1A} and T_{1B} as above, the expression for $E_A(t_b)$ can be written to a good approximation as:

$$E_A(\omega_B = \omega_{Bo};\ t_b) \simeq \tag{IV-17}$$

$$E_{Ao} \cdot \frac{1}{\varepsilon + 1} \exp\left\{ - \frac{\varepsilon}{\varepsilon + 1} \left(\frac{1}{T_{1B}} - \frac{1}{T_{1A}} \right) t_{B\ r.f.} - \frac{1}{T_{1A}}\, t_b \right\}$$

Assume now that $t_{B\ r.f.}$ is varied, while t_b is kept fixed. Then, after the initial rapid equilibration of A and B spin temperatures, there will be an exponential decay at the rate $\frac{\varepsilon}{1+\varepsilon}\left(\frac{1}{T_{1B}} - \frac{1}{T_{1A}}\right)$. When $T_{1B} < T_{1A}$ the slope will be as shown; when $T_{1B} > T_{1A}$ the spin energy will decrease rapidly to a maximum, then slowly increase, and for the special case $T_{1B} = T_{1A}$ one expects that $E_A(t_b)$ will decrease exponentially with a rapid time const $\sim\tau_{AB}$ to a level which then remains unchanged.

It is easy to explain this dependence of the A spin heating rate on the relative values of T_{1A} and T_{1B} by considering the coupled thermal reservoirs shown in Fig. III-1: If the thermal contact is broken immediately after initial equilibration of the A and B temperatures, the A reservoir will heat up at a rate determined by T_{1A}, and at $t=t_b$ the energy $E_A(t_b)$ will have reached a certain value. Keeping the thermal

connection with the B reservoir on after equilibration may increase or decrease $E_A(t_b)$ relative to this value, depending on which way heat flows between the reservoirs.

When the A and B reservoirs heat up at the same rate ($T_{1A} = T_{1B}$), the reservoir temperatures will remain equal after equilibration. Thus, no A-B heat transfer takes place even if the thermal contact is left on and $E_A(t_b)$ will be independent of $t_{B\ r.f.}$.

If $T_{1A} > T_{1B}$, the B reservoir heats up faster than the A reservoir, and heat will flow from the B to the A reservoir as long as the thermal coupling remains on. At t_b, the A temperature will be higher (i.e., $E_A(t_b)$ smaller), the longer the coupling time $t_{B\ r.f.}$.

For $T_{1A} < T_{1B}$, heat flows out of the A system via the thermal A-B coupling during $t_{B\ r.f.}$. As $t_{B\ r.f.}$ increases, the A reservoir will be progressively colder at $t = t_b$, compared to the case where no A-B heat transfer takes place after initial equilibration. The resulting positive $\partial E_A(t_b)/\partial t_{B\ r.f.}$ does not mean that the A reservoir is cooling down, of course, but rather that the rate of heating has been reduced.

IV-B. Double Resonance Lineshape With and Without B Spin Saturation in the Rotating Frame

So far, the influence of the B r.f. frequency on the double resonance process has not been considered. There are three main effects of specific importance in the present case. Two of them stem from the same cause, namely the increase in $\omega_{eB} = \gamma_B H_{eB}$ off resonance. The third is due to the frequency dependence of the B spin temperature at the beginning of the B r.f. pulse.

1) τ_{AB}^{-1} depends on the B r.f. frequency. If the A spin correlation time τ_c is $\ll \tau_{AB}$ (which should apply to most cases of interest here), the cross coupling rate will be (cfr. Section III-B):

$$\tau_{AB}^{-1} = \text{const}_1 \cdot \sin^2\theta \cdot J(\omega_{eB}) = \omega_{1B}^2 \frac{J(\omega_{eB})}{\omega_{eB}^2} \cdot \text{const}_1 \qquad \text{(IV-18)}$$

Here, θ is the angle in the B rotating frame between z-axis and the H_{eB} vector:

$$\sin\theta = \frac{H_{1B}}{H_{eB}} = \frac{\omega_{1B}}{\omega_{eB}}$$

$J(\omega)$ is the spectral density of the local field fluctuations at the B spin sites, due to the A spins. In the fast correlation case it is a monotonically decreasing function of ω. Since $\omega_{eB}^2 = \omega_{1B}^2 + (\Delta\omega_B)^2$, where $\Delta\omega_B = \omega_{Bo} - \omega_B$, ω_{eB} will always increase as $|\Delta\omega_B|$ increases, while $J(\omega_{eB})$ will decrease. Therefore, the cross coupling rate τ_{AB}^{-1} will decrease as ω_B goes off resonance in either direction.

2) For constant H_{1B}, $\varepsilon(\omega_B)$ increases off resonance. From Eq. (IV-6):

$$\varepsilon(\omega_B) = \frac{\omega_{eB}^2}{\omega_{LA}^2} \cdot \text{const}_2 = \varepsilon(\omega_{Bo}) \cdot \frac{\omega_{eB}^2}{\omega_{1B}^2} \qquad \text{(IV-19)}$$

ω_{LA} will be unchanged as long as the sample temperature is constant (ω_{LA} will be essentially independent of the B spins in all experiments where double resonance methods are necessary to study the B spin species, since then the B spins have either low gyromagnetic ratio, low abundance, or both). Therefore, the increase in $\varepsilon(\omega_B)$ off resonance reflects directly the increase in the rotating-frame effective field H_{eB} off resonance. H_{eB} determines the B reservoir heat capacity, which increases symmetrically around ω_{Bo} as $|\Delta\omega_B|$ increases.

3) When the B r.f. pulse is applied suddenly, it creates a B thermal reservoir at a temperature which depends on ω_B. If the B reservoir is at thermal equilibrium with the lattice before the pulse, the B reservoir energy immediately after the pulse starts will be (cfr. Appendix B):

$$E_{Bo} = K(\omega_{Bo} - \omega_B) = K \cdot \Delta\omega_B \qquad \text{(IV-20)}$$

where K is a constant. Thus, ω_B is an important parameter in determining the initial conditions for the thermal relaxation process between the A and B reservoirs and the lattice. When it does not appear explicitly in this and following formulas, one should bear in mind that E_{Bo}, ε and τ_{AB} are not fixed parameters, but depend on ω_B in the manner described above.

Before treating the lineshape obtained after the ADRF-double resonance sequence in Fig. III-2, using a single, unmodulated B r.f. pulse, it will be of interest to see what the predicted lineshape will be <u>if the B spin reservoir is kept at infinite temperature during the double</u>

resonance process. This can be done in practice by continually heating it, using one of the methods outlined in Chapter III. By the definition (Eq. IV-2)), $E_B = 0$ for $T_B = \infty$, and the rate equation for E_A simplifies to

$$\frac{dE_A}{dt} = -C_1 E_A \quad , \text{ where } \quad C_1 = \frac{\varepsilon}{\tau_{AB}} + \frac{1}{T_{1A}} \quad .$$

With $E_A(t = 0) = E_{Ao}$ as before, the solution for E_A is:

$$E_A(\omega_B, t_{B\ r.f.}) \simeq E_{Ao} \cdot e^{-\left(\frac{\varepsilon}{\tau_{AB}} + \frac{1}{T_{1A}}\right) t_{B\ r.f.}}$$

If the A reservoir energy is sampled at a time $t=t_b$, the result is:

$$E_A(\omega_B, t_b) = E_A(\omega_B, t_{B\ r.f.}) \cdot e^{-\frac{(t_b - t_{B\ r.f.})}{T_{1A}}} = \tag{IV-21}$$

$$E_{Ao} \cdot e^{-\frac{\varepsilon}{\tau_{AB}} t_{B\ r.f.} - \frac{1}{T_{1A}} \cdot t_b}$$

The B spin double resonance lineshape is recorded experimentally with constant t_b, $t_{B\ r.f.}$, T_{1A} and T_{1B}. Eq. (IV-21) then shows that the lineshape is determined by the dependence of $\frac{\varepsilon}{\tau_{AB}}$ on ω_B. From Eq. (IV-18) and (IV-19):

$$\frac{\varepsilon}{\tau_{AB}} = \text{const}_3 \cdot \frac{\omega_{1B}^2}{\omega_{LA}^2} \cdot J\ (\omega_{eB})$$

Since ω_{1B} and ω_{LA} are constant during a sweep through the B line, one has:

$$E_A(\omega_B, t_b) = \text{const}_4 \cdot e^{-\text{const}_5 \cdot J\ (\omega_{eB}) \cdot t_{B\ r.f.}} \tag{IV-22}$$

J ($\omega_{eB} = \sqrt{\omega_{1B}^2 + (\omega_B - \omega_{Bo})^2}$) is a maximum for $\omega_B = \omega_{Bo}$ and decreases off resonance. From Eq. (IV -22), then, it is immediately clear that this yields a double resonance line with maximum depletion of A spin energy for $\omega_B = \omega_{Bo}$, and gradually reduced depletion to either side of resonance.

For the case where no reheating of the B spin reservoir takes place after it has been brought into contact with the A spin reservoir, i.e., when an unmodulated square B r.f. pulse is applied with no audio resonance heating, the lineshape can be had from the expressions in Eqs. (IV-9), (IV-11) and (IV-12). $E_A(\omega_B, t_b)$ can be written in the form:

$E_A(\omega_B; t_b) =$

$$E_{Ao} \cdot e^{-t_b/T_{1A}} \left\{ \left(\frac{\lambda_+ - C_1}{\lambda_+ - \lambda_-} + \frac{C_2}{\lambda_+ - \lambda_-} \cdot \frac{E_{Bo}}{E_{Ao}} \right) e^{-(\lambda_- - 1/T_{1A}) t_{B\ r.f.}} + \right. \tag{IV-23}$$

$$\left. \left(\frac{C_1 - \lambda_-}{\lambda_+ - \lambda_-} - \frac{C_2}{\lambda_+ - \lambda_-} \cdot \frac{E_{Bo}}{E_{Ao}} \right) e^{-(\lambda_+ - 1/T_{1A})\ t_{B\ r.f.}} \right\}$$

where all parameters are defined in section IV-A. Exactly on resonance, $E_{Bo} = 0$, and one recovers Eq. (IV-13). As ω_B is swept through the line at ω_{Bo}, the parameters will change, and if $t_{B\ r.f.}$ is considered as a fixed parameter, Eq. (IV-23) yields the lineshape directly. However, τ_{AB} varies over a wide range of values throughout the line and it is not permissible to make assumptions on the relative magnitudes of τ_{AB}, T_{1A} and T_{1B} to obtain a simplified formula describing the whole line. Since the physical meaning of Eq. (IV-23) as it stands is obscure at best, it might be helpful to consider the two limiting cases $\tau_{AB} \ll T_{1A}, T_{1B}$ and $\tau_{AB} \gg T_{1A}, T_{1B}$:

1) $\tau_{AB} \ll T_{1A}, T_{1B}$. As is apparent from Eq. (IV-18) this would correspond to the region around ω_{Bo}, if at all. (In double resonance work in solids, T_{1A} and T_{1B} are generally at least an order of magnitude larger than τ_{AB} on exact resonance.) If the assumption on τ_{AB} holds, one obtains from Eq. (IV-16) and (IV-23):

$$E_A(\omega_B;t_b) \simeq \frac{E_{Ao}}{1+\varepsilon}\, e^{-t_b/T_{1A}}\left\{\left(1+\frac{E_{Bo}}{E_{Ao}}\right)e^{-\frac{\varepsilon}{1+\varepsilon}\left(\frac{1}{T_{1B}}-\frac{1}{T_{1A}}\right)t_{B\ r.f.}} + \left(\varepsilon-\frac{E_{Bo}}{E_{Ao}}\right)e^{-\frac{1+\varepsilon}{\tau_{AB}}t_{B\ r.f.}}\right\} \qquad \text{(IV-24)}$$

which describes both the thermal equilibration between the A and B reservoirs and the slow spin-lattice relaxation heating of the coupled A-B reservoir. If one is only interested in the slow heating of the coupled reservoir, one can make the additional assumption that the A-B thermal equilibration transient has died out: $t_{B\ r.f.} \gg \frac{\tau_{AB}}{1+\varepsilon}$, which leads to:

$$E_A(\omega_B,t_b) \simeq (E_{Ao}+E_{Bo})\,\frac{1}{\varepsilon+1} \times \exp\left\{-\frac{\varepsilon}{\varepsilon+1}\left(\frac{1}{T_{1B}}-\frac{1}{T_{1A}}\right)t_{Br.f.} - \frac{1}{T_{1A}}\cdot t_b\right\} \qquad \text{(IV-25)}$$

This differs from the on-resonance formula in that E_{Ao} has been substituted by $E_{Ao} + E_{Bo}$. This form is expected, since after the initial transient, the two strongly coupled reservoirs behave as a single thermal reservoir with initial energy $E_{Ao} + E_{Bo}$. The only quantities that will vary as ω_B is swept through the line will be ε and E_{Bo}. The dependence of τ_{AB} on ω_B does not show up here since the assumption $t_{B\ r.f.} \gg \tau_{AB}/(1+\varepsilon)$ was made. From Eqs. (IV-19) and (IV-20) one obtains expressions for $\varepsilon(\omega_B)$ and $E_{Bo}(\omega_B)$, which substituted into Eq. (IV-24) yield:

$$E_A(\omega_B,t_b) \simeq \left(E_{Ao}+K \cdot \Delta\omega_B\right)\frac{\omega_{1B}^2}{\varepsilon(\omega_{Bo}) \cdot \omega_{eB}^2 + \omega_{1B}^2} \times$$

$$\exp\left\{-\frac{\varepsilon(\omega_{Bo})\omega_{eB}^2}{\varepsilon(\omega_{Bo})\omega_{eB}^2 + \omega_{1B}^2}\left(\frac{1}{T_{1B}}-\frac{1}{T_{1A}}\right)t_{B\ r.f.} - \frac{1}{T_{1A}} \cdot t_b\right\} \qquad \text{(IV-26)}$$

where, as before: $\Delta\omega_B = \omega_{Bo} - \omega_B$ and $\omega_{eB}^2 = \omega_{1B}^2 + (\Delta\omega_B)^2$.

The value of $E_A(\omega_B, t_b)$ when the term $K \cdot \Delta\omega_B$ is ignored will be defined as $E_A(\omega_B, t_b)_{symmetric}$. One observes that for $T_{1B} \leqslant T_{1A}$, $E_A(\omega_B, t_b)_{symmetric}$ is depleted the least for $\omega_B = \omega_{Bo}$, and increases symmetrically about ω_{Bo} as ω_B goes off resonance in either direction. Instead of a minimum signal at ω_{Bo}, as was the case with continuous B saturation, one here has a local maximum! This paradoxical result is only valid as long as the condition $\tau_{AB} \ll T_{1A}, T_{1B}$ is fulfilled, of course.

$E_A(\omega_B, t_b)$ is obtained from $E_A(\omega_B, t_b)_{symmetric}$ by adding the the obviously antisymmetric term $K \cdot \Delta\omega_B \cdot E_A(\omega_B, t_b)_{symmetric}/E_{Ao}$. Thus, for $\omega_B > \omega_{Bo}$, $\Delta\omega_B$ is negative and $E_A(\omega_B, t_b)$ will be depleted more rapidly on the high-frequency side of ω_{Bo}, less rapidly on the low-frequency side as compared to $E_A(\omega_B, t_b)_{symmetric}$.

As $|\Delta\omega_B|$ increases, τ_{AB} will increase, and the condition $\tau_{AB} \ll T_{1A}$, T_{1B} will be progressively poorly satisfied. Physically, the A-B heating transient will take longer time when τ_{AB} increases, and when the transient no longer has died out at $t = t_{B\ r.f.}$ the depletion of $E_A(\omega_B, t_b)$ will be reduced compared to the case $\tau_{AB} \ll T_{1A}, T_{1B}$.

2) $\tau_{AB} \gg T_{1A}, T_{1B}$. Since $\tau_{AB} \to \infty$ as $\Delta\omega_B \to \infty$, it is always possible to satisfy this condition by going sufficiently far into the wings of the line. $\frac{1}{\tau_{AB}} \ll \frac{1}{T_{1B}}$ means that the thermal coupling between the A and B reservoirs is much weaker than the thermal coupling of the B reservoir to the lattice. Therefore, the B reservoir temperature T_B will relax toward $T_{lattice}$ at a rate much greater than the rate at which it relaxes toward T_A. Starting now at the time t=0 immediately after ADRF, T_A will be very low, corresponding to the energy E_{Ao}. The initial T_B will be very high, corresponding to a low energy E_{Bo}. Because the B reservoir is strongly coupled to the hot lattice, E_B will always be close to zero, but as long as the A reservoir is at a low temperature so that heat is flowing from the B to the A reservoir, E_B will depart slightly from zero, since $\frac{1}{T_{1B}}$ is finite.

This can be cast in a semi-quantitative form. Since the equilibrium value of E_B at the lattice temperature is negligible in this context, it is sufficient to treat the case where $E_{Bo} = 0$, and E_B relaxes toward zero in the rotating frame. Then, according to Eq. (IV-10) and (IV-12):

$$E_B(t_{B\ r.f.}) = E_{Ao} \cdot \frac{C_3}{\lambda_+ - \lambda_-}\left(-e^{-\lambda_+ t_{B\ r.f.}} + e^{-\lambda_- t_{B\ r.f.}}\right) \qquad \text{(IV-27)}$$

$\lambda_\pm$ as given in Eq. (IV-14) can be expanded to first order as a good approximation if

$$\tau_{AB}\left|\left(\frac{1}{T_{1A}} - \frac{1}{T_{1B}}\right)\right| \gg 1 \qquad \text{(IV-28)}$$

which is valid in the present case ($\tau_{AB} \gg T_{1A}, T_{1B}$), provided T_{1A} is not $\simeq T_{1B}$. In the case of interest here, ε is not necessarily negligible compared to 1. Assuming that Eq. (IV-28) is satisfied, one finds:

$$\lambda_+ \simeq \frac{1}{T_{1A}} \tag{IV-29}$$

$$\lambda_- \simeq \frac{1}{T_{1B}} \tag{IV-30}$$

In the special case where $T_{1A} = T_{1B}$, one obtains the exact expressions:

$$\lambda_+ = \frac{\varepsilon+1}{\tau_{AB}} + \frac{1}{T_{1A}}$$

$$\lambda_- = \frac{1}{T_{1B}} = \frac{1}{T_{1A}}$$

When Eq. (IV-28) is satisfied, Eq. (IV-27) takes the form:

$$E_B(t_{B\ r.f.}) \simeq E_{Ao} \cdot \frac{\varepsilon}{\tau_{AB}\left(\frac{1}{T_{1B}} - \frac{1}{T_{1A}}\right)} \left(e^{-\frac{1}{T_{1A}}\ t_{B\ r.f.}} - e^{-\frac{1}{T_{1B}}\ t_{B\ r.f.}} \right) \tag{IV-31}$$

The temporal behavior of E_B in Eq. (IV-31) is just as predicted by the qualitative arguments above: At $t \doteq 0$, the energy $E_{B}(0)$ is zero in this approximation. It grows to a maximum value and then decays to zero. One has for the maximum value of E_B:

$$E_{B,max.} < \varepsilon E_{Ao} \cdot \frac{1}{\tau_{AB}\left(\frac{1}{T_{1B}} - \frac{1}{T_{1A}}\right)} \tag{IV-32}$$

If Eq. (IV-28) is valid, this means that:

$$E_{B,max.}(\tau_{AB} \gg T_{1A}, T_{1B}) \ll \varepsilon \cdot E_{Ao} \tag{IV-33}$$

By Eq. (IV-25), $\frac{E_{Ao}+E_{Bo}}{1+\epsilon} \cdot \epsilon$ is the energy in the B reservoir after equilibration of T_A and T_B if there is no heat transfer to the lattice, in the case $\tau_{AB} \ll T_{1A}, T_{1B}$. Thus

$$E_{B,max}(\tau_{AB} \gg T_{1A}, T_{1B}) \ll E_{B,max}(\tau_{AB} \ll T_{1A}, T_{1B})$$

In the wings of the line where $\tau_{AB} \to \infty$, the B reservoir energy therefore always remains very low, corresponding to a high spin temperature, and one has a situation similar to the one with continuous B reservoir heating.

From the behavior of $E_A(\omega_B)$ in the two regions $\tau_{AB} \lessgtr T_{1A}, T_{1B}$, it is now possible to describe the whole lineshape. For simplicity, some special cases possible when $\left(\frac{1}{T_{1B}} - \frac{1}{T_{1A}}\right) t_{B\ r.f.} < 1$ will not be considered. In the far wings of the line, $\tau_{AB} \gg T_{1B}$, and $T_B \approx \infty$, $E_B \simeq 0$. Thus all relevant parameters are almost identical to the ones in the case where the B reservoir was kept at infinite temperature by continuous saturation. The lineshapes will overlap and are described by Eq. (IV-21). As $|\Delta\omega_B|$ decreases, the depletion of $E_A(t_b)$ ("line depth"), will be less when the square, unmodulated B r.f. pulse is applied than in the case with continuous saturation in the rotating frame. This is because the B reservoir temperature becomes lower as τ_{AB} increases towards T_{1B}, and the heat transfer from the B to the A reservoir is reduced relative to the case with saturation, since τ_{AB} is the same in both cases. Approximately in the regions on both sides of ω_{Bo} where $\tau_{AB} \approx T_{1A}, T_{1B}$, there will be a maximum in the depletion of the A reservoir energy. For lower values of $|\Delta\omega_B|$, the depletion will decrease as $|\Delta\omega_B|$ decreases, and reach a minimum at $\Delta\omega_B = 0$. Between the points of maximum depletion, an asymmetry in the line will be evident. The depletion on

the high-frequency side of ω_{Bo} will be largest, and this also applies to the two depletion maxima.

It is apparent from Eq. (IV -24) that the strength of the B r.f. field, i.e. the magnitude of ω_{1B}, is an important parameter in determining the lineshape in the region $\omega_B \simeq \omega_{Bo}$. Increasing ω_{1B} will depress the peak in $E_A(\omega_B, t_b)$ at ω_{Bo}, and also the curvature at the peak will be reduced, since a relative change in ϵ due to a given change in $\Delta\omega_B$ will be less for a larger ω_{1B}.

IV-C. Applications

The results derived in Sections IV-A and IV-B have some obvious applications which can be grouped into two classes:

First, one can devise experimental techniques that provide data on material or double resonance parameters that may or may not be obtainable by alternative methods. Of special interest here is the B spin rotating-frame spin-lattice relaxation time T_{1B}, which can be measured by a technique described below. It will also be shown how the ratio ϵ of the A and B reservoir heat capacities and the A-B cross-relaxation time τ_{AB} can be measured. The method is experimentally simpler than others used to measure these parameters previously, and it is the only method developed so far, to this author's knowledge, that is capable of measuring short B spin-lattice relation times.

Second, one has at one's disposal a new set of phenomena that can provide a sensitive test of the thermal reservoir model for the double

resonance process. The experimental procedures developed in this chapter for measuring ε , τ_{AB} and T_{1B} cannot be applied with confidence before the validity of the thermal reservoir model has been established for each specific case. Also, the importance of such a test extends beyond the scope of double resonance with unmodulated B r.f., as will be discussed.

IV-C-1. Measurement of ε, τ_{AB} and T_{1B}

Consider first the case where the B r.f. is applied on resonance: $\omega_B = \omega_{Bo}$. The A reservoir energy at time t_b is then expected to depend on the parameter $t_{B\ r.f.}$ as given by Eq. (IV -17). Experimentally, this can be verified by repeating the double resonance cycle several times, varying $t_{B\ r.f.}$ by steps through the range from zero to a time slightly less than t_b, and keeping all other parameters constant from one cycle to the next. The cycle repetition time must be larger than T_{1A} and T_{1B} to allow the A and B reservoirs to come into thermal equilibrium with the lattice before each pulse sequence, unless a correction term is introduced into the equations above. If the thermal reservoir model for the double resonance process as described above applies (cfr Section IV-C-2), experimental curves of the type shown in Fig. IX-4 should be obtained, and extrapolation of the straight portion of the semilogaritmic graph to $t_{B\ r.f.} = 0$ yields:

$$E_A(t_b)_{extr.} = E_{Ao}\ \frac{1}{\varepsilon + 1}\ e^{-\frac{t_b}{T_{1A}}} \qquad \text{(IV-34)}$$

Equation (IV -34) was obtained from Eq. (IV -17), which describes that part of $E_A(t_b)$ which has exponential dependence on $t_{B\ r.f.}$, by formally setting $t_{B\ r.f.} = 0$. The true value of $E_A(t_b)$ when no B r.f. is applied, is of course:

$$E_A(t_b;\ t_{B\ r.f.} = 0) = E_{Ao} \cdot e^{-\frac{t_b}{T_{1A}}}$$

Taking the ratio between $E_A(t_b)_{extr.}$ and $E_A(t_b;\ t_{B\ r.f.} = 0)$, one finds:

$$\frac{E_A(t_b;\ t_{B\ r.f.} = 0)}{E_A(t_b)_{extr.}} = \varepsilon + 1$$

and ε can be determined from the graph as:

$$\varepsilon = \frac{E_A(t_b;\ t_{B\ r.f.} = 0) - E_A(t_b)_{extr.}}{E_A(t_b)_{extr.}} \qquad \text{(IV-35)}$$

Once ε is known, it is simple to measure τ_{AB}. Making a new plot with all parameters unchanged, except that now the B system is kept at infinite temperature (by B r.f. phase-shifting, f.ex.) one obtains a straight line falling off steeply from E_{Ao} at $t_{B\ r.f.} = 0$, as described by Eq. (IV-21):

$$E_A(\omega_B, t_b) = E_{Ao} \cdot e^{-\frac{\varepsilon}{\tau_{AB}} t_{B\ r.f.} - \frac{1}{T_{1A}} t_b} \qquad \text{(IV-36)}$$

The slope $-\frac{\varepsilon}{\tau_{AB}}$, combined with ε determined from Eq. (IV-35), gives τ_{AB}.

Going back to the original curve which yielded ε, one can determine T_{1B} as follows: The slope λ of the straight portion of the graph is, according to Eq. (IV-17):

$$\text{slope} \equiv \lambda = -\frac{\varepsilon}{\varepsilon + 1}\left(\frac{1}{T_{1B}} - \frac{1}{T_{1A}}\right)$$

and therefore

$$\frac{1}{T_{1B}} = -\frac{\lambda(\varepsilon + 1)}{\varepsilon} + \frac{1}{T_{1A}} \qquad \text{(IV-37)}$$

With ε determined from the same curve, as described above, and T_{1A}

obtainable from a direct measurement on the A spin species, T_{1B} can be calculated. Equation (IV-37) applies for both $\lambda \gtrless 0$. In the special case where $\lambda = 0$, $T_{1B} = T_{1A}$ and it is not necessary to determine ε.

A modified version of the experimental procedure is possible, where t_b is allowed to vary from cycle to cycle such that $t_b = t_{B\ r.f.} + \Delta t$. Δt is a fixed time interval which is much shorter than t_b. The equations for $E_A(t_b)$, etc, will change slightly, but the same information on ε, τ_{AB} and T_{1B} can be obtained and no additional physical insight is gained from the method.

Returning now to Eq. (IV-37) and the procedure for measuring T_{1B}, it is apparent that with the exception of $T_{1B} \gg T_{1A}$, the method can be applied for a wide range of T_{1B} values, and is especially well suited in cases where T_{1B} is short (but still $\gg \tau_{AB}$). In this respect it complements very well the method used by McArthur, Hahn and Walstedt,[11] which can be briefly described as follows: The B reservoir in the rotating frame at $\theta \simeq 45°$ is first cooled by cross relaxation with an A reservoir which is at low temperature after ADRF. After the B coupling pulse is turned off, the laboratory frame B system will be in a state of low spin temperature since the B r.f. was applied off resonance. The B system heats up by lab. frame spin-lattice relaxation, and after a suitable time the B reservoir temperature is sampled. This is achieved by first bringing the A dipolar reservoir to infinite spin temperature with a series of saturating pulses, and then applying an off resonance B r.f. coupling pulse similar to the first one. If the B reservoir still retains a low temperature, the A system will be cooled down during the contact, and a dipolar signal will be stimulated by the θ pulse.

Compared with the method based on Eq. (IV- 37), this method is poorly suited to measure short B spin-lattice relaxation times unless τ_{AB} is very short. Since the coupling pulse is applied off resonance, τ_{AB} will be longer than in the on-resonance case, with a correspondingly longer coupling pulse for complete A-B thermal equilibration. For good definition of T_{1B}, the coupling pulse length should be much smaller than T_{1B}. This method is well suited in cases where T_{1B} is long, however, where the method developed in this chapter fails. Thus the two methods together cover the whole range of T_{1B} values from approximately τ_{AB} to infinity.

It should be mentioned that the method developed here measures a rotating-frame spin-lattice relaxation time, while the other measures relaxation times in the lab. frame. If the relaxation is induced by a randomly fluctuating hamiltonian via direct processes, the laboratory frame spin-lattice relaxation time can be written as a sum of spectral densities involving various components of the fluctuating hamiltonian at the laboratory frame transition frequency ω_{Bo}. As will be demonstrated in section V-B for a specific field configuration, the rotating-frame spin-lattice relaxation time will in addition depend on the spectral densities at the rotating-frame transition frequency called ω_{eB} above, and at the sum and difference frequencies $\omega_{Bo} \pm \omega_{eB}$. In certain cases, this will be of no fundamental importance, but it may also prove to be very useful: If T_{1B} is of such magnitude relative to other relevant parameters that both methods can be used, it may be possible to combine the two sets of data to pick out specific spectral density components or combinations of these that would be inaccessible from each data set separately.

Finally, one should consider the case where the B r.f. in applied off resonance. All equations in this section will remain unchanged, but the parameters E_{Bo} and τ_{AB} will vary with ω_B, as discussed earlier. Nothing new needs to be added to the discussion of the on-resonance case, but one can note the following:

The rotating-frame effective field is:

$$H_{eB} = \left\{ H_{1B}^2 + \frac{(\omega_{Bo} - \omega_B)^2}{\gamma_B^2} \right\}^{1/2} = \frac{\omega_{eB}}{\gamma_B}$$

By varying the frequency ω_B and the B r.f. power level, one obtains a rotating-frame transition frequency that varies over a wide range. As described above for the case $\omega_B = \omega_{Bo}$, the rotating-frame T_{1B} will in certain cases be sensitive to the spectral density component of the fluctuating hamiltonian at the frequency ω_{eB}. Here one has the opportunity to vary ω_{eB} throughout a range at the very low end of the frequency spectrum, and record the corresponding variation in T_{1B}.

IV-C-2. Test on the Thermal Reservoir Model

The main underlying assumptions for the thermal reservoir model analyzed above were briefly outlined at the beginning of this chapter, and have also been discussed in a general manner in Chapters II and III. They can be spelled out as follows:

In the absence of applied resonant r.f. fields, the A spins after ADRF are strongly coupled mutually in the rotating frame, weakly coupled to the lattice, and completely decoupled from other spin species in the sample. The macrostate of the coupled A spins can be described by a temperature $T_{LATTICE} \simeq \infty$ when thermal equilibrium with the lattice has been achieved. If a strong r.f. field is applied at a B spin transition frequency, the B spins will experience a strong mutual

coupling, a weak coupling to the A spins and the lattice, and no coupling to other spin species. The B rotating frame macrostate is describable by a temperature. The r.f. field affects the A spin species only indirectly through the A-B coupling, which is assumed weak compared to the mutual interaction between the A spins. If the A-B coupling could be severed without destroying the B reservoir, the A and B reservoir temperatures would relax exponentially towards $T_{LATTICE}$, with time constants T_{1A} and T_{1B}, respectively.

As described in Sections II-A and III-B, these assumptions may be rendered invalid by a number of complicating factors in a given substance. Since the B spin abundance will be fairly high in the cases that apply here, spin diffusion and thermal gradient problems may not be as important as interactions with other nuclear spin species in the sample and slight overlap between the lowest B spin lab. frame frequencies and the high frequency tail of the A spin dipolar spectrum. Also, careful experimental tests on the thermal reservoir model have so far centered on the special cases of pure magnetic or pure quadrupole laboratory frame hamiltonians. The model analyzed in this chapter will be assumed applicable to cases of mixed quadrupole-Zeeman hamiltonians, and it is not trivial that confirmations of the thermal reservoir model in the pure magnetic or quadrupole cases apply in the mixed case, with B r.f. applied on/off resonance.

The analytic results of this chapter, and by inference the thermal reservoir model, were tested experimentally for a specific A-B system, as described in the next chapter. One determined whether the experimentally determined parameter values ε, τ_{AB}, T_{1A} and T_{1B},

combined with the exact analytical expressions based on the thermal reservoir model, can describe the observed A-B spin relaxation behavior and the double resonance lineshape quantitatively. In these tests, all parameters in the theory are uniquely determined by the experimental data, at each value of ω_B:

Parameters that govern T_{1A} (sample temperature, f.ex.) are independent of ω_B. As mentioned in the preceding section, T_{1B} may in certain cases, depend on ω_B, but this case will not be treated here. At the center of the line, τ_{AB} will be a minimum, and the condition (Eq. (IV-15)) will be closest to being satisfied. Therefore, if the expression for $E_A(t_b)$ applies in the range around ω_{Bo}, which can be ascertained experimentally, then it should certainly apply at ω_{Bo} with a sufficiently high accuracy so that reliable values of ϵ and T_{1B} can be obtained at that point by the methods described previously. If $\epsilon(\omega_{Bo})$ is the value of ϵ at $\omega_B = \omega_{Bo}$, then $\epsilon(\omega_B)$ will be given by Eq. (IV-19). An analytical relationship between τ_{AB} and ω_{eB} with general applicability to different samples is not available, and it is therefore necessary to determine $\tau_{AB}(\omega_B)$ experimentally for each value of ω_B. How this is done was described above in connection with Eq. (IV-36). One should bear in mind, however, that τ_{AB} is obtained from the line with continuous B reservoir heating, while it is applied to the case with unmodulated B r.f. where the lineshape, relaxation rates, etc. are generally quite different.

Since these are effectively no adjustable parameters, a critical test on the internal consistency of the theory is obtained, and a good theoretical fit of experimental data will be taken as sufficient justification for the model in subsequent applications.

V. SPIN 3/2 PARTICLE IN A STRONG, RESONANT r.f. FIELD. CASE WHERE QUADRUPOLE AND ZEEMAN ENERGIES ARE OF ARBITRARY RELATIVE MAGNITUDES

Although this problem is of special interest in nuclear double resonance, the nuclear species under study will be treated as isolated from other spin systems in this chapter. In Section A, the effective gyromagnetic ratio in the rotating frame, (as measured by rotary saturation (audio resonance)), is derived for a given field configuration. For the same field configuration, the quadrupolar spin-lattice relaxation rate is calculated in Section B, as a function of the spectral densities of the stationary random lattice vibrations.

V-A. Transformation into the Interaction Representation. Effective Gyromagnetic Ratios in the Rotating Frame

To the author's knowledge, the only explicit computations of effective gyromagnetic ratios made so far have pertained to one of two special cases:

1) Quadrupole interaction negligible or zero compared to the Zeeman interaction in high field. This yields a rotating-frame effective gyromagnetic ratio equal to the laboratory frame γ_{LAB}.[10]

2) Zeeman-interaction negligible or zero compared to the quadrupole interaction. For a spin 3/2 nucleus in zero field one can define two counter-rotating frames of precession. A resonant circularly polarized r.f. field couples to the magnetic moment in the frame rotating in the same direction with an effective gyromagnetic ratio $\sqrt{3}\,\gamma_{LAB}$.[36]

In the following, no restrictions will be placed on the relative magnitudes of the quadrupole and Zeeman interactions, which means that perturbation treatments cannot be used. The experimental configuration

will be assumed as follows: The principal e.f.g. tensor symmetry axis is along the z-axis, and the asymmetry parameter η is taken as zero. The main laboratory field H_o is along the x-axis. Two oscillating fields are applied to the sample: A linearly polarized r.f. field of peak magnitude $2H_1$ parallel to the z-axis, and a linearly polarized field at audio frequencies and of peak magnitude $2H_{Aud}$ parallel to the x-axis.

The hamiltonian for the nuclei being studied is:

$$\mathcal{H} = \mathcal{H}_Q + \mathcal{H}_Z + \mathcal{H}_{r.f.} + \mathcal{H}_{Aud} + \mathcal{H}_1 \qquad (V-1)$$

where ($\hbar = 1$):

$\mathcal{H}_Q$ is the quadrupole hamiltonian with $\eta = 0$:

$$\mathcal{H}_Q = \frac{e^2qQ}{4I(2I-1)} \left(3I_z^2 - I(I+1)\right)$$

$\mathcal{H}_Z$ is the Zeeman hamiltonian in the laboratory frame:

$$\mathcal{H}_Z = -\gamma H_o I_x$$

$\mathcal{H}_{r.f.}$ is the interaction with the r.f. field oscillating at a frequency ω:

$$\mathcal{H}_{r.f.} = -2\gamma H_1 I_z \cos \omega t$$

ω is not necessarily equal to one of the transition frequencies. The peak field strength has been defined as $2H_1$, to give a rotating-frame field strength H_1

$\mathcal{H}_{Aud}$ is the audio resonance hamiltonian:

$$\mathcal{H}_{Aud} = -2\gamma H_{Aud} I_x \cos \omega_{aud} t$$

$\mathcal{H}_1$ includes interactions not mentioned above, specifically the randomly varying component of the quadrupole interaction due to lattice vibrations.

Since the laboratory frame energy levels are defined by

$$\mathcal{H}_o = \mathcal{H}_Q + \mathcal{H}_Z$$

where the quadrupole and Zeeman interactions may be approxi equal, the rotating-frame picture does not apply in the conventional sense, and what has been loosely termed "in the rotating frame" above should properly be termed "in the interaction representation of $\mathcal{H}_o$".

It might be helpful to outline briefly the scheme that will be followed: First, we shall perform a transformation into the interaction representation of $\mathcal{H}_o$, which yields an interaction representation Hamiltonian

$$\mathcal{H}^* = \exp(i\mathcal{H}_o t)\ \mathcal{H}\ \exp(-i\mathcal{H}_o t) - \mathcal{H}_o$$

$$= \mathcal{H}_{r.f.}^* + \mathcal{H}_{Aud}^* + \mathcal{H}_1^* \qquad \text{(V-2)}$$

$\mathcal{H}_1^*$ will be important in the next section (V-B), but will be dropped here. Second, the eigenvalues of the secular part of $\mathcal{H}_{r.f.}^*$ will be computed, which yields the rotating frame energy levels. Finally, matrix elements of $\mathcal{H}_{Aud}^*$ between the eigenstates of $\mathcal{H}_{r.f.}^*$ will be computed, to find which transitions are being observed. Knowledge of the rotating frame transition frequency as a function of the rotating-frame field strength H_1 then yields the effective gyromagnetic ratio.

The transformation operator L_q into the $\mathcal{H}_o$ interaction representation is obviously no simple rotation operator:

$$L_q = \exp(i\mathcal{H}_o t) = \exp\left\{i\left(\frac{e^2qQ}{4I(2I-1)}\left(3I_Z^2 - I(I+1)\right) - \gamma H_o I_x\right)t\right\} \qquad \text{(V-3)}$$

One way to make L_q more tractable is to try to expand the exponential in a spin operator power series, but although this is possible with

$\exp(iI_Z^2 t)$ and $\exp(iI_x t)$ separately, f.ex. by using the Pauli spin operator formalism of Leppelmeier and Hahn,[34] it is not feasible in this case since the operators I_Z^2 and I_x do not commute with each other nor with their commutator $[I_z^2, I_x]$.[39] Successive transformations into the $\mathcal{H}_Q$ interaction representation and then the $\mathcal{H}_Z$ interaction representation is not feasible. Since the quadrupole and Zeeman energies may be of comparable magnitude, it is not legitimate to discard time dependent terms after the first transformation, and the large number of resulting terms in $\mathcal{H}_Z^*$ which do not commute makes the next transformation $\exp(i\mathcal{H}_Z^* t)$ even more difficult than the original one: $\exp(i\mathcal{H}_o t)$.

It is still possible to perform the transformation into the $\mathcal{H}_o$ interaction representation, but one must forgo the convenience of a representation-independent description. By first transforming the total hamiltonian $\mathcal{H}$ into a representation where $\mathcal{H}_o$ is diagonal, called the B- or eigen-representation in what follows, the transformation operator L_q becomes trivially:

$$L_q = \begin{pmatrix} \exp(iE_1 t) & & & \\ & \exp(iE_2 t) & & \\ & & \exp(iE_3 t) & \\ & & & \exp(iE_4 t) \end{pmatrix}_B \qquad \text{(V-4)}$$

where the E_i's are the energy eigenvalues of $\mathcal{H}_o$.

The diagonalization procedure becomes less laborious if one writes the hamiltonian $\mathcal{H}_o$ with γH_o as energy units:

$$\frac{\mathcal{H}_o}{\gamma H_o} = \frac{\lambda}{2}\left(3I_Z^2 - \frac{15}{4}\right) - I_x \qquad \text{(V-5)}$$

where

$$\lambda = \frac{e^2qQ/2I(2I - 1)}{\gamma H_o}$$

is defined so as to conform with Parker's[40] definition. Thus, in the limiting cases where

$$\text{quadrupole interaction/Zeeman interaction} \begin{matrix} \rightarrow \infty \\ \rightarrow 0 \end{matrix}$$

one has

$$\lambda \begin{matrix} \rightarrow \infty \\ \rightarrow 0 \end{matrix}$$

respectively. It is convenient to divide up the analysis which follows into two parts, corresponding to the cases $0 \leqslant \lambda \leqslant 1$ and $0 \leqslant \frac{1}{\lambda} \leqslant 1$.

Consider first the case $0 \leqslant \lambda \leqslant 1$. In the representation where I_z is diagonal, called the A representation in the following, one obtains the secular determinant:

$$\begin{vmatrix} \frac{3}{2}\lambda - T_i & -\frac{\sqrt{3}}{2} & & \\ -\frac{\sqrt{3}}{2} & -\frac{3}{2}\lambda - T_i & -1 & \\ & -1 & -\frac{3}{2}\lambda - T_i & -\frac{\sqrt{3}}{2} \\ & & -\frac{\sqrt{3}}{2} & \frac{3}{2}\lambda - T_i \end{vmatrix}_A = 0$$

corresponding to the usual I_z eigenvectors, in row form:

$$|m_j\rangle = \left(\delta_{\frac{3}{2},m_j}, \delta_{\frac{1}{2},m_j}, \delta_{-\frac{1}{2},m_j}, \delta_{-\frac{3}{2},m_j}\right).$$

Here, the eigenvalues T_i yield the $\mathcal{H}_o$ eigenvalues $E_i = \gamma H_o T_i$. The secular equation is:

$$T_i^4 - \frac{1}{2}(9\lambda^2 + 5)T_i^2 + 3\lambda T_i + \frac{9}{16}(9\lambda^4 + 2\lambda^2 + 1) = 0 \qquad \text{(V-7)}$$

or, in factored form:

$$T_i^2 \pm T_i - \frac{3}{4}(1 \pm 2\lambda + 3\lambda^2) = 0$$

The roots are

$$T_{1,2} = \frac{1}{2}\left(-1 \pm \sqrt{4 + 6\lambda + 9\lambda^2}\right) \; ; \quad \text{Root 1: +} \quad \text{Root 2: -}$$

$$T_{3,4} = \frac{1}{2}\left(1 \pm \sqrt{4 - 6\lambda + 9\lambda^2}\right) \; ; \quad \text{Root 3: +} \quad \text{Root 4: -}$$

In the A representation, the eigenvectors corresponding to these roots are:

$$|E_i\rangle = \begin{pmatrix} \alpha_i \\ \beta_i \\ \gamma_i \\ \delta_i \end{pmatrix}_A$$

For $\lambda \neq 0$, the states are generally nondegenerate. We define the quantities:

$$A_i = \frac{3}{2}\lambda - T_i \; ; \; B_i = \frac{3}{2}\lambda + T_i \qquad \text{(V-8)}$$

In terms of these, the eigenvector components are:

$$\beta_i = \frac{2}{\sqrt{3}} A_i \alpha_i \; ; \; \gamma_i = \left(-\frac{2}{\sqrt{3}} - \frac{\sqrt{3}}{2} A_i B_i\right)\alpha_i \; ; \; \delta_i = \left(-\frac{3}{2A_i} - B_i\right)\alpha_i = \frac{\sqrt{3}}{2A_i}\gamma_i \qquad \text{(V-9)}$$

where α_i may be adjusted to give the eigenvectors $|E_i\rangle$ unit length. As shown in Appendix A, one has for arbitrary λ:

$$\alpha_{1,2} = \delta_{1,2} \; ; \; \beta_{1,2} = \gamma_{1,2} \; ; \; \alpha_{3,4} = -\delta_{3,4} \; ; \; \beta_{3,4} = -\gamma_{3,4}$$

for components of the same vector, and

$$\alpha_1 = \beta_2 \; ; \; \alpha_2 = -\beta_1 \; ; \; \alpha_3 = \beta_4 \; ; \; \alpha_4 = -\beta_3$$

for components of different vectors.

This reduces the number of independent components to four, which will be defined as:

$$a \equiv \alpha_1 = \beta_2 = \gamma_2 = \delta_1 \qquad b \equiv \alpha_2 = -\beta_1 = -\gamma_1 = \delta_2$$
$$c \equiv \alpha_3 = \beta_4 = -\gamma_4 = -\delta_3 \qquad d \equiv \alpha_4 = -\beta_3 = \gamma_3 = -\delta_4 \tag{V-10}$$

The eigenvectors $|E\rangle_i$ corresponding to eigenvalues T_i, E_i are:

$$|E_1\rangle = \begin{pmatrix} a \\ -b \\ -b \\ a \end{pmatrix}_A \qquad |E_2\rangle = \begin{pmatrix} b \\ a \\ a \\ b \end{pmatrix}_A \qquad |E_3\rangle = \begin{pmatrix} c \\ -d \\ d \\ -c \end{pmatrix}_A \qquad |E_4\rangle = \begin{pmatrix} d \\ c \\ -c \\ -d \end{pmatrix}_A \tag{V-11}$$

These define the orthogonal (since $|E_i$ real) matrix

$$U_{AB} = (|E_1\rangle\ |E_2\rangle\ |E_3\rangle |E_4\rangle)_A \tag{V-12}$$

which generates the transformation from the A to the B representation.

Transformation of $\mathcal{H}_{r.f.}$ and $\mathcal{H}_{Aud}$ into the $\mathcal{H}_o$ interaction representation is now straightforward. $\mathcal{H}_{r.f.}$ will be treated first, since it defines the energy levels in the interaction representation:

Transformation into the B representation yields:

(V-13)

$$U_{AB}^{-1}\,\mathcal{H}_{r.f.}\,U_{AB} = -2\gamma H_1 \cos\omega t \left(\begin{array}{cc|cc} & 0 & 3ac+bd & 3ad-bc \\ & & 3bc-ad & 3bd+ac \\ \hline 3ac+bd & 3bc-ad & & \\ 3ad-bc & 3bd+ac & 0 & \end{array}\right)_B$$

and in the $\mathcal{H}_o$ interaction representation one finally has

$$\mathcal{H}_{r.f.}^{*} = L_q\,U_{AB}^{-1}\,\mathcal{H}_{r.f.}\,U_{AB}\,L_q^{-1} = -\gamma H_1(e^{i\omega t} + e^{-i\omega t}) \times \tag{V-14}$$

$$\left(\begin{array}{cc|cc} & 0 & (3ac+bd)e^{i(E_1-E_3)t} & ;(3ad-bc)e^{i(E_1-E_4)t} \\ & & (3bc-ad)e^{i(E_2-E_3)t} & ;(3bd+ac)e^{i(E_2-E_4)t} \\ \hline (3ac+bd)e^{i(E_3-E_1)t} & ;(3bc-ad)e^{i(E_3-E_2)t} & & \\ (3ad-bc)e^{i(E_4-E_1)t} & ;(3bd+ac)e^{i(E_4-E_2)t} & 0 & \end{array}\right)_B$$

If the energy levels E_i are well separated from each other (i.e. by more than a few linewidths), the nonzero elements in the matrix will be highly time dependent before multiplication by $(e^{i\omega t} + e^{-i\omega t})$. By adjusting the frequency ω of the r.f. field so that it matches one of the transition frequencies $|E_i - E_j|$, however, one pair of symmetrically located matrix elements in $\mathcal{H}_{r.f.}{}^*$ can be made secular while the others remain highly time dependent. It is assumed here that the transition frequencies corresponding to different sets of energy levels are separated by at least several linewidths.

Let us assume that the r.f. is applied on resonance for one of the transitions, say $\omega = |E_1 - E_4|$. The secular part of $\mathcal{H}_{r.f.}{}^*$, which determines the audio resonance frequency and the effective gyromagnetic ratio, is (the dash indicates that only secular terms are included):

$$\mathcal{H}_{r.f.}{}^{*\prime} = -\gamma H_1(3ad-bc) \left(\begin{array}{cc|cc} 0 & & 0 & 1 \\ & & 0 & 0 \\ \hline 0 & 0 & & \\ 1 & 0 & & 0 \end{array}\right)_B$$

The eigenvalues of $\mathcal{H}_{r.f.}{}^{*\prime}$ yield the rotating frame energy levels:

$$E_1{}^* = \gamma H_1(3ad - bc) \; ; \; E_2{}^* = E_3{}^* = 0 \; ; \; E_4{}^* = -\gamma H_1(3ad - bc) \qquad \text{(V-16)}$$

The corresponding eigenvectors are: (V-17)

$$|E_1{}^*\rangle = \frac{1}{\sqrt{2}}\begin{pmatrix}1\\0\\0\\1\end{pmatrix}_B \; ; \; |E_2{}^*\rangle = \frac{1}{\sqrt{2}}\begin{pmatrix}0\\1\\1\\0\end{pmatrix}_B \; ; \; |E_3{}^*\rangle = \frac{1}{\sqrt{2}}\begin{pmatrix}0\\1\\-1\\0\end{pmatrix}_B \; ; \; |E_4{}^*\rangle = \frac{1}{\sqrt{2}}\begin{pmatrix}1\\0\\0\\-1\end{pmatrix}_B$$

It now remains to determine which transitions are excited by $\mathcal{H}_{Aud}$. In order to compute matrix elements between the states $|E_i{}^*\rangle$, the audio

hamiltonian is transformed into the $\mathcal{H}_o$ interaction representation by a procedure analogous to that used to find $\mathcal{H}_{r.f.}{}^*$ above:

$$\mathcal{H}_{Aud}{}^* = L_q\, U_{AB}^{-1}\, \mathcal{H}_{Aud}\, U_{AB}\, L_q^{-1} = -\gamma H_{Aud} \cos \omega_{Aud}\, t \left(\begin{array}{cc|cc} \multicolumn{2}{c|}{\multirow{2}{*}{I \quad II \\ III \quad IV}} & \multicolumn{2}{c}{\multirow{2}{*}{0}} \\ & & & \\ \hline \multicolumn{2}{c|}{\multirow{2}{*}{0}} & \multicolumn{2}{c}{\multirow{2}{*}{V \quad VI \\ VII \quad VIII}} \\ & & & \end{array} \right)_B \tag{V-18}$$

Here;

$I = -4\sqrt{3}\, ab + 4b^2$; $II = (2\sqrt{3}\,(a^2-b^2) - 4ab)e^{i(E_1-E_2)t}$

$III = (2\sqrt{3}\,(a^2-b^2) - 4ab)e^{i(E_2-E_1)t}$; $IV = 4\sqrt{3}\, ab + 4a^2$

$V = -4\sqrt{3}\, cd - 4d^2$; $VI = (2\sqrt{3}\,(c^2-d^2) + 4cd)e^{i(E_3-E_4)t}$

$VII = (2\sqrt{3}\,(c^2-d^2) + 4cd)e^{i(E_4-E_3)t}$; $VIII = 4\sqrt{3}\, cd - 4d^2$

Formally, the matrix above can be written

$$\langle E_i |\, \mathcal{H}_{Aud}{}^* | E_j \rangle_B$$

where now the $\mathcal{H}_o$ eigenstates in the B representation are just:

$$|E_i\rangle_B = \begin{pmatrix} \delta_{1,i} \\ \delta_{2,i} \\ \delta_{3,i} \\ \delta_{4,i} \end{pmatrix}_B$$

where $\delta_{i,j} = 1$ if $i = j$, and zero otherwise. The matrix elements of interest here are:

$$\begin{aligned} M_{K',K} &= \langle E_{K'}{}^* | \mathcal{H}_{Aud}{}^* \, | E_K{}^* \rangle_B \\ &= \sum_{i,j} \langle E_{K'}{}^* | E_i \rangle_B \langle E_i | \mathcal{H}_{Aud}{}^* | E_j \rangle_B \langle E_j | E_K{}^* \rangle_B \end{aligned} \tag{V-19}$$

Expanding:

$$|E_K{}^*\rangle_B = \sum_\ell c_{K\ell} |E_\ell\rangle_B$$

one finds

$$M_{K',K} = \sum_{i,j} c_{K'i}^{*}\, c_{Kj}\, \langle E_i | \mathcal{H}_{Aud}^{*} | E_j \rangle_B$$

Finding the expansion coefficients c_{Kj} is trivial in the B representation:

$$|E_1^{*}\rangle_B = \frac{1}{\sqrt{2}} (|E_1\rangle_B + |E_4\rangle_B) \; ; \; |E_2^{*}\rangle_B = \frac{1}{\sqrt{2}} (|E_2\rangle_B + |E_3\rangle_B)$$
$$|E_2^{*}\rangle_B = \frac{1}{\sqrt{2}} (|E_2\rangle_B - |E_3\rangle_B) \; ; \; |E_4^{*}\rangle_B = \frac{1}{\sqrt{2}} (|E_1\rangle_B - |E_4\rangle_B) \qquad \text{(V-20)}$$

To save writing labor in the following, one can define:

$$\langle E_j | \mathcal{H}_{Aud}^{*} | E_j \rangle_B \equiv (i,j)$$

The matrix elements $M_{K',K}$ can now be written out from Eqs. (V-17), (V-18) and (V-19) by inspection (all c_{ij}'s real):

$$\begin{aligned} M_{1,4} &= \sum_{i,j=1} c_{1,i}^{*}\, c_{4,j}\, (i,j) \\ &= \tfrac{1}{2} \{(1,1) - (4,4)\} \\ &= -\tfrac{1}{2} \gamma H_{Aud} \cos \omega_A t \{(-4\sqrt{3}\, ab + 4b^2) - (4\sqrt{3}\, cd - 4d^2)\} \\ &= 2 \gamma H_{Aud} \cos \omega_A t \{-\sqrt{3}\, (ab + cd) + b^2 - d^2\} \end{aligned} \qquad \text{(V-21)}$$

$$M_{1,2} = -\gamma H_{Aud} \cos \omega_A t \{(\sqrt{3}\, (a^2 - b^2) - 2ab) e^{i(E_1 - E_2)t} + (\sqrt{3}\, (c^2 - d^2) + 2cd) e^{i(E_4 - E_3)t}\}$$

$$M_{1,3} = -\gamma H_{Aud} \cos \omega_A t \{(\sqrt{3}\, (a^2 - b^2) - 2ab) e^{i(E_1 - E_2)t} - (\sqrt{3}\, (c^2 - d^2) + 2cd) e^{i(E_4 - E_3)t}\}$$

$$M_{2,4} = -\gamma H_{Aud} \cos \omega_A t \{(\sqrt{3}\, (a^2 - b^2) - 2ab) e^{i(E_2 - E_1)t} - (\sqrt{3}\, (c^2 - d^2) + 2cd) e^{i(E_3 - E_4)t}\}$$

$$M_{3,4} = -\gamma H_{Aud} \cos \omega_A t \{(\sqrt{3}\, (a^2 - b^2) e^{i(E_2 - E_1)t} + (\sqrt{3}\, (c^2 - d^2) + 2cd) e^{i(E_3 - E_4)t}\}$$

Here, one notes that all matrix elements are generally nonzero, but all elements except $M_{1,4}$ contain a high-frequency time dependence corresponding to a perturbation hamiltonian which is strongly off-resonance and thus does not affect the rotating-frame population levels.

The transition being excited by the audio field is therefore between states $|E_1^*\rangle$ and $|E_4^*\rangle$, and the effective gyromagnetic ratio is

$$\gamma_{eff} = \frac{E_1^* - E_4^*}{H_1} = 2(3ad - bc) \cdot \gamma_{LAB}$$

in the rotating frame of an r.f. field vector oscillating at the transition frequency between $\mathcal{H}_o$ eigenstates $|E_1\rangle$ and $|E_4\rangle$. The effect of audio field components along the y and z-axes can be evaluated by the same method. One finds that all matrix elements are either zero or highly time dependent, and accidental misalignment of the audio field will therefore not affect the results derived above.

So far, it has been assumed that the r.f. was applied at a frequency matching the transition energy between the two laboratory frame eigenstates $|E_1\rangle$ and $|E_4\rangle$. For spin $\frac{3}{2}$ nuclei in the case with 4 nondegenerate laboratory frame eigenstates there are in general 6 distinct transition frequencies. Each transition can be treated in the same manner as for $|E_1\rangle \leftrightarrow |E_4\rangle$, and for the field configuration assumed in this chapter the effective gyromagnetic ratios are given in the following table:

Table V.1. Effective gyromagnetic ratios in the rotating frame.

Lab. Frame Transition (Def.)	Lab. Frame Transition Energy	Effective Gyromagnetic Ratio in the Rot. Frame
3	$E_1 - E_2$	Forbidden Transition
4	$E_1 - E_3$	$2(3ac + bd) \cdot \gamma_{LAB}$
1	$E_1 - E_4$	$2(3ad - bc) \cdot \gamma_{LAB}$
6	$E_2 - E_3$	$2(3bc - ad) \cdot \gamma_{LAB}$
2	$E_2 - E_4$	$2(3bd + ac) \cdot \gamma_{LAB}$
5	$E_3 - E_4$	Forbidden Transition

So far, only the case $0 < \lambda \leqslant 1$ has been covered. The range $0 < \frac{1}{\lambda} \leqslant 1$ can be treated in a manner analogous to the above. To avoid singularities when $\mathcal{H}_z \to 0$ (i.e. $\frac{1}{\lambda} \to 0$), it is appropriate to define the main hamiltonian $\mathcal{H}_o$ in terms of the quadrupole energy term $\frac{e^2qQ}{4I(2I-1)}$. With this modification and λ defined as before, the expressions for $\alpha_i(\lambda)$ and $T_i(\lambda)$ leading to the transformation matrix U_{AB} will be different from those given for the case $0 < \lambda \leqslant 1$, but the elements of U_{AB} remain the same when expressed directly in terms of the parameters appearing in $\mathcal{H}_o$. Thus one finds for the whole range $0 < \lambda < \infty$ that the effective gyromagnetic ratios are as given in Table V.1.

Some caution is in order, however, when taking the limits $\lambda \to 0$ and $\frac{1}{\lambda} \to 0$, corresponding to pure Zeeman, respectively pure quadrupole laboratory frame hamiltonians. In these special cases, the values of γ_{eff} are already known, and one may compare with results derived in this chapter. Obviously, one must use the proper expressions with $\gamma_{LAB} \cdot H_o$ or $\frac{e^2qQ}{4I(2I-1)}$ as energy units to avoid singularities, as mentioned previously. More interesting, perhaps, are the following two pitfalls:

First, when the limits of pure quadrupole or Zeeman laboratory frame hamiltonians are approached, all the transition frequencies ω_i

will no longer be well separated, and the overlap leads to additional elements in the r.f. hamiltonian matrix $\mathcal{H}^{*\prime}_{r.f.}$. This in turn changes the rotating frame eigenstates, and thus it is necessary to go back to the secular r.f. hamiltonian in order to obtain the effective gyromagnetic ratios. The procedure is identical to the one outlined above, and leads to the expected result $\gamma_{eff.} = \gamma_{LAB}$ in the case where $\lambda = 0$.

Second, laboratory frame states may arise which are not connected by the r.f. perturbation. This is illustrated in the pure quadrupole case ($\frac{1}{\lambda} = 0$), where the quadrupolar hamiltonian $\mathcal{H}_Q = \frac{e^2qQ}{4I(2I-1)} \times (eI_z^2 - I(I+1))$ obviously commutes with the r.f. hamiltonian $\mathcal{H}_{r.f.} = 2\gamma H_1 I_z \cos \omega t$. One may still find effective gyromagnetic ratios for the pure quadrupole case by assuming that the r.f. field is applied in another direction, say the x direction, and using the same methods as outlined above. In this manner, one finds that the rotating frame eigenstates are doubly degenerate with a level separation $\gamma_{LAB} H_1 \sqrt{3}$. The corresponding effective gyromagnetic ratio in the rotating frame is therefore $\sqrt{3}\, \gamma_{LAB}$, which is the value already cited for this special case.

Comparison with Eq. (V-13) shows that for a given transition between two laboratory frame eigenstates, there is a direct proportionality between the $\mathcal{H}_{r.f.}$ matrix elements of those eigenstates and the effective gyromagnetic ratio in the rotating frame. Formally, therefore, one can define the effective gyromagnetic ratio of a forbidden transition to be zero. As the field configuration is gradually changed so that the matrix element of $\mathcal{H}_{r.f.}$ for the forbidden transition goes from zero to a nonzero value, the effective gyromagnetic ratio

will also increase from zero. For an allowed transition with a small effective gyromagnetic ratio one would expect a weak double resonance line.

The special case of an e.f.g. tensor with $\eta = 0$ and the principal axis perpendicular to the static magnetic field has been treated here, since it will be of interest in a later chapter. A more general case with an arbitrary angle Θ between the principal e.f.g. axis and the magnetic field, and a nonzero asymmetry factor can be treated by a straightforward, but laborious application of the technique shown above. In the special case where $\eta = 0$, $\Theta = 0$ one has $[\mathcal{H}_Q, \mathcal{H}_Z] = 0$, and derivation of the effective gyromagnetic ratios in the rotating frame can be performed entirely in operator form.

Finally, it is easy to show that the rotating frame transition energy $\gamma_{eff.} \cdot H_1$ determined by audio resonance is the same one which is involved in cross-coupling processes with other nuclei in the crystal, a fact which is important in nuclear double resonance, f.ex. Cross-coupling comes about by perturbation of the rotating frame eigenstates due to interaction between the spin magnetic dipole moment and the fluctuating local magnetic fields, and the interaction hamiltonian can be written on the form:

$$\mathcal{H}_{int} = A(t) \cdot I_x + B(t) \cdot I_y + C(t) \cdot I_z$$

A(t), B(t) and C(t) can be treated as c-numbers in this context. To see how $\mathcal{H}_{int.}$ affects the rotating frame populations, one can proceed in direct analogy with the audio saturation case, but now weighting matrix elements with the spectral densities of A(t), B(t) and C(t) at

the rotating frame transition frequencies. As was the case with audio resonance, one finds that regardless of which laboratory frame transition is being excited by the r.f. field, $H_{int.}$ can only cause transitions between the two most widely separated rotating frame energy levels. Thus, the same two levels are involved regardless of whether energy exchange takes place due to flipping neighboring dipoles or to externally generated fields, and one has effectively a 2-level system in the rotating frame.

V-B. Quadrupolar Spin-Lattice Relaxation in the Spin-Lock State

It is well known that the spin-lattice relaxation time for a given nuclear species in a solid can only be a uniquely defined quantity of one specifies the states between which the relaxation takes place. The reason for this is as follows: By suitable preparation of a given spin system it is possible to define several sets of spin system eigenstates (in appropriate reference frames) where the state of the system and its evolution in time is describable by a spin temperature. Each set of eigenstates will generally be different, and the perturbation hamiltonian which causes relaxation will not transform into each reference frame in the same manner, leading to fundamentally different spin-lattice relaxation times.

This has been demonstrated by Leppelmeier and Hahn[34] in the case of a system with pure quadrupole interaction in the laboratory frame, with special application to Cl^{35} in chlorate salts: In zero magnetic field, Cl^{35} has two doubly degenerate levels in the laboratory frame, and relaxation between these levels in described by a single relaxation time $T_{1,LAB}$. Another relaxation time can be defined if the Cl^{35} system is

subjected to a spin lock sequence followed by continuous irradiation by a strong r.f. field at the Cl^{35} laboratory frame transition frequency. The macroscopic magnetization along the rotating-frame magnetic field vector will then decay with a characteristic time $T_{1,S.L.}$. Finally, if one performs adiabatic demagnetization in the rotating frame (ADRF) on the Cl^{35} system which leaves the spin system in a dipolar state (Cfr. II-B),then the spin order evolves towards its final thermal equilibrium value at a rate $1/T_{1.ADRF}$. For the same nuclear species, Cl^{35}, Leppelmeier and Hahn found that the three relaxation times $T_{1.LAB}$, $T_{1,S.L.}$ and $T_{1,ADRF}$ were different in their analytical dependence on the relaxation perturbation and had numerical values that were different, although of the same order of magnitude.

The same three relaxation times may be defined and analyzed in an analogous manner for nuclear species with pure Zeeman hamiltonians in the laboratory frame, although the perturbation hamiltonian may be different (magnetic dipole instead of quadrupole interaction). This leads to the familiar $T_{1,LAB}$ for the equidistant laboratory frame Zeeman levels. Relaxation in the spin-lock state (i.e. described by $T_{1,\rho}$) has been studied by Redfield[10] and other,[21,34] while relaxation after ADRF for the strong collision case first was analyzed by Slichter and Ailion.[32]

The case with mixed quadrupole and Zeeman laboratory frame hamiltonians of arbitrary relative magnitudes is more difficult. Apart from increased analytical complexity, there are two reasons for this: First, since there now are in general several distinct laboratory frame transition frequencies, mutual spin flips will no longer contribute towards establishing a Boltzmann distribution between the laboratory frame energy levels and

it may not be possible to define a spin-lattice relaxation time. For the spin temperature description to be valid, it is then necessary to postulate that other mechanisms, like coupling to other spin species, maintain a Boltzmann distribution, or that the system is initially in a state describable by a spin temperature, and that changes in populations caused by the relaxation perturbation are such that the Boltzmann distribution is conserved during the time evolution of the system. Second, a mixed Zeeman-quadrupole system will permit transitions characterized by different relaxation rates.[41] An example of this is a Zeeman system with a quadrupole perturbation (static). The perturbation causes an admixture of the pure Zeeman states, and as a result relaxation transitions with $\Delta m = 2$ become allowed in addition to the $\Delta m = 1$ transitions allowed in the pure Zeeman case. The transition rates will be different for $\Delta m = 1$ and $\Delta m = 2$, and the relaxation behavior of the system cannot be described by a single time constant. A similar result applies for the Zeeman-perturbed quadrupole levels in the laboratory frame.

Below, the spin-lock state relaxation time $T_{1,S.L.}$ will be computed for spin 3/2 nuclei with no restrictions on the relative magnitudes of the Zeeman and quadrupole laboratory frame hamiltonians. $T_{1,S.L.}$ was chosen since it is of interest in the experimental part of this thesis, but there are also more fundamental reasons why $T_{1,S.L.}$ may be preferred for study rather than $T_{1,LAB}$ or $T_{1,ADRF}$: As was described at the end of Section V-A, the spin system in the spin-lock state can be treated as a two-level system, and one thus avoids the problems of non-Boltzmann population distributions and of non-exponential relaxation that were

involved in the analysis of $T_{1,LAB}$. Expressions for spin-lattice relaxation times in the dipolar state ($T_{1,ADRF}$) cannot be written with as much generality as in the spin-lock case, since the dipolar state spin-lattice relaxation time will depend strongly on the lattice symmetry and-parameters.

Before plunging into the computations necessary for extracting $T_{1,S.L.}$, it might be a possible motivating factor to consider what additional information, if any, may be obtained by extending an investigation to include, say, spin-lattice relaxation times in the spin-lock and dipolar states in addition to the laboratory frame relaxation time. One obvious illustration of this appears in the experimental part of the thesis, where $T_{1,S.L.}$ was the only relaxation time which was experimentally obtainable at all for K^{39} in KDP! More generally, however, one can exploit the fact that $T_{1,LAB}$, $T_{1,S.L.}$ and $T_{1,ADRF}$ depend on the symmetry components of the lattice vibrations (or microscopic motion) in different ways, and also will exhibit different sensitivity to the various parts of the fluctuation spectrum of the relaxation perturbation. Thus, one can to some extent selectively study specific modes of motion, and perhaps the most striking example of this is the use of $T_{1,ADRF}$-measurements in investigations on ultraslow motion. Also, given a set of analytical expressions for $T_{1,LAB}$, $T_{1,S.L.}$ and $T_{1,ADRF}$ in terms of spectral densities of lattice fluctuations (see f.ex. Leppelmeier and Hahn[34]), it is in principle possible to express the spectral densities or linear combinations of these in terms of the spin-lattice relaxation times. Experimental determination of $T_{1,LAB}$, $T_{1,S.L.}$ and $T_{1,ADRF}$ would then yield considerable information on the state of motion of the lattice.

V-B-1. Quadrupole Relaxation. General

The physical background of quadrupolar relaxation can be sketched as follows: The relaxing nucleus, which must necessarily possess a quadrupole moment, can be in one of the energy eigenstates of a time independent hamiltonian. This static hamiltonian may be purely magnetic, arising from interaction with an externally applied magnetic field, it may be purely quadrupolar and due to interaction with the local electric field gradient, or a mixture of both. These energy levels are perturbed by a time-dependent interaction which causes relaxation, and in quadrupolar relaxation, lattice vibrations cause the perturbation by altering and redistributing the charges that are the sources of the electric field gradient at the nucleus. The nuclear quadrupole moment couples to this time varying electric field gradient, and this will still be the case when the static (unperturbed) hamiltonian is purely magnetic, f.ex. when the nucleus occupies a site of cubic symmetry with a resulting zero static quadrupole interaction. A detailed analysis will be given below.

The quadrupole interaction can provide a strong spin-phonon coupling, and in pure insulating solids at lattice temperature $\gtrsim \Theta_{Debye}$, quadrupolar relaxation may dominate over other contributions to the nuclear spin-lattice relaxation rate. Relaxation can come about by either a direct process where a single phonon at the nuclear transition frequency is absorbed, or by one of several indirect processes, of which the two-phonon Raman process is the most important. A Raman process involves annihilation of one phonon at a frequency ω_i and creation of another at ω_j, such that $\omega_i - \omega_j$ is equal to the nuclear transition frequency. In the

high-temperature region, $T \gtrsim \Theta_{Debye}$, the two-phonon process will generally be by far the most important one, since the direct process only can take place in a very narrow region at the extreme low-frequency end of the lattice fluctuation spectrum, while the Raman process ranges over all frequencies in the fluctuation spectrum. Since the direct process depends on the spectral density of the lattice fluctuations at the nuclear transition frequency, the direct process relaxation time will in general be a function of the transition frequency. This is in contrast to the indirect case, where integration of relaxation contributions from all parts of the fluctuation spectrum leads to a frequency-independent relaxation time.

The first detailed analysis of indirect process quadrupolar relaxation was made by Van Kranendonk.[42] Using a model with ionic point charges as sources of the fluctuating electric field gradient (e.f.g.), and with a thermally generated acoustic-mode disturbance of the lattice, he found the Raman process relaxation very inefficient at temperatures much lower than the Debye temperature Θ_{Debye}. At lattice temperatures $T \gtrsim 1/2\Theta_{Debye}$, the leading term in the relaxation rate was found to vary as T^2, a typical feature of Raman relaxation. Later theories on Raman process relaxation have extended the Van Kranendonk theory to include other sources of e.f.g. modulation, such as fluctuations in electronic bonding,[43,44] and lattice vibrations of both acoustic and optic type.[41] The results did not depart dramatically from those of Van Kranendonk.

In a few, but important cases, the direct process can be dominant, namely when the spectral density of the lattice fluctuations in the nuclear transition frequency region (i.e., at very low frequencies compared to

average phonon frequencies) becomes very much larger than predicted by the standard Debye spectrum. Ultrasonic techniques may be used to generate such high phonon densities, but of more interest here is the existence of highly excited low frequency lattice modes, or so-called "soft modes" in ferroelectrics near the Curie temperature T_c. As $T \to T_c$, the spectral density of these modes increases enormously in the low frequency region, and sufficiently close to T_c the direct process relaxation may become very rapid.

V-B-2. Computation of Spin-Lock State Relaxation Times

In this section, analytical expressions will be obtained for direct process quadrupolar spin-lattice relaxation times in the spin-lock state. The relaxing nuclei will be assumed to have spin 3/2, and their static magnetic and quadrupole interactions in the laboratory frame can be of arbitrary magnitudes. Crystal orientation, field configuration and hamiltonian parameters will be assumed identical to those in Section V-A, and the results derived there can be used directly. Results for other field configurations and crystal orientations are obtained by a straightforward extension of the procedure outlined below.

The spin lock state was discussed in Chapter II, and Refield's hypothesis of a spin temperature in the rotating frame was presented. Abundant experimental verification of the hypothesis has been reported in the literature, and in the following, it will be assumed that the behavior of the spin system in the spin-lock state can be described by a spin temperature. This must be verified in each specific case, f.ex. by making experimental comparisons with the results in Chapter IV. The assumption will also be made that the rotating frame effective field,

i.e., the r.f. field strength H_1 on resonance, is much larger than local dipolar fields. This simplifies the analysis in that the energy reservoir of the dipole-dipole couplings can be ignored, and there will be only one thermal reservoir of purely Zeeman character in the rotating frame.

The spin-lattice relaxation time can be defined as the spin temperature decay time, if the spin temperature varies exponentially in time towards a value corresponding to thermal equilibrium with the lattice. The expectation value of any traceless operator will decay at the same rate as the spin temperature, and thus the spin-lattice relaxation process in the spin-lock state can easily be visualized by considering the magnetization: Immediately after spin locking, the spin temperature is generally low, corresponding to a large magnetic moment aligned along the effective field in the rotating frame. Spin-lattice relaxation will cause the rotating frame spin temperature to increase, and the magnetization vector shrinks, while always being parallel to the effective field. The final magnitude of the magnetization depends on the equilibrium value of the spin temperature.

The spin-lock state spin-lattice relaxation time will be determined here by computing the exponential rate of change of the rotating-frame spin temperature towards equilibrium, using the master equation in operator form for the density matrix.[45] The density matrix approach is essentially equivalent to conventional time dependent perturbation theory, but yields the perturbation results in a more useful form, since the density matrix and the spin temperature are very simply related when the system is describable by a spin temperature. Consider now the mixed quadrupole-Zeeman system described in Section V-A. The description

of the spin system given there was incomplete, since the quadrupole interaction was treated as time independent. Now, the total quadrupole hamiltonian will be divided up into a static part corresponding to the time averaged interaction $\mathcal{H}_Q$ and a time dependent part $\mathcal{H}_1(t)$ which represents the instantaneous difference between the total quadrupole hamiltonian and the time averaged one:

$$\mathcal{H}_Q(t) = \mathcal{H}_Q + \mathcal{H}_1(t) \tag{V-22}$$

$\mathcal{H}_Q$, combined with the Zeeman hamiltonian $\mathcal{H}_Z$, defines the energy levels of the nucleus in the laboratory frame, which are eigenvalues of the time independent main hamiltonian:

$$\mathcal{H}_o = \mathcal{H}_Q + \mathcal{H}_Z \tag{V-23}$$

The total laboratory hamiltonian can then be written

$$\mathcal{H}(t) = \mathcal{H}_o + \mathcal{H}_{r.f.}(t) + \mathcal{H}_1(t) \tag{V-24}$$

where $\mathcal{H}_{r.f.}(t)$ respresents the interaction with the strong r.f. field, as given in Eq. (V-1).

$\mathcal{H}_1(t)$ represents a stationary, random perturbation which causes transitions between eigenstates in the reference frame of interest. Bearing in mind that the master equation is a perturbation result , one must require that $\langle \mathcal{H}_1(t) \rangle \ll \langle \mathcal{H}^{*'} \rangle$, where $\mathcal{H}^{*'}$ is the static hamiltonian which defines the energy levels between which relaxation takes place. In the semiclassical treatment of the problem, $\mathcal{H}_1(t)$ can be expanded as

$$\mathcal{H}_1(t) = \sum_q F^{(-q)}(t)\, A^{(q)} \tag{V-25}$$

Here, $F^{(q)}(t)$ are expectation values of lattice operators, and appear in the formalism as stationary random functions of time representing

the random lattice fluctuations coupling to the spin system. $A^{(q)}$ are spin operators, not necessarily Hermitian, and in order for $\mathcal{H}_1(t)$ to be Hermitian it is usual to make the convention

$$F^{(q)}(t) = F^{(-q)c.c.} \text{ and } A^{(q)} = A^{(-q)^\dagger} \tag{V-26}$$

where the c.c. superscript indicates complex conjugate. In the case of quadrupolar relaxation, $\mathcal{H}_1(t)$ can conveniently be expanded in the form (Eq.(V-25)), with:

$$\begin{aligned} A^{(o)} &= 3I_z^2 - I(I-1) \\ A^{(\pm 1)} &= \frac{\sqrt{6}}{2}(I_z I_\pm + I_\pm I_z) \\ A^{(\pm 2)} &= \frac{\sqrt{6}}{2} I_\pm^2 \end{aligned} \tag{V-27}$$

where, as usual $I_\pm = I_x \pm iI_y$. The $F^{(q)}$ defined by this expansion represent the stationary random fluctuations in electric field gradient tensor components of $\mathcal{H}_1(t)$, and will not be specified explicitly.

Master equation in operator form. Laboratory frame.

The master equation in operator form can be written

$$\frac{d\sigma^*(t)}{dt} = -\frac{1}{2}\sum_{q,p} J_q(\omega_p^{(q)})\,[B_p^{(-q)}, [B_p^{(q)}, \sigma^*(t)]] \tag{V-28}$$

This expression is well established in the literature[45] and will not be derived here, but it is necessary to define its scope of applicability and the various quantities involved. First, it must be noted that (Eq. (V-28)) as it stands applies to the case with no strong r.f. fields applied to the crystal. The laboratory frame hamiltonian of the system is

$$\mathcal{H}(t) = \mathcal{H}_o + \mathcal{H}_1(t)$$

where $\mathcal{H}_o$ is the time independent main hamiltonian and $\mathcal{H}_1(t)$ a stationary random perturbation. As shown by Leppelmeier,[46] however, the master equation that applies to the spin lock state can be derived using Eq. (V-28) as a starting point. The quantities $\sigma^*(t)$, $J_q(\omega_p^{(q)})$ and $B_p^{(q)}$ will therefore be considered in some detail:

$\sigma(t)$ is the "reduced" density matrix defined by

$$\sigma(t) = \rho(t) - \rho(\infty) \tag{V-29}$$

where $\rho(t)$ is the standard laboratory frame spin system density matrix, and $\rho(\infty)$ is the density matrix at $t \to \infty$. As the spin system approaches thermal equilibrium with the lattice, one therefore has $\sigma(t) \to 0$. If the spin system is in internal equilibrium at a spin temperature T_s, the density matrix operator can be written

$$\rho = \frac{1}{Z} \; e^{-\mathcal{H}_o \beta_s} \tag{V-30}$$

where $\beta_s \equiv \frac{1}{kT_s}$. In the high temperature approximation one may write

$$\rho = - \frac{\beta_s}{\mathrm{Tr}1} \cdot \mathcal{H}_o \tag{V-31}$$

if all spin operators involved in the analysis are traceless. As in Section V-A, a star denotes a quantity in the interaction representation, and thus in the present case:

$$\sigma^*(t) = e^{i\mathcal{H}_o t} \, \sigma(t) e^{-i\mathcal{H}_o t} = \sigma(t) = - \frac{1}{\mathrm{Tr}1} \left(\beta_s(t) - \beta_s(\infty)\right) \cdot \mathcal{H}_o \tag{V-32}$$

Thus, the master equation (V-28) has been derived in the interaction representation, which is frequently used to simplify the problem by getting rid of the large static interaction $\mathcal{H}_o$. The right-hand side of the master equation then depends only on the perturbation hamiltonian $\mathcal{H}_1(t)^*$ in the interaction representation.

The $B_p^{(q)}$ in Eq. (V-28) arise when the perturbation hamiltonian $\mathcal{H}_1(t)$ is transformed into the interaction representation:

$$\mathcal{H}_1(t)^* = \sum_q F^{(-q)}\, e^{i\mathcal{H}_o t}\, A^{(q)}\, e^{-i\mathcal{H}_o t}$$

(lattice and spin operators commute). One may define

$$A^{(q)}(t) \equiv e^{i\mathcal{H}_o t}\, A^{(q)}\, e^{-i\mathcal{H}_o t}$$

which can be expanded as

$$A^{(q)}(t) = \sum_p B_p^{(q)}\, e^{i\omega_p^{(q)} t} \qquad \text{(V-33)}$$

where $\omega_p^{(q)}$ are transition frequencies between $\mathcal{H}_o$ eigenstates, and $B_p^{(q)}$ are operators connecting the same eigenstates. This can be seen by taking matrix elements of $A^{(q)}(t)$ between eigenstates of $\mathcal{H}_o$. The condition $A^{(q)} = A^{(-q)^\dagger}$ mentioned above imposes the requirement

$$\sum_p B_p^{(-q)^\dagger}\, e^{-i\omega_p^{(-q)} t} = \sum_p B_p^{(q)}\, e^{i\omega_p^{(q)} t}$$

and one choice compatible with this is

$$B_p^{(-q)^\dagger} = B_p^{(q)} \quad \text{and} \quad -\omega_p^{(-q)} = \omega_p^{(q)} \qquad \text{(V-34)}$$

In the semiclassical case (infinite lattice temperature), and assuming that the random phase approximation applies for the $F^{(q)}$'s, one can write to a good approximation:

$$J_q(\omega_p^{(q)}) = \int_{-\infty}^{\infty} F^{(q)}(t)\, F^{(q)}(t-\tau)^*\, e^{-i\omega_p^{(q)}\tau}\, d\tau \qquad \text{(V-35)}$$

and $J_q(\omega_p^{(q)})$ is therefore the spectral density of the lattice fluctuation parameter $F^{(q)}(t)$ at $\omega_p^{(q)}$.

Master equation in operator form. Rotating frame.

Consider now a spin system with a total laboratory frame hamiltonian

$$\mathcal{H}(t) = \mathcal{H}_o + \mathcal{H}_{r.f.}(t) + \mathcal{H}_1(t) \qquad \text{(V-36)}$$

where the r.f. field interaction $\mathcal{H}_{r.f.}(t)$ (Cfr. (V-1)) has been included. It will be assumed that the r.f. frequency is exactly on resonance for one of the laboratory frame transitions. $\mathcal{H}_o$ and $\mathcal{H}_1(t)$ are as before. Transforming into the $\mathcal{H}_o$ interaction representation, one is left with:

$$\mathcal{H}(t)^* = \mathcal{H}_{r.f.}(t)^* + \mathcal{H}_1(t)^* \qquad \text{(V-37)}$$

As noted previously, only the secular part of $\mathcal{H}_{r.f.}{}^*$, denoted by $\mathcal{H}^{*'}_{r.f.}$, needs be retained, since it defines the rotating frame (or interaction representation) energy levels. The nonsecular part represents a negligible perturbation. In the rotating frame the relevant hamiltonian is therefore:

$$\mathcal{H}(t)^*_{\text{Truncated}} = \mathcal{H}_{r.f.}{}^{*'} + \mathcal{H}_1(t)^*$$

where $\mathcal{H}^{*'}_{r.f.}$ now is time independent, while the fluctuating $\mathcal{H}_1(t)^*$ causes relaxation between rotating frame eigenlevels. Note that $\mathcal{H}_1(t)^*$ has picked up a coherent oscillation in addition to the stationary, random fluctuations, which is due to the transformation into the rotating frame.

Assuming that the spin lock state can be described by a spin temperature $T_{S.L.}$ (S.L. stands for spin lock) in the rotating frame, the reduced rotating frame density matrix can be written in analogy with Eq. (V-32):

$$\sigma^{*}(t) = - \frac{1}{\mathrm{Tr}1} \left(\beta_{S.L.}(t)) - \beta_{S.L.}(\infty)\right) \mathcal{H}^{*'}_{r.f.} \qquad \text{(V-38)}$$

Comparing now the hamiltonians pertaining to the spin system in the rotating frame with those given above in the laboratory frame with no r.f. field interaction, one sees that the two cases are fundamentally equivalent, and complete analogy exists at each step in the derivation of the master equation. This implies that the master equation in the spin-lock state should have the form:

$$\frac{d\sigma^{**}(t)}{dt} = - \frac{1}{2} \sum_{q,B} J_q(\omega p^{(q)} \left[B_S^{(-q)*}, \left[B_S^{(q)*}, \sigma^{**}\right]\right] \qquad \text{(V-39)}$$

where

$$\sigma^{**}(t) = e^{i\mathcal{H}^{*'}_{r.f.}t} \sigma^{**}(t) e^{-i\mathcal{H}^{*'}_{r.f.}t} = \sigma^{*}(t) \qquad \text{(V-40)}$$

$J_q(\omega p^{(q)})$ is defined as before, but the spectrum of frequencies $\omega_s^{(q)}$ is different, cfr. $B_p^{(q)*}$ below.

The $B_s^{(q)*}$ appear in analogy with the $B_p^{(q)}$ when transforming the perturbation hamiltonian $\mathcal{H}_1(t)^*$ into the $\mathcal{H}^{*'}_{r.f.}$ interaction representation:

$$\mathcal{H}_1(t)^{**} = \sum_{p,q} F^{(-q)} e^{i\mathcal{H}^{*'}_{r.f.}t} B_p^{(q)} e^{i\omega_p{}^{(q)}t} e^{-i\mathcal{H}^{*'}_{r.f.}t}$$

where one may expand

$$B_s^{(q)}(t) \equiv e^{i\mathcal{H}^{*'}_{r.f.}t} B_p^{(q)} e^{-i\mathcal{H}^{*'}_{r.f.}t} = \sum_r B^{(q)*}_{pr} e^{i\omega_r{}^{(q)}t} \qquad \text{(V-41)}$$

Here $B^{(q)*}_{pr}$ and $\omega_r^{(q)}$ are new quantities defined by Eq. (V-41). Since $\mathcal{H}_1(t)^{**}$ is hermitian, one can write in analogy to Eq. (V-33):

$$\mathcal{H}_1(t)^{**} = \sum_{qpr} F^{(-q)} B^{(q)*}_{pr} e^{i(\omega_p{}^{(q)}+\omega_r{}^{(q)})t} \equiv \sum_{qs} F^{(-q)} B_s^{(q)*} e^{i\omega_s^{(q)}t} \qquad \text{(V-42)}$$

where $B_s^{(q)*} = (B_s^{(-q)*})^\dagger \equiv B_{pr}^{(q)*}$ and $\omega_s^{(q)} = -\omega_s^{(-q)} \equiv \omega_p^{(q)} + \omega_r^{(q)}$. $\omega_p^{(q)}$ and $\omega_r^{(q)}$ are typically level separations in the laboratory and rotating frames, respectively.

From Eq. (V-39) it is seen that if the double commutators yield some number times $\sigma^{**}(t)$ for all $B_s^{(q)*}$, then the spin-lattice perturbation will only cause an overall scale factor change in σ^{**}, and in a given representation, no new elements will be introduced into the density matrix where only zero elements existed before. If the density matrix is initially of the form (Eq. V-38)) with a spin temperature $T_{S.L.}(t=0)$, then Eq. (V-39) shows that $T_{S.L.}(t)$ will decay exponentially towards an equilibrium value $T_{S.L.}(t\to\infty)$. The exponential time constant can be defined as the spin-lattice relaxation time in the spin lock state: $T_{1,S.L.}$.

The master equation (V-39) can now be applied to the case of a mixed Zeeman-quadrupole laboratory frame hamiltonian, with a strong r.f. field applied to the sample. The procedure is quite simple in principle:

1. Compute $\mathcal{H}_{r.f.}^{*'}$ to find $\sigma^{**}(t)$.

2. Compute $\mathcal{H}_1(t)^{**}$, from which the different $B_s^{(q)*}$ can be extracted directly.

3. Evaluate double commutators $[B_s^{(-q)*}, [B_s^{(q)*}, \sigma^{**}(t)]]$ and solve the master equation.

In practice, however, one immediately runs into trouble, because the transformation operator $e^{i\mathcal{H}_o t} = e^{i(\mathcal{H}_Q+\mathcal{H}_Z)t}$ cannot be expanded directly in spin operators. This problem is circumvented, as in Section V-A, by going into eigenrepresentations and expressing spin operators explicitly in matrix form.

Results for $\mathcal{H}_{r.f.}^{*'}$ were already obtained in Section V-A. Depending

on which of the four allowed laboratory frame transitions was driven by $\mathcal{H}_{r.f.}(t)$, one obtained (Cfr. (V-14)):

$$\text{Transition at } \omega_1 = E_1 - E_4\text{: } \mathcal{H}^{*'}_{r.f.,1} = -\gamma H_1(3ad - bc)\cdot\Gamma_1 = -\frac{\omega_1^*}{2}\cdot\Gamma_1$$

$$\omega_2 = E_2 - E_4\text{: } \mathcal{H}^{*'}_{r.f.,2} = -\gamma H_1(3bd - ac)\cdot\Gamma_2 = -\frac{\omega_2^*}{2}\cdot\Gamma_2 \qquad \text{(V-43)}$$

$$\omega_4 = E_1 - E_3\text{: } \mathcal{H}^{*'}_{r.f.,4} = -\gamma H_1(3ac + bd)\cdot\Gamma_4 = -\frac{\omega_4^*}{2}\cdot\Gamma_4$$

$$\omega_6 = E_2 - E_3\text{: } \mathcal{H}^{*'}_{r.f.,6} = -\gamma H_1(3bc - ad)\cdot\Gamma_6 = -\frac{\omega_6^*}{2}\cdot\Gamma_6$$

Here, one has defined ω_i^* as the transition frequency in the rotating frame corresponding to the laboratory transition at ω_i, and made use of the rotating frame effective gyromagnetic moments derived in Section V-A. Also, it **proved** convenient to introduce the definitions:

$$\Gamma_1 \equiv \left(\begin{array}{cc|cc} 0 & & 0 & 1 \\ & 0 & 0 & 0 \\ \hline 0 & 0 & & \\ 1 & 0 & 0 & \end{array}\right)_B;\quad \Gamma_2 \equiv \left(\begin{array}{cc|cc} 0 & & 0 & 0 \\ & 0 & 0 & 1 \\ \hline 0 & 0 & & \\ 0 & 1 & 0 & \end{array}\right)_B;\quad \Gamma_4 \equiv \left(\begin{array}{cc|cc} 0 & & 1 & 0 \\ & 0 & 0 & 0 \\ \hline 1 & 0 & & \\ 0 & 0 & 0 & \end{array}\right)_B;\quad \Gamma_6 \equiv \left(\begin{array}{cc|cc} 0 & & 0 & 0 \\ & 0 & 1 & 0 \\ \hline 0 & 1 & & \\ 0 & 0 & 0 & \end{array}\right)_B$$

It is assumed that all transitions ω_i (i = 1, 2, 4, 6) are well separated so that the lines do not overlap, and the reason for this was discussed at the end of Section V-A. Substitution of the different $\mathcal{H}^{*'}_{r.f.,i}$ (i = 1, 2, 4, 6) into Eq. (V-38) yields four expressions for the reduced density matrix which can conveniently be written:

$$\sigma_i^{**}(t) = \sigma_i^{*}(t) = (\beta_{S.L.}(t) - \beta_{S.L.}(\infty))\cdot C_i\cdot\Gamma_i \qquad \text{(V-44)}$$

with

$$C_1 = \frac{1}{\mathrm{Tr}1}\cdot\gamma H_1(3ad - bc)\text{ , etc.}$$

It might seem alarming from a spin-temperature standpoint that the Γ_i given by Eq. (V-43) and thus $\sigma_i^{**}(t)$ are non-diagonal, but it should be noted that the Γ_i are expressed in the B representation. In the representation where $\mathcal{H}^{*'}_{r.f.,i}$ are diagonal, the Γ_i will be so also.

$\mathcal{H}_1(t)^{**}$ is computed in two steps, starting with $\mathcal{H}_1(t)$ as defined by Eq. (V-25) and (V-27). First an expression for $\mathcal{H}_1(t)$ in the $\mathcal{H}_o$ interaction representation, $\mathcal{H}_1(t)^*$, is derived, which is common to all transitions ω_i. Second, $\mathcal{H}_1(t)^*$ is transformed into the interaction representation of the secular r.f. hamiltonian in the rotating frame. Four different expressions for $\mathcal{H}_1(t)^{**}$ are thus obtained, depending on which $\mathcal{H}^{*'}_{r.f.,i}$ is used.

First interaction representation.

The operators $A^{(q)}$ are first written out explicitly in matrix form, in the usual representation where I_z and I^2 are diagonal (denoted by subscript A). They are then transformed into the $\mathcal{H}_o$ eigenrepresentation (denoted by subscript B), using the transformation matrix U_{AB} derived in Section V-A. In the $\mathcal{H}_o$ eigenrepresentation the transformation matrix $(e^{i\mathcal{H}_o t})_B$ is diagonal (cfr. (V-4)), and one now finds easily:

$$\mathcal{H}_{r.f.}(t)^*_B = \sum_q F^{(-q)} \, (e^{i\mathcal{H}_o t})_B \, U^{-1}_{AB} \, (A^{(q)})_A \, U_{AB} \, (e^{-i\mathcal{H}_o t})_B = \sum_q F^{(-q)} (A^{(q)*})_B \tag{V-45}$$

with

$$(A^{(0)*})_B = (A^{(0)*})^\dagger_B = 6 \left(\begin{array}{cc|cc} (a^2-b^2) & 2ab\cdot e^{i\omega_3 t} & & \\ 2ab\cdot e^{-i\omega_3 t} & -(a^2-b^2) & \multicolumn{2}{c}{0} \\ \hline & & (c^2-d^2) & 2cd\cdot e^{i\omega_5 t} \\ \multicolumn{2}{c|}{0} & 2cd\cdot e^{-i\omega_5 t} & -(c^2-d^2) \end{array} \right)_B$$

$$(A^{(+1)*})_B = (A^{(-1)*})_B^\dagger = 3\sqrt{2}\left(\begin{array}{cc|cc} 0 & -(a^2-b^2)e^{i\omega_3 t} & -(bc+ad)e^{i\omega_4 t} & (ac-bd)e^{i\omega_1 t} \\ (a^2+b^2)e^{-i\omega_3 t} & 0 & (ac-bd)e^{i\omega_6 t} & (bc+ad)e^{i\omega_2 t} \\ \hline -(bc+ad)e^{-i\omega_4 t} & (ac-bd)e^{-i\omega_6 t} & 0 & -(c^2+d^2)e^{i\omega_5 t} \\ (ac-bd)e^{-i\omega_1 t} & (bc+ad)e^{-i\omega_2 t} & (c^2+d^2)e^{-i\omega_5 t} & 0 \end{array}\right)_B$$

$$(A^{(+2)*})_B = (A^{(-2)*})_B^\dagger = 3\sqrt{2}\left(\begin{array}{cc|cc} -2ab & (a^2-b^2)e^{i\omega_3 t} & -(bc+ad)e^{i\omega_4 t} & (ac-bd)e^{i\omega_1 t} \\ (a^2-b^2)e^{-i\omega_3 t} & 2ab & (ac-bd)e^{i\omega_6 t} & (bc+ad)e^{i\omega_2 t} \\ \hline (bc+ad)e^{-i\omega_4 t} & -(ac-bd)e^{-i\omega_6 t} & 2cd & -(c^2-d^2)e^{i\omega_5 t} \\ -(ac+bd)e^{-i\omega_1 t} & -(bc+ad)e^{-i\omega_2 t} & -c^2-d^2)e^{-i\omega_5 t} & -2cd \end{array}\right)_B$$

Second interaction representation

Given $\mathcal{H}_1(t)^*$, the desired $\mathcal{H}_1(t)^{**}$ is found for the transition ω_i of interest by evaluating (in matrix form):

$$(\mathcal{H}_1(t)^{**})_B = (e^{i\mathcal{H}^{*'}_{r.f.,i}t})_B \, (\mathcal{H}_1(t)^*)_B \, (e^{-i\mathcal{H}^{*'}_{r.f.,i}t})_B$$

which yields:

$$(A^{(\pm q)^{**}})_B = (e^{i\mathcal{H}^{*'}_{r.f.,i}t})_B \, (A^{(\pm q)^*})_B \, (e^{-i\mathcal{H}^{*'}_{r.f.,i}t})_B$$

Since the procedure is identical in all four rotating frames, it will be sufficient to outline the derivation of $\mathcal{H}_1(t)^{**}$ for one transition, say the one at ω_1:

Using the expression Eq. (V-43) for $\mathcal{H}^{*'}_{r.f.,1}$, the transformation operator is

$$e^{i\mathcal{H}^{*'}_{r.f.}} = e^{-i\frac{\omega_1^*}{2}\Gamma_1 t}$$

By noting that the matrix Γ_1 in the B representation satisfies

$$\Gamma_1^3 = \Gamma_1$$

the expansion of the exponential can be brought to the form:

$$e^{\pm i\frac{\omega_1^*}{2}\Gamma_1 t} = \Gamma_1^2 \sum_0^\infty \frac{(-1)^\ell}{(2\ell)!}\left(\frac{\omega_1^*}{2}t\right)^{2\ell} \pm i\,\Gamma_1 \sum_0^\infty \frac{(-1)^m}{(2m+1)!}\left(\frac{\omega_1^*}{2}t\right)^{2m+1}$$

$$= \begin{pmatrix} \cos\frac{\omega_1^*}{2}t & 0 & 0 & \pm i\sin\frac{\omega_1^*}{2}t \\ 0 & 0 & 0 & 0 \\ 0 & 0 & 0 & 0 \\ \pm i\sin\frac{\omega_1^*}{2}t & 0 & 0 & \cos\frac{\omega_1^*}{2}t \end{pmatrix}_B$$

Computation of the $(A^{(q)**})_B$ is then straightforward but somewhat tedious, and the different $B_p^{(q)}$ can easily be picked out, keeping in mind that $\omega_s^{(q)} = -\omega_s^{(-q)}$, and checking that $B_s^{(q)*} = B_s^{(-q)*\dagger}$. Nonzero $B_s^{(q)}$ are found for

$$q = 0 : \omega_s^{(0)} = 0, \pm \omega_1^*$$

$$q = \pm 1 : \omega_s^{(\pm 1)} = \pm \omega_1^* , \pm (\omega_1 + \omega_1^*) , \pm (\omega_1 - \omega_1^*) \qquad \text{(V-46)}$$

$$q = \pm 2 : \omega_s^{(\pm 2)} = 0 , \pm \omega_1 , \pm \omega_1^* , \pm (\omega_1 + \omega_1^*) , \pm (\omega_1 - \omega_1^*)$$

According to the master equation (Eq. V-39), for each $\omega_s^{(q)}$ the spectral density $J_q(\omega_s^{(q)})$ is weighted by the magnitude of $[B_s^{(-q)*},[B_s^{(q)*},\sigma^{**}(t)]]$. The double commutators can now be worked out, and choosing as an example $q = 2$, $\omega_s = \omega_1 + \omega_1^*$, one has:

$$[B_s^{(-q)*}, [B_s^{(q)*}, \sigma^{**}(t)]]$$

$$= \left\{\frac{3}{4}\sqrt{2}\ (ac-bd)\right\}^2 (\beta_{S.L.}(t)-\beta_{S.L.}(\infty))C_1 \left[\begin{pmatrix} -1 & 0 & 0 & -1 \\ 0 & 0 & 0 & 0 \\ 0 & 0 & 0 & 0 \\ 1 & 0 & 0 & 1 \end{pmatrix}_B, \left[\begin{pmatrix} -1 & 0 & 0 & 1 \\ 0 & 0 & 0 & 0 \\ 0 & 0 & 0 & 0 \\ -1 & 0 & 0 & 1 \end{pmatrix}_B, \begin{pmatrix} 0 & 0 & 0 & 1 \\ 0 & 0 & 0 & 0 \\ 0 & 0 & 0 & 0 \\ 1 & 0 & 0 & 0 \end{pmatrix}_B\right]\right]$$

$$= 9(ac-bd)^2\ (\beta_{S.L.}(t)-\beta_{S.L.}(\infty))C_1\Gamma_1 = 9(ac-bd)^2\sigma_1^{**}(t)$$

Here it is worth noting that the double commutator does indeed lead to $\sigma^{**}(t)$ times a number, which is important for reasons discussed above. Analogous results are obtained for all $B_p^{(q)}$ (in some cases the double commutator is zero), and plugging the results into the master equation, one obtains:

$$C_1\Gamma_1 \frac{d}{dt}(\beta_{S.L.}(t)-\beta_{S.L.}(\infty)) = -\frac{1}{2} C_1\Gamma_1(\beta_{S.L.}(t)-\beta_{S.L.}(\infty))\Big\{36(a^2-b^2+c^2-d^2)^2 \times$$

$$J_o(\omega_1^*)+144(ab-cd)^2J_2(\omega_1^*)+36(ac-bd)^2(J_1(\omega_1+\omega_1^*)+J_1(\omega_1-\omega_1^*)+J_2(\omega_1+\omega_1^*)+J_2(\omega_1-\omega_1^*))\Big\}$$

Obviously, a solution

$$(\beta_{S.L.}(t) - \beta_{S.L.}(\infty)) = (\beta_{S.L.}(0) - \beta_{S.L.}(\infty))\, e^{-\frac{t}{T_{1,S.L.}}}$$

exists, with

$$\frac{1}{T_{1,S.L.}} = 18(a^2-b^2+c^2-d^2)^2 J_o(\omega_1^*)+72(ab-cd)^2J_2(\omega_1^*)+18(ac-bd)^2\Big\{J_1(\omega_1+\omega_1^*)$$

$$+ J_1(\omega_1-\omega_1^*)+J_2(\omega_1+\omega_1^*)+J_2(\omega_1-\omega_1^*)\Big\}$$

where $T_{1,S.L.}$ can be identified as the spin-lattice relaxation time in the spin-lock state of transition ω_1.

Results for the three other allowed transitions are obtained in the same manner, and may be summarized as follows:

Table V.2. Spin-lock state spin-lattice relaxation rates.

Laboratory Frame Transition	Relaxation Rate
$\omega_i (i = 1,6)$	$\frac{1}{T_{1,S.L.}} = 18(a^2-b^2+c^2-d^2)^2 J_o(\omega_i^*)+72(ab-cd)^2J_2(\omega_i^*)$ $+18(ac-bd)^2\Big\{J_1(\omega_i+\omega_i^*)+J_1(\omega_i-\omega_i^*)+J_2(\omega_i+\omega_i^*)+J_2(\omega_i-\omega_i^*)\Big\}$
$\omega_i (i = 2,4)$	$\frac{1}{T_{1,S.L.}} = 18(a^2-b^2-c^2+d^2)J_o(\omega_i^*)+72(ab+cd)^2J_2(\omega_i^*)$ $+18(ab+cd)^2\Big\{J_1(\omega_i+\omega_i^*)+J_1(\omega_i-\omega_i^*)+J_2(\omega_i+\omega_i^*)+J_2(\omega_i-\omega_i^*)\Big\}$
$\omega_i (i = 3,5)$	$\frac{1}{T_{1,S.L.}}$ not defined. (Forbidden transition)

For reasons of comparison, one may apply the method outlined above to the case of a pure quadrupole laboratory frame hamiltonian, where an analytic expression already has been obtained by Leppelmeier and Hahn,[34] using an operator formalism where higher order spin operators are represented by Pauli matrices.

Pure quadrupole interaction corresponds to the limit $1/\lambda \to 0$, i.e., $a = c = 1/\sqrt{2}$ and $b = d = 0$. In this limit, the r.f. perturbation will <u>not</u> connect the doubly degenerate laboratory frame energy eigenstates, with the field configuration assumed in this chapter, and the results presented in Table V.2 cannot be used (cfr. comments at the end of Section V-A). An r.f. field applied in the x-direction, with the experimental configuration otherwise unchanged, leads to nonzero transition probabilities, however, and the procedure outlined above applies. In this case the r.f. hamiltonian matrix contains twice as many elements as in the nondegenerate case (cfr. Eq. (IV-14)). One obtains:

$$\frac{1}{T_{1,SL}} = 18\, J_o(\omega^*) + 9[J_1(\omega_o+\omega^*) + J_1(\omega_o-\omega^*) + J_2(\omega_o+\omega^*) + J_2(\omega_o-\omega^*)]$$

where $\omega_o = 3e^2qQ/2I(2I-1)$ is the laboratory frame transition frequency and $\omega^* = \sqrt{3}\,\gamma_{LAB}\,H_I$ is the transition frequency in the rotating frame.

This result is identical to that of Leppelmeier and Hahn.

VI. EXPERIMENTAL CONSIDERATIONS

A pulsed, single-coil NMR spectrometer was used in conjuction with a Varian 12-inch magnet and Varian gas flow sample temperature control system. Parts of the electronic system, especially gate circuits and transmitters, were the same that have been described in detail by McArthur,[12] and will only receive a brief treatment here.

VI-A. Pulse Sequence and Timing

In the double resonance experiments of interest here, magnetic fields were applied to the sample at three different frequencies:

"A spin" transition frequency in the laboratory frame: 11.011 MHz (fixed)

"B spin" transition frequency in the laboratory frame: Apparatus tunable from ~260 kHz to ~3.25 MHz

"B spin" transition frequency in the rotating frame: Audio range

The fields had to be accurately modulated in phase and amplitude; an example is the ADRF double resonance cycle shown in Fig. III-2. A master time unit (Digital Pulse Generator--Model 1") initiated each cycle of pulses and controlled the sequence of events through a series of pulse delay units and gated pulse generators, cfr pulse steering shown in block diagram of the apparatus in Fig. VI-1. The master time unit contained a crystal oscillator for time reference, and digital logic circuits which controlled start and stop times for three separate gates. Using the start of one of these gates as time reference, the starting times of the two others could be delayed up to 99.9 msec in steps of 0.1 msec. Gate stop time for all three channels could be set individually from 0.001 sec to 999.999 sec in steps of 1 msec. In addition, short trigging pulses were provided, marking the leading and trailing edges of

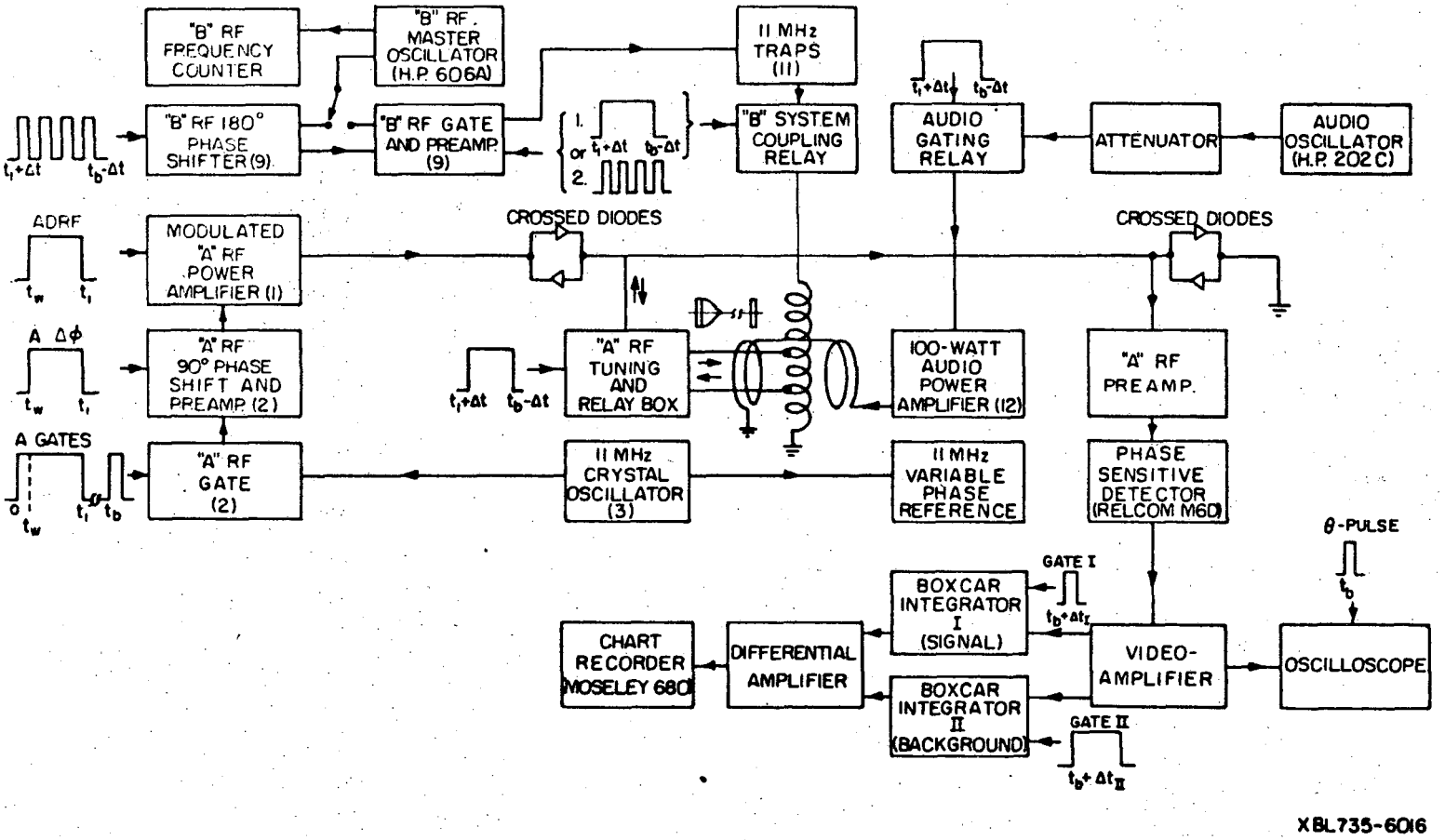

Fig. VI-1. Simplified block diagram of the ADRF double resonance apparatus. Master time unit, pulse amplifiers and pulse delay units not shown.

the pulse in each channel. The cycle repetition rate could be set from 10 msec to 999.99 sec, in steps of 10 msec. The master time unit and the pulse delay units providing gates for signal sampling (boxcar gates) were designed and built by the Physics Department Electronic Shop. No circuit description of these units will be given here. The rest of the pulse delay units and pulse generators were Tektronix 160 series modules, triggered and gated directly from the master time unit via pulse amplifiers, or cascaded.

Five different subsystems which required timing control will be described separately below. They are:

"A" transmitter system

"A" receiver system

"B" transmitter system

Audio system

Signal sampling system

As usual, A and B pertain to abundant and rare spin species, respectively.

VI-B. Cable and Coil Arrangement

A single coil served both as A and B transmitter coil and as A receiver coil. Partly, this was possible due to the difference in A and B frequencies, and partly because B r.f. was only applied when A r.f. was neither transmitted nor received. The relay circuit disconnecting the A system during B r.f. irradiation is shown in Fig. VI-2. In order to avoid relay contact ageing or damage due to the high current levels during the A r.f. transmitting period, and especially to ensure low contact resistance and noise during the receiving period, mercury wetted contact relays were used (C. P. Clare Type HG1003). The A tank circuit tuning capacitor was located in the relay box. The

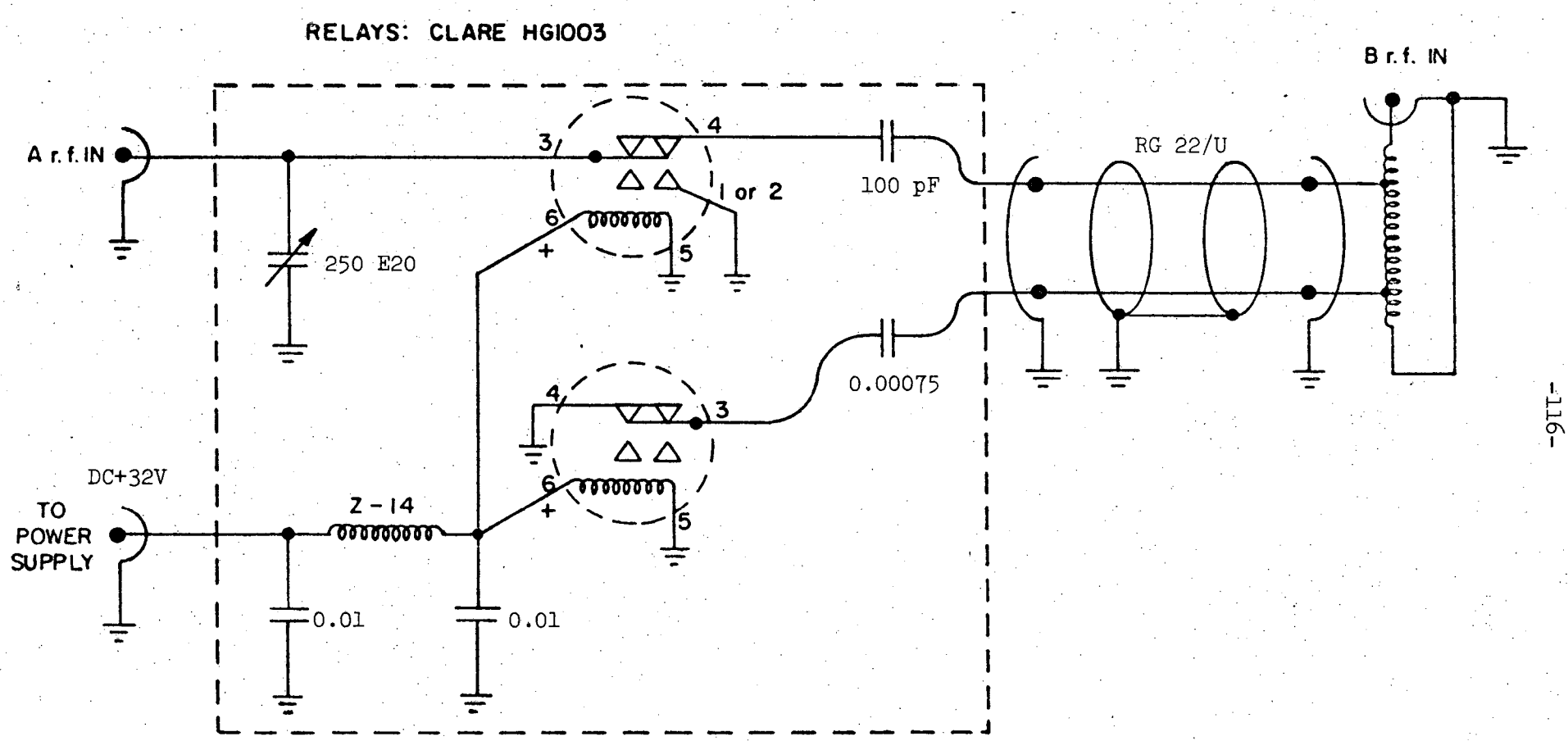

Fig. VI-2. A-B coil switching relays and A tank circuit.

distance between the capacitor and the A coil was approximately 1 m, compared to the free space wavelength of 27 m at 11 MHz.

Sample coils were made of #16 insulated Cu wire, reinforced with epoxy. Approximately a third of the windings in the center of the coil made up the A coil, which was connected by wires soldered to the side of the coil. The total length of the coils, i.e., the B portion, was from 4 to 8 cm, with 30 to 40 windings. Typical inductances were 1.3-2.6 μH and 4.7-5.7 μH for the A and B portions of coil, respectively. The B coil was approximately twice as long as the samples and thus provided a homogeneous B r.f. field at the sample, which is necessary for sharply defined energy levels in the rotating frame. The relatively short A part of the solenoid might have resulted in some loss of A signal, since a varying A r.f. field strength over the sample volume leads to different $\pi/2$ pulse requirements and poorer spin locking efficiency.

Since the same coil connections were used both in transmitting and receiving at the A frequency, special care had to be taken to keep r.f. power from leaking into the receiver during the transmitting period. A scheme described by Lowe and Tarr[47] was adopted, where one made use of the impedance transformation properties of a $\lambda/4$ cable, cfr. Fig. VI-3:

Connecting cables were made of such length that the electrical distance at 11 MHz was $\lambda/2$ along the cables from transmitter to sample tank circuit, and $\lambda/2$ from the sample tank circuit to the receiver

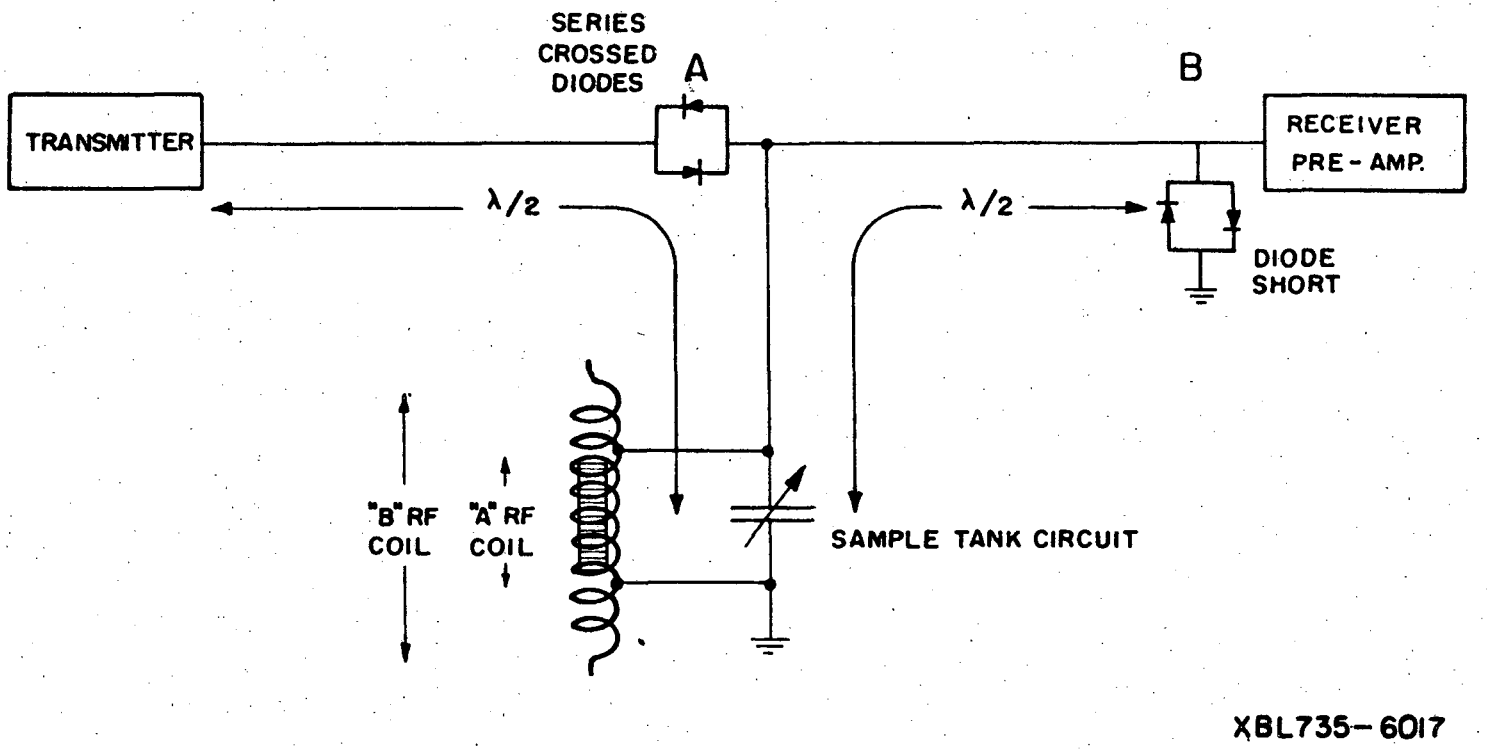

Fig. VI-3. "A" r.f. transmitter, tank circuit and receiver arrangement.

input. As shown in Fig. VI-3, a bank of series crossed diodes were interposed in the transmitter arm close to point A, and a bank of crossed diodes led to ground at the receiver input (point B). Six to eight pairs of IN 604 were used at both points. The distance A-B was $\lambda/4$.

The diodes have low forward impedance at the high voltage and current levels during transmitting, and high impedance at the low voltage levels (<1 mV) during receiving. Thus, when the r.f. power is applied, the diodes at A pass the current with little attenuation, while the heavily conducting diodes at B keep the voltage at the receiver input clamped at a low level and effectively constitute a short on the line. This short transforms to an open ended circuit as seen from the distance $\lambda/4$ at A, and ideally all power flows from transmitter to tank circuit, which should be matched to the line when on resonance. In the receiving period, all diodes have high impedance. The series diodes at A isolate the transmitter from the tank circuit and receiver, while the diodes at B have regligible effect, and the receiver is matched to the tank circuit. The electrical distances along the cables from the tank circuit and to the transmitter and receiver were each chosen equal to a half wavelength. These lengths are irrelevant when perfect matching to the line obtains, but make matching requirements less critical. One may note here that the distributed A tank circuit with tuning capacitor at a distance from the coil provided stable capacitance values and ease of tuning, but might have had some adverse effect on the impedance matching to the cable.

As pointed out by Lowe and Tarr, the single-coil design outlined above is very efficient in its use of r.f. power to produce a large rotating field component at the sample site. It does not involve the critical balancing of a crossed coil or bridge circuit, and features short recovery times.

The A/B coil axis was vertical, i.e., perpendicular to the magnetic field H_o, and the sample was inserted from above at the end of a mounting rod. The internal coil diameter was 13.5-14 mm, and a good filling factor was obtained with 12-13 mm ϕ cylindrical samples. The lower part of the mounting rod was of teflon to reduce thermal conduction from the sample and possible disturbance of the r.f. field pattern in the coil. The sample axis was parallel to the magnet pole faces within 1°. Samples could be rotated about the vertical axis by turning the sample rod which extended out of the sample Dewar, and angles of rotation could be measured and reset within ±0.5°.

A Helmholtz coil pair with the coil axis parallel to H_o was used to create homogeneous audio fields at the sample.

VI-C. The A System

Both the A transmitter and receiver systems are shown in the block diagram on Fig. VI-1. In the ADRF operating mode, a single trigger pulse from the master time unit starts the ADRF pulse sequence by triggering the first of three connected pulse delay units. A long (several seconds) gate pulse from the master time unit then activates the relays which disconnect the A coil during B r.f. irradiation. After the relays have returned to resting position, a single trigger pulse

from the master time unit causes transmitting of the θ sample pulse, and at the same time starts the pulse generators which provide sampling gates for the receiving system. By blocking the ADRF and 90° phase shift gates, the zero reference for dipolar signal could be obtained, and the gate pulses could easily be modified to yield π/2 - π/2 sequences, etc.

A free-running crystal controlled 11 MHz oscillator provided CW r.f. to the A r.f. gate and a phase sensitive detector in the receiver system, crf. schematic on Fig. VI-4. The oscillator frequency 11.0119 MHz was stable to $1:10^6$ over periods of weeks.

VI-C-1. Transmitter

The electronics in the A R.F. GATE AND 90° PHASE SHIFTER, and the MODULATED A R.F. POWER AMPLIFIER have been described in detail by McArthur,[12] and only a functional description will be given here. Schematics are shown in Figs. VI-5, VI-6 and VI-7. R.f. from the 11 MHz oscillator will only pass through the A r.f. gate as long as the gate pulse is on. The r.f. will be phase shifted by 90° whenever A r.f. gate and phase shift gate pulses are supplied simultaneously. The π/2 pulse spin locking waveform is thus obtained by delaying the phase shift gate by t_w, the π/2 pulse width. The gated and phase shifted A r.f. then passes into the first stage of the modulated A r.f. power amplifier, which consists of an ADRF wave shaper and cathode follower, a preamplifier, a driver, pulse tail damping circuits and finally a power amplifier. Application of the ADRF pulse leads to a smooth turn-off of the r.f., with a time constant less than 1 msec. The A r.f. gate, 90° phase shift gate and ADRF gate were chosen considerably longer than this (typically 4.4 msec, 5.2 msec and 5.2 msec, respectively) to ensure that the

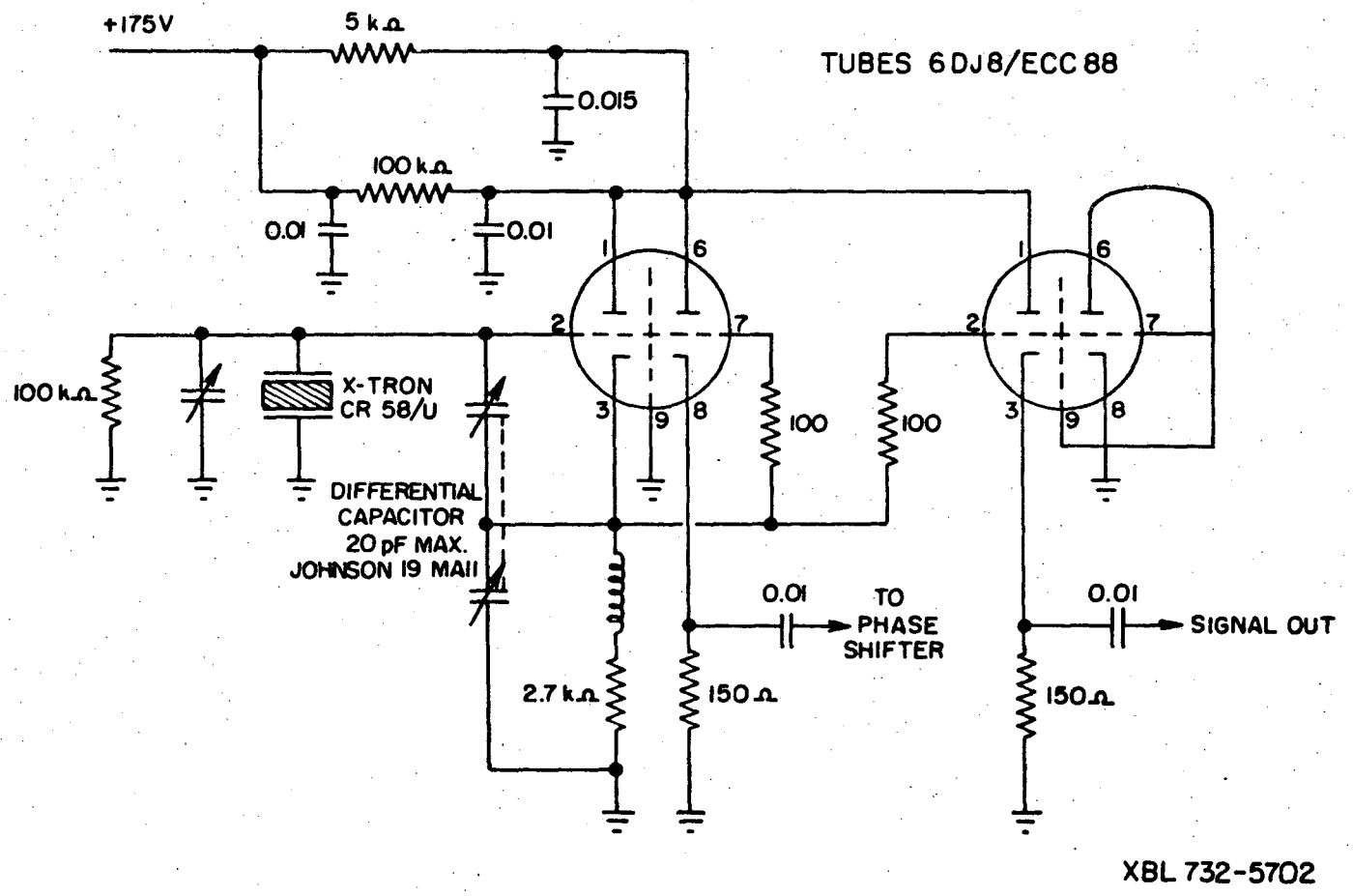

Fig. VI-4. 11 MHz crystal controlled master oscillator.

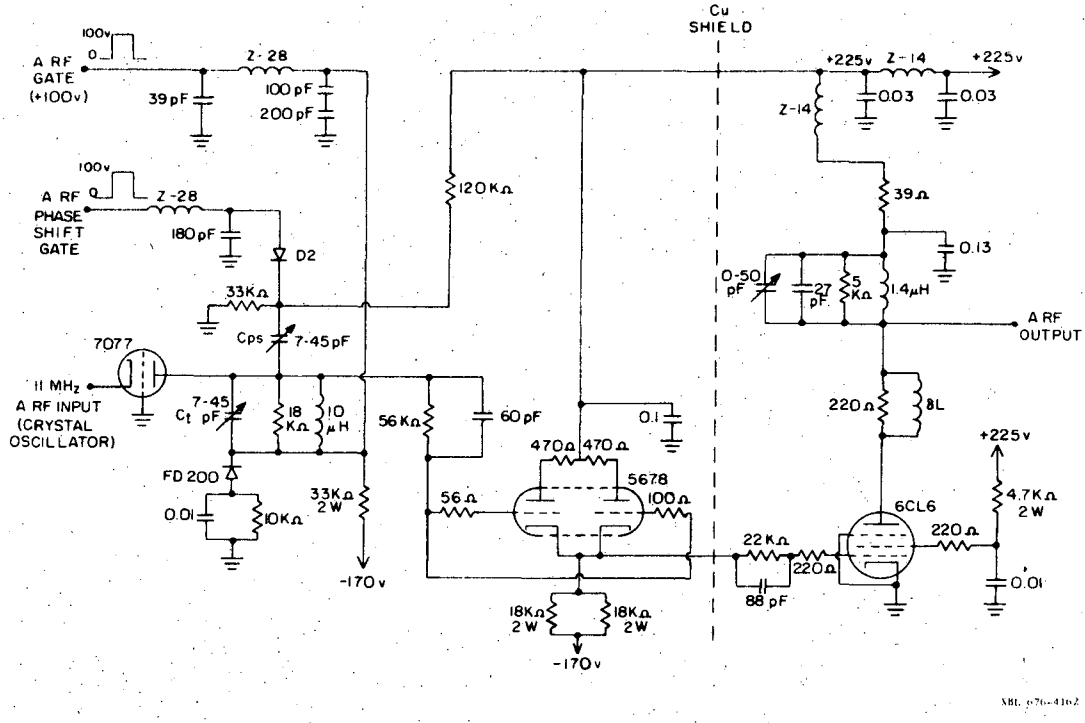

Fig. VI-5. A r.f. gate and 90° phase shift circuit (chassis 2) (after D. A. McArthur[12]).

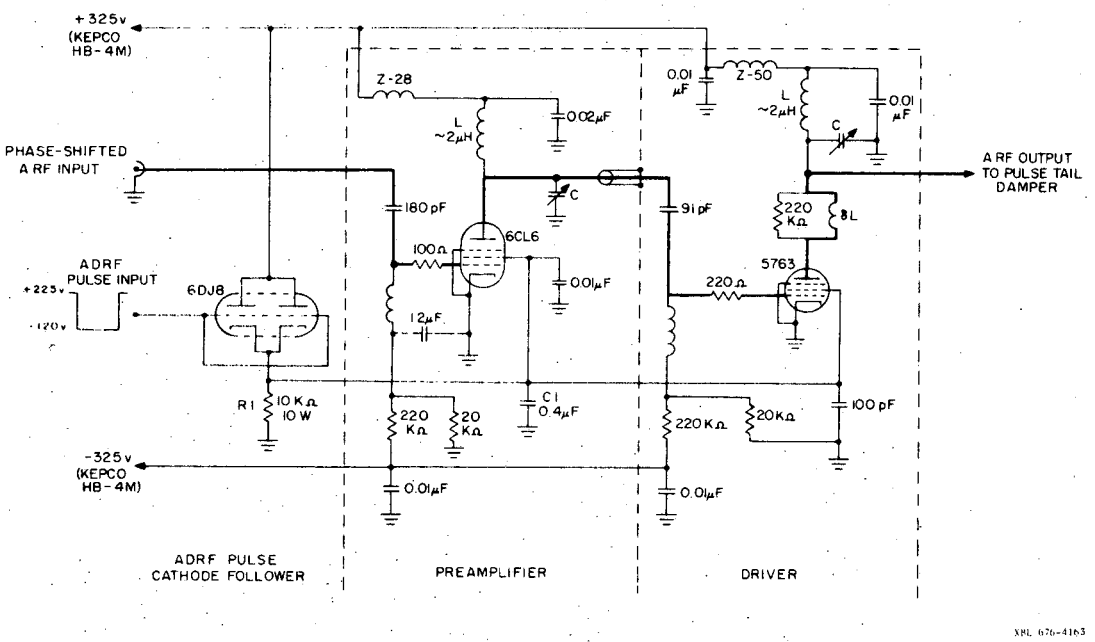

Fig. VI-6. Modulated A r.f. power amplifier (chassis 1) (after D. A. McArthur[12]).

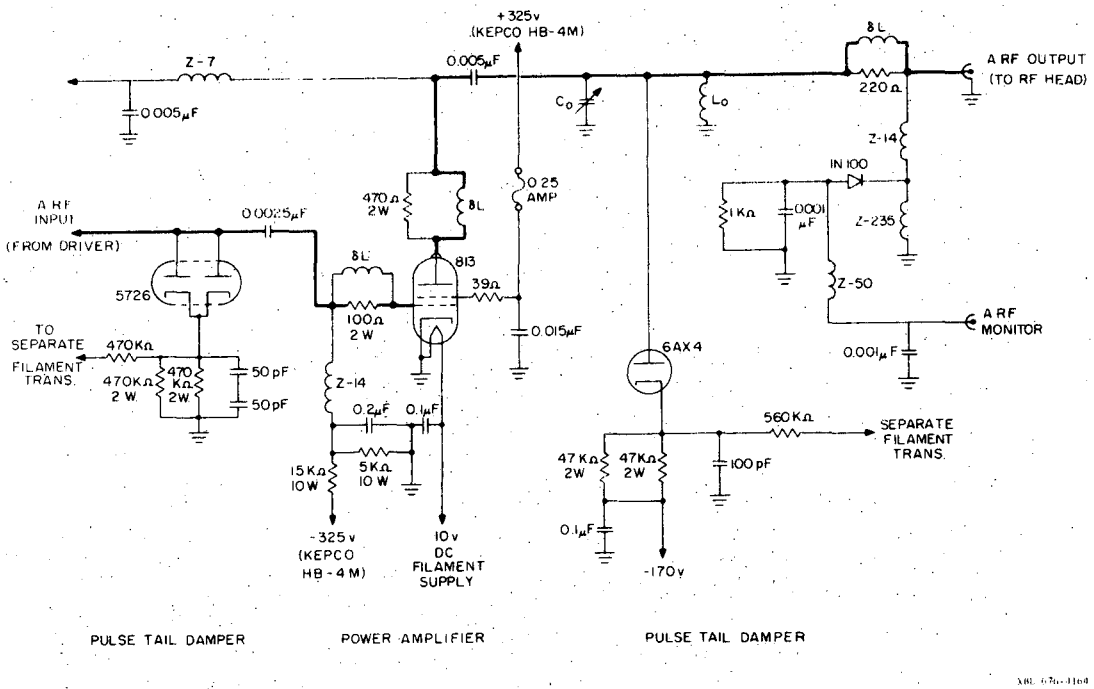

Fig. IV-7. Modulated A r.f. power amplifier (chassis 1) (after D. A. McArthur[12]).

adiabatic turn-off be complete. The pulse tail damping circuits suppressed ringing in the 11 MHz turned transmitter circuits when the driving pulse was turned off. An 813 class C amplifier driven at 1300-1500 volts was used in the final power stage. The system produced an 11 MHz rotating field component of 8.4 gauss peak in the sample coil.

Tuning of the transmitter system was done successively at the sample tank circuit and at the output of the transmitter. A leakage monitor signal from the power stage and the Zeeman free induction signal after a $\simeq\pi/4$ pulse were maximized. The 90° phase shift adjustment was monitored by leaking part of the output from the A r.f. gate and phase shifter directly into the phase sensitive detector signal input.

VI-C-2. Receiver

The receiver was of the wideband type. With a preamplifier recovery time <4 μs, the total system recovery time (<14 μs) was determined by the sample tank circuit at 11 MHz.

Signals from the sample first passed through the PREAMPLIFIER and PHASE SENSITIVE DETECTOR. The detected signal was amplified further in the VIDEO AMPLIFIER, and could then be monitored on an oscilloscope or captured by the BOXCAR INTEGRATORS. The boxcar output was recorded continuously on a MOSELEY 680 CHART RECORDER.

Unity signal to noise ratio for the total system was obtained at 0.4 μV_{RMS}, referred to the preamplifier input, and at a detected signal frequency of 120 kHz. A receiver gain and linearity check was made at this frequency by feeding a calibrated low-level signal from a Hewlett-Packard 606B oscillator into the preamplifier input. The 607B frequency was set to give beats at 120 kHz, which was well within the preamplifier and

phase sensitive detector bandwidths, and beat amplitudes were measured as a function of input signal. Voltage gain was found to be $3 \cdot 10^4$ and was linear within measurement errors (2%) in the input signal range 0-50 μV, which covers the range of signals from the sample.

The PREAMPLIFIER was designed by Dr. M. Schwab and co-workers at LBL, Livermore and featured short recovery time (2-4 μs), wide bandwidth (5 MHz at 6 db and 11 MHz), and a voltage gain of approximately 700 at 11 MHz. As shown on Fig. VI-8, the preamplifier consisted of three equivalent push-pull stages coupled by Relcom wideband transformers. Transistors in each stage were thermally balanced by a common heat sink. The crossed diodes at the input were in addition to the bank of crossed diodes before the receiver input, and therefore not essential. Special care had to be taken in the lay-out to avoid instability.

The amplified 11 MHz signal was fed to the PHASE SENSITIVE DETECTOR, along with a reference signal from the PHASE REFERENCE UNIT, as shown on Fig. VI-9 : The 11 MHz CW signal from the crystal controlled oscillator could be phase delayed by slightly more than 360° in the AD-YU 505B delay line. Phase shifted r.f. was then amplified and limited to make the reference output stable and insensitive to delay angle, and a cathode follower provided low impedance output. During early experiments, phase drift due to temperature variations in the delay line was a problem. The delay line and connecting leads were therefore encased completely in molding styrofoam, with some improvement in signal stability. The phase reference output into 50 Ω could be varied up to approximately 0.4 V_{RMS}. Phase sensitive detection was achieved with a Relcom double balanced mixer type M6D, which has a flat frequency response from 50 kHz to 200 MHz: The

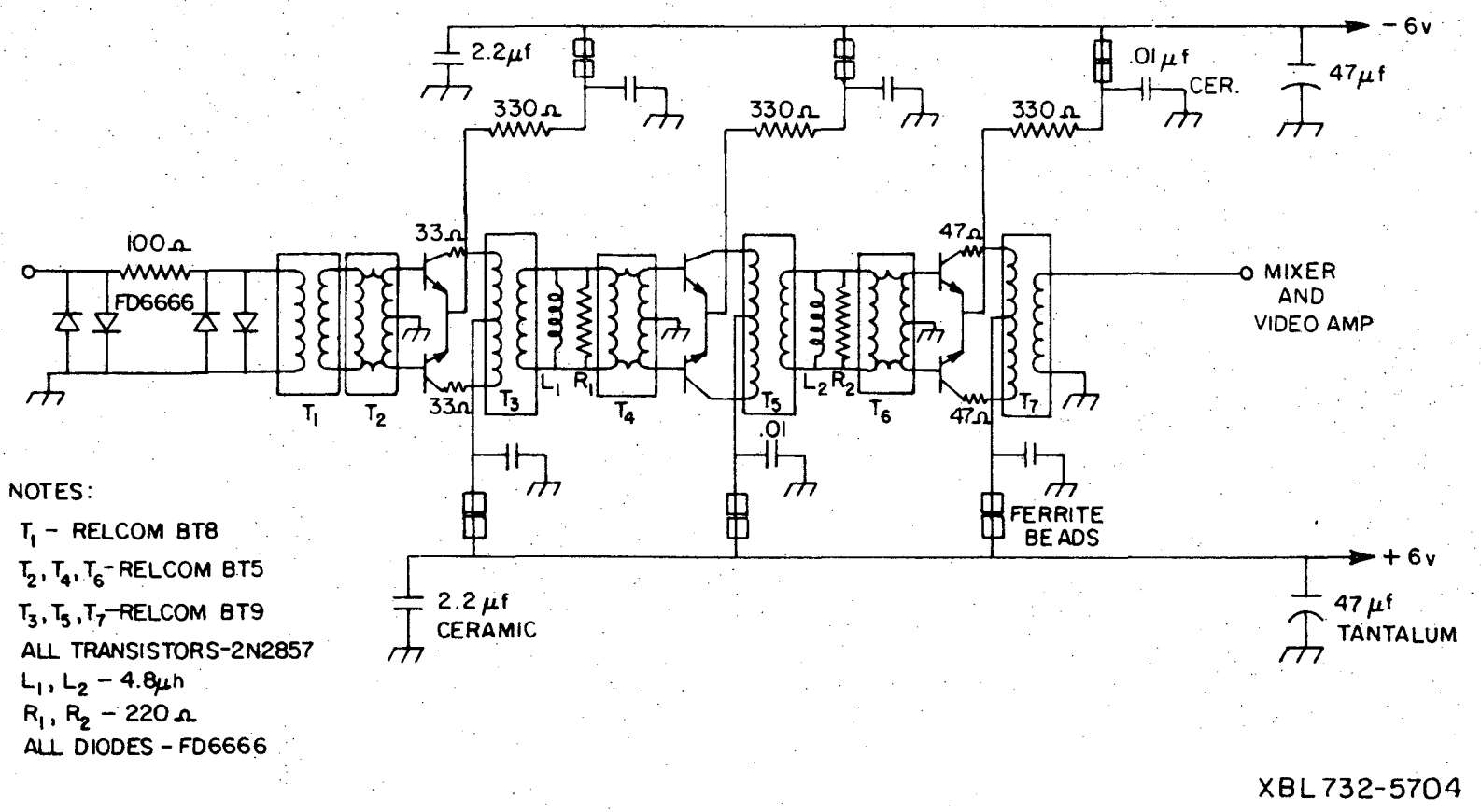

Fig. VI-8. Wideband A r.f. pre-amplifier.

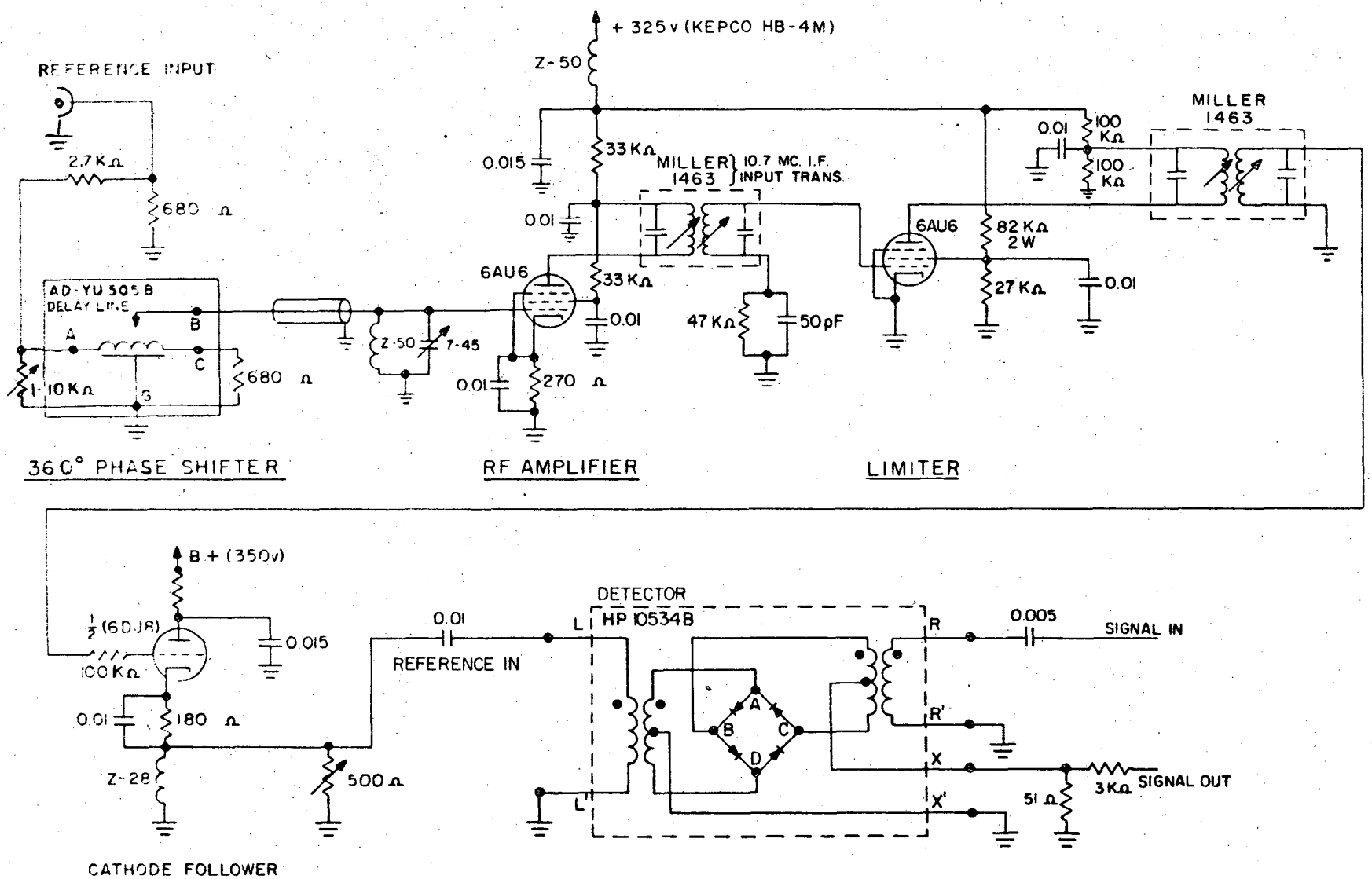

XBL 676-4168A

Fig. VI-9. A r.f. phase reference unit and phase sensitive detector.

reference supplied at the L port was at least an order of magnitude above the signal level. Current direction in the diode bridge would then be such that the effective ground potential created by voltage division in the bridge was switched once every half period from one end of the signal transformer secondary to the other. If a CW signal of the same frequency as the reference is supplied at the R port, a voltage with fixed polarity relative to ground will appear at the output port I, since the ground reference is switched in step with the current direction in the signal transformer secondary. The output signal will vary sinusoidally about zero as the relative phase between reference and signal is changed.

The detected output was amplified in the VIDEO AMPLIFIER, which was built by the Physics Department Electronic Shop. As shown on Fig. VI-10, the unit consisted of a DC-coupled operational amplifier with stabilizing feedback. Voltage gain was approximately 50 at DC, and dropped by 7 db in going to 250 KHz. (Rise time of typical signals from the sample was approximately 10 μs.)

Signals were recorded with a double BOXCAR INTEGRATOR system as shown on Fig. VI-1. The box cars were designed and built by the Physics Department Electronic Shop, and operated in two modes: When a gate pulse was supplied, the transient signal would charge up an RC-circuit to a voltage depending on the signal level and the adjustable RC time constant. In the holding mode, this voltage was kept constant by a circuit which compensated for leakage currents. Minimum holding time, defined by 1% deviation from initial voltage, was 10 seconds. In practice, the chart recorder could be run continuously from the boxcar

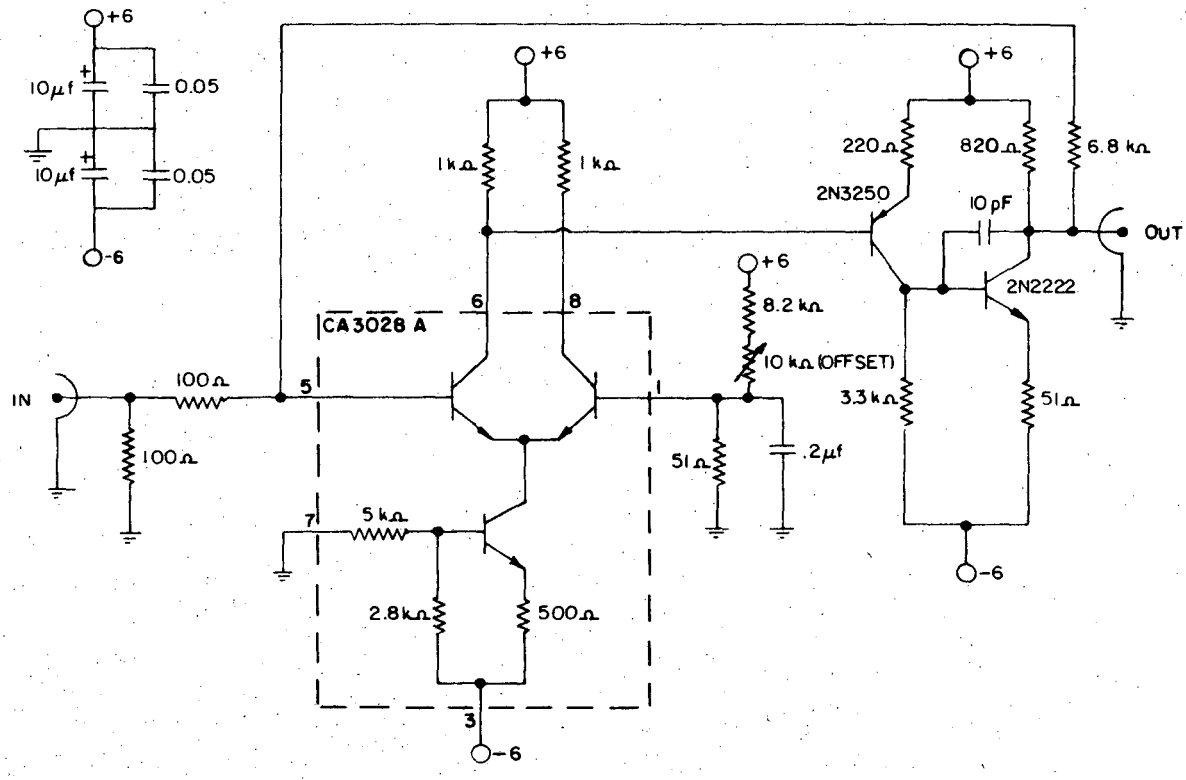

Fig. VI-10. Video amplifier for detected "A" signal.

output with no detectable drift, even when time between samplings was several minutes. In order to eliminate slow drift in the background level due to variations in r.f. leakage or thermal drift in the receiver, two boxcars were run in parallel. One boxcar sampled a portion of the transient signal about its peak value, while the other sampled the background level after the signal transient had died out. The background sampling gate was made very wide (200 μs-2 ms) to reduce contributions to random noise from the background sampling. The background was subtracted from the sample signal in a DIFFERENTIAL AMPLIFIER of Physics Department Electronic Shop construction. The output from the differential amplifier was recorded continuously on a MOSELEY 680 CHART RECORDER. In a check on the differential amplifier and chart recorder linearity and chart recorder hysteresis, one found that the response for the differential amplifier/chart recorder combination was linear within 0.5% at DC signal levels 0-0.5 V. Signals from the sample were usually in this range.

Finally, a word about r.f. leakage into the receiver, which was one of the most serious headaches experimentally. Space does not allow a description of shielding arrangements, but one can mention that leakage from units fed by the 11 MHz master oscillator resulted in a slowly varying DC bias at the detector output. Heavy low-pass filtering at the preamplifier DC power connections was essential to block this kind of r.f. pick-up from the power supplies and power lines. R.f. pick-up from autonomous oscillators resulted in beats at the detector output, which were recorded as noise or cyclical variations on the chart recorder,

depending on relative frequency differences and phase stability between the 11 MHz oscillator and the r.f. pick-up source. An example of this was pick-up from the 100 kHz oscillator in the master time units. The r.f. leaked into the receiver via the line to the relay coils in the relay box where switching between A and B coils operation was done. A low-pass filter was interposed between line and relay box. A third kind of pick-up resulted in random noise at the detector output. As an example, the thermocouple leads seemed to act as receiving antennaes, and especially the leads to the junction on the sample were effective in injecting noise into the receiver. This problem was sought overcome by shielding the thermocouple leads, with only scant success.

VI-D. The B System

The B r.f. system was operated in one of three pulse modes: a) A square pulse lasting from 0.1-0.2 sec and up to 15-20 sec b) Same as a) but with sudden 180° phase shifting at intervals of approximately 1 msec c) A train of equal pulses lasting from a few μsec to several msec, and spaced by time intervals of comparable magnitude.

A Hewlett-Packard 606A oscillator provided CW r.f. at the B system frequency. The r.f. was gated, phase shifted and amplified by the units shown on Figs. VI-11, VI-12 and VI-13.

Gate pulses for the B r.f. phase shift and B r.f. gate were generated in two ways: A digital logic unit connected with the master time unit could be triggered to deliver from 1 to 999 pulses of given length and mutual spacing. Repeated triggering yeilded multiples of this pulse number. Alternatively, several gated Tektronix 160 Series pulse delay units could be combined to produce the pulse train.

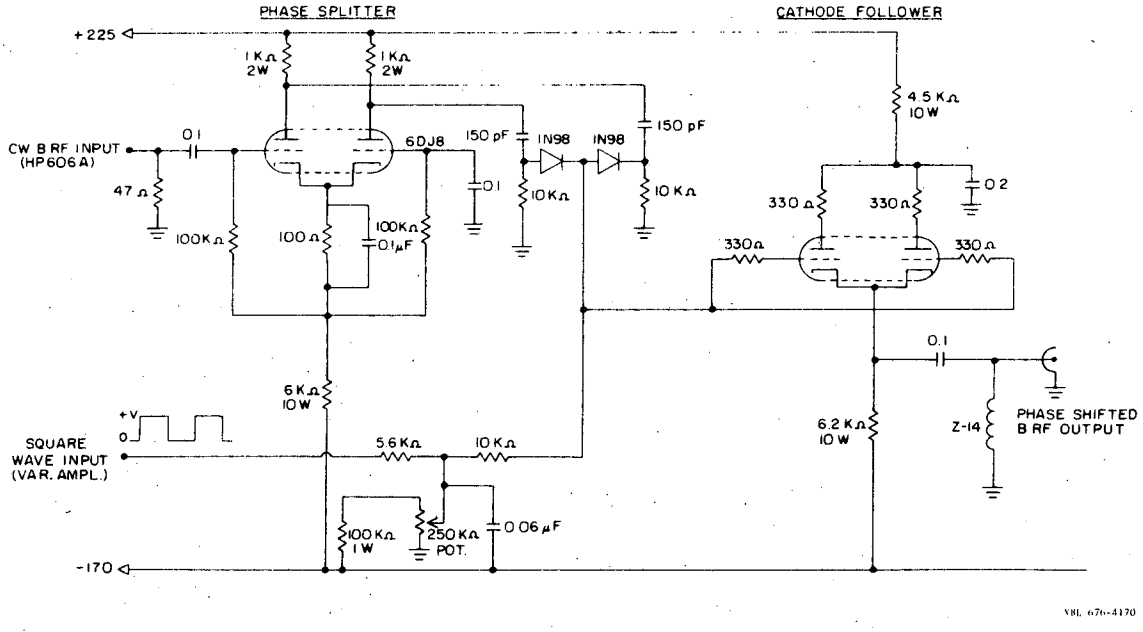

Fig. VI-11. B r.f. 180° phase shifter (chassis 9) (after D. A. McArthur[12]).

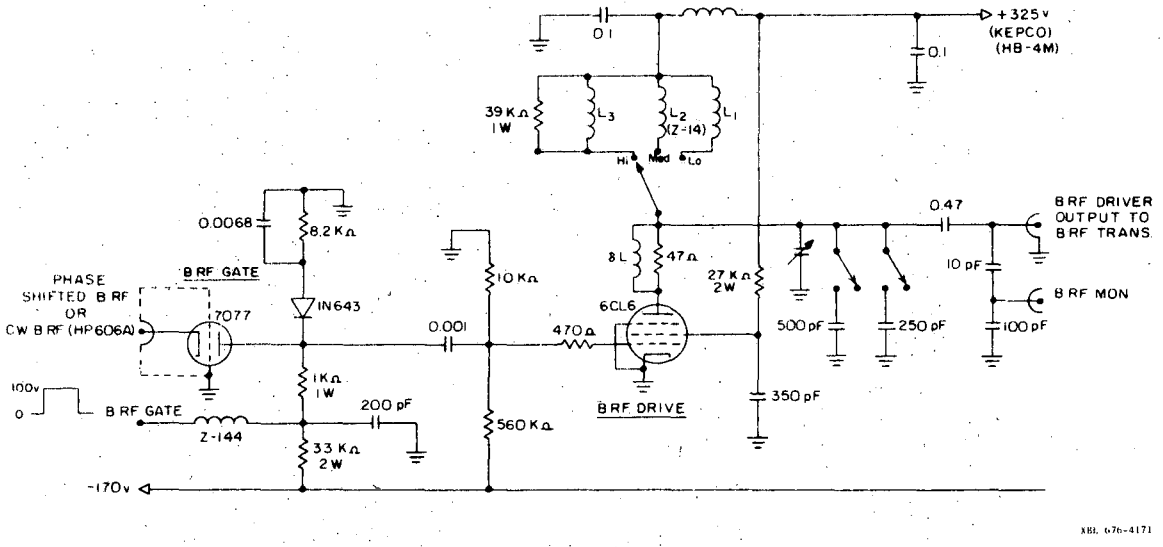

Fig. VI-12. B r.f. gate and preamplifier (chassis 9) (after D. A. McArthur[12]).

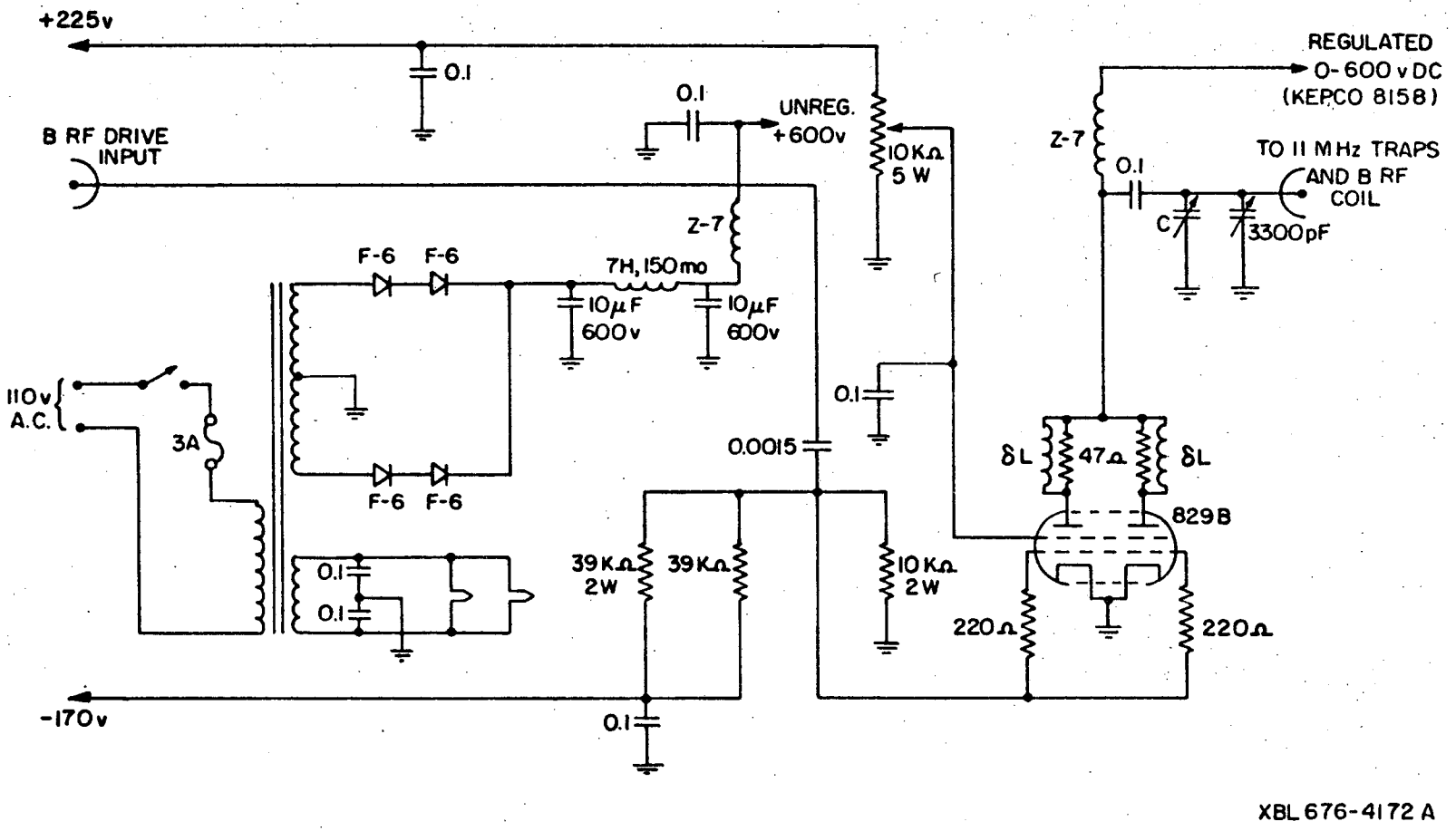

Fig. VI-13. Tunable B r.f. power amplifier (chassis 10).

The B r.f. gate and phase shift circuits will not be described here (cfr. McArthur[12]). Note, however, that the sharpness of the 180° phase change and symmetry between 0° and 180° phase pulse envelopes could be controlled to some extent by adjusting the B r.f. phase shift gate pulse amplitude (nominally +25 V) and the bias pot. meter. Smooth shifting is desirable to reduce sideband content in the B r.f., but too slow shifting results in reduced B spin reservoir heating. The driver stage tuning range was from 265 kHz to 3.15 MHz.

Power was supplied to the B coil from the TUNABLE B R.F. POWER AMPLIFIER, which was an 829B Class C amplifier with the B coil in a tuned plate circuit. Since pulse power stability was important in many of the experiments, KEPCO 815B regulated power supplies were used instead of the internal plate and screen voltage supplies. B r.f. power drop during long pulses was less than 1%.

Frequency components at 11 MHz in the B r.f. power amplifier output, in practice higher harmonics of the B frequency, were effective in destroying the proton signal and could create a false "double resonance" signal. To avoid this, traps tuned to 11 MHz were inserted into the line leading to the B coil, cfr. Fig. VI-14. With the traps, no direct depletion of proton signal due to harmonics was observed. In measurements on KDP, signal depletion was observed when harmonics hit the P^{31} reservoir, however. The proton and phosphorous reservoirs are strongly coupled and exchange energy rapidly. This effect was no serious problem in the experiments described here.

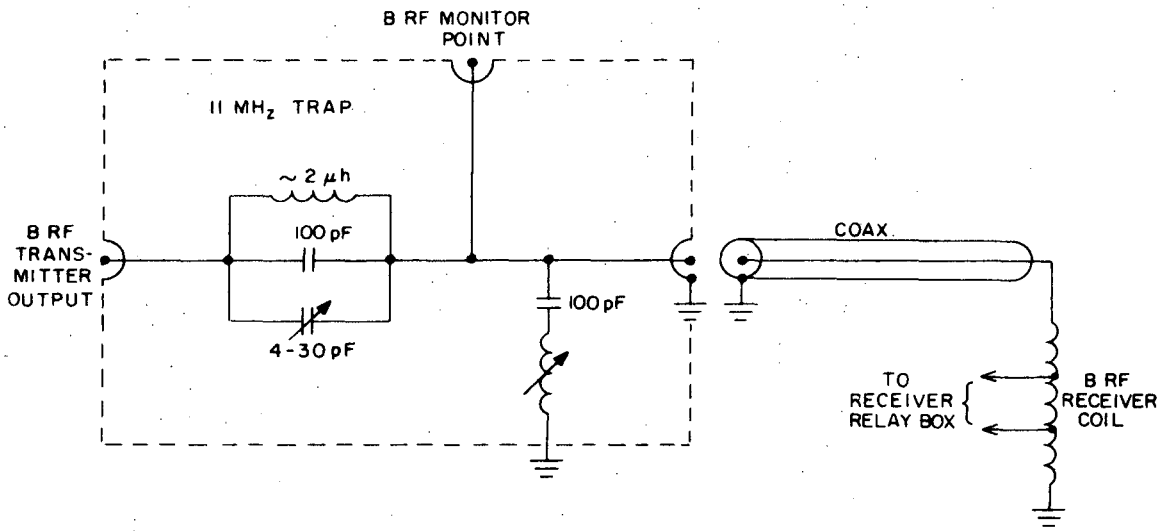

Fig. VI-14. 11 MHz traps and B r.f. monitor point (chassis 11) (after D. A. McArthur[12]).

B r.f. power during long pulses was measured at the monitor point shown on Fig. VI-14, with a Hewlett-Packard 410B VTVM. Using rotary saturation on Ca^{43} in CaF_2, the VTVM reading was related to the rotating B r.f. magnetic field component at the sample sits. With the coil used in most of the experiments, one found

$$H_{1B}(\text{gauss}) = \frac{V_{RMS}\ (\text{Volt})}{\nu_B\ (\text{kHz})} \cdot (140 \pm 2)$$

Depending on frequency, plate and screen voltages, etc. the B r.f. system could deliver pulses lasting several seconds with H_{1B} up to 30-50 gauss.

After the strong A r.f. pulses, ringing was observed at the receiver output. The oscillations were traced to the B circuit, but it was not determined whether the 11 MHz power pulse excited the B tank circuit or the 11 MHz traps. Since ringing occurred during the signal sampling period after the θ pulse, the line to the B r.f. transmitter was severed by a relay during the A transmitting and receiving periods. The relay was a Potter and Brumfield 11 DG 24 V_{DC} relay with two 10 Amp contacts in parallel, and with diode and resistor protection for the +DC pulse amplifier driving the relay. Thus two sets of relays were activated during the B r.f. pulse: One set switched the receiver cable leads from the A coil connections to ground, while the other connected the B coil to the B r.f. transmitter.

VI-E. Audio System

Pulsed audio power was generated as follows: The CW output from an AUDIO OSCILLATOR (Hewlett-Packard 202C) passed a RELAY GATE which was driven in parallel with the B r.f. gate. The gated audio wave was amplified and fed to a Halmholtz coil pair in the magnet gap by a 100-WATT AUDIO POWER AMPLIFIER, which had a flat frequency response throughout the audio range.

The system is described in more detail by McArthur.[12]

VI-F. Electromagnet and Field Stabilization

A Varian 12-inch magnet in connection with a Varian V 2100 power supply provided the magnetic field, which was monitored by an NMR proton probe at a fixed position in the magnet gap.

The magnetic field was set so that the proton Larmour frequency at the sample site was equal to the frequency of the 11 MHz master oscillator ((11011.65 ± 0.05) kHz, long term). When this condition obtained, no beats between free induction signals and the 11 MHz reference would be generated during phase sensitive detection. Accurate field setting was obtained as follows:

The $\pi/2$ pulse proton free induction signal at the output of the video amplifier was monitored on an oscilloscope. The phase reference for the phase sensitive detector was adjusted to yield zero signal during the initial parts of the free induction decay, and the magnetic field set at a value where no beats in the free induction signal was observed. The signal was then zero during the entire free induction decay period, and both phase and field setting were optimal for the ADRF cycle (Zeeman and dipolar r.f. signals are in quadrature). In this way,

the magnetic field could be adjusted to give a beat frequency of less than 300 Hz, as compared to the 11 MHz Larmour frequency.

Given the field setting, the measured field at the monitor probe position was used to maintain the magnetic field at its initial set value. Due to field gradients in the gap, the proton Larmour frequencies at the sample and in the monitor probe differed by approximately 2 kHz, and a separate r.f. source with continuously variable frequency was required to excite the probe. At the same time strict stability requirements had to be imposed on this r.f. source, since the long-term field stabilization is limited by the relative frequency stability of the monitor system. A Hewlett-Packard 606B oscillator phase locked to a crystal oscillator controlled Hewlett-Packard 8708A Synchronizer was used. This combination had a frequency stability better than $2 \cdot 10^{-7}$ per 10 min (manufacturer's specifications). The 606B output was fed into the reference signal path in a Varian F-84 Fluxmeter after a bypassed internal oscillator. The Varian F-84 Fluxmeter excited the monitor probe MNR head and field sweep coils, compared the probe Larmour frequency to the reference frequency and provided an error signal which could be fed directly to the Varian V2100 magnet power supply for automatic field regulations. Alternatively, the error signal could be used for manual regulation of the field.

Due to the near coincidence of the Larmour frequencies at the sample and probe sites, r.f. leakage from the monitor system led to 2 kHz beats on the signal at the receiver output. Shielding and low-level operation of the monitor system reduced the beat amplitude to a few percent of typical signals from the sample. Due to phase drift between

the two oscillators between samplings, the beats were detected on the chart recorder as additional noise. In experiments where a maximum signal to noise ratio was important, the probe was not excited during signal sampling, and manual adjustment of the field was made periodically (every 1/4-1/2 hour). Because of the high inherent stability in the magnet and power supply system, periodic control was fully adequate, but substitution of the original proton sample in the Fluxmeter probe by a sample containing other nuclei (F^{19}, P^{31}) was considered as an alternative.

VI-G. Temperature Control System

The sample temperature was controlled by a Varian Variable Temperature Control system Type V-4257, which consisted of a Dewar gas flow conduit and an electronic control unit:

Pure, dry N_2 gas from pressure bottles passed through a spiral heat exchanger in a liquid N_2 bath. The cooled gas entered at the bottom of the Dewar containing the sample and r.f. coil where a hot filament brought the gas temperature to the desired level. The gas then passed a Pt resistance wire which served as feedback temperature sensor for the electronic control unit, before flowing over the sample and exhausting into the air through a vent at the top of the Dewar. During operation at low sample temperatures, condensation at the exhaust vent and on the electrical feed-throughs into the Dewar was a problem. The whole volume between the magnet pole faces was therefore enclosed in a plastic bag which was slowly purged with dry N_2 gas, and exhausting N_2 from the Dewar was led out of the bag with a 2 foot piece of plastic tubing.

In the electronic control unit, the desired sample temperature could be set continuously on a dial. According to manufacturer's specifications, the temperature range was -185°C to +300°C, with a temperature resettability of ±2°C (at sample) and temperature control ±1°C (at sensor). Throughout the range of temperatures of interest here, our measurements with liquid N_2 as a coolant and N_2 gas flowing in the system indicated a temperature resettability within ±1°K and temperature control within ±0.5°K, both referring to the sample site.

Sample temperatures were measured with Cu-constantan thermocouples, using ice water or liquid N_2 as references. Thermovoltages were measured on a Hewlett Packard VTVM type 425A in the early stages of this work. The bulk of the K^{39} spin-lattice relaxation time measurements were done with thermovoltages being measured on a Keithley Digital Multimeter Model 160. With an average thermocouple response of 28 μV/°K in the range 80°K to 280°K, the maximum voltmeter error (Keithley 160: 0.1% of range) corresponds to less than 0.2°K temperature error in all cases. In order to eliminate errors due to thermovoltages at the voltmeter input connections, measurements were checked by switching the connectors.

Two sets of thermocouples were used: In one set, the sensing junction was permanently mounted 1 cm above the top edge of the sample r.f. coil, i.e., approximately 6 cm downstream in the N_2 flow compared to the sample center. Calibration curves at 10, 20 and 30 SCFH gas flow rates

were used to determine sample temperatures from readings obtained at this junction. The other thermocouple set had the sensing junction in a groove in the sample crystal. Sample and junction were wrapped in teflon tape and fitted into a thin-walled teflon tube. Thermal insulation provided by the teflon increased the time constant for heat exchange between the N_2 gas and the sample, which is desirable for good sample temperature stability, but might have accentuated the r.f. sample heating during long, powerful B r.f. pulses. Due to r.f. heating in the junction itself, the sample temperature rise could not be measured directly, but from the observed thermocouple readings during and between r.f. pulses, one can infer that the sample temperature rise due to r.f. heating always was $<0.5°K$. Another consequence of the thermal insulation of the sample could have been reduction of thermal gradients across the sample, since heat fluxes into and out of different portions of the sample is reduced.

The major reason for temperature gradients in the sample seemed to be that the cold N_2 gas gradually warmed up on passing downstream. To check on this, measurements were made on the axial thermal gradient in a teflon cylinder at the sample site. The cylinder was 38 mm long and with 12 mm diameter (typical KDP sample size), and had thermocouple junctions lodged in small bore holes, approximately 7 mm inside each end surface. Both thermocouple wires were led close together and entered at the upper end surface. Thermal contact at the junctions was sought improved with GC #8101 Transistor Z-5 Silicon Compound. Connecting the two junctions, the temperature differences between the

two sites were obtained at different gas flow rates. As expected, the gradient increases as the sample temperature and gas flow rate are lowered. In the region around the KDP Currie temperature T_c = 123°K, the temperature difference between top and bottom of the teflon cylinder is 2°K at 40 SCFH and 3°K at 30 SCFH. Measurements on K^{39} transition frequencies close to T_c, however, showed that the gradient must be less in the KDP samples, with 1°K as an upper limit at $T = T_c$, and 30 SCFH flow rate. This could be due to the difference in thermal conductivities and the teflon thermal shielding of the KDP sample, as mentioned above.

VII. CRYSTAL GROWING AND SAMPLE PREPARATION. PIEZOELECTRIC SIGNAL SUPPRESSION

The KDP samples used in this investigation were single crystal cylinders of diameter 10-13 mm and length 25-30 mm. They were of optical quality, but with roughly ground surfaces. There were three sources of crystals:

(a) Crystals used in proton spin-lattice relaxation and most double resonance measurements: These were grown by Dr. D. A. McArthur and Dr. R. E. Walstedt and this laboratory by the method described below. High-field T_1 for these crystals was approximately 33 sec (cfr. VIII-B). A specific sample with the crystallographic Z-axis parallel to the sample cylinder axis will be termed the "standard sample" in the following. It was used extensively throughout this investigation, and specifically in the measurements of the K^{39} spin-lattice relaxation times.

(b) Twenty-five percent deuterated crystals: These were supplied by Isomet Corp., Palisades Park, N. J. According to Isomet, they were made from analytical grade raw material. High-field T_1 was initially longer than necessary for double resonance applications, and the samples were therefore γ-irradiated from a Co^{60} source. A dose of 4.78×10^4 Rads brought the high-field T_1 down to approximately 52 sec.

(c) Other KDP samples of natural isotopic composition and deuterated by 4% were prepared as described below and had initially very long high-field T_1 values. Measurements on the samples of natural isotopic composition showed that even a dose 10 times that given the 25% deuterated crystals did not bring the high-field T_1 below 200 seconds, although a reduction in T_1 was detected. Irradiation caused no visible

discoloration of the samples. The samples, especially those with 4% deuteration, were prepared for applications of the type described under Section XII-C (Suggestions for Further Work). Further irradiation of the samples was not done, since it was decided that these applications would carry outside the scope of this work.

Crystal Growing

KDP single crystals were grown from an aqueous solution by the cooling method. Analytic grade KH_2PO_4 granules were dissolved in a glass vat containing approximately 8 liters of distilled H_2O, so that the solution was saturated at 70°C. Where partial deuteration was desired, D_2O was added to the solvent, and the degree of deuteration was estimated from the initial D^2/H^1 proportion in the saturated solution. Theoretically, the deuteron/proton signal strengths should also indicate degree of deuteration. From KDP crystals at hand, seeds were cut in the form of slices approximately 4 cm × 5 cm × 0.7 cm perpendicular to the crystallographic Z-axis. The seeds were fastened on a special mounting rod ("spider") so that when the rod was immersed in the solution and rotated about its axis, liquid flowed perpendicular to the 001 surfaces. For a brief period after immersion, the solution temperature was raised 3-5°C above the saturation temperature to dissolve away unwanted KDP microcrystals. A motor continuously rotated the mounting rod throughout the growing process, the direction of rotation being reversed every 15 sec or so. This provided mixing of the solution and even growth of the crystals. The temperature of the solution was controlled by a balanced bridge circuit with a temperature sensor (thermistor) in one arm of the bridge and a reference

resistor in another. Bridge unbalance voltage was fed into the power amplifier providing heating current to the glass vat. The reference resistance was slowly varied by a motor to lower the temperature by approximately 2-3°C in 24 hrs, and the system provided temperature control within 2°C. The glass vessel containing the solution was thermally insulated on its lower half only. On the inside walls above liquid level and lid water condensed and dripped down, which might have helped avoid spurious seeds from forming at the liquid surface.

The seeds quickly formed 101 pyramids on the 001 surfaces, and grew as straight prisms capped by pyramids in the (001)-direction. At approximately 40°C the sides of the prisms started to curve away from the Z-direction, and this became more pronounced as the temperature was lowered further. A similar effect has been reported earlier on adjusting the solvent P.h. The crystals obtained were large (typically 5 cm × 6 cm × 12 cm; weight 600g), of optical quality and with well-defined surfaces.

Sample Cutting

The KDP single crystals were very sensitive to mechanical and thermal stresses and precise cutting and grinding of samples without creating internal cracks was not quite straightforward. The method finally adopted was string-saw cutting by dissolving. The string was a taut rubber O-ring that was wetted by a sponge and driven through pulleys and guides by a motor. Final rounding of the samples was made by careful grinding on a sharpening stone, using water paste and grinding powder.

After final mounting in the NMR coil, the sample alignment deviated less than 1-2° from the optimal, as evidenced by rotation patterns of the K^{39} and K^{41} spectra (cfr. X-A).

At the end of this investigation, it was also demonstrated that a disc saw with diamond powder could be used to obtain precise cuts with little or no damage. The crystal was then glued to the saw table and the saw advanced very slowly, with no coolant.

Piezoelectric Signal Suppression

KDP is piezoelectric, and special precautions had to be taken to avoid "ringing" after application of the strong r.f. pulses. Peak-Peak voltages across the sample coil reached very high levels (Θ(100V)) during the pulses, and the oscillating electric fields would set up electromechanical vibrations in the sample. These vibrations could persist after the r.f. had been turned off, and were observed as a strong, damped oscillation superposed on the NMR signal.

It is interesting to note that straight, cylindrical samples with end surfaces perpendicular to the axis were less prone to ring than samples with more irregular shapes. The latter were straight cylinders with the lower end surface at an angle to the axis, or with slices taken off two opposite sides of the cylinder.

Several methods are known to get rid of piezoelectric ringing, and the methods are based on introducing either mechanical or electrical losses.

Effective mechanical damping (good impedance match) can be obtained by immersing the crystal in a liquid, but this was impractical in the present case, both because of space limitations and because

measurements were made down to low temperatures (approximately 99°K). No proton-free liquids with suitable melting and boiling points were available. An adhesive tape wrapped around the sample is a trick that was not tried, but it seemed that gluing the end surface of the sample to the mounting rod helped.

The chief means of suppression were electrical, however. A 2 mil Mylar film with a 100Å Al layer was wrapped around the sides of the sample. To avoid eddy current damping of the r.f. pulse, thin strips of Al were removed parallel to the cylinder axis and at intervals of approximately 0.5 mm. Since the skin depth of Al is $\simeq 10^5$Å at 11 MHz and 99°K, the Al did not provide appreciable shielding of the r.f. fields, but would cause damping of the free vibration of the crystal. The sample with the Mylar Al foil and teflon mount were enclosed in a cage of insulated #39 Cu wire at ground potential, which shielded from the r.f. fields. The wires were glued side by side at maximum density and parallel to the sample cylinder axis. Electrical connections to the wires were made so that the shielding should create low losses and disturbance on the applied r.f. field.

These precautions proved sufficient to eliminate ringing in all cases. The most dramatic improvement was in the region from the ferroelectric Curie temperature T_c and up to approximately T_c + 8°K.

VIII. MEASUREMENTS OF PROTON SPIN-LATTICE RELAXATION TIMES IN KDP. ULTRASLOW MOTION

VIII-A. General Considerations

Proton spin-lattice relaxation measurements were made partly because of their intrinsic information on the state of motion in the crystal, partly because protons were used as abundant (A) spin species in double resonance experiments: As was discussed in Chapter III, the A spin-lattice relaxation times pertinent to the specific double resonance method to be used are essential to both the maximum double resonance sensitivity and information gathering rate which is possible with a given experimental set-up. The proton relaxation data presented here pertain to relaxation in the laboratory frame and in the rotating frame after ADRF, and are thus relevant to ADRF double resonance.

In this and later chapters, it is necessary to specify the direction of the applied static magnetic field H_o relative to the KDP crystal axes. Figure VIII-1 shows a convenient convention[48] for cases where the magnetic field is perpendicular to one of the crystallographic axes (x,y,z). Except for accidental misalignments, this will always be the case in the work reported here. The structures of KDP in the para- and ferro-phases were described in the Introduction, where the x,y,z (a,b,c) axes were defined. In the para-phase, rotation about the z axis by 90° reproduces a given field/crystal structure configuration, and also there are in general two sets of equivalent protons. These correspond to hydrogen bond directions nearly parallel to either the x- or y-axis (called x- and y-bonds in the following). In the special case $\theta_z = (45° \pm n \cdot 90°$, n = integer number), all protons are equivalent.

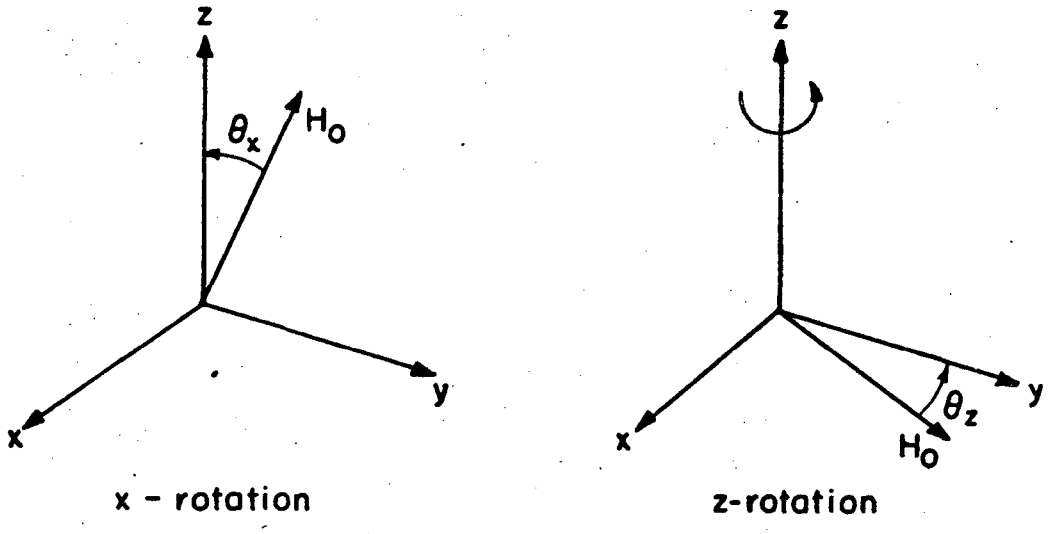

Fig. VIII-1. Definition of X- and Z-rotations.

As described in Chapter VII, several KDP crystals were available with widely varying laboratory frame, high-field spin-lattice relaxation times. The data in this chapter were obtained with different cuts from the crystals grown by McArthur and Walstedt. These were the samples with the highest impurity contents, as indicated by their short laboratory frame spin-lattice relaxation times.

VIII-B. High-Field Spin-Lattice Relaxation Times in the Laboratory Frame

The relaxation times were measured by conventional pulse methods throughout a temperature range extending from room temperature and down to 92°K. The bulk of the measurements were made by saturating the laboratory frame transition by a strong (rotating frame field $H_1 \simeq 60$ gauss) burst of resonant r.f. field and recording the recovery of laboratory frame magnetization by applying a $\pi/2$ pulse at various times after the saturating pulse.

The relaxation curves thus obtained proved to be non-exponential in various degrees, with steeper initial slopes. Relaxation times determined from the lowest slopes on the relaxation curves were from 5% to 30% longer than the ones determined from the initial slopes. Since the scatter in the data points on the relaxation curves was relatively larger at long times, the largest discrepancies reported above need not have been entirely due to non-exponential relaxation. The following checks were made to eliminate certain trivial explanations for the non-exponential behavior:

Nonlinear receiver response: Direct measurements of receiver linearity as described in VI-C-2 showed that the receiver could not

be the source of the non-exponential relaxation curves. This was confirmed by two additional measurements: Before entering the pre-amplifier, the signal from the coil was attenuated by 10 dB, and relaxation curves were recorded. When renormalized, the new curves coincided (well within the experimental scatter) with the curves obtained with no attenuation. In the other test, tap water was used instead of the crystal sample, and exponential relaxation curves obtained.

Experimental technique: The Zeeman signal after complete saturation evolves as

$$S(t) = S(\infty)\ (1 - e^{-t/T_{1.LAB}})$$

where t is the time elapsed between the saturating pulse and the $\pi/2$ sampling pulse, and $S(\infty)$ is the maximum proton signal, obtained for long times t. Since relaxation curves were derived from $[S(\infty) - S(t)]/S(\infty)$, an error in $S(\infty)$ will lead to apparent non-exponential relaxation. To avoid systematic errors in $S(\infty)$, the longest times t that were used in recording each relaxation curve was typically 240 sec, corresponding to 6-9 times the average lab frame spin-lattice relaxation times that were measured. The difference in signal from the case where $t \to \infty$ is then $O(10^{-3})$, which is negligible compared to the noise, at a signal to noise level of approximately 50. Another possible source of error is detection of dipolar signal components due to order accidentially being created in the dipolar reservoir during the saturating pulse (as described below, the dipolar T_{1_d} is much shorter than $T_{1.LAB}$). The reference phase for the phase sensitive detector exhibited both short-and long-term drift, which would have led to

detection of possible dipolar signal components and to variable gain for the Zeeman signal. It seems improbable that such effects should yield reproducible data of the type observed, but to check whether the non-exponential behavior was related to the experimental method used, several alternative saturating pulse sequences were tried: a) A long (approximately 20 msec) square r.f. pulse. Since the proton T_2 as determined by free induction decay measurements was approximately 40 μs, the spin temperature at the end of the pulse should effectively be infinite, both in the laboratory and rotating frame. b) A single $\pi/2$ pulse gave poorer saturation than in a), but the relaxation behavior was the same. c) A comb of 10 $\pi/2$-pulses gave a high degree of saturation, but unchanged relaxation behavior. d) Inverting the lab frame population with a π pulse yielded the same curve shape as before, when renormalized.

As mentioned in Section VIII-A, there are two sets of equivalent protons in KDP for $\theta_z \neq (45° + n \cdot 90°)$, which correspond to the two different angles between the static magnetic field H_o and the hydrogen bond direction. To check whether there were two sets of protons which relaxed at different rates, measurements were made to determine the relaxation behavior at $\theta_z = 45°$. The relaxation time $T_{1.LAB}$ was found to be longer than at $\theta_z = 90°$, but the non-exponential behavior was the same.

Crystal imperfections could lead to different relaxation rates, but such perturbations were not observed in the electric field gradient data for K^{39} (Cfr. Chapter X).

The main object of the $T_{1.LAB}$ measurements was to establish the maximum permissible double resonance cycle repetition rates at different

temperatures. No further experimental or theoretical attempts were therefore made to determine the reason for the non-exponential behavior, and one made no special effort to obtain a large body of accurate $T_{1.LAB}$-data.

Since the slopes of the relaxation curves were relatively constant during the first 15-20 seconds of relaxation, these were used in defining the relaxation time. Most of the relaxation times were recorded with the crystal orientation $\theta_z = 90°$ ($z \perp H_o \parallel x$). This was the orientation used in the $T_1(K^{39})$ - measurements, and the results in Fig. VIII-2 were obtained with the same sample called the "standard sample" in the following. Also shown in the figure are $T_{1.LAB}$ values obtained with $\theta_z = 45°$ and at two different sample temperatures.

The results in Fig. VIII-2 are consistent with a nearly temperature independent relaxation time $T_{1.LAB}$ throughout the temperature range from room temperature to 99°K. In the paraelectric phase ($T > 123°K$) and for $\theta_z = 90°$, one found $T_{1.LAB} \approx 33.3$ sec. Below approximately 110°K one found $T_{1.LAB} = 37.5$ sec. At $\theta_z = 45°$, $T_{1.LAB} \simeq 39$ sec in the paraphase. With the estimated error limits indicated in Fig. VIII-2, one should not pay much attention to minor temperature trends in the data, but $T_{1.LAB}$ appears to be slightly longer at low temperatures, and any anomaly at the Curie temperature must be weak. The longer T_{LAB} at $\theta_z = 45°$ is possibly due to different spin diffusion rates at the two orientations. The temperature dependence of $T_{1.LAB}$ indicates that the dominant relaxation mechanism is spin diffusion to paramagnetic impurities. This affords one possible explanation to the non-exponential relaxation behavior, namely inhomogeneous distribution of the paramagnetic

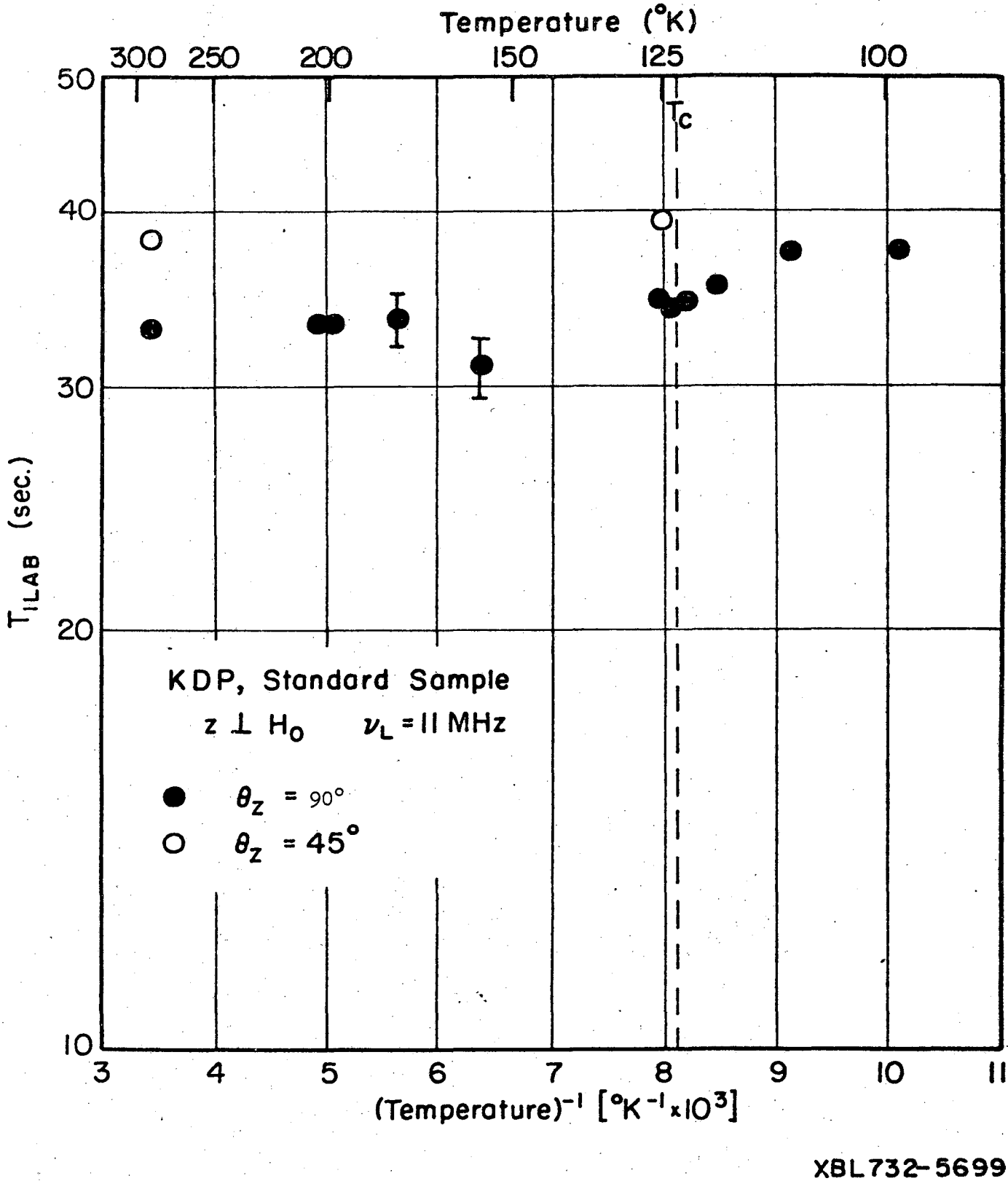

Fig. VIII.2. High field laboratory frame proton spin-lattice relaxation rates as a function of temperature. H_o = 2586G.

impurities which act as relaxation centers. Clearly, if measurements of $T_{1.LAB}$ are to yield information on lattice motion in the crystal, a much higher degree of sample purity is required. Measurements of this type have been made by R. Blinc, et al.[49]

VIII-C. Rotating-Frame Spin-Lattice Relaxation Times After ADRF. Ultraslow Motion

As described in Section II-B, the ADRF sequence preferentially aligns the protons along their local fields in the rotating frame. We shall assume that dipole-dipole couplings rapidly establish a state for the whole proton system which can be described by a spin temperature which initially is very low. Due to spin-lattice relaxation, the spin temperature will evolve towards the lattice temperature at a characteristic rate which will be defined as the dipolar spin-lattice relaxation time $T_{1.dip}$ since it pertains to the dipole-dipole coupled system. $T_{1.dip}$ is generally different from $T_{1.LAB}$.

Dipolar spin-lattice relaxation times were measured by applying an ADRF pulse sequence to the sample and recording the decay of the dipolar signal as the time separation t_b between the ADRF sequence and the $\pi/4$ sampling pulse was increased. In contrast to the measurements of $T_{1.LAB}$, one here had to allow the protons to come into thermal equilibrium with the lattice before each pulse sequence. Typically, the protons were allowed to polarize at least 120 sec after the $\pi/4$ sampling pulse, before the next ADRF sequence was applied. For the KDP standard sample ($z \perp H_o$) this led to proton signals that were slightly lower (~2%) than would have been obtained from a proton system is equilibrium with the lattice. This discrepancy was less than typical

measurement errors due to drift and noise, however.

Relaxation curves (proton dipolar signal vs t_b) were obtained with the standard sample and other samples from the same crystal batch. These curves also exhibited deviations from exponential behavior, but here the shape of the curves depended on the temperature in a very interesting manner: At sample temperatures below approximately 210°K the curves were close to exponential throughout the range of t_b-values used, which generally was 0.2 sec $\leq t_b \leq$ 15 sec. For t_b longer than this, a tendency towards a more shallow slope was observed. At high temperatures a steeper initial slope becomes evident, and above approximately 250°K one can clearly resolve two exponential decay curves. At temperatures 300°K and above the data are uncertain, but indicate that the two relaxation times approach each other so that there is only a single averaged relaxation time at high temperatures. These results are typical for all samples that were studied in this way. In Fig. VIII-3 are shown $T_{1.dip}$ values obtained with the KDP standard sample at $H_o \parallel x$. The relaxation times in the high temperature region are plotted separately in Fig. VIII-4, where data obtained with another crystal ($H_o \parallel z$) are also included.

Before going on to a physical interpretation of the $T_{1.dip}$-data, one can now assess how well protons in these specific samples are suited for use as indicator spins ("A" spins) in ADRF double resonance applications. Since the dipolar signal decays due to spin-lattice relaxation, $T_{1.dip}$ will define an upper limit for how long the time t_b can be, and thus also for the time the double resonance A-B coupling

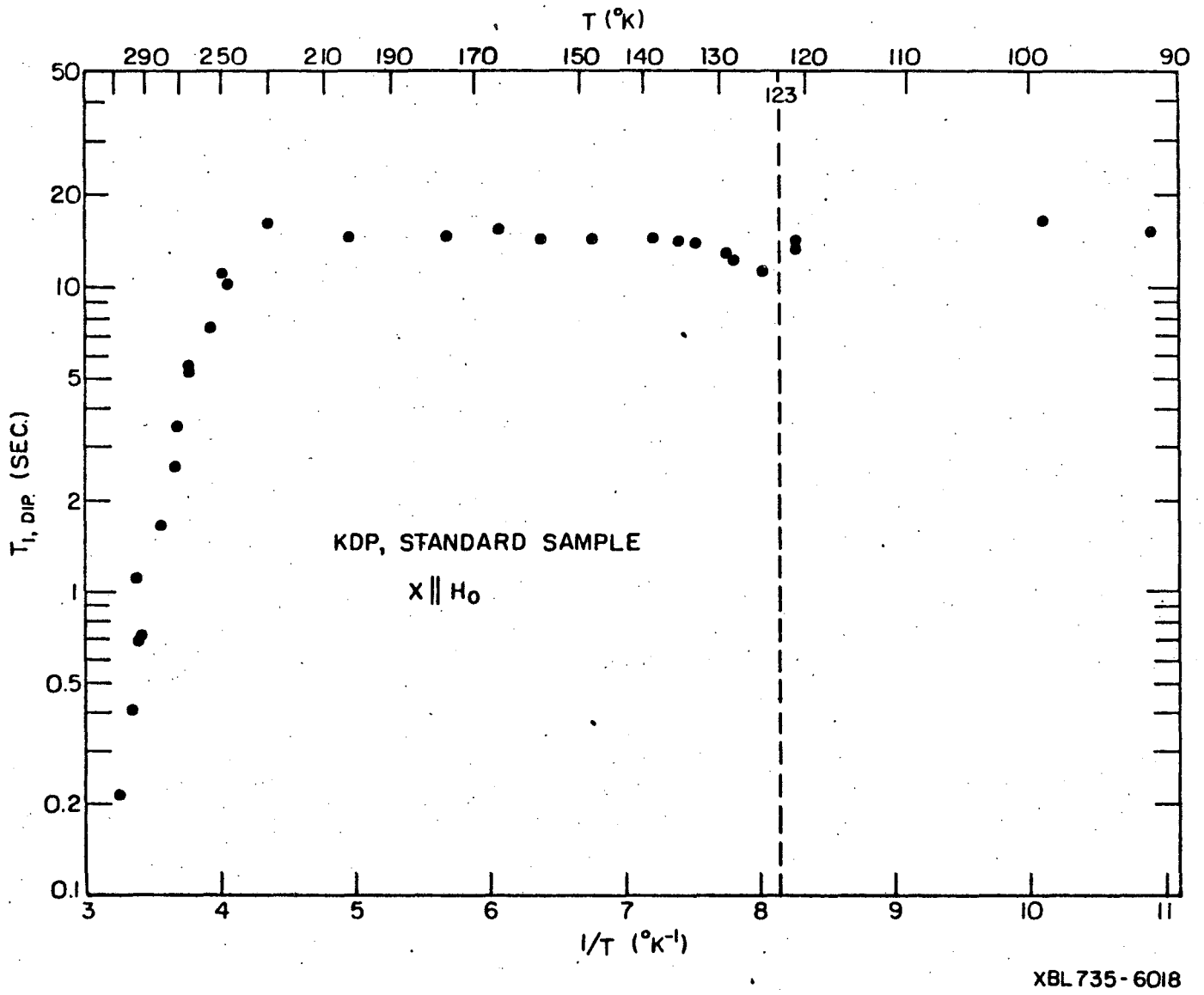

Fig. VIII-3. Temperature dependence of proton-spin-lattice relaxation times in the rotating frame after ADRF. H_o = 2586 G.

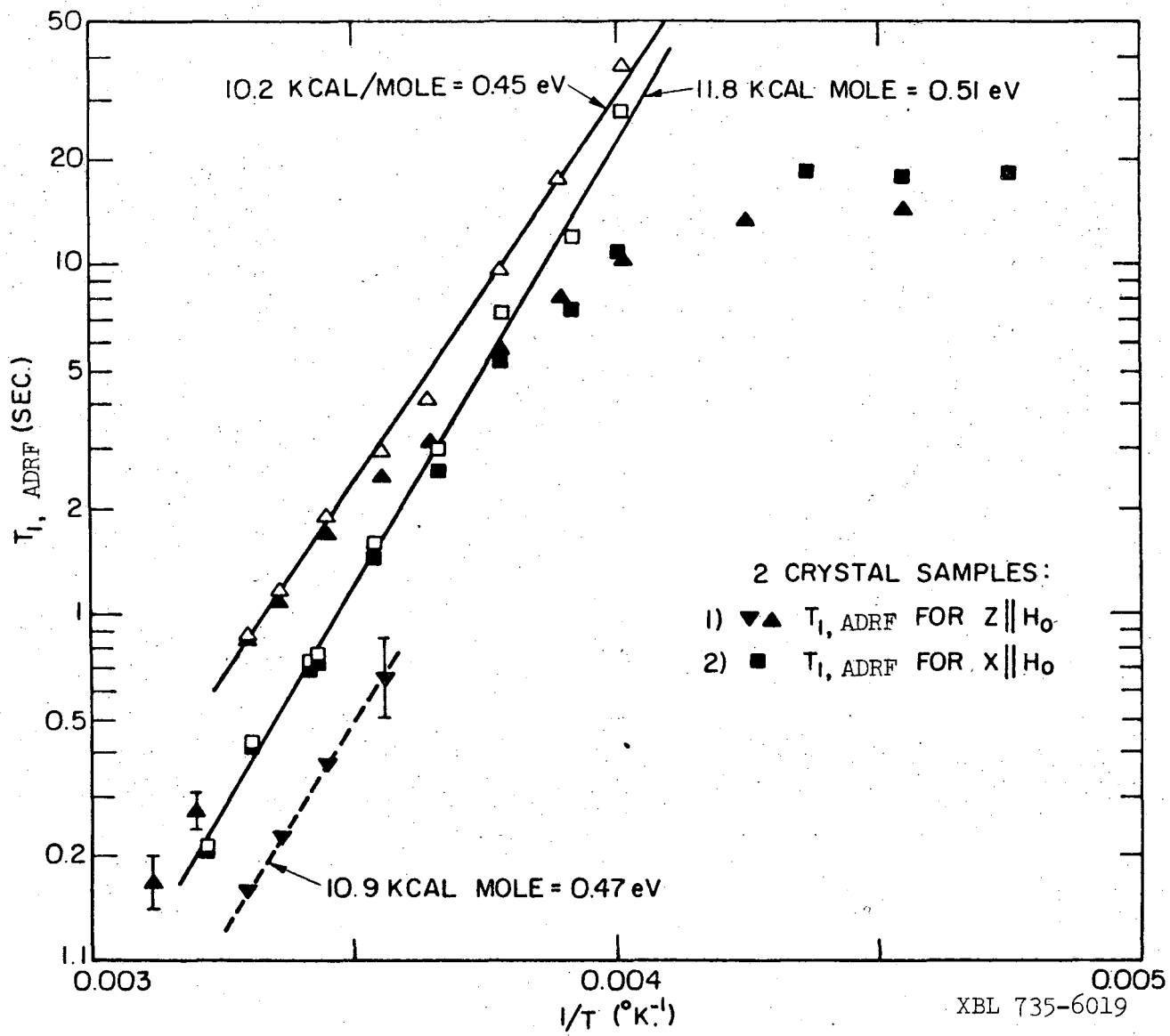

Fig. VIII-4. Proton spin-lattice relaxation times in the rotating frame after ADRF. Dual relaxation rates observed at high temperatures are only shown for the Z ‖ H_o sample. Relaxation rates indicated by open symbols were obtained by subtracting 1/15 sec^{-1} and 1/19 sec^{-1} from the total observed relaxation rates at Z ‖ H_o and X ‖ H_o, respectively. H_o = 2586 G.

can be maintained. The choice of t_b depends on the signal-to-noise ratio required, but $t_b = T_{1.dip}$ can be used as a rough guide. The data in Figs. VIII-3 and VIII-4 show that $T_{1.dip}$ is nearly constant and equal to approximately 14 sec at temperatures below 240°K. Assuming typical cross-relaxation rates, etc, this should be adequate for high-sensitivity detection of all rare nuclear species in KDP, given a signal/noise ratio of 50 at t_b = 10 sec. As the temperature is increased above 250°K, however, $T_{1.dip}$ rapidly becomes shorter, which ultimately makes the A-B coupling time too short for detection of the rare spins. The temperature where this occurs, depends on the abundance of the rare spin species, the A-B cross-coupling time, apparatus parameters, what type of measurements are being made, etc, but for K^{39} and K^{41} in KDP one found that double resonance spectroscopy could be done up to 290-300°K. Quantitative measurements of double resonance signal amplitudes required lower temperatures, however. The $T_{1.LAB}$-data indicated that quantitative signal amplitude measurements could be done with cycle repetition times as short as 120 seconds, and one can conclude that protons are well suited as double resonance indicator spin in these samples.

As described in Section II-C, a temperature dependent $T_{1.dip}$ combined with a nearly temperature independent $T_{1.LAB}$ indicates that ultraslow motion is taking place. Both the present results and data published in the literature establish clearly that this ultraslow motion in KDP can be linked to the protons. Schmidt and Uehling[50] have studied the dynamics of deuterous in the deuterated isomorph and were able to show that two distinct types of deuteron motion takes

place: A rapid intrabond motion, where deuterons jump between two adjacent equilibrium positions on a given hydrogen bond, and a much slower interbond motion, where deuterons jump from one bond to a neighboring one. Schmidt and Uehling used electrical conductivity and NMR data, and later measurements with similar methods have established that protons in KDP behave in the same manner, cfr. below. It is reasonable that large-scale low-frequency motion in the temperature range of interest would be linked to the protons which are bound by the relatively weak hydrogen bond, rather than the stronger covalent and/or ionic bonds of the other nuclear species in the crystal.

Turning now to Fig. VIII-3, it is evident that one must consider several different contributions to the total relaxation rate $1/T_{1.dip}$: a) A nearly temperature independent contribution from paramagnetic impurity relaxation with an average value 0.068 sec^{-1}, corresponding to a relaxation time 14.7 sec. b) A contribution at high temperatures ($T \gtrsim 230°K$). c) A contribution which has its maximum at or close to the Curie temperature $T_c = 123°K$. b) and c) are treated separately below:

b) Relaxation at high temperatures ($T \gtrsim 230°K$)

Details of the relaxation behavior in this temperature range are shown on Fig. VIII-4 for two samples with $x \parallel H_o$ and $z \parallel H_o$, respectively. Subtracting the impurity relaxation contribution, one obtains relaxation rates that clearly are governed by an activation energy E_a, as shown. This is evident for both the fast and slow relaxation rates observed simultaneously in this temperature range. For the slow relaxation component, one found $E_a = (0.51 \pm 0.05)$ eV for the $x \parallel H_o$ sample, with

E_a 10% smaller in the $z \parallel H_o$ sample. These results are typical for measurements on other samples also. Within experimental uncertainty, the same activation energy was found for the rapid relaxation component in samples of both orientations. The data spread does not allow a quantitative comparison of activation energies in the two orientations for the rapid relaxation component.

After these data had been recorded, similar results for KDP and two isomorphs were published by Blinc and Pirs.[51] Their data on KDP, obtained with $z \parallel H_o$, were essentially in agreement with those presented above, but they do not report dual relaxation rates in the high temperature region, nor an increase in relaxation rate at T_c. The activation energies measured by Blinc and Pirs were: In KDP:(0.64 ± 0.1) eV (single crystal), in RbH_2PO_4:(0.82 ± 0.03) eV, (powder sample), and in CoH_2PO_4:(1.4 ± 0.4) eV (powder sample). Blinc and Pirs concluded that the relaxation was due to hindered rotation about a single axis, and that it is the size of the cation that controls the rotation and not the hydrogen bond energy, which is roughly the same in all three isomorphs. From these data and spin-lattice relaxation measurements in the spin-lock state, they also found that the rotation correlation time had a temperature dependence

$$\tau_c = \tau_o \exp(E_a/KT) \qquad \text{(VIII-1)}$$

where $\tau_c = 1.2 \cdot 10^{-3}$ sec at 300°K and rapidly decreases at higher temperatures. Our data agree well with this, and from the relaxation rate one may roughly estimate $\tau_c \simeq 1$ sec at 250°K. Using the value $E_a = 0.51$ eV, Eq. (VIII-C-1) then yields a pre-exponential factor τ_o

of the order of magnitude 10^{-10} sec. These results apparently contradict the measurements of Schmidt and Uehling[50] of deuteron interbond jump times τ_{xy}, which are so long that they cannot be reconciled with the correlation times above. As pointed out by Blinc and Pirs, however, the discrepancy can be resolved by taking into account that τ_{xy} pertains specifically to motion between x- and y-bonds, while $T_{1.dip}$ is sensitive to jumps between two x-bonds or two y-bonds as well.

It is interesting to note that the observed activation energies are the same, within experimental uncertainty, as those obtained from deuteron and proton conductivity data.[50,52] This demonstrates that proton transport by H_2PO_4 rotations defines the rate of change transfer and thus the electrical conductivity in KDP.[51] Also, the observed activation energy of 0.5 eV is in itself a strong indication that the proton motion is rotation of H_2DO_4 groups, i.e., a cooperative process, rather than proton interbond jumping:[51,53] Single-proton diffusion or interbond jumping requires the breaking of a hydrogen bond of energy 5 eV, which is roughly ten times the observed activation energy.

One may now list some possible explanations for the double exponential relaxation observed in the dipolar state at high temperatures. Clearly, imperfect samples is a possibility, but nontrivial explanations cannot be ruled out. Blinc and Pirs did not report double exponential relaxation in their paper,[51] but according to Blinc,[54] such behavior was observed in some cases. Also, as was especially evident in some cases, we observed two well defined relaxation rates, rather than the continuous distribution which one would expect due to random perturbations from crystal imperfections or an inhomogeneous impurity distribution. A striking feature

of the double exponential relaxation rates is that both relaxation rates exhibit a temperature dependence corresponding to the same activation energy. This suggests that also the fast relaxation is related to hindered rotation of H_2PO_4 groups. One possibility is that x-bond and y-bond protons relax at different rates, depending on the angle between each bond and the magnetic field H_o. In that case, a single relaxation rate would be observed in the $z \parallel H_o$ orientation, where all bonds are equivalent. This was not found to be the case experimentally. Before leaving the subject of the double relaxation rates, one should mention that the protons after ADRF are coupled by mutual dipole-dipole interactions to the other nuclear species in KDP, of which the most important are P^{31} and possibly K^{39}. It is conceivable that the cross-relaxation and spin-lattice relaxation rates could depend on the temperature in such a way that they would lead to the observed proton relaxation behavior.

c) Relaxation rate anomaly at $T \simeq T_c$.

As is evident from Fig. VIII-3, there is a small, but definite increase in the relaxation rate close to the Curie temperature, with an apparent maximum at T_c. A somewhat similar anomaly at T_c has been reported by Blinc and Zumer,[8] who measured high-field spin-lattice relaxation times for P^{31} in very pure KDP samples. Blinc and Zumer concluded that the perturbation mechanism responsible for the relaxation anomaly at T_c was proton-phosphorous magnetic dipole interaction, modulated by a specific low-frequency lattice mode, the "ferroelectric

mode". This mode, which is discussed further in Chapter XI, becomes strongly excited and lower in frequency ("goes soft") as the Curie point is approached. The same explanation probably does not apply in the present case, since the correlation frequency is restricted to the kilohertz range, as indicated by the absence of an anomaly in the $T_{1.LAB}$ data. All experimental evidence obtained on the ferroelectric mode in KDP so far, shows that the ferroelectric-mode fluctuation spectrum is essentially white throughout the frequency range of interest here (a few kHz to 11 MHz), even within millidegress K of the Curie point. Also, a comparison with the Blinc and Zumer results suggests that the impurity level in our samples was so high that relaxation by phonon-modulated magnetic dipole coupling would be too slow to be observed. As was described above, however, ultraslow proton motion can be effective in relaxing protons in the dipolar state after ADRF. A possible perturbation mechanism at $T \approx T_c$ is proton interbond motion either by single-proton jumping or rotation of H_2PO_4 groups. (The correlation time of intrabond motion is too short, cfr. Ref. 49.) This is supported by Schmidt and Uehling's measurements of the x-y bond jumping rate[50] which indicate an anomalous rate increase as $T \rightarrow T_c$.

In connection with the relaxation rate anomaly at T_c one should mention that Blinc, et al. have found a different type of anomaly in high-field laboratory frame proton relaxation times for very pure samples of KDP.[49] These results show a BPP-type relaxation rate maximum <u>below</u> T_c. With the low purity crystals used in the work reported here, the relaxation anomaly reported in Ref. 49 would be small compared to the relaxation rate due to paramagnetic impurities. Still, it is

disturbing that no such anomaly was detected either in our $T_{1.LAB}$ or $T_{1.dip}$ data even though few data were obtained in the temperature region in question. Later measurements by R. Blinc, et al. have thrown doubt on the data in Ref. 49, however.[54] The more recent data yielded a protion relaxation rate maximum at $T = T_c$ which is interpreted as being due to the slowing down of the proton motion in the hydrogen bonds.

To conclude, then: Protons are well suited as A (or indicator)-spins for ADRF double resonance in the KDP samples investigated. In addition, the following items can be listed which suggest further experimental investigation:

The difference in activation energy for H_2PO_4-rotations in the orientations $z \perp H_o$ and $z \parallel H_o$.

The two relaxation rates observed in the high temperature $T_{1.dip}$-relaxation curves.

The anomaly in $T_{1.dip}$ at the Curie temperature.

Although these phenomena might yield valuable information on KDP lattice dynamics, a main goal in this investigation was to develop and apply alternative methods capable of supplementing information of the type shown above. Thus, time did not permit more careful and encompassing measurements of the type presented in this chapter, and work on proton relaxation in KDP was not pursued further.

IX. TEST ON THEORIES DEVELOPED IN CHAPTERS IV AND V: PROTON K^{39} SYSTEM IN KDP

In Chapter IV, explicit expressions were obtained that apply to double resonance with a single, unmodulated B r.f. pulse, and in Chapter V effective gyromagnetic ratios in the rotating frame were computed for the case where laboratory frame quadrupole and Zeeman interactions are of arbitrary relative magnitudes.

Here, experimental verification of these results will be sought by double resonance in KDP. H^1 and K^{39} are used as A and B spins in double resonance with unmodulated B r.f., and effective gyromagnetic ratios in the rotating frame are measured directly for K^{39} by audio saturation double resonance. These spin systems offer specific advantages, to be listed below, but it is necessary to investigate the effect of a third spin species, P^{31}, on the double resonance mechanism described in Chapter IV. Also, the analysis in Chapter V applies for a single spin species, and the effects of double resonance detection must be taken into account. Other interactions between K^{39}, K^{40}, K^{41}, O^{17} and H^2 can be neglected, due to low abundances or low gyromagnetic ratios. For the purposes of this analysis, the total spin hamiltonian during B r.f. irradiation can be written:

$$\mathcal{H} = \mathcal{H}_o^A + \mathcal{H}_o^B + \mathcal{H}_o^C + \mathcal{H}_{dd} + \mathcal{H}_{r.f.}^B \qquad \text{(IX-1)}$$

where

$$\mathcal{H}_{dd} = \mathcal{H}_{dd}^{AA} + \mathcal{H}_{dd}^{AB} + \mathcal{H}_{dd}^{CB} + \mathcal{H}_{dd}^{CC} + \mathcal{H}_{dd}^{AC}$$

A, B and C represent protons, K^{39} and P^{31}, respectively. Furthermore,

$\mathcal{H}_o^A$, $\mathcal{H}_o^C$ are H^1 and P_{31} Zeeman hamiltonians.

$\mathcal{H}_o^B$ is the K^{39} mixed Zeeman-quadrupole hamiltonian.

$\mathcal{H}_{dd}$ represents the magnetic dipole interactions within the coupled A, B, C system. $\mathcal{H}_{dd}^{BB}$ has been omitted due to the low K^{39} gyromagnetic ratio.

$\mathcal{H}_{r.f.}^B$ is the K^{39} interaction with a strong r.f. field which is assumed on resonance for one of the K^{39} transitions. The r.f. frequency is assumed for removed from A and C transition frequencies.

As indicated in Chapter III, the coupling and energy transfer between the A, B and C spin systems is analyzed by transforming the hamiltonian into the rotating frames of the spin systems involved. The appropriate transformation operator in the present case is:

$$L_q = \exp[i(\mathcal{H}_o^A + \mathcal{H}_o^B + \mathcal{H}_o^C)t]$$

Only secular terms in the interaction representation hamiltonian

$$\mathcal{H}^* = L_q^{-1}\mathcal{H}L_q - \mathcal{H}$$

need be considered, since these terms contribute to A-B-C energy transfer in the rotating frames and define the energy levels in the B rotating frame

$$\mathcal{H}^*(s) = \mathcal{H}_{dd}^*(s) + \mathcal{H}_{r.f.}^{B*}(s) \qquad \text{(IX-2)}$$

Here,

$$\mathcal{H}_{dd}^*(s) = \mathcal{H}_{dd}^{AA*}(s) + \mathcal{H}_{dd}^{AC*}(s) + \mathcal{H}_{dd}^{CC*}(s) + \mathcal{H}_{dd}^{AB*}(s) + \mathcal{H}_{dd}^{CB*}(s)$$

Stars indicate interaction representation, the s in parenthesis indicates secular part. The AA, CC and AC couplings are very strong in the present case due to the large H^1 and P^{31} gyromagnetic ratios, and one can define a single thermal reservoir for the A and C spins, with one spin temperature. This reservoir is represented by

$$\mathcal{H}_{dd}^{AA*}(s) + \mathcal{H}_{dd}^{CC*}(s) + \mathcal{H}_{dd}^{AC*}(s) \qquad \text{(IX-3)}$$

In the double resonance applications below, the coupled spin system H^1-P^{31} can therefore be treated as a single thermal reservoir, where the heat capacity now is determined by the hamiltonian Eq. (IX-3). For simplicity, the coupled H^1-P^{31} system will be termed the "A system" in Sections IX-A and IX-B below and in subsequent chapters.

The effective gyromagnetic ratios in the $B(K^{39})$ rotating frames are affected by magnetic dipolar couplings to the $A(H^1)$ and $C(P^{31})$ nuclei, represented by the hamiltonian terms:

$$\mathcal{H}_{dd}^{AB*}(s) + \mathcal{H}_{dd}^{CB*}(s) \qquad \text{(IX-4)}$$

The appropriate hamiltonian for calculations of B rotating frame eigenlevels is a sum of $\mathcal{H}_{r.f.}^{B*}(s)$ and those parts of Eq. (IX-4) which do not commute with $\mathcal{H}_{r.f.}^{B*}(s)$. As the B r.f. field strength is reduced, the dipolar field interaction will gradually become more important, and ultimately the calculations of γ_{eff} in Chapter V will no longer apply. Static dipolar field components in the B rotating frame are of order 1 gauss in the present case (cfr. f.ex. Tsutsumi[55]). If the B r.f. field component H_{1B} is not much larger than this, the rotating frame transition frequencies will be higher than those computed from Table V-1 in Chapter V, and will not be proportional to H_{1B}.

In this chapter, a detailed knowledge of the K^{39} transitions involved is not necessary, and the transitions will simply be identified by a number, as defined in Chapter X. Also, the center frequency and the crystal orientation relative to the static field H_o are sufficient for identification.

IX-A. Verification of the Thermal Reservoir Model for Double Resonance With Unmodulated B r.f.

As was stressed in Chapter IV, the analysis is only relevant to double resonance applications where the B spin species has high abundance, and yet requires double resonance methods for detection. This applies ideally to K^{39}, which has a natural isotopic abundance of 93.08% and weak quadrupole and Zeeman interactions in the laboratory frame (cfr. data in Chapter X).

Below, the internal consistency of the results in Chapter IV will be tested quantitatively. Theoretical and experimental dependence on specific parameters appearing in the theory will be compared by curve fitting. Data sets of two main types were recorded:

a) The B r.f. irradiation time was varied stepwise through a certain range, typically from 0 to approximately 10 sec, keeping all other parameters constant. This yielded the time variation of the proton energy due to proton and K^{39} spin-lattice relaxation. Curves were obtained for different values of ω_B, ω_{1B}, τ_{1A} and T_{1B}.

b) In another series of measurements, the B r.f. frequency was swept stepwise through the K^{39} line, with all other external parameters kept constant. This was done for different values of ω_{1B} and $t_{B\ r.f.}$, and thus families of characteristic line shapes were obtained.

The experimental procedure is perhaps most easily understood by referring to Fig. III-2, which shows the r.f. pulse requence. In both recording modes mentioned above, the double resonance cycle would typically be repeated at intervals of 120 sec, i.e., 3 to 4 times the proton laboratory frame T_1. This allowed the protons to reach nearly ($\gtrsim$ 95%) equilibrium polarization along the applied field H_o before each cycle. The sweep in ω_B or $t_{B\ r.f.}$ was obtained by varying the relevant parameter in steps from one cycle to the next. A typical cycle would be initiated with proton ADRF, followed after 0.1 sec by a square, unmodulated r.f. pulse at the K^{39} transition frequency. The irradiation time $t_{B\ r.f.}$ was essentially limited by the proton spin-lattice relaxation time after ADRF, since the relaxation gradually destroys the proton signal. Depending on the signal to noise ratio that was required, maximum irradiation times were usually in the range from 8 to 18 seconds. In the recording mode where the duration of the B r.f. field was the parameter being varied, the proton $\pi/4$ sampling pulse was applied at a fixed time t_b for all values of $t_{B\ r.f.}$ in a run, after the $B_{r.f.}$ field had been turned off. (With time origin at the beginning of the $B_{r.f.}$ pulse, one used: $t_b = t_{B\ r.f.}(\text{max}) + 0.1$ sec). In the line shape recording mode, both t_b and $t_{B\ r.f.}$ were constant, with $t_b = t_{B\ r.f.} + 0.1$ sec. Baseline measurements of zero proton signal were usually made at least once before and after each sweep of

either ω_B or $t_{B\ r.f.}$, by the following procedure: During the ADRF-sequence, the spin-lock phase shift and adiabatic turn-off of the B r.f. was omitted, with loss of the ordered dipolar state. As a check, runs were made periodically both with no B r.f. applied and with saturation of the K^{39} system. No residual dipolar order was detected either by this indirect saturation or after direct $\pi/2$ pulse saturation of the proton system. Unit amplitude for the normalized proton signal would then correspond to:

$$1 \equiv \text{(proton signal with no B r.f. - proton signal with disrupted ADRF)}$$

It is convenient to look at data obtained in the two recording modes separately:

IX-A-1. Time Variation of the Proton Energy During Proton-K^{39} Coupling

The proton energy as a function of B r.f. irradiation time was given by the exact expression Eq. (IV-23). Exact in this connection means that no assumptions were made on the relative magnitudes of the parameters involved. Equation (IV- 23) is difficult to interpret directly, however. Since the measurements described in this paragraph were not done in the wings of the line where τ_{AB} is largest, the approximate formula (Eq. (IV- 24)) which requires τ_{AB}/T_{1A}, $\tau_{AB}/T_{1B} \ll 1$ might apply. Below, both exact and approximate formulas have been used for comparison with experimental data, and where the approximate expression proved valid, the data confirmed very well the intuitive picture of the double resonance process which can be based on Eq. (IV-24). To recapitulate, Eq. (IV- 24) predicts that:

Immediately following contact with K^{39} reservoir, the proton reservoir energy drops rapidly towards a value corresponding to thermal equilibrium between the two reservoirs. The equilibration is exponential, with a time constant

$$\tau \cong \tau_{AB}/(1 + \varepsilon)$$

After thermal equilibrium has been established between the two reservoirs, the proton energy will vary exponentially in time, and the normalized proton signal is (cfr. Eq. (IV-25)):

$$S_A = \frac{1+\frac{E_{Bo}}{E_{Ao}}}{1 + \varepsilon} \cdot \exp\left(-\frac{\varepsilon}{1 + \varepsilon}\left(\frac{1}{T_{1B}} - \frac{1}{T_{1A}}\right) t_{B\ r.f.}\right)$$

If the K^{39} reservoir is kept hot by saturation, the normalized proton signal during thermal contact between the reservoirs is expected to vary exponentially as described by Eq. (IV- 21):

$$S_A = \exp\left(-\frac{\varepsilon}{\varepsilon_{AB}} \cdot t_{B\ r.f.}\right)$$

Here, the proton signal decay time is $\tau = \tau_{AB}/\varepsilon$, and the initial slope of the proton signal decay curve is steeper than in the case with no B r.f. phase shifting.

A large amount of experimental data has been obtained which verifies quantitatively the behavior described above. Statistically significant deviations from the theory were not observed. Some typical experimental data are presented in the figures below, where solid lines correspond to best fit theoretical curves (Eq. (IV-24)). Experimental conditions were adjusted so that parameters in the theory were varied in different ways:

$\omega_B = \omega_{Bo}$. Sample temperature constant. ω_{1B} (i.e. B r.f. field strength) varied .

The results are shown on Fig. IX-1. Two B r.f. power levels were used: $\omega_{1B}/2\pi = (4.35\pm0.05)$kHz and $\omega_{1B}/2\pi = (7.2\pm0.2)$kHz. The curves clearly have the expected qualitative behavior, with an initial rapid decay of the proton signal due to thermal equilibration between the proton and K^{39} reservoirs, followed by an exponential decay (straight line in the logarithmic graph) due to spin-lattice relaxation heating of the coupled reservoirs.

By fitting with the expression (Eq. (IV-24)), one can construct the two theoretical curves shown in the figure. The parameter values used are shown beside each curve. The T_{1B} values were determined by using the value $T_{1B} = 14.7$ sec obtained from a separate measurement. As a quick check on the internal consistency of these results, one can form the ratios of the squared rotating frame transition frequencies and of the heat capacity ratios:

$$\left(\frac{4.35\ \text{kHz}}{7.2\ \text{kHz}}\right)^2 = 0.36\pm0.02\ ;\ \frac{\varepsilon(4.35\ \text{kHz})}{\varepsilon(7.2\ \text{kHz})} = 0.365\pm0.09$$

According to Eq. (IV -19) the ratios should be equal, which they certainly are within the experimental errors. The error limits on the ε's are the same as were obtained in the approximate treatment below. $\Delta\omega_{1B}/2\pi \simeq 0.15$ kHz.

Least squares fitting of the same data with the approximate expression (Eq. (IV- 25)) yields:

$\omega_{1B}/2\pi = 4.35$ kHz : $\varepsilon(4.35\ \text{kHz}) = (0.29\pm0.05)$; $T_{1B} = (3.9\pm0.6)$ sec

$\omega_{1B}/2\pi = 7.2$ kHz : $\varepsilon(7.2\ \text{kHz}) = (0.61\pm0.10)$; $T_{1B} = (3.7\pm0.7)$ sec

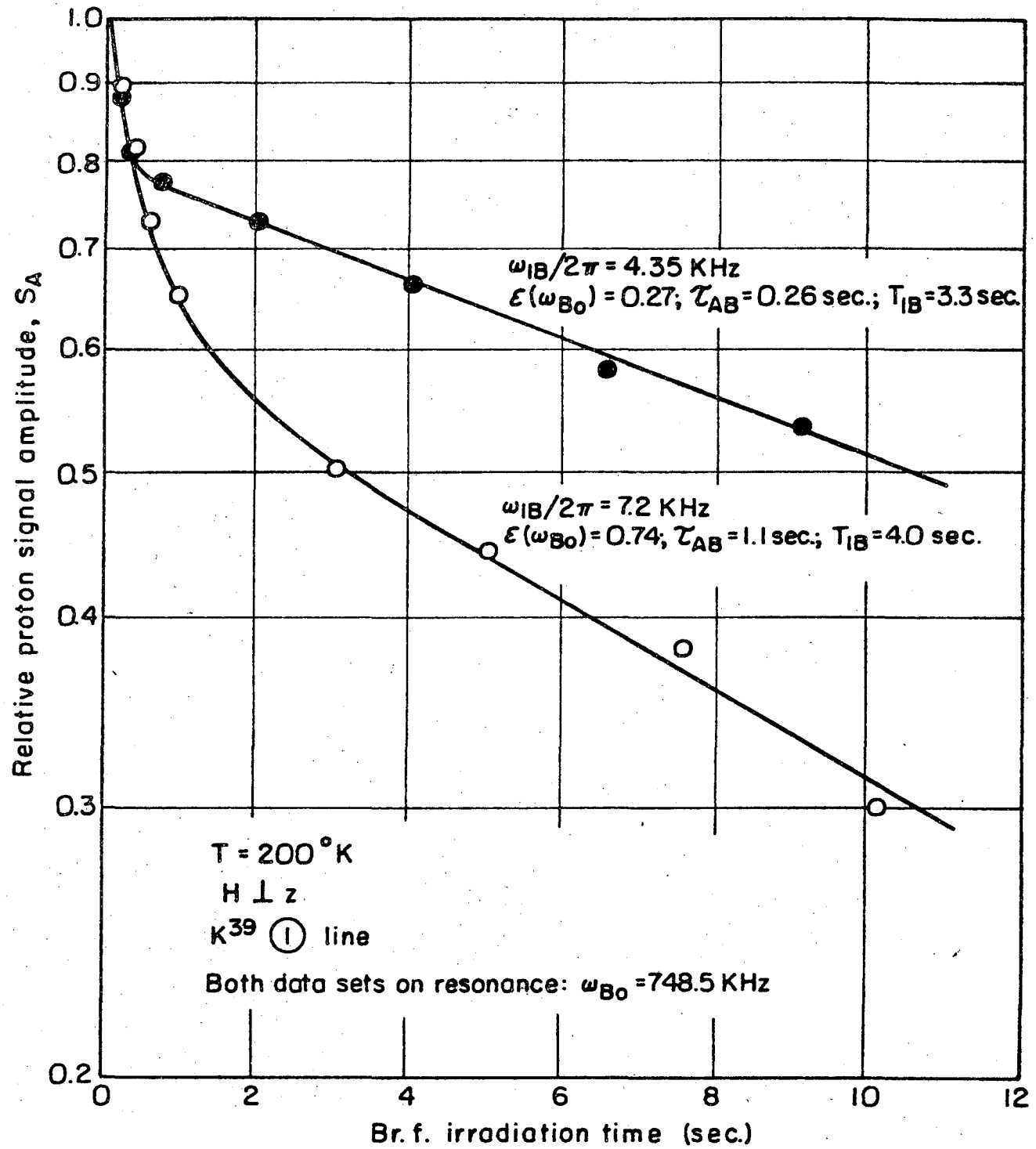

XBL732-5705

Fig. IX-1. Double resonance with unmodulated B r.f. at two different B r.f. field strengths. Curves were computed from Eq. (IV-24), with parameter values as shown in the figure and with T_{1A}=14.7 sec E_{Bo}=0.

With the observed error limits, the expression (Eq. (V-24)) must be used to obtain a correct ε-value for the 7.2 kHz curve, while Eq. (IV-25) is sufficiently accurate for analysis of the 4.35 kHz curve. This is not surprising, since the approximation error is expected to increase with ε. If data precision were increased substantially, f.ex. by data accumulation, the exact expression should also be used in analyzing the 4.35 kHz curve.

Figure IX-2 shows how the proton signal decays when the K^{39} reservoir is kept hot by phase shifting the B r.f. field by π once every millisecond. Curves are shown corresponding to the two B r.f. power levels $\omega_{1B}/2\pi$ = 1.28 kHz and 7.2 kHz. The decay is clearly exponential. Using ε-values obtained from separate measurements and assuming that Eq. (IV-21) holds, i.e., $\tau_{AB} = \tau \cdot \varepsilon$, one obtains

$$\text{Curve A:} \quad \tau_{AB}(1.28 \text{ kHz}) = (0.10 \pm 0.03) \text{ sec}$$

$$\text{Curve B:} \quad \tau_{AB}(7.2 \text{ kHz}) = (1.0 \pm 0.2) \text{ sec}$$

Thus τ_{AB} increases with ω_{1B}, as anticipated in Section IV-B. According to Eq. (IV -24), the cross relaxation terms in the expression for the proton energy can be obtained by subtracting the spin-lattice relaxation term (straight line in Fig. IX-1) from the experimental data. This was done for the 7.1 kHz curve in Fig. IX-1 , which due to the slow cross relaxation is best suited for analysis. Normalizing the difference to one at $t_{B\ r.f.} = 0$, curve C on Fig. IX-2 was obtained. Assuming an exponential time constant $\tau = \tau_{AB}/(1 + \varepsilon)$, one finds:

$$\text{Curve C:} \quad \tau_{AB}(7.2 \text{ kHz}) = (1.1 \pm 0.3) \text{ sec}$$

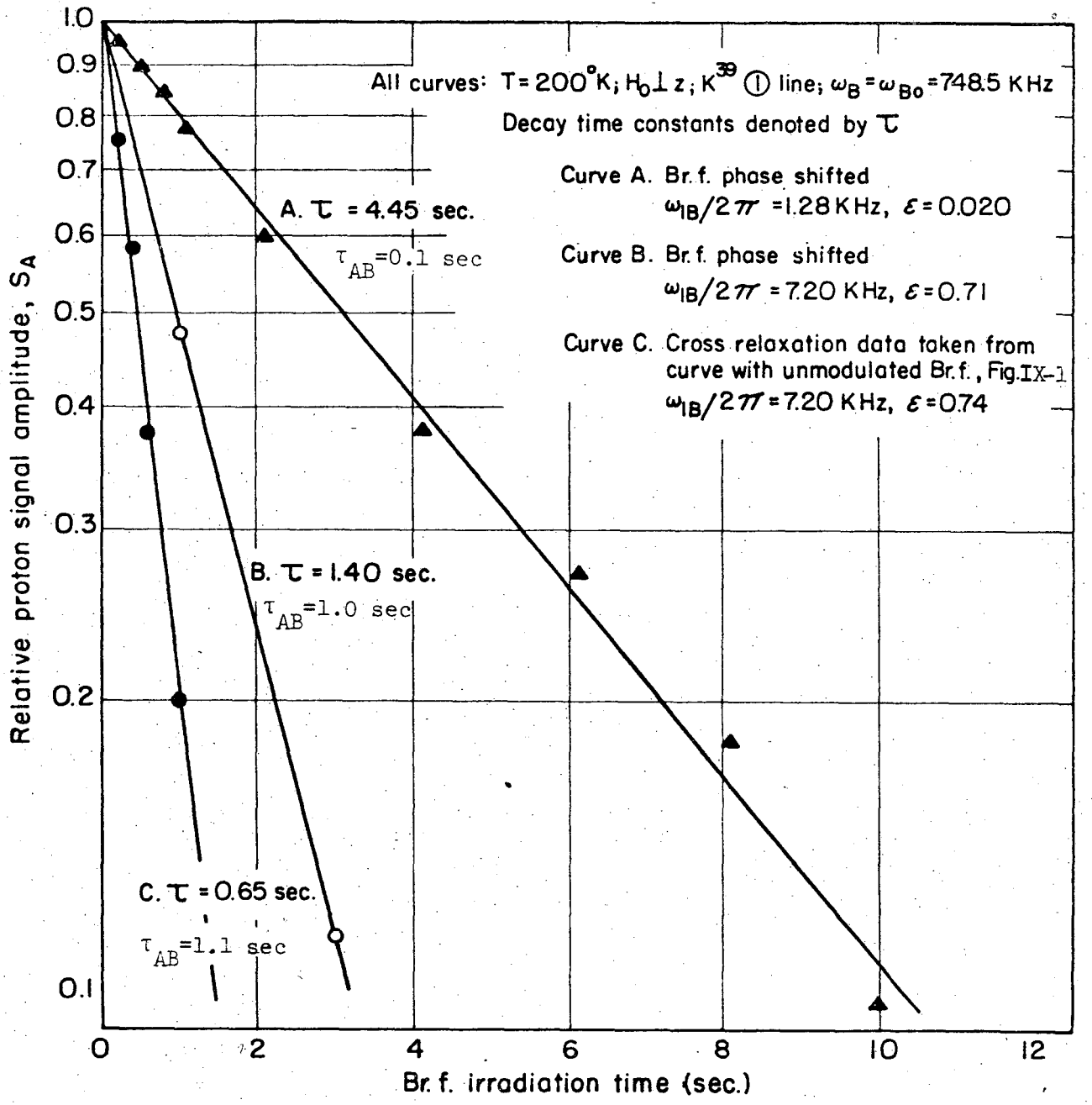

XBL 732-5706

Fig. IX-2. Measurement of A-B reservoir cross-relaxation rates at 2 B r.f. power levels. Curves A and B: Phase shifted B r.f. Curve C: Computed from A-B thermal equilibration transient on 7.2 kHz curve, Fig. IX-1.

Due to the uncertainty in the data used for constructing curve C, this result can only serve as a rough check on the theory. Also, Eq. (IV- 24) is based on the approximation $\tau_{AB} \ll T_{1A}, T_{1B}$. For the 7.2 kHz curve,

$$\tau_{AB}/T_{1A} < \tau_{AB}/T_{1B} \simeq 0.20$$

which in relation to the criterion above represents one of the worst cases in the work reported here.

It is interesting to note in this connection that a best fit of expression (Eq. (IV-24)) to the 7.2 kHz data in Fig. IX-1 yields $\tau_{AB} = (1.0 \pm 0.1)$ sec. Thus, one can conclude that the three methods used in determining τ_{AB} for the 7.2 kHz case yield mutually consistent results.

ω_{1B} constant. Sample temperature constant. ω_B varied.

In Fig. IX-3, two curves are shown which were recorded at the same temperature and with the same B r.f. field strength. One was obtained with the B r.f. 2 kHz below, the other 5 kHz above the line center frequency $\omega_{Bo}/2\pi = 1331$ kHz: $\omega_B/2\pi = 1329$ kHz and 1336 kHz.

The curves look different in several respects. The initial thermal equilibration is obviously slower for the 1336 kHz curve, which is farthest from resonance. This is expected due to the larger ω_{eB} and the smaller value of $(\sin \theta)^{-2}$, where θ is the $\bar{H}_{eB}$ tilt angle in the rotating frame, cfr. Eq. (IV- 18). As before, the curve with the larger ω_{eB}, i.e., the 1336 kHz curve, has the steepest slope in the

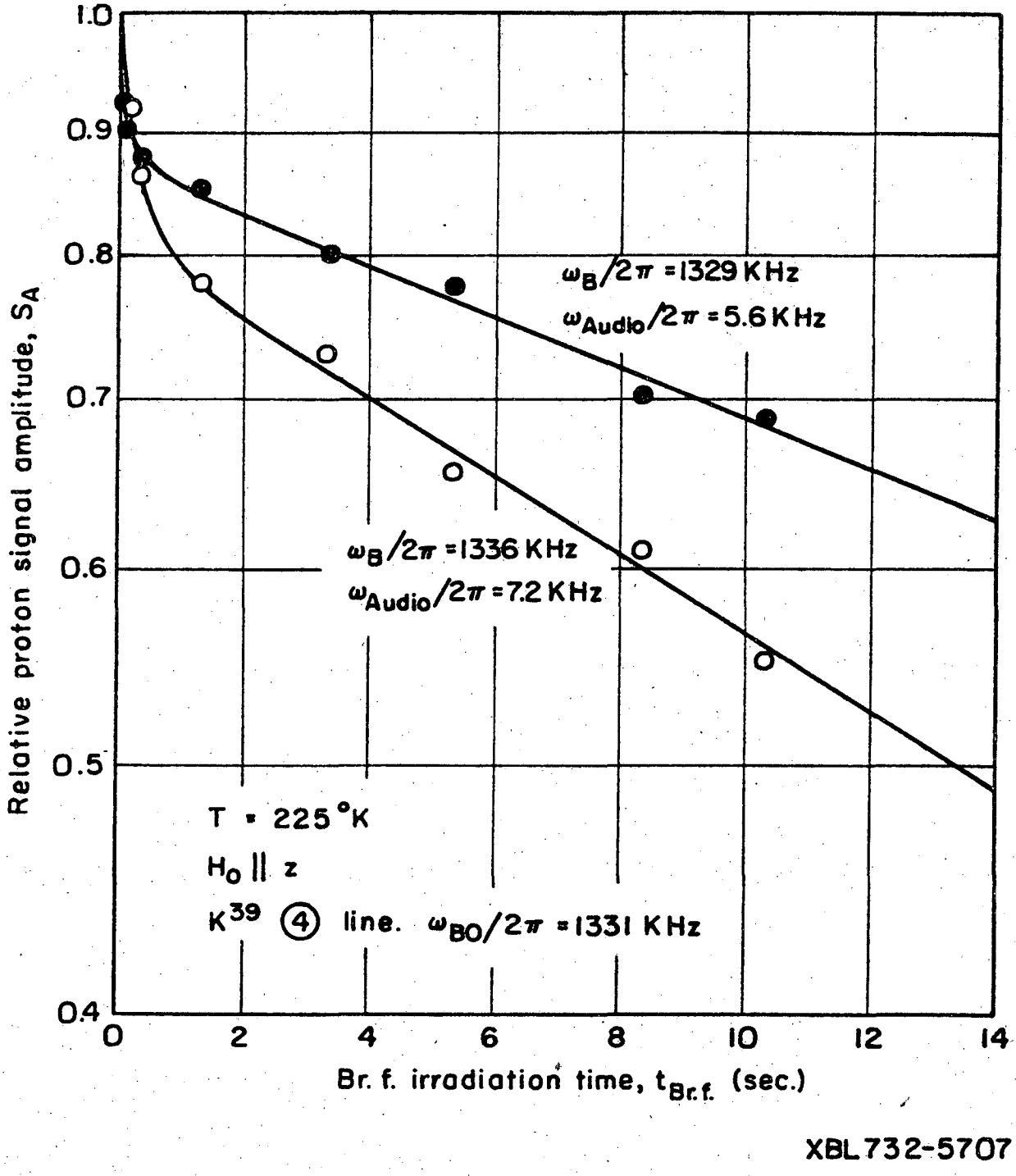

XBL732-5707

Fig. IX-3. K^{39} double resonance with unmodulated B r.f. and at different degrees of resonance. Curves show best fit of Eq. (IV-24) with:

$\omega_B/2\pi$=1329 kHz , ε=0.16 , $(1/T_{1B}-1/T_{1A})$=0.17 sec^{-1} , τ_{AB}=0.20 sec

$\omega_B/2\pi$=1336 kHz , ε=0.25 , $(1/T_{1B}-1/T_{1A})$=0.19 sec^{-1} , τ_{AB}=0.25 sec

$t_{B\ r.f.} \gg \frac{\tau_{AB}}{1+\varepsilon}$ regime, reflecting the larger K^{39} reservoir heat capacity. Extrapolation to $t_{B\ r.f.} = 0$ yields

$$\frac{\varepsilon(1329\ \text{kHz})}{\varepsilon(1336\ \text{kHz})} = \frac{0.149}{0.235} = 0.64$$

According to Eq. (IV-19) this ratio should be the same as the squared ratio between the ω_{eB}'s. On resonance ($\omega_B = \omega_{Bo}$) one found by audio resonance: $\omega_{1B}/2\pi = 5.2$ kHz. Using $\omega_{eB}^2 = \omega_{1B}^2 + (\Delta\omega_B)^2$, one has

$$\left(\frac{\omega_{eB}(1329\ \text{kHz})}{\omega_{eB}(1336\ \text{kHz})}\right)^2 = \left(\frac{5.6\ \text{kHz}}{7.2\ \text{kHz}}\right)^2 = 0.60$$

which agrees well with the value 0.64 above.

The K^{39} spin-lattice relaxation time is readily determined from the two curves. With $T_{1A} = 14.5$ sec determined by an independent measurement, one finds by Eq. (IV-B-8):

$\omega_B/2\pi = 1329$ kHz: $(1/T_{1B} - 1/T_{1A}) = 0.180$; $T_{1B} = 4.0$ sec

$\omega_B/2\pi = 1336$ kHz: $(1/T_{1B} - 1/T_{1A}) = 0.187$; $T_{1B} = 3.9$ sec

The data derived from Fig. IX-3 for the crystal orientation $H_o \| z$ and for the K^{39} ④ transition are of course not immediately comparable with the other results obtained in this section for the case $H_o \| z$ and K^{39} ① transition.

$\omega_B = \omega_{Bo}$. $\omega_{eB} = \omega_{1B}$ = const. Sample temperature, i.e. $\left(\frac{1}{T_{1B}} - \frac{1}{T_{1A}}\right)$ varied.

If one assumes that the theory developed in Chapter IV is valid, then data to be presented in Chapter X shows that $T_1(K^{39})$ varies over a wide range as the sample temperature is brought from room temperature to below the Curie temperature T_c = 123°K. By comparison with the proton relaxation results in Chapter VII, it becomes clear that one can make $\left(\frac{1}{T_{1B}} - \frac{1}{T_{1A}}\right) \gtrless 0$ by adjusting the sample temperature. According to Eq. (IV- 25), the proton energy during double resonance with unmodulated B r.f. should vary as $\exp\left(-\frac{\varepsilon}{1+\varepsilon}\left(\frac{1}{T_{1B}} - \frac{1}{T_{1A}}\right)t_{B\ r.f.}\right)$ for $t_{B\ r.f.} \gg \tau_{AB}/(1+\varepsilon)$. This behavior is borne out quite clearly in Fig. IX-4, where data recorded on the K^{39} ① -line at different temperatures are presented. The data obtained at the lowest temperature T = 99°K are especially striking. There $T_{1B} > T_{1A}$, and the proton signal <u>increases</u> after thermal equilibration between the two reservoirs has been achieved. In this low temperature range, the slopes are very shallow. This is partly due to the small spin-lattice relaxation rates, but also to the near-equal values of T_{1A} and T_{1B}. Curve B in the figure has zero slope, and one therefore immediately knows that $T_{1B} = T_{1A}$. As will be shown in Section IX-B, this feature can be used to advantage in certain cases.

IX-A-2. <u>Double Resonance Lineshape</u>

The two approximate expressions (Eqs. (IV-24) and IV-25)) should also describe the double resonance lineshape, since the lineshape recording mode only corresponds to a different choice of parameters being varied. In order to compare with theoretical lineshapes, two sets of experimental double resonance lines are shown in the following.

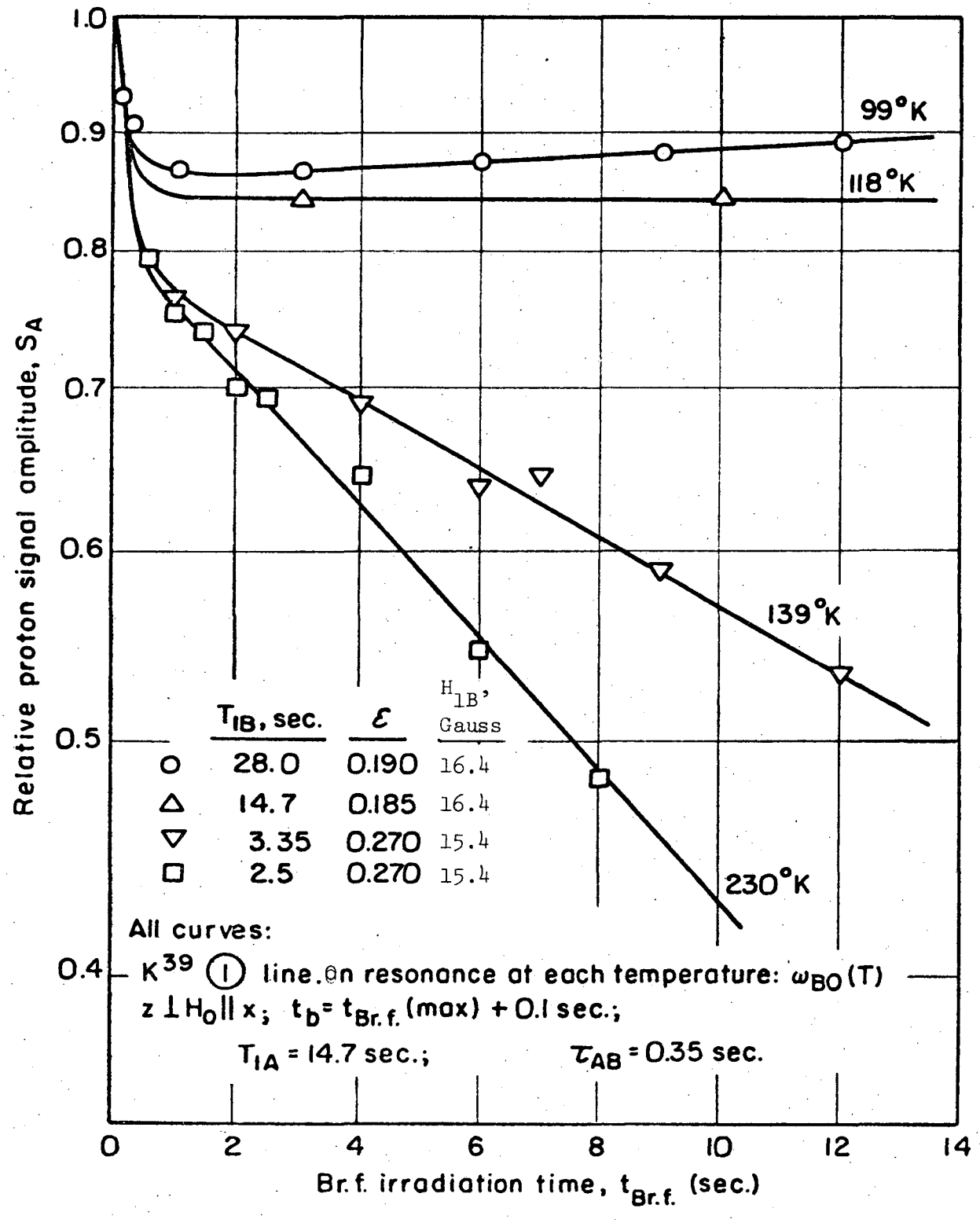

Fig. IX-4. K^{39} double resonance with unmodulated B r.f., at four different sample temperatures. The curves were computed from Eq. (IV-24) with parameter values as shown in the figure.

In one set, four lines were recorded with different values of the B r.f. field strength ω_{1B}/γ_{eff}, but with $t_{B\ r.f.}$ constant. In the other set, four lines were recorded with different $t_{B\ r.f.}$ but the same ω_{1B}/γ_{eff}.

$t_{B\ r.f.}$ constant, ω_{1B} varied.

It is of interest to check lineshapes predicted by both the approximate and exact expressions (Eqs. (IV- 25) and (IV-23)). The same set of experimental data was used in both cases, and the results are shown on Fig. IX-5. By inspection, it is immediately clear that several of the salient features of the lines are as predicted by the theory: The lines have a double minimum with the on-resonance maximum depressed more and more as the B r.f. field strength, i.e., the B reservoir heat capacity, is increased. The curvature of the line at $\omega_B = \omega_{Bo}$ decreases as the B r.f. field strength is increased, reflecting the reduced sensitivity to the off-resonance field $\frac{\Delta\omega_B}{\gamma_{eff}}$ in the rotating frame as H_{1B} increases. The line depth is slightly larger on the high-frequency side of $\omega_{B\phi}$, corresponding to the large initial B reservoir energy (negative spin temperatures) when the B r.f. pulse is turned on suddenly.

First, the quantitative analysis will be done for the approximate expression (Eq. (IV- 25)). Since the approximation is better, the shorter τ_{AB}, the approximate lineshapes should give the best fit to experimental data close to the line center. This is borne out clearly in Fig. IX-5, where the broken line curves were obtained from Eq. (IV- 25) by plugging in appropriate values for ε, T_{1A}, T_{1B}, E_{Bo} and $t_{B\ r.f.}$ at each frequency ω_B, cfr. Eq. (IV-26). The parameter values used are listed in Table IX.1.

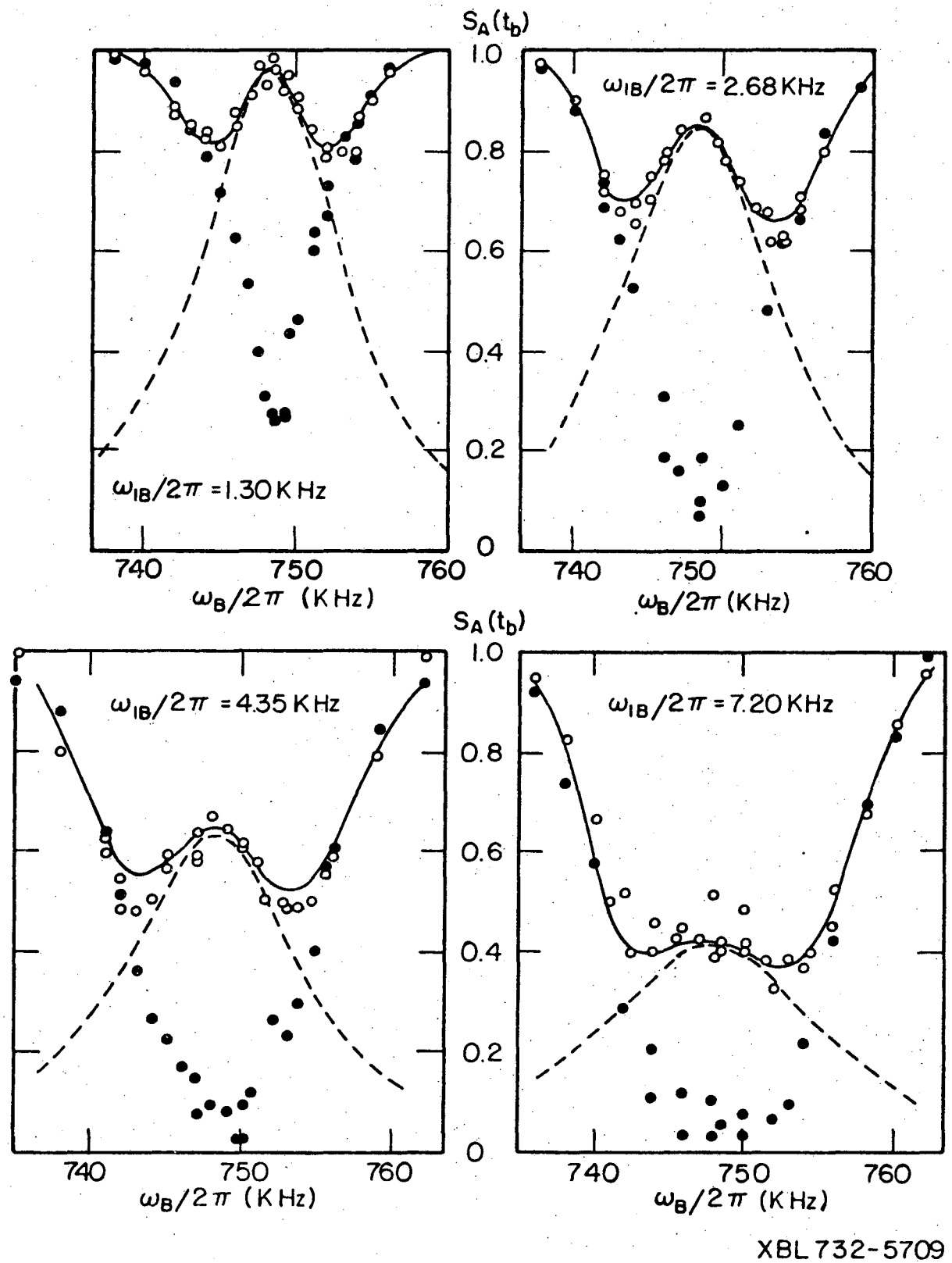

Fig. IX-5. Double resonance lineshapes at different B r.f. field strengths. Dots/open circles represent data obtained with/without B r.f. phase shifting. Theoretical curves computed from Eq. (IV-23) and Eq. (IV-25) are drawn with full and dashed lines, respectively. Curve parameters are given in Tables IX.1 and IX.2.

Table IX.1. Parameter sets used in computing theoretical lineshapes by the approximate formula (Eq. (IV- 25)). Curves drawn with broken lines in Fig. IX-5.

$\omega_{1B}/2\pi$ [kHz]	$\varepsilon(\omega_{Bo})$	T_{1A} [sec]	T_{1B} [sec]	Asymmetry Const. $C_{A\,symm.}$ [rad^{-1} sec]
1.30	0.022	14.7	3.3	0.0015
2.68	0.095	14.7	3.7	0.0015
4.35	0.250	14.7	3.3	0.0015
7.20	0.685	14.7	4.1	0.0015

Here, $t_{B\ r.f.}$ was measured directly, and T_{1A} was found by a standard proton relaxation time measurement after ADRF. ε was determined from on-resonance curves like those on Fig. IX-1, using Eq. (IV- 25). In order to test the theory as severely as possible, the ε-values at all frequencies and for all four curves were computed from a single measurement of the on-resonance $\varepsilon(\omega_{Bo})$ at $\omega_{Audio}/2\pi = 4.35$ kHz. In each curve, the off-resonance values of ε were related to the on-resonance one by Eq. (IV- 19). T_{1B} was measured separately for each line from proton signal decay curves like those on Fig. IX-1, and was taken as constant throughout each line. The assumption of a constant T_{1B} is partly justified below by the measured small dependence on ε within the appropriate ε-ranges.

The asymmetry constant $C_{Asymm.}$ deserves a closer description. The frequency dependence of the initial B system rotating frame energy E_{Bo} is derived in Appendix B, and was indicated by

$$E_{Bo} = K \cdot \Delta\omega_B$$

in Section IV-B. With

$$E_{Ao} \exp(-t_b/T_{1A}) \equiv 1 \quad ,$$

the relevant parameter describing the degree of lineshape asymmetry in both the exact and approximate expressions (Eqs. (IV-23) and (IV-26)) becomes

$$C_{Asymm.} \equiv \frac{E_{Bo}}{E_{Ao}} \frac{1}{\Delta\omega_B} = \frac{K}{E_{Ao}}$$

Explicit expressions for E_{Bo} and E_{Ao} are obtained from Eq. (B-9) in Appendix B and from Eq. (II-4). Since the temperature in question here is the lattice temperature, the high temperature approximation can be used:

$$C_{Asymm.} = \frac{N_B \hbar \Delta\omega_B (E_4 - E_1)}{4kT} \cdot \frac{3kT}{N_A I(I+1) \hbar \gamma_A^2 H_o H_{LA}} \cdot \frac{1}{\Delta\omega_B}$$

All quantities appearing in this expression were defined in connection with Eq. (B-9) and Eq. (II-4). In the present case, one has I = 1/2, and one may write:

$$C_{Asymm.} = \frac{N_B}{N_A} \frac{\omega_{Bo}}{\omega_L \omega_{LA}}$$

where

$N_B/N_A = 0.93/2 = 0.47$ (K^{39}/proton abundances)

$\omega_{Bo} = (E_4-E_1)/\hbar = 748$ kHz (line center frequency K^{39} ①)

$\omega_L = \gamma_A H_o = 11$ MHz (proton Larmour frequency)

$\omega_{LA} = \gamma_A H_{LA} = 3.2$ kHz (proton Larmour frequency in local dipolar field $H_{LA} = 0.73$ G).

With these values one obtains

$$C_{Asymm.} = 0.0015 \text{ (rad sec}^{-1})^{-1} \quad .$$

This may be compared with computer best fits to the experimental curves which yielded values in the range

$$0.0010 \text{ (rad sec}^{-1})^{-1} \lesssim C_{Asymm.} \lesssim 0.0016 \text{ (rad sec}^{-1})^{-1}$$

One may now return to the broken curves in Fig. IX-5. For the lines with low B r.f. power, the agreement between experimental data and theoretical curves is very good in the frequency region about ω_{Bo}, and significant errors only start to develop as the lineshape minima on either side of ω_{Bo} are approached. At the highest B r.f. power level, τ_{AB} is larger and the agreement is poorer. It is interesting to note that the theoretical curves generally lie below the experimental ones. This is expected, since the theoretical curves do not include the off-resonance increase in τ_{AB}, which gives a bottleneck effect in the depletion of the proton signal.

Lineshapes generated from the exact expression (Eq. (IV- 23)) are shown in Fig. IX-5 (full drawn lines). The same experimental data were used as above, with the addition of data points obtained with phase shifted B r.f. The curve fitting was done by the procedure outlined in Section IV-C. ε and T_{1B} at $\omega_B = \omega_{Bo}$ were determined by the exact expression (Eq. (IV- 23)), and $\tau_{AB}(\omega_B)$ was determined from computed values of $\varepsilon(\omega_B)$ and the lineshape data obtained with phase shifted B r.f. The parameter sets are given in the Table IX-2:

Table IX.2 . Parameter sets used in computing theoretical lineshapes by the exact formula (Eq. (IV- 23)). Curves drawn with full lines in Fig. IX-5.

$\omega_{1B}/2\pi$ [kHz]	$\varepsilon(\omega_{Bo})$	T_{1A} [sec]	T_{1B} [sec]	Asymmetry Const. $C_{Asymm.}$ [rad^{-1} sec]
1.30	0.024	14.7	3.3	0.0015
2.68	0.102	14.7	3.7	0.0015
4.35	0.270	14.7	3.3	0.0015
7.20	0.740	14.7	4.0	0.0015

For each curve there is good agreement in the regions around the line center and in the wings of the line. In the regions about the line minima, the theoretical curves tend to lie too high. One possible explanation for the discrepancy is that the cross coupling times $\tau_{AB}(\omega_B)$ used for computing the theoretical curves were too long: Around the line center and the wings of the line the lineshape is almost insensitive to variations in τ_{AB}. At the line center this is because τ_{AB} there has its minimum value, and also $t_{B\ r.f.}$ was chosen so long that the thermal equilibration transient had died out. In the wings of the line the B reservoir energy is only perturbed very little by the slow A-B energy exchange. Consequently, errors in the determination of τ_{AB} would show up mainly in the regions where discrepancies were observed in Fig. IX-5.

The method of determining τ_{AB} used here is convenient and fits smoothly into the theoretical framework that was built up in Chapter IV, but it is vulnerable to systematic errors. Two effects will be mentioned in particular, both of which lead to too long τ_{AB}-values. First, there is the effective reduction of the B r.f. amplitude during phase shifting. During each phase cycle, the B r.f. power envelope went from zero to a maximum and back to zero again. As described in Chapter XI, the turn-on and turn-off was made smoothly in order to avoid sidebands, and as a consequence the mean B r.f. field strength was roughly 3% lower during phase shifting. The power reduction was monitored on a VTVM in each case, and the curves in Fig. IX-5 obtained with phase shifted B r.f. have been corrected for this by a slightly increased depth. Instead of trying to do the correction analytically on the basis of Eq. (IV-18) which requires

knowledge of $J(\omega_{eB})$ that is not available in the present case, the slight correction was made by interpolation and extrapolation of data obtained from the phase shifted lines in Fig. IX-5 at each ω_B. For each line the VTVM power readings with and without phase shifting of the B r.f. were used. The second source of systematic errors in τ_{AB} is that the B r.f. phase shifting may not have kept the B reservoir at an infinite temperature. The phase shifting method was described in Section III-B, where one assumed idealized conditions (instantaneous phase shift by exactly π radians, etc). Unfortunately, it is difficult to make even a very rough assessment of the degree of saturation attained in the current experiment. The results above do establish that each phase cycle was much less than all τ_{AB}'s in question, and thus lowering of the B reservoir temperature by cross relaxation cooling should be negligible. Information on the K^{39} T_2 in the rotating frame is lacking, however, and one can therefore not rule out possible phase coherence effects. The details of the phase shifted B r.f. wave, f.ex. with respect to harmonic content and the phase behavior during each phase cycle, are not accurately known. In addition to this there are uncertain points regarding the saturation efficiency for different values of ω_B off resonance.

ω_{1B} constant; $t_{B\ r.f.}$ varied.

As was shown above, the approximate formula (Eq. (IV-25)) gives a good qualitative description of the center ridge in the double resonance line obtained with unmodulated B r.f. It can be written

$$S_A(\omega_B, t_{B\ r.f.}) = S_{Ao} \cdot f_1(\omega_B) \exp(-f_2(\omega_B) \cdot t_{B\ r.f.})$$

where $f_1(\omega_B)$ and $f_2(\omega_B)$ are defined by Eq. (IV-25). If $t_{B\ r.f.} \rightarrow t_{B\ r.f.} + \Delta$, one has

$$S_A(\omega_B, t_{B\ r.f.} + \Delta) = S_A(\omega_B, t_{B\ r.f.}) \exp(-f_2(\omega_B) \cdot \Delta)$$

Since $f_2(\omega_B)$ is a positive, monotonously increasing function in ω_B, an increase in $t_{B\ r.f.}$ tends to decrease the overall signal level and thus ultimately the curvature of the center ridge in the line. On the other hand, as Δ increases, the off-resonance signal is reduced relatively more than the on-resonance one. The net effect is that the central ridge in the line remains quite pronounced even for long $t_{B\ r.f.}$ where the depletion of the proton signal is large. This behavior was indeed verified experimentally, as shown on Fig. IX-6. The qualitative difference in saturation behavior from the case where the B r.f. field strength was varied, is quite clear.

IX-A-3. Conclusion

For the case of K^{39} in KDP, and for a wide range of experimental conditions, excellent agreement has been found between the thermal reservoir theory developed in Chapter IV and experiment. As discussed in Section IV-C, comparison involves no adjustable parameters, since all parameters are uniquely determined from experimental data. On the basis of this, one can conclude that the theory applies to K^{39} in KDP within the range of experimental parameters that appear in the analysis above, at the very least. Experimental data have been obtained, moreover, indicating that the theory applies to other lines and field configurations

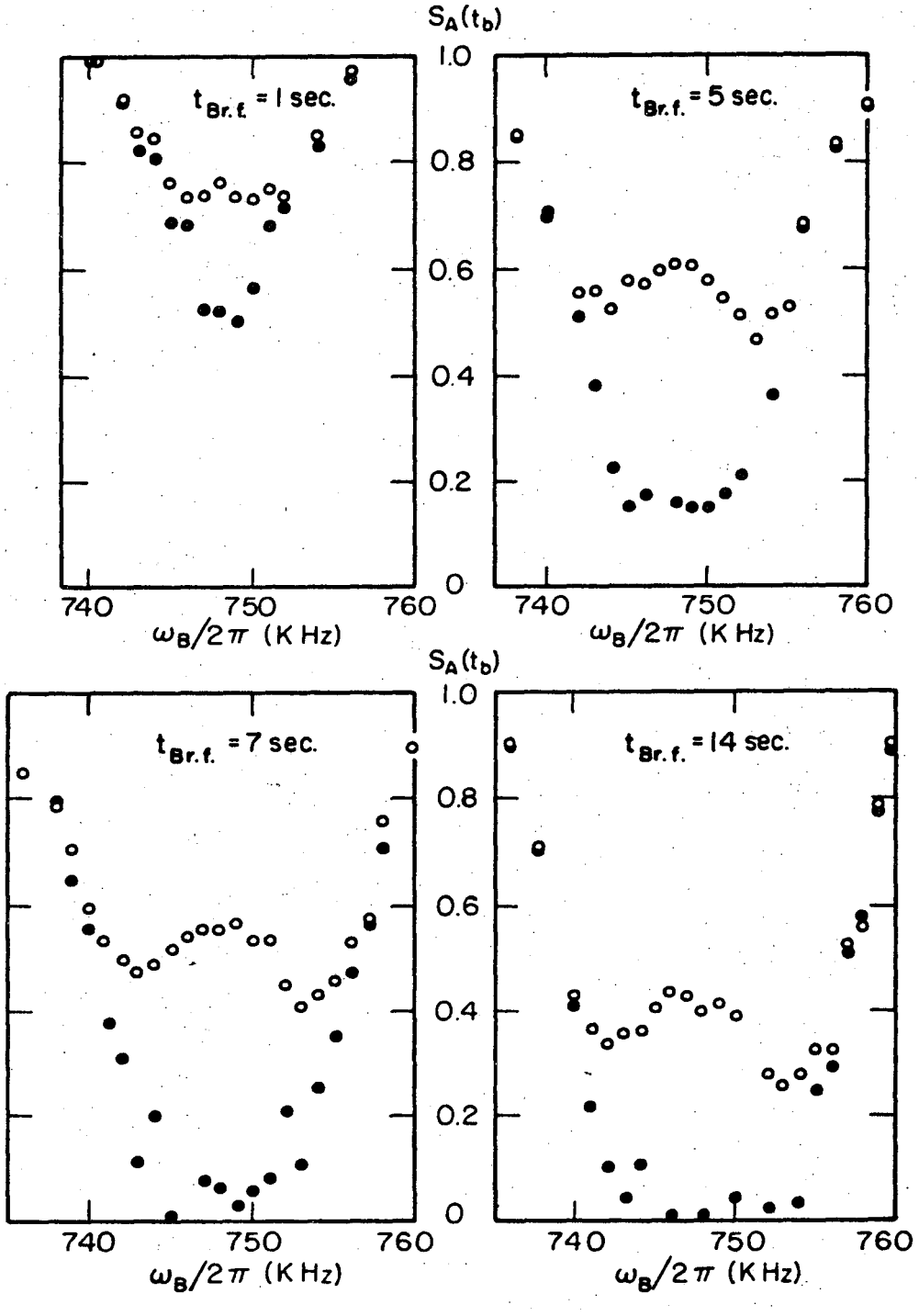

Fig. IX-6. Double resonance lineshapes with unmodulated B r.f. showing dependence on the B r.f. irradiation time $t_{B\ r.f.}$.
All Curves: K^{39} ① line , $H_o \perp Z$, T = 200°K
$\omega_{1B}/2\pi$ = 4.5 kHz , ω_{Bo} = 748 kHz , t_b = 14.1 sec
Dots/Open Circles: Phase shifted B r.f./Not phase shifted B r.f.

as well. Also, the derivation of the theory was quite general, and one can expect that the results should apply equally well to other nuclear species and other substances. The amount of experimental evidence obtained so far thus adds another element to the mass of evidence supporting the thermal reservoir model for double resonance in general.

The simplified expressions derived in Chapter IV were shown to approximate the experimental data with the expected degree of precision. Experimentally, parameter sets were encountered above where the approximate theory introduced errors into ϵ that were comparable to the experimental errors. For high-accuracy measurements, therefore, the exact version of the theory must be used unless the ratio of the cross-coupling times τ_{AB} to T_{1A} and T_B are much smaller than in the case above. The approximate expressions are valuable in making quick estimates of ϵ and T_{1B}, however. Also, the approximate expressions provide intuitive understanding of experimental results like those presented above, and of how the parameters in the theory influence those results.

IX-B. Measurements of Effective Gyromagnetic Ratios in the K^{39} Rotating Frame

IX-B-1. Introduction

K^{39} in KDP is well suited for testing the results in Chapter V, since Zeeman and quadrupole interactions which define the laboratory frame eigenlevels are of comparable magnitudes and yield a wide range of transition frequencies ν_{Bo} in the laboratory frame. As will be shown in Section X-A, the K^{39} quadrupole coupling constant in KDP is a function of temperature, and it is therefore possible to vary λ, defined by:

$$\lambda = \frac{e^2qQ/2I(2I-1)}{\gamma_{LAB}H_o}$$

without altering the static magnetic field strength H_o. Thus the dependence of γ_{eff} on λ can be measured without the need to retune the A system at each value of λ. Finally, K^{39} yields a strong double resonance signal, and the rotating frame transition frequencies can easily be determined by audio saturation double resonance, as described in Chapter III.

IX-B-2. Experimental Results and Discussion

A single crystal KDP sample was used (the "standard sample" described in Chapter VII). The field configuration was as assumed in the calculations in Chapter V, with the crystallographic **x**-axis parallel to the static magnetic field H_o and the audio field vector direction, and the z-axis parallel to the axis of the B r.f. coil.

Measurements of γ_{eff} were made by ADRF double resonance, with protons as A spins and K^{39} as B spins. The results reported here were all obtained with the B r.f. exactly on resonance for each K^{39} transition, and with proton Larmour frequency equal to 11 MHz. The magnitude of the B r.f. rotating field component H_{1B} was determined by measuring the RMS voltage across the B coil and using calibration data from audio resonance on Ca^{43} in a CaF_2 sample, cfr. Chapter VI. With a rotating frame transition frequency ν_{Audio} measured by audio resonance, the experimentally determined γ_{eff} then is by definition:

$$\gamma_{eff} = \frac{\nu_{Audio}}{H_{1B}} \qquad \text{(IX-5)}$$

Two series of measurements on γ_{eff} will be described: a) At a fixed temperature, the γ_{eff} corresponding to all observable K^{39} laboratory frame transitions were determined. b) For a specific transition, γ_{eff} was measured as a function of temperature (i.e., as a function of λ).

a. Fixed Temperature, Different Transitions

The experimentally determined values of $\gamma_{eff}/\gamma_{LAB}$ at T = 158°K are shown in Table IX.3 (γ_{LAB} = 0.1987 MHz/k gauss). Also listed are theoretical values computed from the expressions in Table V.3. γ_{eff} for forbidden transitions have been set equal to zero, cfr. the discussion in Section V-A. The transition numbering was defined in Section V-A.

Table IX.3. Effective gyromagnetic ratios in the K^{39} rotating frame (θ_x = 90°, λ = 0.513, T = 158°K.

Transition Number	ν_{Bo} [KHz]	ν_{Audio} [KHz]	H_{1B} [Gauss]	$(\gamma_{eff}/\gamma_{LAB})$ Experimental	Theoretical
1	742	4.40	15.7	1.41 ± 0.08	1.462 ± 0.007
2	838	3.70	14.7	1.26 ± 0.07	1.294 ± 0.005
3	1580	Not Observed		0	0
4	190	Uncertain			2.483 ± 0.006
5	932	Not Observed		0	0
6	1770	0.5	9.5	0.26 ± 0.13	0.146 ± 0.002

The agreement between theory and experiment is very good, with the possible exception of γ_{eff} at transition 4. Indicated error limits in the experimental γ_{eff} reflect an estimated 4% error in H_{1B} (VTVM-reading and calibration data), and individually determined measurement uncertainties in ν_{Audio}. Relative errors in ν_{Audio} were large at low frequencies, due to linewidths up to approximately 1 kHz. Sources of error in the theoretically determined γ_{eff} stem from measurements of sample temperatures:

$$\frac{1}{\lambda}\frac{d\lambda}{dT}\Delta T \simeq 1 \cdot 10^{-3} \quad \text{at} \quad \lambda = 0.513,\ \Delta T = 2^{\circ}K$$

and K^{39} laboratory frame transition frequencies ν_{Bo}

$$\frac{1}{\lambda}\frac{d\lambda}{d\nu}\Delta\nu \simeq 2 \cdot 10^{-3} \quad \text{at} \quad \lambda = 0.513\ ,\ \Delta\nu = 1\ \text{kHz}$$

Possible error due to sample misalignment has been neglected, since discrepancies between all observed and theoretically computed ν_{Bo} were less than 0.6 kHz, and thus $\lesssim$ measurement errors. In connection with the data in Table IX.3, one may note specifically:

Transitions 3 and 5 are forbidden (cfr. Section V-A) in the present field configuration. A slight misalignment causes sufficient admixture of states for the transitions to be observed, however, and weak lines at the 3 and 5 transition frequencies were observed on several occasions. The data in Table IX.3 were obtained with a z-rotation sample, and while the 3 transition was not detected, a weak line at the 5 transition frequency was observed at certain z-rotation angles. In order to check that the line was observed due to sample misalignment, the line depth was monitored during a full 2π rotation of the sample about an axis $\perp H_o$. If the crystallographic z-axis did not coincide with the rotation axis, there should be two angles of rotation, separated by π, where $z \perp H_o$, yielding zero line intersity. This was indeed observed experimentally. As shown in Section V-A, a direct proportionality exists between the matrix elements of the B r.f. hamiltonian between B spin laboratory frame eigenstates, and effective gyromagnetic ratios in the corresponding rotating frames. Forbidden transitions are thus represented by $\gamma_{eff} = 0$. It is interesting to note that at the angles where the

5 transition was observed, the corresponding $\gamma_{eff}/\gamma_{LAB}$ was very low, of order 0.1.

Transition 4 has a large γ_{eff}, and should have been observed. Unfortunately, the transition frequency of 190 kHz was well below the lowest tuning frequency (approximately 265 kHz) for the B driver amplifier, and it was necessary to do the measurements off resonance for this unit. This might have affected the B r.f phase shifting which was used for B reservoir heating. A weak line seemed to be indicated at 190 kHz, but the signal to noise ratio was so close to 1 that no definite conclusions could be drawn. An audio resonance search at 190 kHz was negative, but the H_{1B} calibration data available were dubious in this low frequency range, and the audio frequency sweep might not have been extensive enough. Even though the off-resonance transient response of the B r.f. system is not known, pulsed B r.f. saturation might have been more suitable than phase shifting or audio resonance in the present case. This was not tried.

b. Fixed Transition, Different λ

Experimental conditions were as under part a. before, but now with the sample temperature as a variable parameter. Measurements were made in the temperature range from 125°K to 246°K, where λ varies nearly linearly from 0.504 (at 125°K) to 0.533 (at 246°K), in a field H_o = 2590 G. Transition 1 was chosen, mainly because it was used in the K^{39} spin-lattice relaxation time measurements described in Chapter XI.

Experimental and theoretical values of $\gamma_{eff}/\gamma_{LAB}$ are shown in Fig. IX-7, as a function of temperature. All data were recorded with

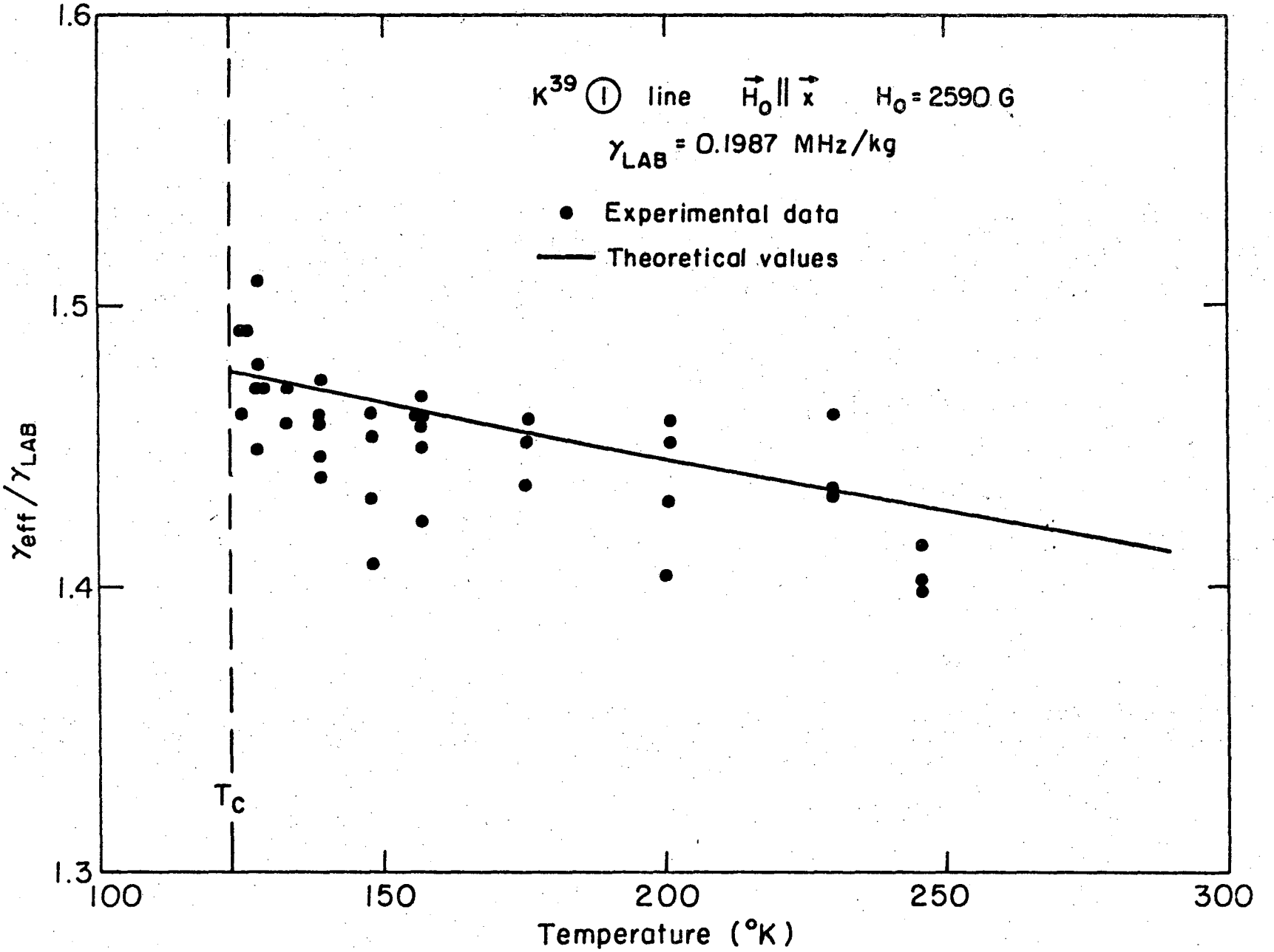

XBL 732-5716

Fig. IX-7. Effective gyromagnetic ratio as a function of temperature.

ν_{Audio} = 4.4 kHz and on resonance $\nu_B = \nu_{Bo}(T)$. Errors in single-measurement experimental and theoretical $\gamma_{eff}/\gamma_{LAB}$ - values were as shown for transition 1 in Table IX.3. As is apparent from Fig. IX-7, the temperature dependence of $\gamma_{eff}/\gamma_{LAB}$ is small, but is borne out clearly by the experimental data, and experimental and theoretical values agree within the established error limits.

As mentioned at the beginning of this chapter, local dipolar fields cause deviations from proportionality between the transition frequency and B r.f. field strength H_{1B} in the rotating frame, when H_{1B} is small. A rough check to eliminate this source of error in the measurements described above was made by measuring $\lambda_{eff}/\lambda_{LAB}$ for transition 1 at 3 values of H_{1B}. For H_{1B} = 31, 19 and 9 gauss, one found $\lambda_{eff}/\lambda_{LAB}$ = 1.393, 1.415 and 1.404, respectively, indicating no systematic trend. This is as expected at these relatively large fields.

X. DOUBLE RESONANCE STUDIES ON K^{39} AND K^{41} IN KDP

X-A. Spectroscopy, Conventional Double Resonance Methods

The spectra of K^{39} and K^{41} in KDP were already published[56] during the early phases of this investigation, and will therefore only be given a brief treatment here. Knowledge of spectra and quadrupole coupling constants is necessary in the present context to identify transitions and to compute quantities of interest, such as the effective gyromagnetic ratio in the rotating frame.

The ADRF double resonance methods described in Section III-B were used, with protons as A spins and K^{39} or K^{41} as B spins. The P^{31} will affect heat capacity ratios and possibly cross-relaxation rates, but can be ignored in the following analysis. Other nuclear species have too weak interactions with K^{39} and K^{41} to be of importance.

We recall that K^{39} and K^{41} are both spin 3/2 particles with natural isotopic abundances 93.08% and 6.91%, respectively. K^{39} requires double resonance methods for detection, despite high abundance, due to its weak quadrupole and Zeeman interactions.

X-A-1. Spectral Rotation Patterns. Sample Alignment

Both K^{39} and K^{41} are quadrupole coupled to the local e.f.g., and will in general have six allowed transitions. The hamiltonian defining the laboratory frame eigenlevels is

$$\mathcal{H} = \mathcal{H}_z + \mathcal{H}_Q$$

where $\mathcal{H}_z$ is the usual Zeeman interaction: $\mathcal{H}_z = -\gamma_B \hbar I_z H_o$. $\mathcal{H}_Q$ represents the quadrupole interaction. Since the crystal structure changes on going through the Curie point. $\mathcal{H}_Q$ will have two forms, corresponding to the para- and ferroelectric phase, and the two cases will be treated separately.

For both K^{39} and K^{41} in KDP, the quadrupole and Zeeman interactions are of the same order of magnitude, and perturbation treatments cannot be used.

Paraelectric Phase

As demonstrated in Ref. 48, crystal symmetry considerations show that the e.f.g. tensor at the potassium site is axially symmetric about the crystallographic z-axis and that all four potassium atoms in the unit cell are equivalent. Thus, a single set of resonance frequencies is expected for both K^{39} and K^{41}, and energy eigenvalues are defined by the hamiltonian

$$\mathcal{H} = -\gamma\hbar I_z H_o + \frac{e^2qQ}{4I(2I-1)}(3I_z^2 - I(I+1))$$

The energy eigenvalues have been computed numerically by Parker[40] for several different crystal orientations and for several different values of the parameter λ:

$$\lambda = \frac{e^2qQ/2I(2I-1)}{\gamma\hbar H}$$

This quantity is identical to λ as defined in Chapter V.

The spectra were recorded at various crystal orientations relative to the magnetic field H_o. Typically, one of the cryallographic axes was kept perpendicular to the magnetic field vector, while the sample was rotated stepwise about this axis. Depending on the axis of rotation, the spectra will be referred to as x-, y- and z-rotation patterns, cfr. Fig. VIII-1.

In Fig. X-1 are shown the observed x-rotation transition frequencies for K^{39} and K^{41} at 240°K. (Due to the symmetry of the e.f.g. tensor in the paraelectric phase, the y and z rotations yield no additional information). The curves show theoretical transition frequencies

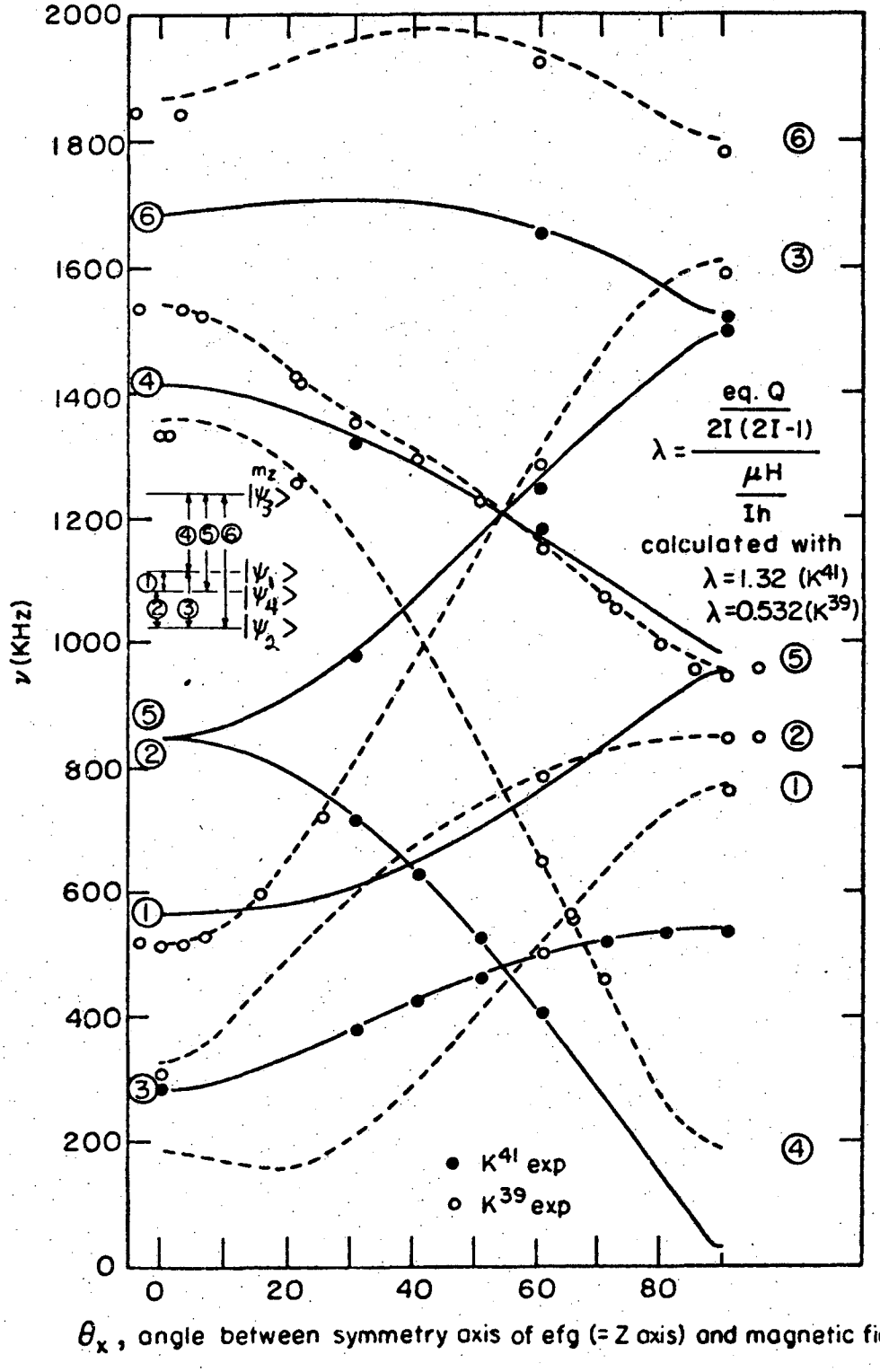

XBL732-5712

Fig. X-1. X-rotation spectra of K^{39} and K^{41} in KDP. Paraelectric phase: 240°K. H_o = 2586 G.

corresponding to $\lambda = 0.532$ for K^{39} and $\lambda = 1.32$ for K^{41}. With $H_o \simeq 2586G$, one has for the quadrupole coupling constants:

$$K^{39}: \quad |e^2qQ/h| = (1.64 \pm 0.01) \text{ MHz}$$
$$K^{41}: \quad |e^2qQ/h| = (2.24 \pm 0.01) \text{ MHz}$$

at 240°K. As will be shown explicitly below, the strength of the quadrupole coupling varies with temperature.

The laboratory frame energy level scheme is shown in Fig. X-1, where the different transitions are defined by a number. At a general angle θ_x, the eigenstates are linear superpositions of several Zeeman eigenstates $|m_i\rangle$, but at $\theta_x = 0°$, one has $H_o \parallel z$ and thus

$$[\mathcal{H}_Q, \mathcal{H}_z] = 0 \quad .$$

At this angle, the $|m_i\rangle$ will be eigenstates of the total hamiltonian $\mathcal{H} = \mathcal{H}_z + \mathcal{H}_Q$, and the energy eigenvalues are:

$$E_m = -\gamma\hbar H_o m + \frac{e^2qQ}{4I(2I-1)} \left(3m^2 - I(I+1)\right)$$

One can identify:

$$|\psi_3\rangle = |-3/2\rangle \,, \quad |\psi_1\rangle = |-1/2\rangle \,, \quad |\psi_4\rangle = |3/2\rangle \,, \quad |\psi_2\rangle = |1/2\rangle \quad .$$

Since no mixing of Zeeman eigenstates is present at $\theta_x = 0°$ and the selection rule $\Delta m = \pm 1$ applies, it is clear that the only allowed transitions are ②, ③ and ④. Experimentally, the lines ①, ⑤ and ⑥ were not observed at $\theta_x = 0°$, cfr. Fig. X-1. Only a slight rotation away from $\theta_x = 0°$ was sufficient for the lines to be observed, however.

Ferroelectric Phase

In the temperature range below the Curie point (T_c = 123°K), the crystal symmetry is orthorhombic Fdd2. The e.f.g. tensor at the K^{39} sites has a nonzero asymmetry factor η in the ferroelectric phase, and as pointed out in Ref. 48, this implies that there are two nonequivalent potassium sites in the unit cell (when a magnetic field is applied at an angle to the z axis). These sites will be called A and B. In the ferroelectric phase, domains exist with polarizations either parallel or antiparallel to the z-axis. Denoting the A and B sites in the two types of domains as A, B and A', B' respectively, one finds that there are in general four nonequivalent potassium sites in the unit cell corresponding to A, B, A' and B'. Thus four sets of transition frequencies are expected at a general orientation, for both K^{39} and K^{41}. The set $\theta_Z = 0° + n \cdot 90°$ (n = an integer) represents an exception, since A, B' and A', B become equivalent at these angles. In the x-rotation, only two sets of transition frequencies are observed, since A and B' are equivalent at $x \perp H_o$, and likewise A' and B.

Even though symmetry considerations show that the z axis is a principal axis of the e.f.g. tensor, the asymmetric e.f.g. components and number of nonequivalent potassium sites make the extraction of the quadrupole coupling constant and asymmetry parameter somewhat involved. The procedure of Brown and Parker[57] was used in Ref.48 to determine all relevant quadrupole coupling parameters for K^{39} at 770°K, and the data were later extended[58] to cover the temperature range from 77 °K and up to room temperature. In light of this, no systematic effort was made to obtain quadrupole coupling parameters in the ferroelectric

phase. Partial z-rotation spectra were recorded however, both in order to identify transitions used in Chapter XI, and to check on sample alignment. In Fig. X-2 are shown transition frequencies obtained in the z-rotation, as a function of sample temperature. In the ferroelectric phase, all data were recorded with $\theta_z = 90°$.

Significant line broadening was observed in the ferroelectric phase above approximately 118°K. The broadening can be explained by large-scale atomic fluctuations which lead to a time dependent quadrupole hamiltonian. If the fluctuation correlation time τ is short compared to the inverse static linewidth, the motional narrowing formula yields:

$$\langle \Delta\omega \rangle \propto \langle \mathcal{H}_Q^2(t) \rangle \tau$$

where $\mathcal{H}_Q(t)$ is the difference between the instantaneous and the time averaged quadrupole hamiltonians, and τ is the fluctuation correlation time. If this formula applies, line broadening can come about both by increased fluctuation amplitudes and by slower fluctuations. No attempt was made to obtain quantitative line broadening data for a thorough analysis, however.

z-rotation samples were used extensively in the measurements of K^{39} spin-lattice relaxation, and the spectra provided a quick procedure for checking on the sample alignment in situ:
In the paraelectric phase, the e.f.g. tensor is axially symmetric about the z-axis, and the energy levels are unchanged when the sample is rotated about this axis. Thus all K^{39} and K^{41} transition frequencies should be stationary under the z-rotation. If the angle between the magnetic field and the crystallographic z-axis is different from 90°,

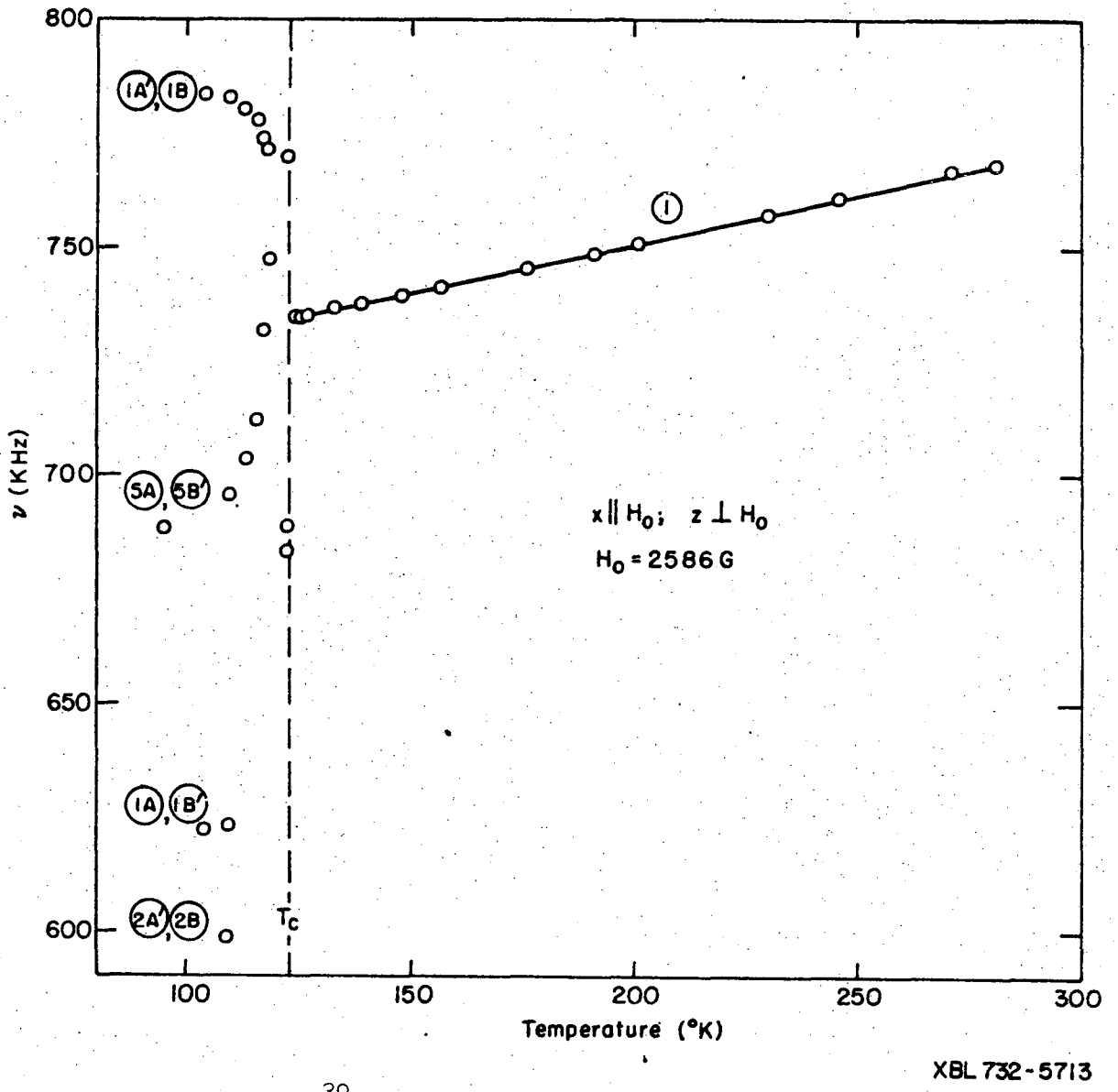

Fig. X-2. Partial K^{39} spectra in KDP. Circled numbers indicate transitions as defined in Fig. X-1.

the transition frequencies will oscillate two full periods about their values at 90° as the sample is rotated once about the z axis. As an example, the ① line at 240°K shifts by approximately 2 kHz when the angle between the z-axis and the magnetic field is changed from 90° to (90 ± 1)°. In the ferroelectric phase, the transition frequencies depend strongly on the z-rotation angle. At $\theta_z = 0° + n \cdot 90°$ (n = integer) the transition frequencies pertaining to A, B' sites and A', B sites are equal and the z-rotation transition frequency pattern is symmetric about the $\theta_z = 0° + n \cdot 90$ points. For certain transitions, only a slight rotation away from $\theta_z = 0° + n \cdot 90°$ is sufficient to split and shift the lines substantially, crf. Fig. X-3. In practice, the z-rotation spectra could be used to determine the x(y) axis orientation with an accuracy better than 1°.

X-A-2. Temperature Dependence of K^{39} Quadrupole Coupling Constants

Since the Zeeman interaction was the same at all temperatures, Fig. X-2 demonstrates that the quadrupole coupling energy changes with temperature. In the paraelectric phase, the only hamiltonian parameter which varies is the e.f.g. parameter q in the quadrupole coupling constant. Using the observed transition frequencies, one can determine e^2qQ as a function of temperature, as shown in Fig. X-4. The results are consistent with similar data reported previously.[58] The quadrupole coupling constant increases linearly with temperature from 1.555 MHz at 124°K to 1.670 MHz at 291°K, corresponding to a relative slope

$$\frac{1}{|q|}\left(\frac{d|q|}{df}\right)_f = 4.60 \cdot 10^{-4}\ [°K^{-1}]$$

at mid-range (190°K).

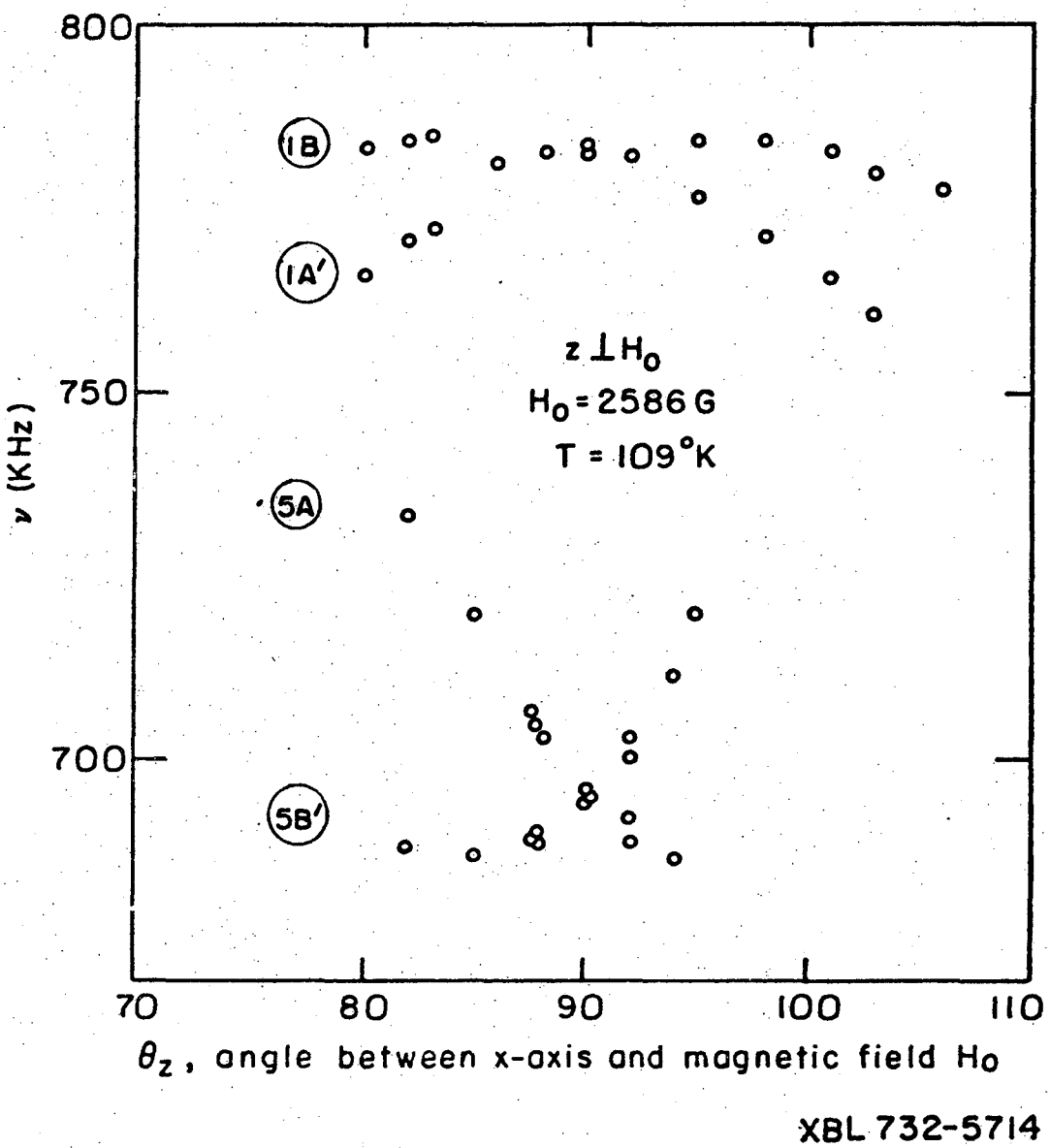

Fig. X-3. Partial K^{39} Z-rotation spectra used for sample orientation; ferroelectrid phase. Transitions are identified by circled numbers.

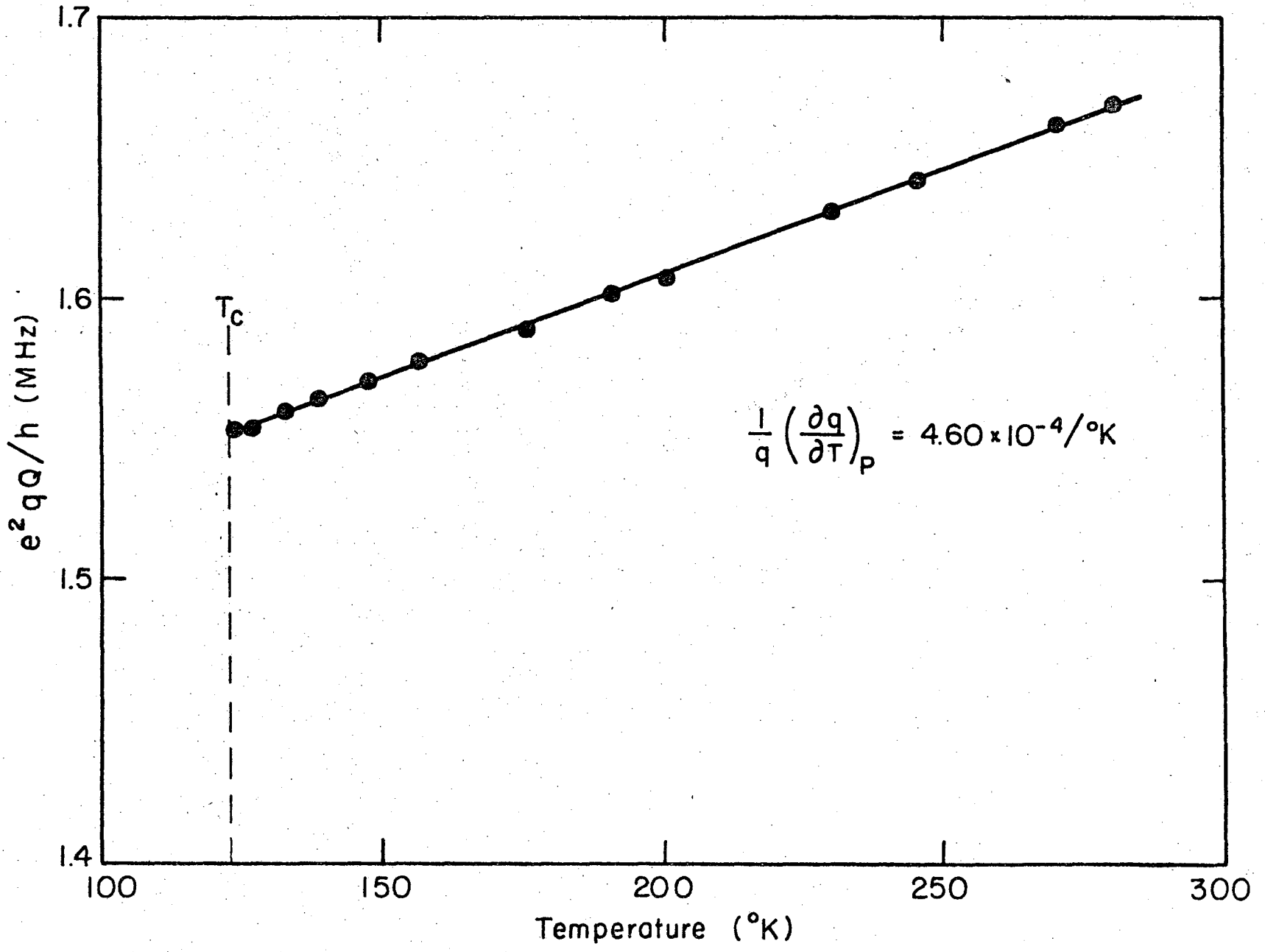

Fig. X-4. K^{39} quadrupole coupling constant in KDP.

XBL732-5715

The increase in the quadrupole coupling constant with increasing temperature is contrary to what is usually observed, and thermal expansion would also lead to an opposite temperature trend. Measurements[59,60,61] on Rb^{87} quadrupole coupling constants in the KDP isomorphs RbH_2AsO_4 and RbH_2PO_4 have yielded an anomalous temperature behavior of the same type. This problem has been discussed at some length in Ref. 59 and 60, and it seems clear that the anomalous e.f.g. temperature dependence in the paraelectric phase is linked to the collective atomic fluctuations which trigger the phase transition at T_c. No quantitative verification of specific dynamic models has been obtained so far for the K^{39} and Rb^{87} data (the long range ionic origin of the e.f.g. at the cation sites makes analysis difficult). As shown in Ref. 60, however, experimental As^{75} e.f.g. data for CsH_2AsO_4 demonstrate that a strong proton-lattice coupling exists. In this model, As nuclei take part in the collective atomic fluctuations, and the temperature dependence of the e.f.g. tensor reflects the dynamic proton, disordering between the six possible Slater configurations (cfr. Ref. 62). The model also yields correct qualitative temperature dependence for K^{39} and Rb^{87} quadrupole coupling constants. The Cs^{133} quadrupole coupling constant in CsH_2AsO_4 was found[63] to be temperature independent in the paraelectric phase, in strong contrast to the K^{39} and Rb^{87} results. This can be compared with a qualitative difference in Cs^{133} and K^{39} spin-lattice relaxation temperature dependences in the paraelectric phase. A further discussion will be given in Chapter XI, where experimental data on K^{39} spin-lattice relaxation times are presented.

X-B. Spectroscopy on K^{39} With a Single, Unmodulated B r.f. Pulse

The thermal reservoir model for double resonance with a single, unmodulated B r.f. pulse was introduced in Chapter IV and verified experimentally in Chapter IX. It is clear that information can be extracted from the spectral lines obtained in this double resonance mode, which is not available by the usual double resonance methods with B spin saturation. Double resonance spectra of K^{39} in KDP and at high temperatures demonstrate this clearly:

As the sample temperature was increased from 152°K to 287°K, one observed the dramatic change in line structure which is shown in Fig. X-5. In addition to the overall shift towards higher frequencies, due to the change in the K^{39} quadrupole coupling constant, the characteristic center ridge was gradually smeared out and disappeared completely. At the same time, the line narrowed and the depth at the line center increased.

Explanation of this behavior is straightforward with the aid of the thermal reservoir model: The fact that the line depth at the center of the line increases with increasing temperature, while the curvature of the center ridge becomes less sharp, implies unambigously that the heat capacity ratio

$$\varepsilon = \frac{N_B S(S+1)\ \gamma_B^2 H_{eB}^2}{N_A I(I+1)\ \gamma_A^2 H_{LA}^2}$$

increases at higher temperatures. The K^{39} system heat capacity was kept constant by monitoring the K^{39} rotating frame transition frequency and consequently the local dipolar field H_{LA} in the proton rotating frame must decrease at high temperatures. This is consistent with the

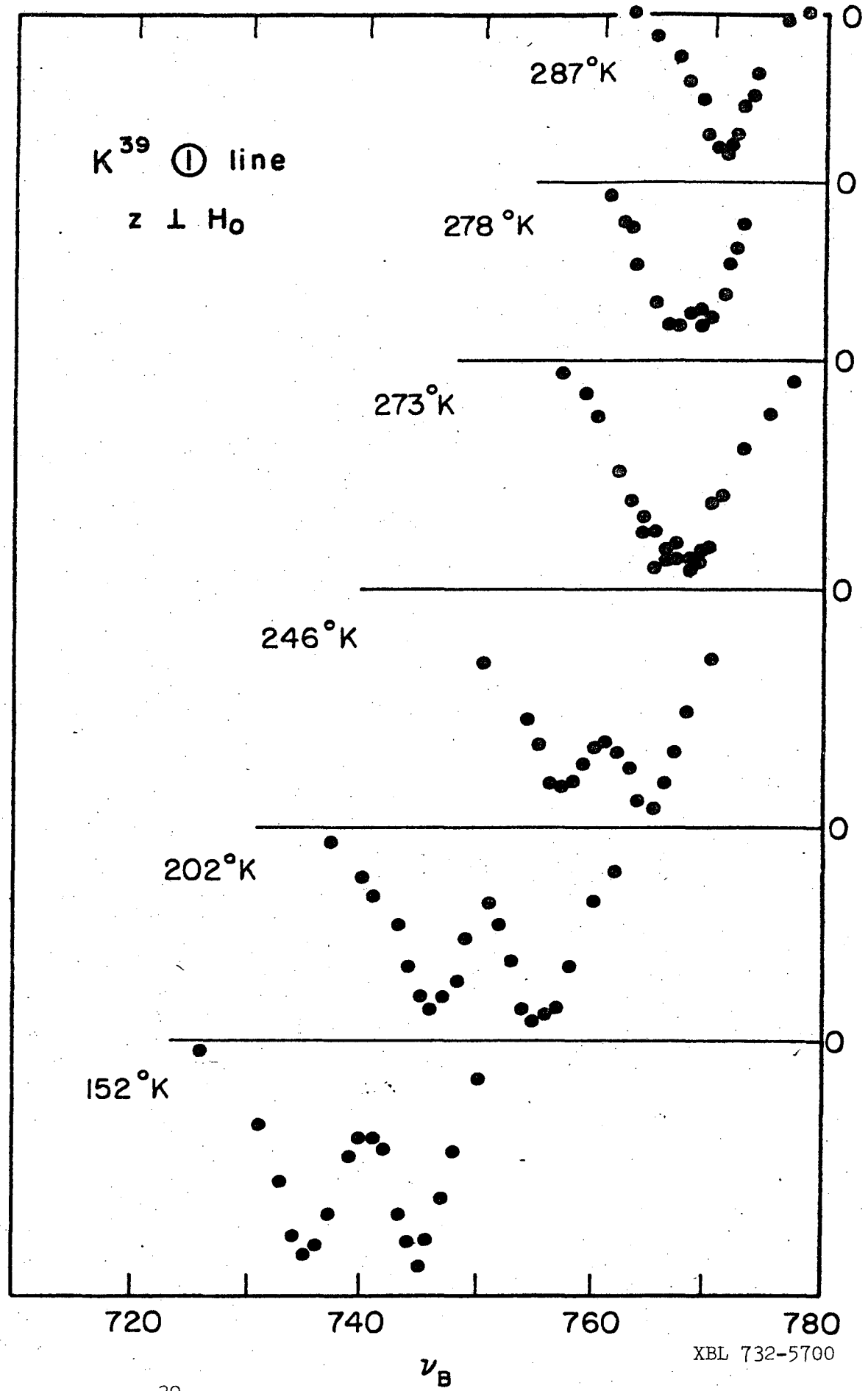

Fig. X-5. K^{39} double resonance lineshapes with unmodulated B r.f. H_o=2586 G.

observed line harrowing at high temperatures, which implies an increase in the A-B cross coupling time τ_{AB}. As demonstrated in Chapter IX, τ_{AB} increases as the B r.f. power is increased, which is related to the requirement of energy conservation during A-B cross relaxation:

$$\gamma_B \cdot H_{eB} \simeq \gamma_A \cdot H_{LA}$$

As the sharply defined $\gamma_B H_{eB}$ is increased, matching to the quasi-continuous proton dipolar spectrum, represented by $\gamma_A H_{LA}$, becomes poorer (cfr. Section III-B). Equivalently, in the present case $\gamma_B H_{eB}$ is constant at a given frequency offset from the line center, while the dipolar spectrum becomes narrower as the temperature is increased.

The lineshape is thus consistent with a narrowing of the proton dipolar spectrum at high temperatures. A plausible mechanism for this is thermally activated motional narrowing, and one can now turn to the data presented in Chapter VIII on proton spin-lattice relaxation times in the dipolar state. Comparing Figs. VIII-4 and X-5, one notes that both the proton relaxation and K^{39} lineshape data start to exhibit the motional effect at approximately 240°K. Thus it is highly probable that the change in the K^{39} lineshape is caused by ultraslow rotation of H_2PO_4 groups. It is interesting to note that in the onset region the change in the K^{39} lineshape appears to be an even more sensitive indicator for such motion than the proton relaxation rates. One potential application of the thermal reservoir model in this context is to determine how the fluctuation correlation time τ of the local fields vary with temperature. ϵ can be measured by the methods described in Chapter IV, and thus one obtains a measure of the relative change in H_{LA} as a function

of temperature. In cases where the local fields seen by the moving nuclei are modulated within a fixed range, such as in rotation, the motionally narrowed linewidth

$$\Delta\omega_A \simeq \frac{1}{2\pi} \langle (\gamma_A H_{LA,static})^2 \rangle \cdot \tau$$

will have a temperature dependence governed by τ, and since $\Delta\omega_A \propto H_{LA} \propto \varepsilon^{-1/2}$, one has

$$\tau(T) \propto \varepsilon(T)^{-1/2}$$

These formulas apply when $2\pi/\tau \gg \gamma_A H_{LA,static}$. Unfortunately, motionally induced reduction in T_{1ADRF} made it difficult to measure ε accurately at temperatures above 270-290°K, while τ only reaches the kilohertz range at approximately 300°K.[51] This does not rule out the feasibility of this method in applications to other substances, however.

Finally, it should be mentioned that the K^{39} line structure changed when approaching T_c. In the temperature region from approximately 150°K to 125°K, the center ridge in the line gradually smoothed out and almost disappeared at 125°K. Separate measurements did not reveal any change in ε in this region, but $T_1(K^{39})$ decreased rapidly on approaching T_c, which is evident from the overall increase in line depth. The short $T_1(K^{39})$ cannot explain the smoothing out of the center ridge, however, which was not explained.

X-C. Transient Oscillations in the Rotating Frame: Proton-K^{39} System

A brief description of transient oscillations in the rotating frame was given in Section III-C. This effect was studied in KDP with protons as A spins and K^{39} as B spins, and qualitatively different results were obtained in the para- and ferroelectric phases.

X-C-1. Experimental Results

Measurements were made with the crystal x-axis parallel to the magnetic field H_o. The pulse sequence was identical to the one used in ADRF double resonance with pulsed B r.f., but here the B r.f. was always kept on resonance ($\omega_B = \omega_{Bo}$), while the proton dipolar signal amplitude S_A was measured as a function of the pulse length (cfr. Fig. X-6). The total number of pulses, n, and the time between the start of successive pulses was kept constant in each run.

Some results obtained in the para- and ferroelectric phases are shown in Fig. X-6:

At T = 164°K are shown two runs with H_{1B} = 31 gauss and 48 gauss. The oscillations are quite prominent, and the oscillation period at each H_{1B} is $\approx \frac{2\pi}{\omega_{1B}}$.

At T = 119°K a single run at H_{1B} = 33 gauss is shown. There is no clear evidence of oscillations at all. Pulse trains at higher power had to be kept short to avoid heating the sample towards the Curie point, and therefore yielded low double resonance sensitivity. No transient oscillations were observed at H_{1B} = 56 gauss.

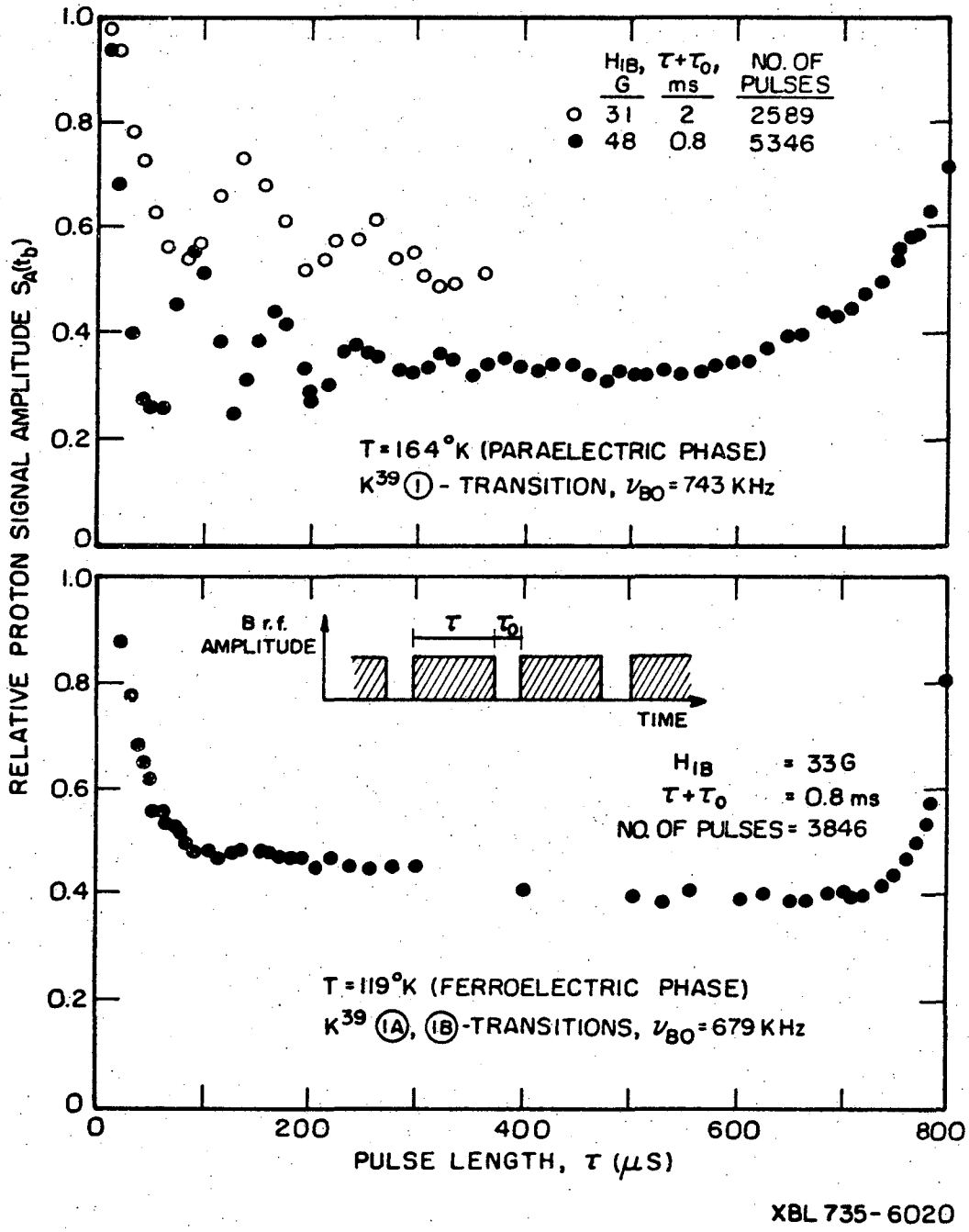

Fig. X-6. Transient oscillations in the para- and ferroelectric phases. K^{39}-proton system. Crystal orientation : $\theta_z = 90°$ ($x \parallel H_o$).

X-C-2. Discussion

There is little doubt that the observed oscillations in Fig. X-6 (para-phase) are of the type described in Section III-C. At all H_{1B}, the oscillation frequency agreed within experimental error with ω_{1B} as measured by audio resonance, and $\delta(\tau)$ as computed from experimental data by Eq. (III-19) exhibits a transient oscillatory behavior compatible with Eq. (III-20) and Eq. (III-21), cfr. Ref. 11. By adjustment of parameter values, Eqs. (III-20) and (III-21) can also yield a behavior qualitatively similar to that observed in the ferro-phase.

A quantitative analysis of the transient oscillations is of interest, expecially as it pertains to the fluctuation spectra of the A-B coupling hamiltonian. Unfortunately, no concrete information is available on the A-B dipolar coupling correlation function $g(\tau)$ in the present case, and thus transient oscillation data must be supplemented by careful experimental studies on double resonance cross relaxation rates as described in Ref. 11, f.ex. A possibility in the absence of such hard and fast data is to try data fitting with a plausible $g(\tau)$. Here one will only call attention to some qualitative physical arguments which might help explain the observed data in Fig. X-6.

The theory in Section III-C was derived under the assumptions of "extreme narrowing" ($\tau_c \ll \tau_{AB}$) and $\tau \ll \tau_{AB}$. At the B r.f. field strengths of interest here, $\tau_{AB} = O(1\ \text{sec})$, while $\tau = O(1\ \text{msec})$. τ_c is typically of order 10-100 μs and the assumptions on τ, τ_c and τ_{AB} are well justified. The presence of a third interacting spin species (P^{31}) is a complication which should be considered more closely, but

as discussed in Chapter IX, the proton-phosphorous coupling is so strong that it seems justified to treat both H^1 and P^{31} as a composite A spin species here.

A rough picture of parameters which influence the oscillatory behavior can be had by assuming for $g(\tau)$ a Lorentzian (Eq. (III-15), as observed by McArthur, Walsted and Hahn for the Ca^{43}-F^{19} system.[11] Differentiating Eq. (III-21) twice with respect to τ and combining with Eq. (III-20) obtains:

$$\frac{d^2\delta(\tau)}{d\tau^2} \propto \omega_{1B}^2\, g(\tau)\, \cos\omega_{1B}\tau \propto \omega_{1B}^2\, (1 + \tau/\tau_c)^{-1}\, \cos\omega_{1B}\tau \qquad \text{(X-1)}$$

which indirectly exhibits the damping out of the oscillations in $\delta(\tau)$ as τ increases. According to Eq. (X-1), strong B r.f. fields ($2\pi/\omega_{1B} \ll \tau_c$) should be used to observe clear oscillatory behavior. Given a Lorentzian $g(\tau)$ and $\omega_{1B} \approx$ const., the disappearance of oscillations on going from the para- to the ferro-phase can thus be interpreted as a reduction of τ_c in the ferrophase. This is not implausible in light of the change in crystal structure at the Curie point, and the ordering of protons on the hydrogen bonds in the ferro-phase.

Another factor which will affect the transient oscillations results is the effective halving of the number N_B of K^{39} spins participating in the A-B coupling in the ferro-phase, as compared to the para-phase (at the field configuration of interest here: $H_o \,||x$). This is due to the increased number of non-equivalent potassium sites in the ferro-phase, cfr. Section X-A. As is evident from Eq. (III-20), $\delta(\tau) \propto N_B$

as a first approximation, and the halving of N_B will thus lead to a weaker double resonance signal, but no qualitative change in the oscillatory behavior.

Other factors which will not be considered here are: a) Effective K^{39} gyromagnetic moment in ferro-phase. b) Effect of ferroelectric mode close to T_c. c) Possibility of inhomogeneous broadening (magnetic or quadrupolar). d) Possible A-B decoupling mechanisms in ferro-phase.

Finally, it should be pointed out that no systematic measurements have been performed on the temperature dependence of the transient oscillations. Such measurements should be made throughout the para- and ferroelectric phases. Parallel rigid-lattice calculations of T_c and experimentally determined proton spin-spin relaxation times might then help identify the mechanism responsible for the disappearance of the transient oscillations in the ferro-phase.

XI. MEASUREMENTS OF K^{39} SPIN-LATTICE RELAXATION TIMES IN KDP. THE FERROELECTRIC MODE

In Chapter IV, a new method was introduced which makes it possible to measure spin-lattice relaxation times of nuclear species that require double resonance techniques for detection. The spin-lattice relaxation time being measured is pertinent to the spin-lock state, and describes the rate of decay of a magnetization locked to the stationary r.f. field vector in the rotating frame. As was demonstrated in Section X-A, the method can be used on K^{39} in KDP, and in Section XI-A below, it is used to determine K^{39} spin-lattice relaxation times in KDP as a function of sample temperature. These data contain information on the state of motion in the crystal, and an analysis of this is made in Section XI-B, with special emphasis on a relaxation rate singularity at the Curie point.

The K^{39} spin-lattice relaxation time in the spin-lock state will be written $T_1(K^{39})$ in the following. Protons will be referred to as A spins, K^{39} nuclei as B spins.

XI-A. K^{39} Spin-Lattice Relaxation Times in the Spin-Lock State

As is evident from the analysis in Chapter IV, the double resonance cross-relaxation time τ_{AB} must be so short that the A-B thermal equilibration transient is over in a short time compared to the total time of contact between the A and B reservoirs. This suggests that one should use a <u>weak</u> r.f. field at the K^{39} transition frequency. On the other hand, the heat capacity of the B reservoir should be large to ensure an easily detectable depletion of the A reservoir energy, which indicates that a <u>strong</u> r.f. field be used. In the present case, τ_{AB} = 0.3 sec

was chosen as a suitable compromise. The corresponding B r.f. field strength as determined by the transition frequency in the rotating frame of the K^{39} ① transition (Cfr. IX-A), was $\omega_{eB}/2\pi = 4.4$ kHz. Measurements on τ_{AB} at fixed B r.f. field strength revealed no temperature trend, and the observed relationship between ω_{eB} and τ_{AB} is consistent with a τ_{AB} of the form

$$\tau_{AB} \propto \exp(-\omega_{eB} \cdot \text{const})$$

This is the same as has previously been found[11] for Ca^{43}·F^{19} cross-relaxation i CaF_2.

All $T_1(K^{39})$ data in the series were taken on exact resonance for the K^{39} ① line, and with the crystallographic x-axis parallel to the magnetic field H_o. The maximum A-B thermal contact time was typically 8-10 seconds, at temperatures below approximately 210°K. Since the proton relaxation time T_{1dip} decreases rapidly as one goes to higher temperatures, the maximum thermal contact times were shorter there, a typical value at 240°K was 5 seconds.

Evidently, there is a maximum temperature above which measurements cannot be made by the method used here: On raising the sample temperature, the proton dipolar order after ADRF ultimately decays so rapidly that the proton dipolar signal falls below the detection limit by the time the A-B thermal equilibration is completed. The practical limit for application of the method is at temperatures well below this, and was at approximately 240°K in the present case. There is, however, one special case where qualitative measurements of the proton energy decay curve during A-B thermal contact is sufficient. If $T_{1dip} = T_1(K^{39}) \equiv T_1$ at some temperature,

one finds from Eq. (IV- 24) that the proton signal should vary as

$$E_A(\omega_B = \omega_{Bo}, t_b) = E_{Ao} \exp(-t_b/T_1) \frac{1}{\varepsilon+1} \{1 + \varepsilon \exp(-t_{Br.f.}(\varepsilon+1)/\tau_{AB}))\}$$

regardless of the relative magnitudes on τ_{AB} and T_1. Thus, the proton signal is independent of the thermal contact time after the initial transient. Conversely, if one can find a sample temperature where the proton decay curve has zero slope after the initial transient, one can conclude that $T_1(K^{39}) = T_{1dip}$, and a direct measurement of T_{1dip} is sufficient to determine both. An example of this is shown in Fig. IX-4.

ε and $T_1(K^{39})$ were calculated from the data using the exact formula (Eq. (IV- 13)) for the on-resonance case and T_{1dip}-data from Chapter VIII. $T_1(K^{39})$ as a function of temperature is shown in Fig. XI-1. The exact formula was used, due to the relatively long cross-relaxation time τ_{AB}, and the short $T_1(K^{39})$ in the high temperature region and at $T \to T_c$. $T_1(K^{39})$ data in Fig. XI-1 were extracted from raw data as follows:

1) First ε and $T_1(K^{39})$ were adjusted simultaneously to yield a least squares fit in the logarithms of the proton signal levels. This resulted in a large number of ε, $T_1(K^{39})$ sets. A salient feature of the ε-data was that ε had two distinct values in the temperature range from 99°K to 240°K.

$$T < T_c: \qquad \varepsilon_{Average} = 0.185 \pm 0.015$$

$$T_c < T \lesssim 240°K: \qquad \varepsilon_{Average} = 0.279 \pm 0.002$$

At the highest temperature in the series, $T \simeq 246°K$, a higher value of ε was found:

$$T \simeq 246°K: \qquad \varepsilon_{Average} = 0.330 \pm 0.020$$

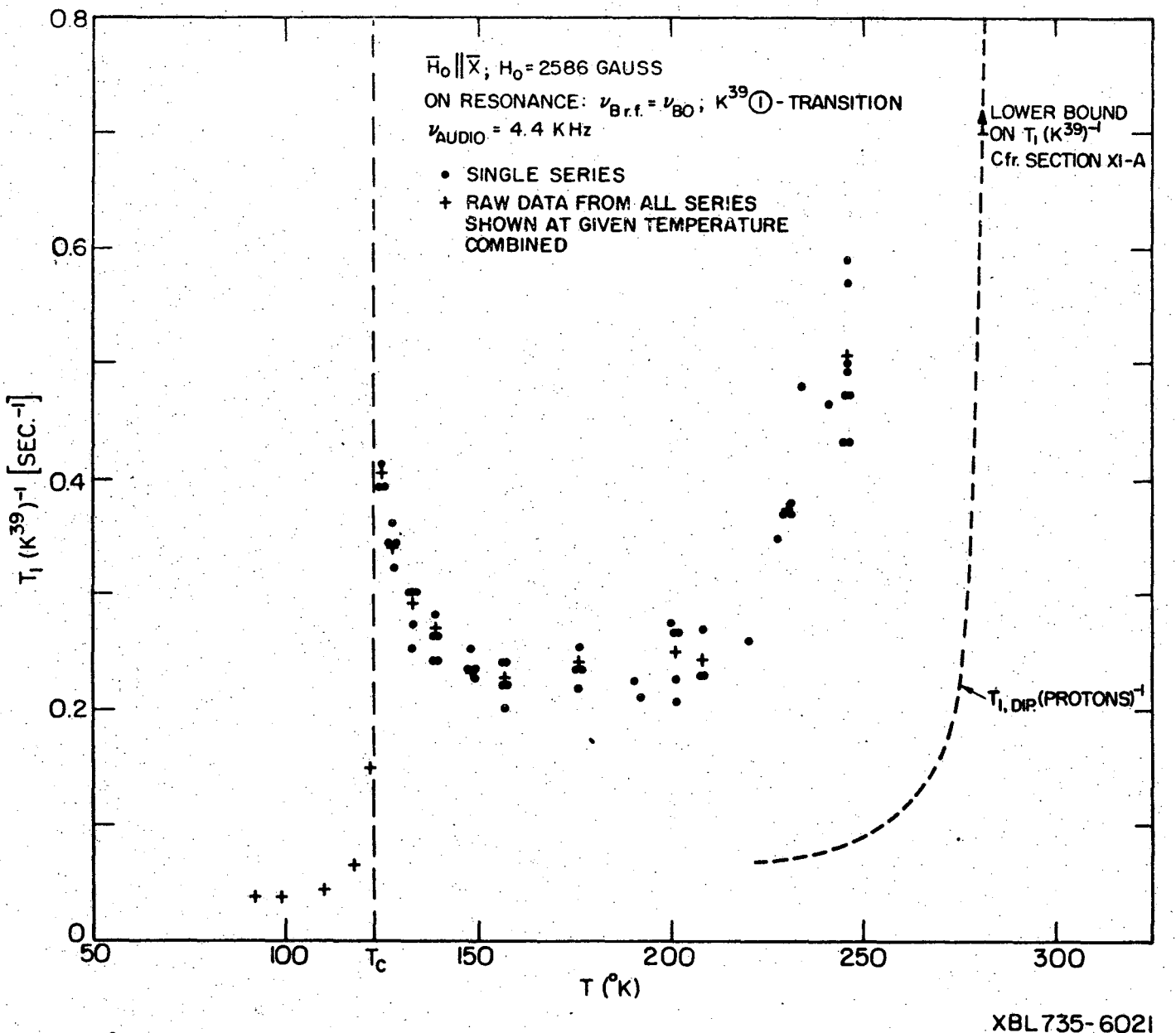

Fig. XI-1. K^{39} spin-lattice relaxation rates in the spin-lock state, as a function of temperature. The high temperature proton relaxation rate $T_{1.dip}^{-1}$ (dashed curve) represents a lower limit on the high-temp. $T_1(K^{39})^{-1}$ up to and beyond 218°K. Data were obtained with the KDP "standard sample" described in Chapter VII.

The uncertainties represent one standard deviation on the average in each group. Within each group, no temperature trend in ε could be detected.

This result is not surprising. The heat capacity ratio was defined by Eq. (IV-6) as:

$$\varepsilon = \frac{N_B S(S+1)\,\omega_{eB}^2}{N_A I(I+1)\,\omega_{LA}^2}$$

where

$$\omega_{1B} = \gamma_{eff,B}\, H_{1B} \text{ on resonance: } \quad \omega_B = \omega_{Bo}$$

and

$$\omega_{LA}^2 = \gamma_A^2 H_{LA}^2 = \gamma_A^2 T_r\{\mathcal{H}_d^A(s)^2\}/\{M_x^{A\,2}\}$$

In the expression for ε, the quantities N_B, ω_{eB} and ω_{LA} may change on going from the para- to the ferrophase:

N_B: As described in Section X-C-2, the increased number of non-equivalent potassium sites in the ferro-phase effectively halves N_B in the present case.

ω_{eB}: The B r.f. field strength was checked by audio resonance during each run. All para-phase data were recorded at $\omega_{eB}/2\pi = 4.4$ kHz. In the ferro-phase, one had $\omega_{eB}/2\pi = 4.6$ kHz. Line broadening could have increased the B reservoir heat capacity, since $\omega_{eB}^2 - \omega_{eB}^2 \gtrsim 0$, but such an effect must be small, as indicated by lineshape data.

Before taking possible changes in ω_{LA} into account, these values for N_B and ω_{eB} would yield a ratio

$$\frac{\varepsilon(\text{ferro-phase})}{\varepsilon(\text{para-phase})} = 0.55 \pm 0.05$$

as compared to the observed ratio 0.66 ± 0.06.

ω_{LA} is determined by the trace of the secular part of the dipolar hamiltonian. Dipolar coupling is chiefly proton-proton and proton-phosphorous. Since the crystal structure changes in going from the paraelectric to the ferroelectric phase, a change in the average local dipolar fields is expected, but no attempt at quantitative assessment of this effect will be made here. Motional narrowing is a potentially important factor at high temperatures, where thermally activated proton interbond motion takes place (cfr. Chapter VIII). Narrowing of the proton dipolar spectrum was indicated by the high temperature K^{39} lines in Fig. X-5, and might explain the high values of ε recorded at $T \simeq 246°K$, but since $\tau \gtrsim 10^{-2}$ sec even at 273°K the effect should be quite small.

One can conclude, then, that both experiment and theory indicate a constant ε throughout each range: $T < T_c$ and $T_c < T \lesssim 240°K$. This suggests the next step in the data analysis.

2) Using a fixed ε equal to the average measured in the pertinent temperature range, the least squares fitting was repeated, with only $T_1(K^{39})$ as the variable parameter. These are the data shown in Fig. XI-1.

3) In addition to the data at randomly chosen temperatures, several data sets were accumulated at each of a series of temperatures. At each of these temperatures, simultaneous least squares fitting was performed with respect to <u>all</u> data at that temperature to yield a single set ε and $T_1(K^{39})$. This was done both with ε and $T_1(K^{39})$ as variable parameters, and with ε fixed at the average value for the appropriate temperature range. The two methods yielded $T_1(K^{39})$ values that agreed very well mutually (within 0.3 sec at most temperatures).

4) As is evident from the large experimental scatter at 246°K, the highest temperature in the series, this temperature represents an upper limit for the practical applicability of the method. In the special case where $T_1(K^{39}) = T_{1dip}$, however, the proton signal after A-B thermal equilibration will be independent of the B r.f. irradiation time (cfr. Section IV-C-1 and the 118°K curve on Fig. IX-4), which can be ascertained by a qualitative measurement. As one may recall from Chapter VIII, T_{1dip} starts decreasing rapidly at temperatures above approximately 250°K, and if the decrease is more rapid than that in $T_1(K^{39})$, a temperature exists where $T_1(K^{39}) = T_{1dip}$. An experimental search up to 270°K established that $T_1(K^{39}) < T_{1dip}$ up to this temperature, and this has been indicated in Fig. XI-1 by a portion of the $1/T_{1dip}$ curve at high temperatures, which represents a lower bound on $1/T_1(K^{39})$.

Finally, it should be mentioned that an attempt was made at measuring the laboratory frame $T_1(K^{39})$ by the McArthur, Hahn and Walstedt method[11] which is described briefly in Section IV-C-1. This proved impossible with the present apparatus, since the maximum proton signal obtained had a signal to noise ratio in the range 1:1 to 2:1. This result is not unexpected: The method requires off-resonance B r.f. irradiation at a high level, which in this specific application leads to so slow cross-relaxation ($\tau_{AB} \gtrsim 1$ sec, cfr. Chapter X) that spin order is destroyed by proton and K^{39} spin-lattice relaxation before sampling can be performed.

XI-B. Analysis of K^{39} Spin-Lattice Relaxation Data. The Ferroelectric Mode.

XI-B-1. Spin-Lattice Relaxation by the Ferroelectric Mode

During the last decade, it has been established that a microscopic description of ferroelectric phase transitions can be obtained in terms of specific lattice modes of vibration. Due to anharmonic phonon interactions, these modes become unstable at a critical temperature T_C, where the mode frequency goes to zero, accompanied by a strong increase in amplitude (hence the term "soft modes"). Below T_C, the atomic displacement pattern corresponding to that of the soft mode above T_C is "frozen in", leading to a spontaneous dielectric polarization, which is defined as the transition order parameter. This soft mode picture was originally applied to "displacive" transitions, but has also been applied with considerable success to describe transitions of the "order-disorder" type, cfr. below. In certain cases, it is necessary to consider several modes which couple close to T_C, and the critical temperature corresponding to a given soft mode therefore does not necessarily coincide exactly with the phase transition temperature.

The current theoretical description of soft mode lattice dynamics can be traced back to several papers published about 1960,[64,65,66] where transitions in displacive-type ferroelectrics were linked with the softening of a long-wavelength T.O. mode near T_C. Later extensions of the lattice dynamic approach include quasi-spin-wave descriptions of order-disorder transitions[67,68] and the quasi-spin-wave phonon modes discussed by Kobayashi.[69] The latter are of specific interest in

the present context, and will be described briefly in Section XI-B-2. Recent reviews on the dynamic description of ferroelectric phase transitions are found in Ref. 3, 70 and 71.

The slow, large-amplitude soft mode atomic displacements close to T_o perturb the nuclear energy levels by modulating the magnetic dipole-dipole interactions or the nuclear quadrupole moment interaction with the local electric field gradient. In certain cases the soft mode contribution may dominate the total spin-lattice relaxation rate due to all relaxation mechanisms, in a temperature region around T_C which is sufficiently large so that the temperature dependence of the soft-mode relaxation contribution can be determined. This temperature dependence can be related to specific models for the interaction between microscopic polarizable units in the ferroelectric (e.g. quasi-spins) which triggers the phase transition. Several theoretical and experimental NMR studies of this type have recently appeared in the literature, and a brief sketch of the underlying theory for the method used here is given below. The presentation follows that of Ref. 72, but emphasis is on ultimate application to the case of spin-lattice relaxation in the spin-lock state for K^{39} in KDP:

The ferroelectric will be represented by interacting dipoles on a lattice. The interaction may be isotropic or anistropic, and the dipoles will be assumed to have 2 allowed orientations. This model is not unreasonable for KDP, in light of the proton tunnelling between 2 equilibrium sites on each hydrogen bond, and the $K\text{-}PO_4$ dipoles that flip along the crystal Z-axis (cfr. Section XI-B-2). To simplify the analysis, the soft mode will be assumed overdamped, which should apply for KDP.[71,73]

The dominant spin-phonon relaxation process in the case of heavily damped phonon modes is direct.[72] The expressions for spin-lattice relaxation rates obtained by the spectral density approach in Section V-B should therefore apply for the ferroelectric-mode contribution to the K^{39} spin-lattice relaxation rate in KDP (quadrupolar spin-phonon coupling is dominant here; cfr. Ref. 74). These relaxation rates can be written on the form (cfr. Table V.2):

$$\frac{1}{T_{1\ S.L.}} = \sum_{n\mu} C_{\mu n} J_{\mu}(\omega_n) \qquad \text{(XI-1)}$$

where $T_{1\ S.L.}$ is the spin-lattice relaxation time in the spin-lock state, $C_{\mu n}$ are constant coefficients (at a given temperature), and $J_{\mu}(\omega_n)$ are spectral densities at the different nuclear transition frequencies ω_n:

$$J_{\mu}(\omega_n) \equiv \int_{-\infty}^{\infty} \exp(-i\omega_n \tau) \langle F_{\mu}(t)\, F_{\mu}(t-\tau) \rangle\, d\tau \qquad \text{(XI-2)}$$

Here $F_{\mu}(t)$ are the lattice fluctuation parameters introduced in Section V-B, representing the time dependent electric field gradients at the nuclear sites. (μ rather than q will be used as a labeling index here, to avoid confusion with the wave vector $\vec{q}$).

In the model introduced above, one can write:

$$F_{\mu}(t) = \frac{1}{2} \sum_i A_{\mu}^i\, \sigma_i(t) \qquad \text{(XI-3)}$$

where summation over i represents contributions from all N dipoles in the sample; $\sigma_i = \pm 1$; and A^i is the difference caused in $F_{\mu}(t)$ when dipole no. i flips between its 2 positions. A_{μ}^i and $\sigma_i(t)$ can be expressed in wave vector space by their Fourier transforms $\sigma(\bar{q},t)$ and $A_{\mu}(\bar{q})$

$$\sigma_i(t) = \frac{1}{\sqrt{N}} \sum_{\bar{q}'} \sigma(\bar{q}',t) \exp(-i\bar{q}'F_i)$$
$$A_\mu^i = \frac{1}{\sqrt{N}} \sum_{\bar{q}'} A_\mu(\bar{q}') \exp(-i\bar{q}'F_i) \qquad \text{(XI-4)}$$

In the random phase approximation, substitution of Eq. (XI-4) into Eq. (XI-2) yields:

$$J_\mu(\omega_n) = \frac{1}{4N} \sum_{\bar{q}} A_\mu(\bar{q})\, A_\mu^*(\bar{q}) \int_{-\infty}^{\infty} \exp(-i\omega_n\tau) \langle \sigma(q,0)\, \sigma(-\bar{q},\tau) \rangle\, d\tau$$

Explicit evaluation of the autocorrelation function $\langle \sigma(\bar{q},0)\, \sigma(-\bar{q},\tau) \rangle$ for the polarization fluctuations can be avoided by resorting to the fluctuation-dissipation theorem, which relates the spectral density of $\sigma(\bar{q},t)$ to the imaginary part of the generalized dielectric susceptibility χ. Thus, in the high temperature approximation:

$$\int_{-\infty}^{\infty} \exp(-i\omega_n t)\, \langle \sigma(\bar{q},0)\, \sigma(-\bar{q},t) \rangle\, dt = -\frac{2kT}{N\omega_n}\, \chi''(\bar{q},\omega_n)$$

Equation XI-1) can then be written:

$$\frac{1}{T_1\ \text{S.L.}} = \sum_{\mu n} C_{\mu n}\, \frac{kT}{2\omega_n}\, \frac{1}{N^2} \sum_{\bar{q}} A_\mu(\bar{q})\, A_\mu^*(\bar{q})\, \chi''(\bar{q},\omega_n) \qquad \text{(XI-5)}$$

Here, the spin-lattice relaxation rate depends on whether the fields creating the local electric field gradients are long- or short-range, which determines the $\bar{q}$-dependence of $A_\mu(\bar{q})$. The e.f.g. from point charges or dipoles fall off as r^{-3} or faster. It is therefore reasonable to assume a short-range form for A_μ^i, and thus an $A_\mu(\bar{q})$ which is nearly independent of $\bar{q}$. In ferroelectric transitions the long-wavelength modes get strongly excited near T_C, and the dominant contribution to the sum in Eq. (XI-5) comes from terms with $q \simeq 0$. As a result, one can write

$$\frac{1}{T_{1\ S.L.}} \approx \sum_{\mu n} C_{\mu n} \frac{kT}{2\omega_n} \frac{1}{N_2} |A_\mu(0)|^2 \sum_{\bar{q}} \chi''(\bar{q},\omega_n) \qquad \text{(XI-6)}$$

Equation (XI-6) can be evaluated explicitly for specific models by approximating the sum over all $\bar{q}$'s by an integral over the Brillouin zone. Two models are of relevance here, in light of Kaminow and Damen's results:[73]

One is the purely relaxational or diffusive mode,[75] characterized by the response function:

$$\chi(q,\omega) = \frac{\chi(\bar{q},0)}{1 + i\omega\tau(\bar{q})} \qquad \text{(XI-7)}$$

where

$$\chi(\bar{q},0) = \frac{N}{kT} \cdot \frac{\tau(\bar{q})}{\tau(0)} \; ; \; \tau(\bar{q}) = \frac{\tau_o}{1 - J(\bar{q})/kT}$$

$J(q)$ is the Fourier transform of the dipole-dipole interaction between the Ising spins, while τ_o is the relaxation time with the dipole-dipole interaction turned off. For ferroelectrics where the lattice instability occurs at the Γ point in the Brillouin zone, the general form of $J(q)$ will be

$$J(q) \cong J(0)\ (1 - \alpha q^2 - \delta^2 \cos^2\theta) \qquad \text{(XI-8)}$$

where α and δ are constants, and θ is the angle between q-vector and the axis of ferroelectric polarization.

The other soft mode model is that of the generalized damped oscillator,[76] where the response function is similar in form to that of a single-particle damped oscillator, but with a q-dependent resonance frequency, due to the interaction between the polarizable microscopic units in the ferroelectric. In the limit where the mode frequency $\omega(q)$ always is much higher than the frequencies ω_n, one may

Write the generalized damped oscillator response function

$$\chi(q,\omega) = \frac{\chi(\bar{q},0)\,\omega^2(\bar{q})}{\omega^2(\bar{q}) - \omega^2 + i2\Gamma\omega} \quad \omega << \omega(q) \quad \frac{\chi(q,0)}{1 + i\omega\,\frac{2\Gamma}{\omega^2(\bar{q})}} \tag{XI-9}$$

with

$$\chi(\bar{q},0) = \frac{\lambda}{\omega^2(\bar{q})}$$

Γ is the soft mode damping constant, and λ is a material constant. The soft mode frequency $\omega^2(q)$, defined as the poles of the response function, can be written on the general form

$$\omega^2(\bar{q}) = a(T - T_o) + \gamma_q^2 + \varepsilon \cos^2\theta \tag{XI-10}$$

where anisotropic interaction is introduced through the ε-term. a and γ are constants, and T_o is the critical temperature

$$T_o \equiv J(0)/k$$

Comparison between Eqs. (XI-9) and (XI-7) shows that for $\omega << \omega(\bar{q})$, $\chi(\bar{q},\omega)$ has the same qualitative form for both the diffusive mode and the generalized damped oscillator soft mode, and evaluation of Eq. (XI-6) yields the same type of temperature dependence for the relaxation rate singularities in the two cases. This applies both for isotropic and anisotropic interactions:

$$\text{Isotropic interaction:} \quad T_{1\,\text{S.L.}}^{-1} \propto (T - T_o)^{1/2} \;;\; (T - T_o) \to 0_+ \tag{XI-11}$$

$$\text{Anisotropic interaction:} \quad T_{1\,\text{S.L.}} \propto \ln(T - T_o) + \text{const} \;;\; (T - T_o) \to 0_+ \tag{XI-12}$$

In the theory outlined here, the expression for $T_1^{-1}{}_{S.L.}$ in the case of isotropic interaction, as given in Eq. (XI-11), always applies sufficiently close to the Curie point (for criteria on applicability, see f.ex. Ref. 77). A more general expression for the isotropic case is

$$T_1^{-1}{}_{S.L.} \propto (T - T_c)^{-n} \qquad \text{(XI-13)}$$

where $0.5 \leq n \leq 2$, depending on the distance between the ferroelectric dipoles and on the Brillouin zone size.[77,78]

One must keep in mind that these results pertain to short range source fields for the e.f.g., and should therefore apply well for covalently bonded nuclei. When the e.f.g. is of ionic origin, however, the $A_\mu(\bar{q})$ terms in Eq. (XI-7) may have to be retained in the $\bar{q}$-sum, leading to a weaker singularity at T_o.

In the ferro-phase, an analysis similar to the one outlined above leads to an expression for the relaxation rate singularity at T_c which contains the factor $(1 - p^2)$. p is the order parameter, where $p = 0$ and $p = 1$ correspond to complete disorder and complete order, respectively.

XI-B-2. Analysis of the K^{39} Spin-Lattice Relaxation Data.

A salient feature in the spin-lattice relaxation data in Fig. XI-1 is the strong relaxation rate increase as $T \to T_c$. This increase can be related to the ferroelectric mode, and a brief recapitulation of current knowledge about the lattice dynamics in KDP near the Curie point is in order:

The importance of the proton dynamics was recognized early, due to the strong shift in Curie temperature on deuteration (123°K → 213°K). Theoretical and experimental investigations[67,79,80] have demonstrated that the protons tunnel between two potential wells on each hydrogen bond, and via their mutual couplings, a quasi-spin wave can be set up which exhibits an instability at a critical temperature. Other degrees of freedom for the soft mode atomic displacements must be included, however. The hydrogen bonds are nearly perpendicular to the direction of spontaneous polarization (crystal Z-axis), and protons contribute much less to the ferroelectric polarization than the K^{+}, P^{5+} and O^{-2} ions which in the ferrophase are displaced along the polarization direction.[81] Also, proton ordering cannot explain the magnitude of the isotope effect on the saturated polarization upon deuteration.

An optic-mode model involving displacements of K and PO_4 ions in opposite directions along the Z-axis has also been shown to lead to a phase transition,[82] but experimental evidence seems to favor a coupled mode model, where a phonon mode and a proton tunneling mode interact to bring about the instability. Cochran[83] and Kobayashi[69] have discussed the case of strong coupling between the modes, and found that the frequency of the ferroelectric mode (Cochran ω_{-}-mode, cfr. Fig. XI-2) varies as

$$\omega^2 \propto |T - T_c|$$

in their model for the transition in KDP (cfr. Eq. (XI-10). The same relationship has been found to apply in displacive ferroelectrics. The KDP ferroelectric mode model above leads to a mixed order-disorder and displacive transition.

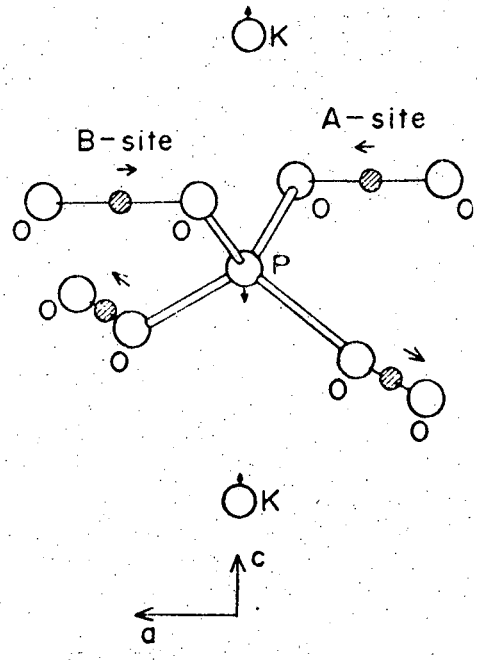

Fig. XI-2. The ferroelectric mode (ω_-) (after K. K. Kobayashi[69]).

Also, theories have been proposed which take into account a temperature dependent decoupling of the phonon and proton tunneling modes at $T \neq T_c$. Thus, the anomalous increase in the e.f.g. at the K^{39} sites as the temperature is increased (cfr. Fig. X-4) can be explained by a gradual increase in phase coherence between the motion of potassium nuclei and protons as $T \to T_c$, in analogy with the results if Blinc, et al. on RbH_2PO_4.[59]

Finally, the Raman scattering experiment of Keminow and Damen[73] should be mentioned, since it is of particular relevance for the following analysis. Kaminow and Damen found the ferroelectric mode in KDP to be overdamped, with a spectral density distribution which peaks strongly around zero frequency as $T \to T_c$. In the range of temperatures and frequencies of interest here ($T - T_c \gtrsim 2°K$; $\omega_n \lesssim 11$ MHz), the spectral density distribution is essentially flat, however. These results have been corroborated by others,[84] and the assumptions made in deriving formulas (XI-11) above should therefore be valid for KDP.

Below, an attempt will be made to extract from the relaxation data on Fig. XI-1 contributions due to different relaxation mechanisms. At least 4 temperature ranges with different temperature dependences can be singled out:

$T \lesssim 110°K$: Relaxation rate nearly temperature independent.
$T \simeq T_c$: Relaxation rate peaks strongly at T_c.
$160°K \lesssim T \lesssim 200°K$: Relaxation rate nearly temperature independent.
$T \gtrsim 200°K$: Relaxation rate steeply increasing with temperature.

It seems easiest to separate out the different contributions to the total relaxation rate by starting in the region:

$\underline{T \lesssim 100°K}$, where the relaxation rate is small ($\simeq 0.04$ sec^{-1}) and nearly temperature independent. This contribution appears due to paramagnetic impurities, in which case a constant relaxation rate contribution is expected throughout the temperature range covered by the present investigation. The rate of 0.04 sec^{-1} seems high compared to the proton relaxation rate $T_{1\,ADRF}^{-1} = 0.05$ sec^{-1} in the same temperature range, in light of the large proton gyromagnetic ratio: $\gamma_{proton}/\gamma_{K39} \approx 21$ (Roughly speaking, the theoretical rate is proportional to γ^2, cfr. Ref. 85). A direct comparison is not strictly relevant, however. From the discussion in Section V-B, one may anticipate that relaxation of K^{39} in the spin-lock state and of protons in the dipolar state after ADRF will depend differently on the spectral density of the perturbing impurity dipolar fields, and different spin diffusion rates may also yield different overall relaxation rates. Comparison with the high-temperature relaxation rates suggests that spin-phonon relaxation below 110°K must be small, and one can at the very least establish the rate 0.04 sec^{-1} as an upper limit for paramagnetic impurity relaxation. This rate is small relative to the total relaxation rates observed above T_c, and the following analysis is relatively insensitive to fractional changes in a background level $\simeq 0.04$ sec^{-1}. Regardless of the relaxation mechanism below 110°K, extrapolation to the region $T \simeq T_c$ and immediately above should not introduce serious errors, due to the steep increase in relaxation rate on approaching T_c from below, which leads to a short extrapolation range.

$110°K \lesssim T \lesssim T_c$: A relaxation rate singularity at T_c is clearly indicated, but the data in this temperature range do not warrant a quantitative analysis. The relaxation rate falls off much more steeply below T_c than above, which might reflect the increase in the order parameter in the ferrophase (cfr. the temperature dependence of the spontaneous polarization in the temperature region immediately below T_c,[86] and the comments at the end of Section XI-B-1).

$T_c \lesssim T \lesssim 160°K$: The relaxation rate increase as T approaches T_c from above suggests that relaxation by the ferroelectric mode is an important or dominant relaxation mechanism in this temperature range.

In order to establish the net relaxation rate due to other mechanisms than paramagnetic impurity relaxation, a constant rate $= 0.04\ sec^{-1}$ was subtracted from the observed rates throughout the paraelectric phase, on the implicit assumption that the observed rate below 110°K is due to paramagnetic impurity relaxation which is temperature independent in the region of interest.

The temperature dependence of the net relaxation rate close to T_c was then compared with those predicted by the expressions Eqs. (XI-12) and (XI-13). The results are shown in Figs. XI-3 and XI-4, where the net relaxation rate $(T_1(K^{39})^{-1} - 0.04)$ $[sec^{-1}]$ is plotted vs temperature, with scales chosen so as to reveal a logarithmic or a power low singularity at T_c, respectively. In both representations a sharp change in temperature dependence is evident at 150-160°K. This can be explained as follows: 150°-160°K constitutes the transition between temperature regions where different relaxation

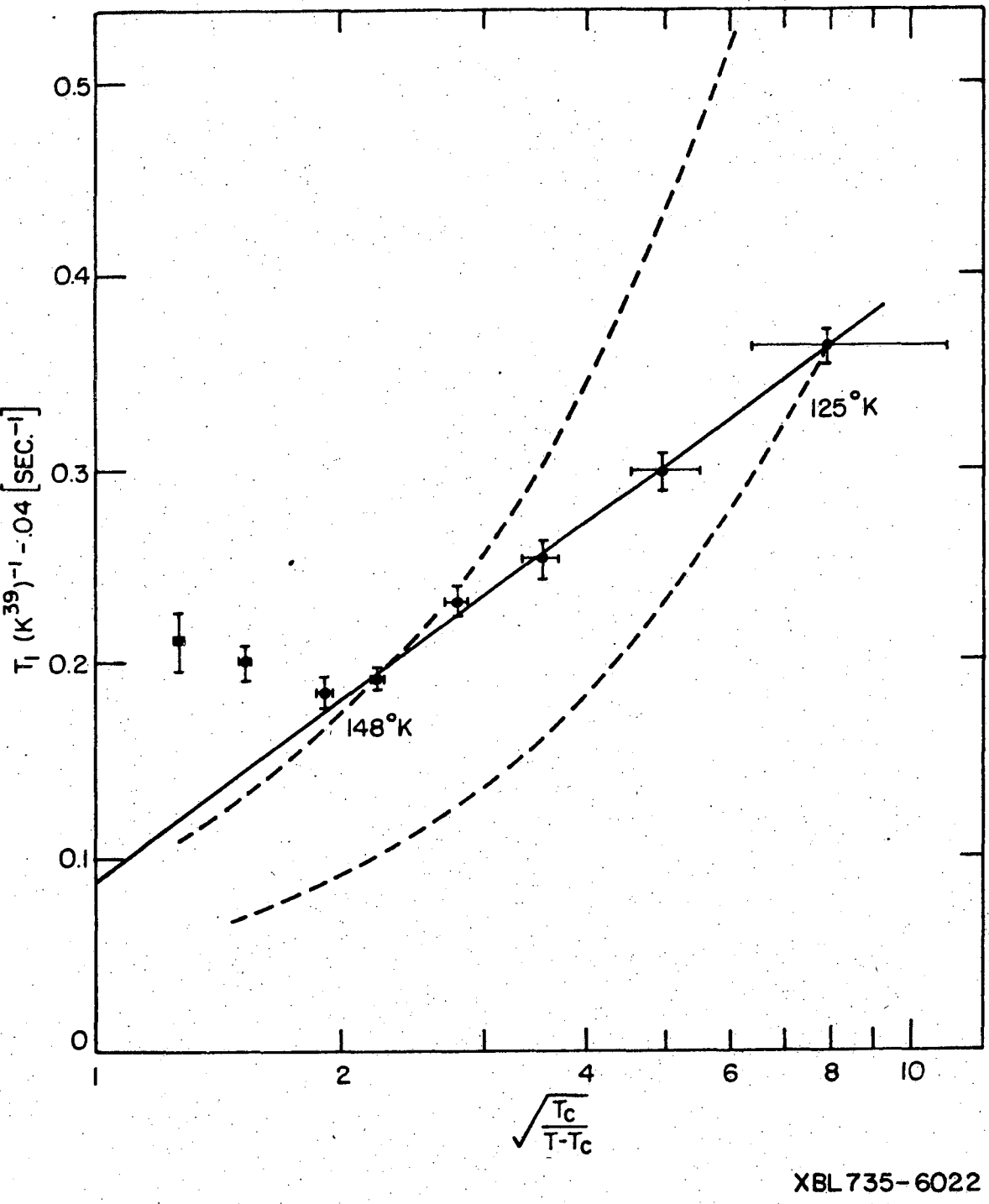

Fig. XI-3. $T_1(K^{39})^{-1} - 0.04\ sec^{-1}$ (from Fig. XI-1) plotted in a semilogarithmic representation. The straight line represents the function: $T_1(K^{39})^{-1} - 0.04\ sec^{-1} = \left(0.131 \ln \sqrt{\frac{T_c}{T-T_c}} + 0.09\right) sec^{-1}$. Functions $A\, T_c / ((T-T_c))^{1/2}$ with A adjusted for best fits at 125°K and 148°K are represented by dashed curves.

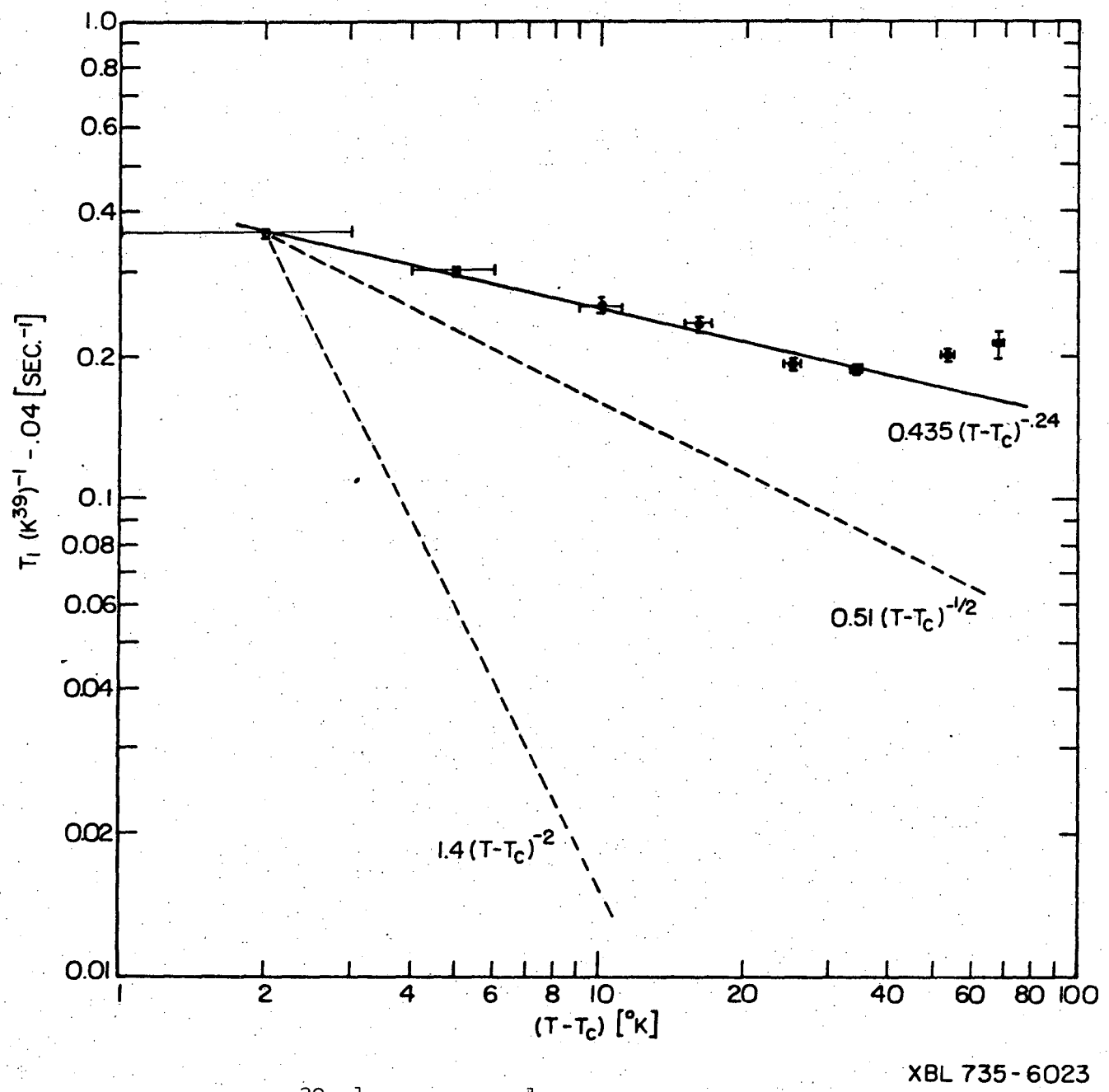

Fig. XI-4. $T_1(K^{39})^{-1} - 0.04\ sec^{-1}$ plotted to reveal possible power law singularity $(T-T_c)^{-n}$, where $1/2 \leq n \leq 2$. Dashed lines represent the limiting cases $n = 1/2$ and $n = 2$, fitted to the 125°K data.

mechanisms are dominant: Below, the largest contribution to the relaxation rate is spin-phonon relaxation by the ferroelectric mode. Above approximately 160°K, other relaxation mechanisms become important, as evidenced by the steep relaxation rate increase at high temperatures. Evaluation of the ferroelectric-mode contribution to the relaxation rate was therefore restricted to the temperature range $T_c \lesssim T \lesssim 160°K$.

From Fig. XI-3 it is seen that the following expression yields a very good fit to the data in this temperature range:

$$(T_1^{-1}(K^{39} - 0.04)\ \text{sec}^{-1} = (0.13\ \ln(T_c/(T - T_c)^{1/2} + 0.09)\ \text{sec}^{-1}. \quad \text{(XI-14)}$$

The dashed curves in Fig. XI-3 represent a power law dependence as given by Eq.(XI-13) with n = 0.5, and with parameters adjusted for optimal fit at 125°K and 148°K. The experimental data indicate a much weaker singularity at T_c than the weakest one compatible with Eq. (XI-13), which corresponds to n = 0.5. This is borne out clearly by the slopes of the straight lines in Fig. XI-4. The data fit indicated by the solid line yields an $n \simeq 0.24$, i.e., well outside the range of n-values compatible with Eq. (XI-13), and the fit is somewhat poorer than that obtained with the logarithmic expression Eq. (XI-14).

Within the framework of the theory outlined above, one can thus conclude that the observed relaxation rates definitely indicate a logarithmic singularity at T_c, corresponding to the heavily damped or diffusive ferroelectric mode model with anisotropic interaction between the ferroelectric dipoles.

$T \gtrsim 160°K$: Here, the relaxation rate is nearly temperature independent up to 210-220°K, and increases sharply at higher temperatures. The increase at high temperatures is in striking contrast to spin-lattice relaxation results obtained on Cs^{133} in CsD_2AsO_4 (cfr. Ref. 87) and on Rb^{85} in RbH_2PO_4 (Ref. 54). These nuclei are located at lattice sites equivalent to those of K^{39} in KDP, and also posses a quadrupole moment.

Analysis of the relaxation behavior at high temperatures was made difficult by the short proton $T_{1\ ADRF}$, which set an upper limit for the temperature at which data could be recorded, and led to the large data spread at 246°K. Another factor is the ferroelectric mode relaxation rate contribution, which is weakly temperature dependent in the model used here, and cannot be neglected in the high temperature region. (With the high-temperature relaxation models considered below, the latter complication was not encountered in extracting the ferroelectric-mode relaxation contribution close to T_c). Extrapolating the logarithmic temperature dependence in Fig. XI-3 to temperatures higher than 160°K, one finds a ferroelectric-mode contribution to the relaxation rate at 240°K which is approximately 0.9 sec^{-1}. This implies that a correction for the ferroelectric-mode contribution must be made throughout the high-temperature range, when trying to determine the relaxation mechanism which dominates in that region. The logarithmic dependence indicated by the straight line in Fig. XI-3 will be used here, since it yielded a good fit with experimental data below approximately 160°K. Other models yielding fits to the experimental data in the range $T_c \leqslant T \leqslant 160°K$ are only expected to lead to significantly different

ferroelectric-mode relaxation rates at temperatures $\gg$160°K, where the ferroelectric-mode contribution to the total relaxation rate is small.

The net high temperature relaxation rate was obtained by subtracting the paramagnetic impurity contribution (0.04 sec^{-1}) and the ferroelectric mode contribution (as given by the straight line in Fig. XI-3) from the observed relaxation rate. As shown in Fig. XI-5, and Fig. XI-6, the net rate is negligible below approximately 160°K and increases strongly at higher temperatures. The spread in experimental data is large, and no positive identification of the dominant high temperature relaxation mechanism is attempted on the basis of data available at present. Some possibilities are listed below.

a) Two-phonon Raman process: Experiments have demonstrated that nuclei possessing an electric quadrupole moment in many cases experience a strong spin-phonon coupling via the fluctuating local e.f.g., leading to spin-lattice relaxation rates that may dominate over those due to other relaxation mechanisms. Quadrupolar relaxation by the direct process was discussed in Section V-B. In the absence of condensation into low frequency modes of the type encountered at $T \simeq T_c$ in KDP, however, the dominant high-temperature spin-phonon relaxation mechanism will be a two-phonon Raman process. Van Kranendonk[42] found the following temperature dependence for Raman quadrupolar relaxation by acoustic modes in ionic solids:

$$T_1^{-1} = aT^2 - b \qquad \text{(XI-15)}$$

where a and b are constants. Equation (XI-15) applies at temperatures

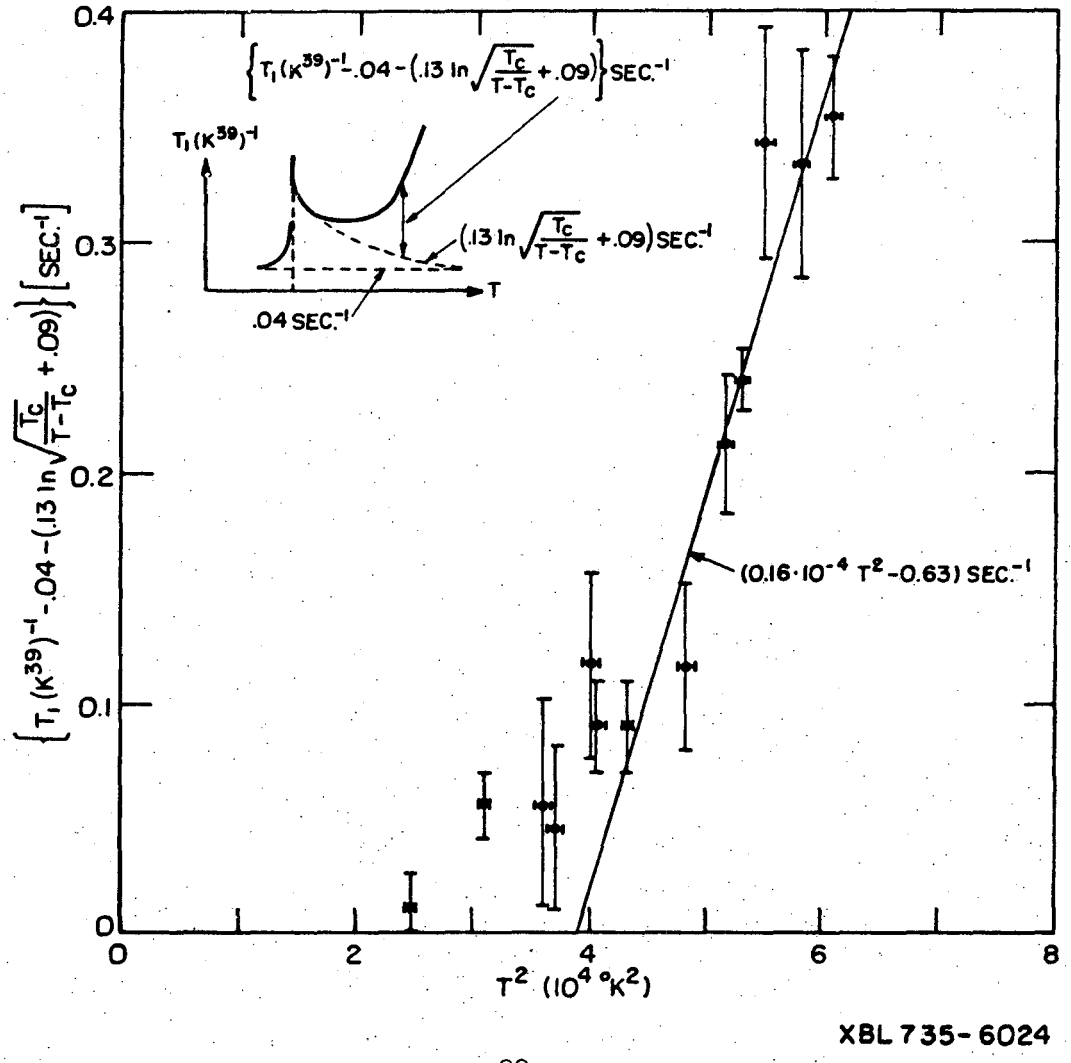

Fig. XI-5. Analysis of K^{39} high temperature spin-lattice relaxation rates, derived from Fig. XI-1 as shown in drawing at upper left. The straight line represents the function $(0.16 \times 10^{-4} T^2 - 0.63)$ sec^{-1} (cfr section on Raman relaxation).

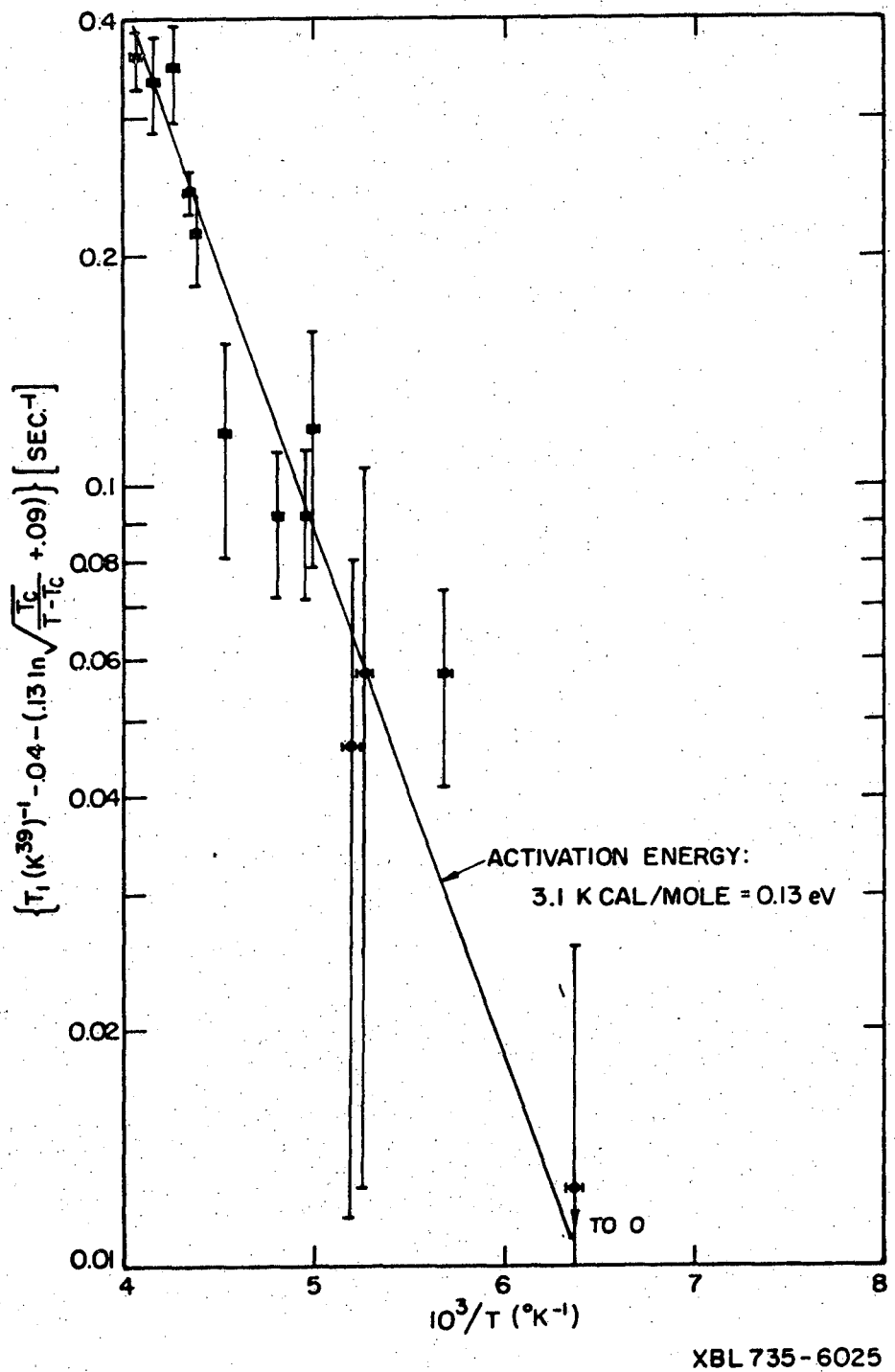

Fig. XI-6. Analysis of K^{39} high temperature spin-lattice relaxation rates derived from Fig. XI-1 as shown in Fig. XI-5. The straight line represents possible motional relaxation with activation energy E_a=0.13 eV.

$T \gtrsim \frac{1}{2}\ \theta_{Debye}$. An induced dipole relaxation mechanism by long-wavelength optical modes was later analyzed by Wikner, Blumberg and Hahn.[41] At high temperatures, their results deviate little from Eq. (XI-15) when the degree of bonding covalency is low. Yosida and Moriya have considered the case of quadrupole relaxation in the case of covalent bonding,[43] which is of little interest in this context since the e.f.g. at the potassium sites in KDP mainly is of ionic origin.

In Fig. XI-5, the experimental results are compared with the relaxation rate temperature dependence in Eq.(XI-15). The net high temperature spin-lattice relaxation rate, defined as {total relaxation rate - relaxation rate due to paramagnetic impurities - ferroelectric mode induced relaxation rate}, is plotted vs. T^2. A best fit to the data above 200°K is obtained with a function of the type in Eq. (XI-15), and with parameters $a = 0.16 \cdot 10^{-4}$ [$sec^{-1}\ °K^{-2}$] and $b = 0.63$ [sec^{-1}].

b) Hindered motion: The net high temperature relaxation rate as defined in a) and Fig. XI-5 increases from zero at temperatures where proton relaxation rates T_{1dip}^{-1} and K^{39} lineshapes with unmodulated B r.f. indicate the onset of slow hindered proton motion. If the K^{39} spin-lattice relaxation rate at high temperatures is dominated by this or some other hindered motion contribution (proton inter-bond migration or K^{39} jumping between quasi-stable sites along the z-axis, f.ex.), then the motional correlation time and thus the spin-lattice relaxation time will depend exponentially on the activation energy E_a in the slow motion regime $\omega_i \tau \gg 1$ (ω_i: nuclear transition frequencies, τ: motional correlation time):

$$T_1^{-1} \propto \exp(-E_a/kT) \qquad \text{(XI-16)}$$

The observed net high temperature relaxation rates should thus lie along a straight line in the plot on Fig. XI-6. As is evident from Fig. XI-6 , a good fit to the experimental data is obtained with a function of the type in Eq. (XI-16) and $E_a = 0.13$ eV.

XI-C. Discussion

Interest will be focused on the mechanisms responsible for the observed strong K^{39} relaxation rate increase at $T \simeq T_c$ and $T \gtrsim 180°K$.

XI-C-1. Relaxation rate anomaly at T_c.

As shown in Figs. XI-3 and XI-4, the ferroelectric-mode induced spin-lattice relaxation rates clearly exhibit a logarithmic (cfr. Eq. (XI-12)) rather than a power law (cfr. Eq. (XI-13)) temperature dependence at T_c and above. Experimental data on spin-lattice relaxation rate anomalies in ferroelectrics near the Curie point T_c are still relatively scarce, but available data generally exhibit logarithmic or weaker relaxation rate singularities at T_c. Blinc and Zumer have observed a logarithmic singularity for P^{31} laboratory frame spin-lattice relaxation in KDP, and attribute the singularity to magnetic dipolar coupling to the ferroelectric mode.[8,88] The magnetic dipolar interaction yields a weak spin-phonon perturbation, and in order to observe the P^{31} relaxation rate anomalies at T_c, exceptionally pure crystals and stable apparatus are required (P^{31} and H^1 are spin 1/2 nuclei, and quadrupolar spin-phonon coupling is absent). In this connection, it is instructive to compare Figs. VIII-1, VIII-2 and XI-1, which show proton relaxation rates in the laboratory frame and in the dipolar state after ADRF, and K^{39} relaxation rates in the spin lock states, respectively. As expected on the basis of the K^{39} quadrupole

coupling to the local e.f.g., the ferroelectric-mode induced spin-lattice relaxation rate is much larger in the K^{39} case, and this was one of the motivating factors for the work presented in this thesis.

KDP does not contain any quadrupolar nuclei which are easily accessible to spin-lattice relaxation measurements by conventional NMR methods, but several isomorphs do. Measurements have been made on deuterons in KD*P, KD*A and CsD_2AsO_4, and on Cs^{133} in CsD_2AsO_4, As^{75} in KH_2AsO_4 and CsH_2AsO_4, and Rb^{87} in RbH_2PO_4.[54,78, 87, 89, 90] The results are generally similar to those for K^{39} above, with logarithmic or near-logarithmic ferroelectric-mode relaxation rate temperature dependences at T_c. For Cs^{133} in CsD_2AsO_4 a relaxation rate singularity somewhat weaker than logarithmic has been reported[87] which was attributed to the ionic character of the sources of the local e.f.g. tensor at the Cs sites (cfr. remarks at the end of Section XI-B-1).

Having established the logarithmic relaxation rate singularity at T_c, indicating strongly anisotropic interaction between the "ferroelectric dipoles", a logical next step would be to relate it to the microscopic structure and atomic motion in KDP. This will not be attempted here. Several possible extensions of the K^{39} spin-lattice relaxation measurements will also have to be left undone due to time and space limitations. Some examples:

a) The theoretical dependence of $T_{1,SL}(K^{39})$ on rotating and laboratory frame transition frequencies was given in Table V-2, for the different allowed transitions. The parameters a, b, c and d can be computed in each specific case, and thus in principle a qualitative measure of the ferroelectric mode spectral density in the low frequency

region could be obtained by varying the rotating frame (or laboratory frame) transition frequencies. This would provide a check on the assumption implicit in the analysis above, of a relaxation perturbation with "white" spectral density at NMR frequencies. This assumption was based on the Raman scattering results of Kaminow and Damen,[73] who found a large and constant ferroelectric mode damping, and a characteristic ferroelectric mode frequency

$$\omega_o/2\pi = (99\ \mathrm{cm}^{-1})\ [(T - T_o)/T]^{1/2}$$

Thus, the ferroelectric mode frequency should be much higher than 11 MHz down to approximately $T_c + 10^{-4}{}^{o}K$, and combined with the large damping this leads to an essentially "white" spectral density at all NMR transition frequencies of interest. A check of this type was made by Bonera, Borsa and Rigamonti[72] on the spin lattice relaxation rate of Na^{23} in $NaNO_3$ at 8 MHz and 84 MHz. They found no clear temperature dependence, indicating that the ferroelectric mode frequency was much higher than the Na^{23} Larmour frequency at all temperatures included in their data.

b) The fluctuating e.f.g. tensor which is responsible for the ferroelectric mode induced spin-lattice relaxation does not necessarily have the same symmetry as that of the static e.f.g. tensor. One possible consequence would be an anisotropic relaxation rate in the Z rotation. Such an anisotropy should be most pronounced close to T_c, where relaxation by the ferroelectric mode dominates over other, isotropic relaxation mechanisms, and the temperature dependence of the anisotropic could be an aid in extracting the ferroelectric-mode

induced relaxation rate from the total observed rate. Given relaxation rate expressions of the type presented in Table V-2, anisotropy data could be used to determine the symmetry and parameter values of the fluctuating e.f.g. tensor, cfr. Ref. 72.

XI-C-2. Relaxation Rate Increase at High Temperatures.

To the author's knowledge, no relaxation rate increase at high temperatures has been reported for any other heavy nuclei in KDP or its isomorphs. Protons (deuterons) represent a special case, since they participate in the hindered rotation of H_2PO_4 groups. The qualitative difference between the K^{39} high temperature relaxation rate reported here and data reported on Rb^{89} and Cs^{133} in the isomorphs RbH_2PO_4 and CsD_2AsO_4 is surprising view of the similarity in crystal structure, ferroelectric properties, etc.

A weak link in the analysis of the high temperature K^{39} relaxation behavior is the subtraction of the ferroelectric-mode induced spin-lattice relaxation rates, as represented by the extrapolated curve in Fig. XI-3, from the total observed rate. Estimated extrapolation errors have been included in Figs. XI-5 and XI-6 below, but these errors do not reflect the possible systematic errors which would be introduced if the ferroelectric-mode induced relaxation rate has a temperature dependence different from logarithmic in the extrapolated region. Some specific high temperature relaxation models are discussed below:

a) Quadrupolar two-phonon spin-lattice relaxation. As is apparent from Fig. XI-5, the relaxation data above approximately 200°K can be described by an expression of the Van Kranendonk form (Eq. (XI-15))

with parameter values as shown, but a separate mechanism must be inferred to explain the data below 200°K. In principle, the parameter values can be computed theoretically, but only a qualitative discussion seems warranted at this stage. The large data spread permits wide latitude in interpretation of the data, and a quantitative analysis would require an effort outside the scope of this work.

The discrepancy between the K^{39} relaxation data of high temperatures, and the cited data for Rb^{87} and Cs^{133} ought to be explainable by qualitative arguments, however. One may note that the K^{39} data pertain to spin-lattice relaxation in the spin-lock state, while the Rb^{87} and Cs^{133} relaxation rates pertain to the laboratory frame. Raman relaxation rates are insensitive to NMR transition frequencies ω_i, however, and in the high temperature approximation ($\hbar\omega_i/kT \ll 1$), the temperature dependence of the Raman relaxation rate enters only through the equilibrium phonon occupation numbers, yielding the general high-temperature results $T_1^{-1} \propto T^2$. This would indicate that the laboratory frame $T_1\ (K^{39})^{-1}$ also should increase rapidly at high temperatures, in qualitative disagreement with the Rb^{87} and Cs^{133} results. A possible explanation is that Rb^{87} and Cs^{133} exhibit the same qualitative relaxation behavior as K^{39}, but that the high-temperature relaxation rate increase is either much weaker or appears at high temperatures where no data are available, due to weaker spin-phonon couplings (quadrupolar Raman relaxation rates are $\propto|Q|^2$, where Q is the nuclear quadrupole moment). Straightforward comparison of quadrupole moments is not sufficient for estimates of the relative relaxation rates, however, due to antishielding effects. No estimates of relative

quadrupolar Raman relaxation rates for K^{39}, Rb^{87} and Cs^{133} in KDP, RbH_2PO_4 and CsD_2AsO_4 will be attempted here.

b) Spin-lattice relaxation by hindered rotation of H_2PO_4 groups has already been identified as the mechanism responsible for the rapid increase in the proton relaxation rate in the dipolar state and at high temperatures (Section VIII-C), and it is interesting to note that the observed onset of the relaxation rate increase occurs at roughly the same temperature for protons and K^{39} (~200°K). An explanation close at hand is to attribute K^{39} slow motion relaxation to hindered H_2PO_4 rotation, since protons contribute to the e.f.g. at the potassium sites. Assuming that an activation energy governed slow motion is responsible for the rapid K^{39} high temperature relaxation rate, one finds an activation energy $E_a = (0.13 \pm 0.04)$ eV. This is much lower than the activation energy $E_a = (0.51 \pm 0.05)$ eV deduced from the proton relaxation data in Fig. VIII-4, which again is much lower than the 5 eV required for proton interbond diffusion. Proton slow motion by H_2PO_4 rotation or interbond diffusion therefore seems unable to account for the observed K^{39} relaxation rate increase at high temperatures.

One possibility is motion of the potassium nuclei themselves. Blinc and Mali have discussed[59] the motion of Rb nuclei in the KDP isomorph RbH_2AsO_4, where Rb occupy sites equivalent to those of K in KDP. They observed a Rb^{87} quadrupole constant which increased with temperature, and showed that this could be attributed to Rb jumping along the crystal Z axis between close-lying equilibrium positions. Associated with the Rb motion they postulated a coupled proton motion along the hydrogen bonds, the degree of Rb and proton motional correlation

being temperature dependent with complete decoupling at high temperatures. An increasing quadrupole coupling constant with increasing temperatures was also observed for K^{39} in KDP (cfr. Section X-A), and K^{39} motion is indicated, in analogy with the Rb motion in RbH_2AsO_4. If the motional correlation time τ is long in the temperature region of interest, than very simple arguments based on the BPP (Bloembergen, Purcell and Pound, cfr. Ref. 19) formula

$$T_1^{-1} = \omega_d^2 \frac{\tau}{1 + \omega_o^2\tau^2} \; (\omega_o\tau \gtrsim\gg 1) \; \left(\frac{\omega_d}{\omega_o}\right)^2 \cdot \frac{1}{\tau} \qquad \text{(XI-17)}$$

offers a straightforward explanation of the differences in high temperature relaxation rates observed for K^{39} on the one hand and Rb^{87} and Cs^{133} on the other. In Eq. (XI-17), ω_d is a measure of the strength of the perturbation causing the relaxation, while ω_o is the NMR transition frequency:

K^{39} spin-lattice relaxation rates were recorded in the spin-lock state, with ω_o = 4.4 kHz, while Rb^{87} and Cs^{133} laboratory frame rates were obtained with ω_o in the MHz range. In the case of slow motion, relaxation rates are inversely proportional to ω_o^2 as is evident from Eq. (XI-17), and this is the basis of the slow motion methods discussed in Section II-C.

Equation (XI-17) also suggests a possible method of discriminating between slow motion and Raman relaxation, since the latter should be independent of ω_o. If slow motion relaxation is dominant at high temperatures, $T_1\,(K^{39})^{-1}$ is expected to be increasingly dependent on ω_o from approximately 190°K and upwards. A systematic check on the frequency dependence was not made, but spot checks at 200°K and 238°K

did indicate a frequency trend in rough agreement with Eq. (XI-17). Thus, at 238°K, the net high temperature relaxation rate increased from (0.36 ± 0.15) sec^{-1} to (0.67 ± 0.3) sec^{-1} on lowering $\omega_o/2\pi$ from 4.15 kHz to 1.9 kHz. The observed ratio: T_1^{-1} (1.90 kHz)/T_1^{-1} (4.15 kHz) = (2.1 ± 1.3) may be compared to the value predicted by Eq. (XI-17): $(4.15 \text{ kHz}/1.90 \text{ kHz})^2 = 4.8$. A close quantitative agreement cannot be expected with the data uncertainties here, but the trend is clear.

XI-D. Concluding Remarks

Within the framework of the theory reviewed in this chapter the analysis of the K^{39} spin lattice relaxation data close to T_c is unambiguous and reveals a ferroelectric mode which is diffusive or heavily damped, and with anisotropic interaction between the ferroelectric dipoles.

Experimental data on the strong relaxation rate increase at high temperatures are difficult to interpret, mostly due to large data scatter, and both Raman spin-phonon and motional relaxation are compatible with the data at high temperatures, but the Raman mechanism yields a poor fit below approximately 200°K. Some simple extensions of the present measurements can be made, however, to aid in a positive identification of the dominant relaxation mechanism at high temperatures:

The $T_1(K^{39})^{-1}$ data in Fig. XI-1 should be supplemented with similar data obtained at different rotating frame transition frequencies ω_i^*. A relaxation rate dependence on ω_i^* could then be interpreted as being due to motional relaxation.

Measurements of spin lock state relaxation rates for Rb^{87} in RbH_2PO_4 and Cs^{133} in CsH_2AsO_4 should be performed to check whether the high temperature relaxation behavior is similar to that reported here

for K^{39} in KDP. If so, slow motion is strongly indicated, which would explain the difference between our $T_1(K^{39})^{-1}$ results and those cited above for Rb^{87} and Cs^{133} spin-lattice relaxation in the laboratory frame.

Several other highly speculative relaxation models might be considered, but sufficient space has already been devoted to the presently available high temperature data.

XII. DOUBLE RESONANCE SPECTROSCOPY ON VERY LOW ABUNDANCE NUCLEAR SPECIES IN KDP. PRELIMINARY RESULTS AND SUGGESTIONS FOR FURTHER WORK

The high-sensitivity double resonance methods described in Chapter III should in principle allow detection of all nuclear species in KDP that possess a magnetic moment, as listed in Table I.2 in the Introduction. Detection of rare spin species was not of primary interest in this thesis, but several transitions not due to H^1, P^{31}, K^{39} or K^{41} were observed during the experiments. Parts of these results are presented here, and may serve as starting points for further investigations.

XII-A. Deuterium

Deuterium has a natural isotopic abundance of $1.56 \cdot 10^{-2}\%$, and cannot be detected by conventional methods. The data that exist on spectra of deuterium in natural abundance are scarce, and mostly limited to organic substances. As of this writing, no detection of deuterium in natural abundance in KDP has been reported, but numerous deuterium magnetic resonance studies have been made on the fully deuterated isomorph KD*P.[50,91-95] Deuterium has a nonzero quadrupole moment, and deuterium spectra therefore contain information about the local electric field gradient tensor. The spectra of deuterium in low abundances are of specific interest in light of the pronounced ferroelectric isotope effect on deuteration.

The first deuterium magnetic resonance study on KD*P was made by Bjorkstam and Uchling.[91] Some of their results of particular relevance here, will be summarized briefly. Only the paraelectric case will be discussed:

Deuterium has spin 1 and therefore 2 transitions which are rendered non-degenerate by the quadrupole interaction. As will be shown in the present case, the quadrupole interaction can be treated as a perturbation on the magnetic dipole interaction with the static field H_o, and to first order the frequency splitting of the degenerate Larmour lines is:

$$(2\Delta\nu)_Z = -\frac{1}{2} k\phi_{ZZ} + \frac{1}{2} k(\phi_{XX} - \phi_{YY}) \cos 2\theta_Z \qquad \text{(XII-1)}$$

in the Z rotation (cfr. Fig. VIII-1). X, Y and Z denote the crystal axes a, b, c shown in Fig. I-1, θ_Z is the angle between H_o and the X axis, and $\phi_{i,j}$ (i,j = X,Y,Z) are the electric field gradients at the center of the hydrogen bonds. K is defined by

$$K \equiv \frac{3eQ}{2h}$$

Expressions for the X- and Y-rotations are obtained from Eq. (XII-1) by permuting the subscripts.

The hydrogen bonds are nearly parallel with the crystal X- and Y-axes, and will be classified as X- or Y-bonds. The bond angle with respect to the XY plane is 0.5°. Crystal symmetry considerations show that the Y (or X) axis is a principal axis for the e.f.g. tensor at the center of X (or Y) bonds. Experimental data revealed that the bond direction is a principal axis, and the third principal axis makes an angle 0.5° with the Z axis. For a general direction of the magnetic field H_o relative to the crystal axes, there are 4 non-equivalent deuterons in each unit cell, and thus altogether 8 transitions. In the special cases where $\vec{H}_o$ is in the XY, YZ or XZ planes, some of the lines coalesce. Thus, in the Z rotation deuterons on the two bonds parallel to the X-axis have common transitions. The same applies for

the two Y-bond deuterons, and 4 transitions are observed in all. In the X- and Y-rotations, deuterous on the bonds parallel to the axis of rotation have common transition frequencies, and there are in general 6 transitions. With the crystal axes defined by X, Y, Z and the e.f.g. tensor principal axes by x, y, z, Bjorkstam and Uehling found the following X-bond deuterium coupling constants in the fully deuterated isomorph KD*P:

$$K\phi_{XX} = 179.2 \text{ kHz} \; ; \; k\phi_{YY} = -85.2 \text{ kHz} \; ; \; k\phi_{ZZ} = -94.0 \text{ kHz}$$

or

$$|eQ\phi_{zz}/h| = \frac{2}{3} K\phi_{zz} = 119.5 \text{ kHz}$$

$$\eta = (\phi_{xx} - \phi_{yy})/\phi_{zz} = 0.049$$

The largest e.f.g. tensor component is thus along the bond direction, and the e.f.g. is slightly asymmetric about that direction. These e.f.g. tensor components represent the time average "seen" by the deuteron during intrabond jumping.

It is now possible to check on the perturbation approach, which only included first order terms. The second order correction is $\Delta\nu_m^{(2)} \approx \frac{(2\Delta\nu)^2}{12} \nu_L(H^2) \approx 0.45$ kHz and thus negligible. Here $(2\Delta\nu) = k\phi_{zz}$ is the maximum splitting between the quadrupole satellites on either side of $\nu_L(H^2)$.

Turning now to deuterium in natural abundance, the symmetry arguments quoted above should apply, assuming no clustering of deuterium. As will be shown below, the change in deuterium spectra was small in going from 100% to 25% deuterium abundance, with all transitions contained in the range ~1600 kHz to ~1780 kHz, in the present field $H_o = 2590$ G. Several double resonance sweeps were made in the range

~1590 kHz to ~1800 kHz on KDP of natural isotopic composition, and some sweeps with $H_o \perp Z$ are shown in Fig. XII-1. The transition at 1769 kHz can be readily identified as K^{39} ⑥, but the remaining line patterns are not consistent with the observed deuterium line patterns in KD*P. A weak line was observed at the deuterium Larmour frequency $\nu_L(H^2) \approx 1690$ kHz. The line was only observed at high B r.f. power levels, and its center frequency did not depend on the crystal orientation or sample temperature ($T \gtrless T_c$), which would be typical characteristics of a deuterium double quantum transition $m = -1 \rightarrow m = +1$. To check on this, the magnetic field H_o was varied within the limits set by the A r.f. system, and the line shift was recorded. The results, shown in Table XII-1, are consistent with the assumption of a deuterium double quantum transition, and reflect no magnetic dipole interaction shift from nearest neighbors.

Table XII.1. Check on field dependence of line at the deuterium Larmour frequency.

Proton Larmour Frequency [kHz]	Orientation	Deuterium Larmour Freq. [kHz]	Observed Line Freq. [kHz]
10985.4	$H_o \parallel Z$	1686.4	1687.3±1.0
10998.4	$H_o \parallel Z$	1688.2	1688.4±1.0
11011.7	$H_o \perp Z$	1690.4	1690.0±1.0

In Fig. XII-2 is shown a recording of this line in the orientation $H_o \parallel Z$. The signal to noise ratios were approximately 10:1 at high B r.f. levels (rotating frame field components $H_{1B} \simeq 14$ gauss), and it is puzzling that the direct deuterium transitions apparently were not observed. To clarify this problem, double resonance measurements were

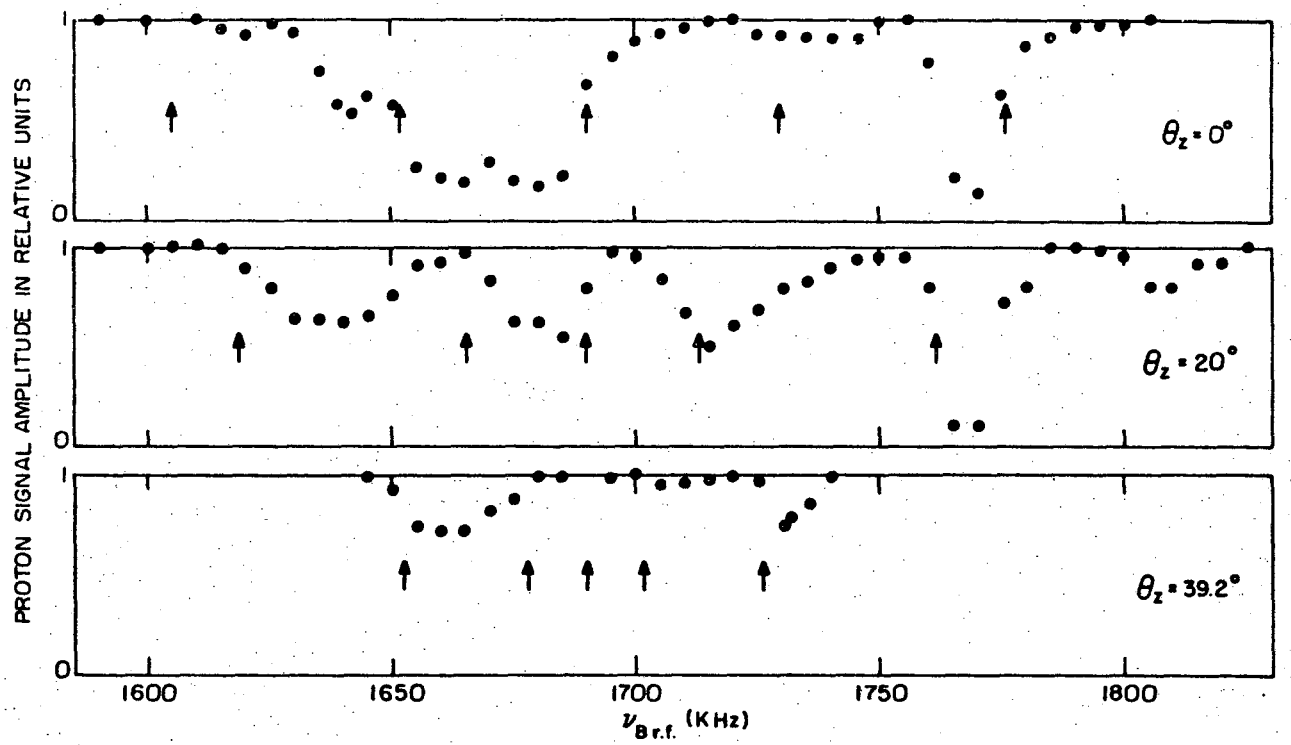

Fig. XII-1. Double resonance sweeps in the Z-rotation ($H_o \perp Z$), for a KDP single crystal of natural isotopic composition. Arrows indicate the observed deuterium transition frequencies in 25% deuterated KDP. H_o = 2590 gauss; H_{1B} = 14 gauss; $t_{B\,r.f.}$ = 15 sec; T = 140°K.

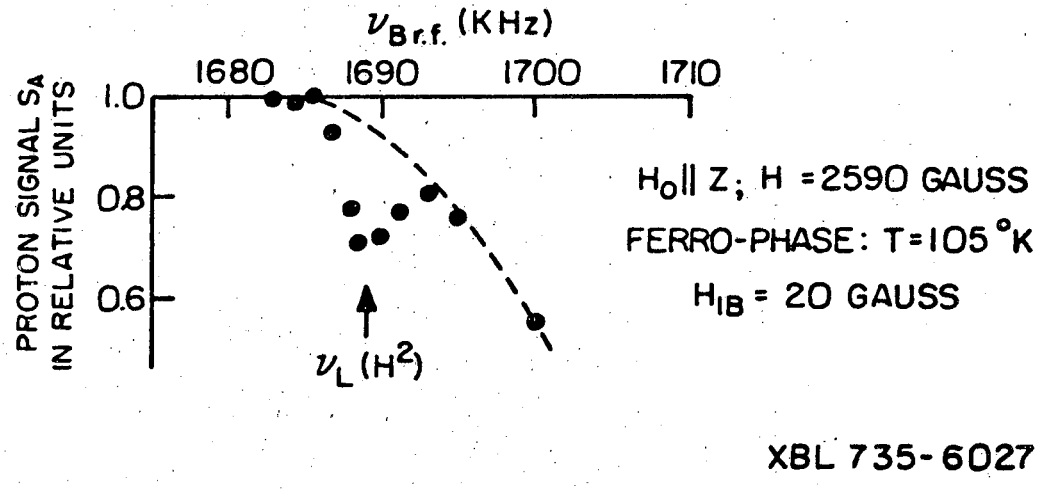

Fig. XII-2. Line at deuterium Larmour frequency, on KDP sample of natural isotopic composition. The broken line shows the flank of the K^{39} ⑥ transition in the ferroelectric phase.

made on KDP samples with deuterium in 25% isotopic abundance. Very strong lines which could readily be identified with deuterium were observed even at low B r.f. power levels (signal/noise 10:1 to 20:1 at $H_{1B} \simeq 1.2$ gauss). The Z-rotation pattern is shown in Fig. XII-3, where the theoretical curves have been fitted according to Eq. (XII-1). High B r.f. power was still required in order to observe the transition at the deuterium Larmour frequency. The Z-rotation in Fig. XII-3 must be supplemented by another rotation pattern in order to determine all three quadrupole coupling parameters $K\phi_{i,i}$ (i = x,y,z), but this was not of specific interest here. The deuterium transitions at the various angles θ_Z in Fig. XII-3 have been indicated in Fig. XII-1, for reference.

One may now try to establish why the double quantum transition was observed for deuterium in natural abundance, while the direct transitions were not. It should be mentioned that a similar case has been reported for naturally abundant deuterium in gypsum,[12] and there is a possibility that a double resonance "quenching" mechanism is responsible. Here, one might recall the "spin quench" effect,[13] where asymmetric field gradients at the deuterium sites lead to expectation value zero for the deuterium angular momentum components and thus no double resonance coupling. Since a magnetic field lifts the quenching, this mechanism cannot be responsible here, however, and the strong deuterium lines observed in the 25% deuterated sample also indicate that no effective $H^1 - H^2$ decoupling is present.

It is possible to determine the expected intersities of the direct transitions ($m = \pm 1 \rightleftharpoons m = 0$) on the basis of the data above: A rough estimate[12] shows that the double quantum and direct transitions should be of equal intersities when the rotating B r.f. field component is

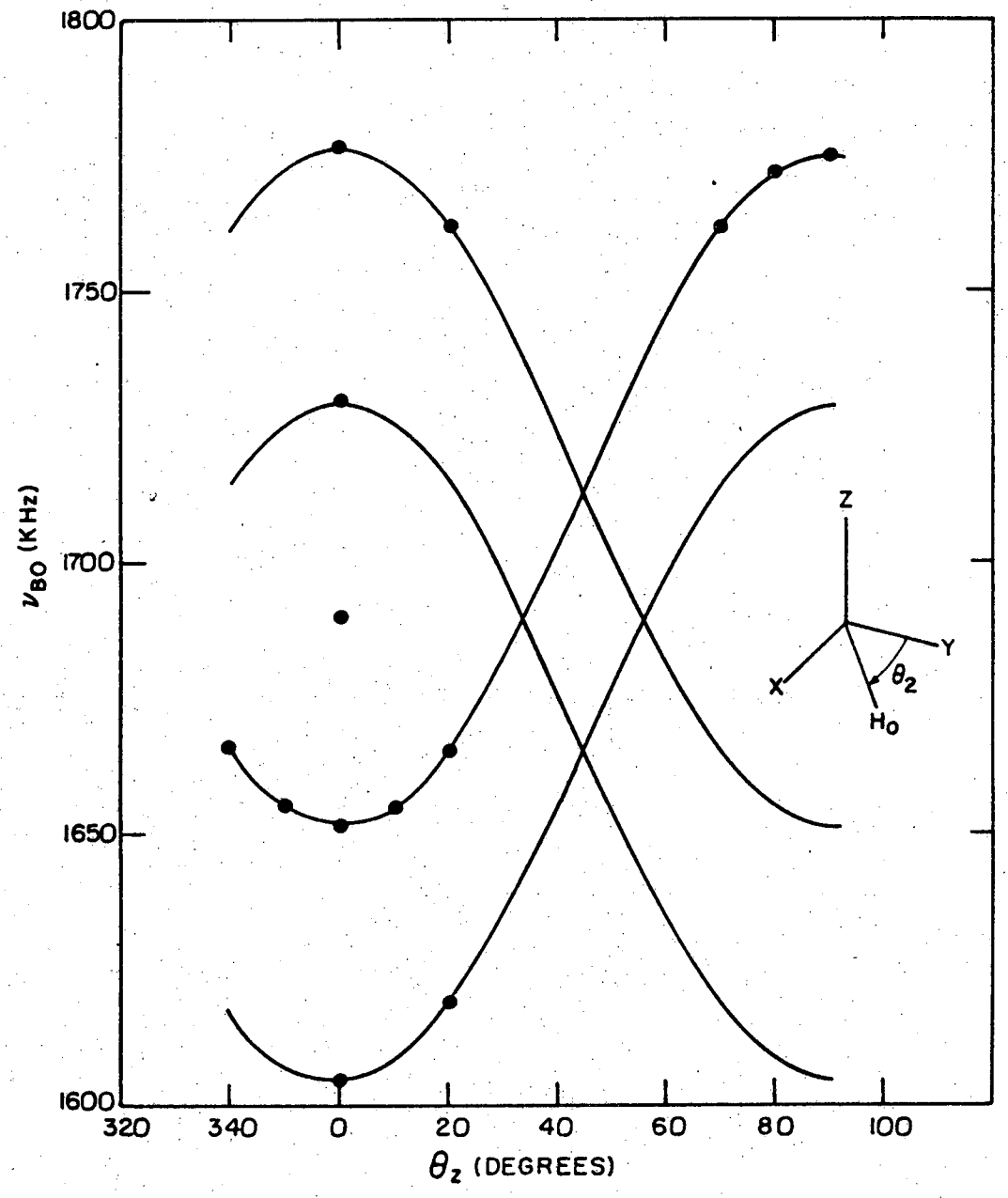

XBL735-6028

Fig. XII-3. Z rotation pattern for deuterons of 25% isotopic abundance in KDP, at T = 191°K and with H_o = 2590 G. The fitted curves correspond to e.f.g. tensor components $K\phi_{zz}$ = -171 kHz and $K(\phi_{xx} - \phi_{yy})$ = 250 kHz in the principal axis system.

$$H_{1B} \simeq 97\ (\mu^2 - 1)\ \text{gauss}$$

where μ is the cosine of the angle between the z principal axis of the e.f.g. tensor and the magnetic field H_o. Thus, for $H_o \parallel X, Y$, direct transitions should be observed with a signal-to-noise ratio at least equal to that of the double quantum transition, which was 5:1 to 10:1 in samples of natural isotopic composition. One must, however, take into account that the direct transitions have linewidths double that of the double quantum transitions. Also, all deuterium nuclei contribute to the double quantum line, while there are up to 4 non-equivalent deuterium sites for a general direction of $\vec{H}_o$ with respect to the crystal axes. In the Z-rotation, there are 2 nonequivalent sites for $\theta_Z \neq 45°$, and including the line broadening effect one arrives at an anticipated signal to noise ratio for direct transitions equal to 1:1 to 3:1. This is so close to the detection limit that it might explain why the transitions were not observed. A more careful investigation is required, however, in order to resolve this problem. Further discussion is deferred to Section XII-C (Suggestions for Further Work).

XII-B. Unidentified Transitions. K^{40} and O^{17}

By elimination, the observed transitions not due to H^1, H^2, P^{31}, K^{39}, K^{41} or higher harmonics of the transitions frequencies of these nuclei should be due to either O^{17} (spin I = 5/2, abundance 3.7×10^{-2}%) or K^{40} (spin I = 4, abundance 1.9×10^{-2}%). Detection of impurities or crystal imperfections is also a possibility. Since no systematic search was made for O^{17} or K^{40}, the results reported here are not complete, but indicate the existence of hitherto undetected nuclear species in KDP which yield easily observable double resonance lines. Some unidentified transitions that were observed are listed in Table XII.2.

Higher harmonics of the proton and phosphorous Larmour frequencies have been excluded.

Table XII.2. Unidentified transitions observed at $H_o \parallel Z$; $H_o = 2583$ gauss; $T = 240°K$.

Center Frequency [kHz]	Line Halfwidth [kHz]	Comments
1100	40	Strong
1216	6	Weak
1224.5	6	Weak
1278	8	Strong
1553	20	Weak
1770	4	Weak
1844	32	Strong
1879	70	Possibly Several Transitions

It is easy to compare these data with the expected K^{40} transition frequencies at this field configuration, since the z principal axis of the e.f.g. tensor at the K^{39} and K^{41} sites is parallel to the crystal Z axis and thus H_o. Assuming that the e.f.g. symmetry to the same at all potassium sites, the energy eigenvalues are:

$$E_m = -\gamma\hbar H_o m + \frac{e^2qQ}{4I(2I-1)}\left(3m^2 - I(I+1)\right)$$

where m is the magnetic quantum number. Using the ratio[96]

$$\frac{Q_{40}}{Q_{39}} = 1.244$$

one finds the following set of K^{40} transition frequencies which can be compared with the data in Table XII.2:

Table XII.3. Theoretical K^{40} transition frequencies in KDP. $H_o \parallel z$; $H_o = 2583$ gauss; $T = 240°K$.

ν_{Bo} [kHz]	ν_{Bo} [kHz]
256	693
365	802
474	911
583	1020

These frequencies do not match any observed transitions. A more systematic and careful search is necessary, however, before it is possible to exclude the possibility of K^{40} detection under the experimental circumstances in question. Double resonance lines for K^{40} are expected to be weak compared to those of K^{39} or K^{41}, due to the large number of K^{40} transitions (spin $I = 4$ leads to 8 allowed transitions at $H_o \parallel Z$), and the lower abundance.

The only isotope in KDP that remains for identification with the transitions in Table XII.2 is O^{17}. Unfortunately, the large number of non-equivalent oxygen sites for a general direction of $\vec{H}_o$ relative to the crystal axes complicates the interpretation of observed spectra. No attempt at analysis will be made here. One may note, however, that if the deuterium quadrupole coupling undergoes no dramatic changes from 25% to natural isotopic abundance, then none of the transitions in Table XII.2 can be due to deuterium. Also, in Fig. XII-1, the asymmetric line pattern about the deuterium Larmour frequency cannot be due to deuterium alone. K^{40} is also ruled out, since the transition frequencies shifted in the Z-rotation (cfr. Fig. XII-1).

XII-C. Suggestions for Further Work

The preliminary data above demonstrate the possibility of obtaining the spectra of spin species not detected before in KDP, which is of some interest in itself. More accurate and complete data complementing those presented above are desirable for more fundamental reasons, however, and a few comments and suggestions are made below in this connection.

H^2: It is still not quite clear why the direct transitions were not observed in the sample of natural isotopic composition. A KDP sample with deuterium in 4% isotopic abundance was prepared in order to study the deuterium spectra at this concentration, but time did not allow this project to be carried further. If necessary, one could prepare several samples with deuterium abundance between 25% and the natural abundance, and monitor the deuterium lines as the abundance was lowered. One important parameter, the deuterium linewidth, could then be monitored as a function of deuterium concentration. Some line broadening is expected due to the increased local dipolar fields as the proton concentration increases ($\gamma(H^1)/\gamma(H^2) = 6.5$), and in certain cases this may be important for the deuterium detectability.[93] A possible shift in e.f.g. parameters with the degree of deuteration might also be of interest (f.ex. with respect to deuterium/proton dynamics). The slight discrepancy between the e.f.g. tensor components for the 25% deuterated sample (above) and in the fully deuterated case (Ref. 91) could thus be an isotope effect, but further measurements are required to establish a possible trend.

K^{40}: No new information about e.f.g. symmetry or strength at potassium sites is expected from the K^{40} spectra, but data on the quadrupole moment $Q(K^{40})$ are sparse, and an independent determination

of $e^2qQ(K^{40})/e^2q(K^{39})$ would be of interest.

O^{17}: Apart from impurities, O^{17} is the most likely candidate for explaining the unidentified resonances. The first detection of O^{17} in natural abundance was made recently[97] in various quinones, and few data on O^{17} quadrupole coupling parameters exist so far. In KDP, e.f.g. tensor data for oxygen sites would have a bearing on the degree of distortion of PO_4 tetrahedra, and the contribution to the e.f.g. tensor from the hydrogen bond is also of interest. The large number of O^{17} transitions for a general direction of the magnetic field $\vec{H}_o$ relative to the crystal axes makes interpretation difficult, as long as all observed transitions cannot be possitively associated with O^{17}. Several simplifying considerations can be made, however. In the special case where $H_o \parallel Z$, f.ex., all O^{17} in the unit cell yield the same set of transitions. Discrimination against K^{40} transitions can easily be made by checking whether the frequencies shift in the Z-rotation. An example of this is shown in Fig. XII-1, where the K^{39} ⑥ transition is stationary at 1769 kHz, while the other transitions shift with θ_Z. An additional aid in identifying transitions is the use of audio resonance saturation once all transitions have been localized: Overlapping transitions are more easily resolved by audio resonance than f.ex. by phase shifted B r.f. due to the narrow audio resonance lines. Discrimination can also be made in certain cases when the effective gyromagnetic ratios in the rotating frames differ significantly.

ACKNOWLEDGEMENT

The author would like to express his sincere appreciation to Professor E. L. Hahn for his continuous encouragement and guidance. Doing physics in Professor Hahn's group has been a stimulating and colorful experience, and I am indebted to many members of the group, past and present, for the benefit I have reaped from discussions and for help and advice in experimental matters.

Most particularly, I wish to thank Dr. D. Stehlik for his active interest and helpful suggestions throughout this work. I am grateful to Dr. R. Hilt for experimental help and enlightening discussions.

I am indebted to Shirley Ashley and Jean Wolslegel at the LBL Inorganic Materials Research Division, who have been exceedingly helpful and competent in all matters regarding the thesis preparation.

Finally, I would like to thank my wife for her support during this work, and for cheerfully accepting the hardships that befall a graduate student's wife.

This work was supported at various stages by the U. S. Atomic Energy Commission, the National Science Foundation and the Norwegian Council for Science and the Humanities (NAVF).

APPENDIX A
EIGENVECTORS AND DIAGONALIZING MATRIX FOR THE HAMILTONIAN $H_o = H_Q + H_Z$ OF CHAPTER V

As shown in Section V-A, the hamiltonian $\frac{1}{\gamma H_o}\mathcal{H}_o = \frac{1}{\gamma H_o}(\mathcal{H}_Q + \mathcal{H}_Z) = \frac{\lambda}{2}(3I_Z^2 - \frac{15}{9}) - I_x$ has eigenvectors $|E\rangle_i = (\alpha_i, \beta_i, \gamma_i, \delta_i)_A$ in the representation where I_z is diagonal, and the following relationships hold:

$$\beta_i = \frac{2}{\sqrt{3}} A_i \alpha_i \; ; \; \gamma_i = -\frac{\sqrt{3}}{2}\alpha_i - \frac{2}{\sqrt{3}} A_i B_i \alpha_i \; ; \; \delta_i = -\frac{3}{4}\frac{1}{A_i}\alpha_i - B_i\alpha_i$$

$$A_i = \frac{3}{2}\lambda - T_i \; ; \; B_i = \frac{3}{2}\lambda + T_i$$

$$T_{1,2} = \frac{1}{2}\left(-1 \pm \sqrt{4 + 6\lambda + 9\lambda^2}\right) \; ; \; \text{Root 1: } + \quad \text{Root 2: } -$$

$$T_{3,4} = \frac{1}{2}\left(1 \pm \sqrt{4 - 6\lambda + 9\lambda^2}\right) \; ; \; \text{Root 3: } + \quad \text{Root 4: } -$$

The 16 different vector components are interrelated, and as will be shown, the number of different components is 4 for the case of general λ.

First, consider components which belong pairwise to the same vector. Using the notation $\beta_{1,2} = \gamma_{1,2}$ for $\beta_1 = \gamma_1$ and $\beta_2 = \gamma_2$, it is easy to show:

$$\alpha_{1,2} = \delta_{1,2} \; ; \; \beta_{1,2} = \gamma_{1,2} \; ; \; \alpha_{3,4} = -\delta_{3,4} \; ; \; \beta_{3,4} = -\gamma_{3,4} \qquad \text{(A-1)}$$

Take, for example, $\alpha_{1,2} = \delta_{1,2}$. From the above, one has:

$$\delta_{1,2} = -\frac{1}{A_{1,2}}\left(\frac{3}{4} + A_{1,2}\cdot B_{1,2}\right)\alpha_{1,2} = -\frac{1}{\frac{3}{2}\lambda - T_{1,2}}\left(\frac{3}{4} + \frac{9}{4}\lambda^2 - T_{1,2}^2\right)$$

Using the secular equation in factored form which corresponds to roots 1 and 2, (Eq. (V-7)), one can substitute for $T_{1,2}^2$.

The result is:

$$\delta_{1,2} = \frac{-1}{\frac{3}{2}\lambda - T_{1,2}} \left(\frac{3}{4} + \frac{9}{4}\lambda^2 + T_{1,2} - \frac{3}{4} - \frac{3}{2}\lambda - \frac{9}{4}\lambda^2\right) \alpha_{1,2} = \alpha_{1,2}$$

For components belonging to different vectors, one can show:

$$\alpha_1 = \beta_2 \; ; \; \alpha_2 = -\beta_1 \; ; \; \alpha_3 = \beta_4 \; ; \; \alpha_4 = -\beta_3 \qquad \text{(A-2)}$$

Since orthonormal vectors are needed for the diagonalization matrix, one must have, using the results above,

$$\begin{aligned} &\text{Vectors 1,2: } (\alpha_i, \beta_i, \beta_i, \alpha_i)_A \quad \text{Normalization: } (\alpha_i^2 + \beta_i^2) = \frac{1}{2} \\ &\text{Vectors 3,4: } (\alpha_i, \beta_i, -\beta_i, -\alpha_i)_A \quad \text{Normalization: } (\alpha_i^2 + \beta_i^2) = \frac{1}{2} \end{aligned} \qquad \text{(A-3)}$$

Thus for all vectors:

$$\alpha_i = \frac{1}{\sqrt{2\left(1 + \frac{4}{3}A_i^2\right)}} \; ; \; \beta_i = \frac{2}{\sqrt{3}} A_i \alpha_i = \frac{\text{sgn}\,(A_i)}{\sqrt{2\left(1 + \frac{3}{4}\frac{1}{A_i^2}\right)}} \alpha_i \qquad \text{(A-4)}$$

The expression for α_i establishes normalization of each vector. $\alpha_1 = \beta_2$ if, for all λ:

$$\text{Sgn}\,(A_2) = +$$

$$\frac{4}{3}A_1^2 = \frac{3}{4}\frac{1}{A_2^2} \quad , \quad \text{or } A_1 A_2 = \pm \frac{3}{4}$$

The first condition obviously holds since λ is always positive:

$$A_2 = \frac{3}{2}\lambda + \frac{1}{2}\left(1 + \sqrt{4 + 6\lambda + 9\lambda^2}\right).$$

Secondly:

$$A_1 A_2 = \left(\frac{3}{2}\lambda - T_1\right)\left(\frac{3}{2}\lambda - T_2\right) = -\frac{3}{4} \; .$$

Analogously, one finds:

$$\text{Sgn}\ (A_1) = - \ ; \ \text{Sgn}\ (A_3) = - \ ; \ \text{Sgn}\ (A_4) = + ; \ \text{and} \ A_3 A_4 = -\frac{3}{4}$$

which establishes the rest of Eq. (A-2).

Together, Eq. (A-1) and (A-2) reduces the 16 components to 4 sets of different components. The quantities a, b, c and d are defined by

$$a = \alpha_1 \equiv \delta_1 = \beta_2 = \gamma_2 \qquad b \equiv \alpha_2 = \delta_2 = -\beta_1 = -\gamma_1$$

$$c = \alpha_3 \equiv -\delta_3 = \beta_4 = -\gamma_4 \qquad d \equiv \alpha_4 = -\delta_4 = -\beta_3 = \gamma_3$$

The transformation matrix from the representation where I_z is diagonal (called the A representation in V-A) to the eigen-representation of $H_o = H_Q + H_Z$ (B representation) is therefore:

$$U_{AB} = \begin{pmatrix} a & b & c & d \\ -b & a & -d & c \\ -b & a & d & -c \\ a & b & -c & -d \end{pmatrix} .$$

Obviously, the eigenvectors are mutually orthogonal. Since a, b, c and d are real, U_{AB} is orthogonal: $U_{AB}^{-1} = \tilde{U}_{AB}$.

APPENDIX B
ROTATING-FRAME ENERGY IN A STRONG r.f. FIELD. SUDDEN APPROXIMATION

An intuitive understanding of the problem can best be obtained by looking at a simple system first, namely that of a spin 1/2 nuclear species with no quadrupole moment, in a high static magnetic field $H_o \parallel x$.

Assume that the spins are allowed to reach a state of thermal equilibrium, characterized by Boltzmann distributed energy level populations and the absence of macroscopic phase coherence between spins. In this state, there will be a macroscopic magnetization

$$M_x = C H_o/T \tag{B-1}$$

where C is the Curie constant (the field configuration is chosen so as to conform to that in Chapter V).

Here, one will make use of the "sudden approximation": if a strong C.W. r.f. field is turned on in a time $\ll \gamma H_1$, where $\vec{H}_1$ is the rotating r.f. field vector, then the state of the system immediately after application of the r.f. field will be approximately equal to that preceding the pulse.

The magnetization (Eq. (B-1)) will remain unchanged after transformation into a rotating frame where the r.f. field vector is stationary. If the r.f. frequency is $\omega (\simeq \omega_o \equiv \gamma H_o)$, the magnetization M_x will couple to the off-resonance part of the rotating-frame effective field

$$H_{eff.} = [H_1^2 + (\omega_o - \omega)^2/\gamma^2]^{1/2} \equiv [H_1^2 + \Delta\omega^2/\gamma^2]^{1/2}$$

to yield the initial rotating-frame energy

$$E_o = - \frac{C H_o \Delta\omega}{\gamma T} \tag{B-2}$$

Thus, exactly on resonance, $E_o = 0$, and E_o will be positive or negative depending on the sign of $\omega_o - \omega$. The result (Eq. (B-2)) is also obtained by a quantum mechanical analysis.

One may now proceed to the more difficult case of spin systems where quadrupole and Zeeman laboratory frame interactions are of arbitrary relative magnitudes, and where the field configuration is as described in Chapter V. In this case, an intuitive classical description is no longer possible. Instead of the simple rotating frame in the pure Zeeman case, one must now seek out the frame of reference where the full hamiltonian including the r.f. perturbation has a non-vanishing time average, which is necessary for the existence of time independent "rotating-frame" energy and eigenstates. This is achieved by transformation into a representation where the hamiltonian becomes static (with the exception of high-frequency terms due to other transitions or a counter-rotating r.f. field vector).

As an example, take the case of an r.f. field exciting transitions between states 1 and 4 as defined in Chapter V. In the interaction representation of the static laboratory frame quadrupole and Zeeman hamiltonian $\mathcal{H}_o$, the total hamiltonian can be written (cfr. Eq. (V-)):

$$\mathcal{H}_{r.f.*} = -\gamma_{eff.}\,\hbar\, H_1 \begin{pmatrix} 0 & 0 & 0 & \exp(i\Delta\omega t) \\ 0 & 0 & 0 & 0 \\ 0 & 0 & 0 & 0 \\ \exp(-i\Delta\omega t) & 0 & 0 & 0 \end{pmatrix}_B \qquad (B\text{-}3)$$

B is the eigenrepresentation of $\mathcal{H}_o$, and one has defined

$$\Delta\omega \equiv (E_1 - E_4)/\hbar - \omega$$

$$\gamma_{eff} \equiv \gamma_{LAB}^2(3ad - bc)$$

It is assumed that $\omega \simeq (E_1 - E_4)/\hbar$, so that matrix elements corresponding to other transitions can be neglected.

In Eq. (B-3), a nonzero $\Delta\omega$ will make $\mathcal{H}^*_{r.f.}$ time dependent. In that case, it is possible to transform into a new interaction representation, and it is convenient to write (henceforth, zero matrix elements will not be written explicitly):

$$\mathcal{H}^*_{r.f.} = -\frac{1}{2}\gamma_{eff}\hbar H_1\left[\cos\Delta\omega t\begin{pmatrix} & 1\\ 1 & \end{pmatrix}_B + i\sin\Delta\omega t\begin{pmatrix} & 1\\ -1 & \end{pmatrix}_B\right]$$

Defining the following 4 by 4 matrices in analogy with the Pauli spin matrices σ_x, σ_y, σ_z:

$$\Gamma_x \equiv \frac{1}{2}\begin{pmatrix} & 1\\ 1 & \end{pmatrix}_B;\quad \Gamma_y \equiv \frac{1}{2}\begin{pmatrix} & -i\\ i & \end{pmatrix}_B;\quad \Gamma_z \equiv \frac{1}{2}\begin{pmatrix} 1 & \\ & -1\end{pmatrix}_B$$

the same commutation and multiplication rules apply, and in particular:

$$\exp(-i\Gamma_z\phi)\,\Gamma_x\exp(i\Gamma_z\phi) = \Gamma_x\cos\phi + \Gamma_y\sin\phi$$

One may then write

$$\mathcal{H}^*_{r.f.} = -\gamma_{eff}\hbar H_1[\cos\Delta\omega t\cdot\Gamma_x - \sin\Delta\omega t\cdot\Gamma_y]$$

$$= -\gamma_{eff}\hbar H_1\exp(i\Gamma_z\Delta\omega t)\,\Gamma_x\exp(-i\Gamma_z\Delta\omega t)$$

Recalling the interaction representation transformation formula for general $\mathcal{H}_1$ $\mathcal{H}_o$ and F(t) :

$$\mathcal{H}^{*} = \exp(iF(t)/\hbar)\, \mathcal{H}_{o}\, \exp(-iF(t)/\hbar) - dF/dt$$

one obtains in the present case with $F(t) = -\Gamma_z \Delta\omega\hbar t$

$$\begin{aligned} \mathcal{H}^{**}_{r.f.} &= -\gamma_{eff}\, \hbar\, H_1 \Gamma_x + \Delta\omega\, \Gamma_z \\ &= -\gamma_{eff}\, \hbar\, H_1 \begin{pmatrix} & 1 \\ 1 & \end{pmatrix}_B + \hbar\Delta\omega \begin{pmatrix} 1 & \\ & -1 \end{pmatrix}_B \end{aligned} \tag{B-4}$$

Here, all time dependence has been transformed out.

The energy in this interaction representation can be evaluated by:

$$E^{**}_{o} = N_B \mathrm{Tr}(\rho^{**}\, \mathcal{H}^{**}_{r.f.}) \tag{B-5}$$

where ρ^{**} is the density matrix and N the number of nuclei. In the laboratory frame:

$$\rho = \frac{1}{Z} \exp(-\mathcal{H}_o/kT)$$

where

$$\mathcal{H}_o = \mathcal{H}_{\text{Quadrupole}} + \mathcal{H}_{\text{Zeeman}}$$

and Z is the partition function. Obviously,

$$\rho^{*} = \exp(i\mathcal{H}_o t/\hbar)\, \rho\, \exp(-i\mathcal{H}_o t/\hbar) = \rho$$

and one also finds

$$\rho^{**} = \rho^{*} = \rho\ . \tag{B-6}$$

In the thermal equilibrium state immediately before application of the r.f. pulse, ρ will be diagonal in the B representation, and one has trivially:

$$\rho = \frac{1}{Z}\begin{pmatrix} \exp(-E_1/kT) & & \\ & \exp(-E_2/kT) & \\ & & \exp(-E_3/kT) \\ & & & \exp(-E_4/kT) \end{pmatrix}_B \qquad \text{(B-7)}$$

Combining Eqs. (B-4), (B-5), (B-6) and (B-7), one obtains:

$$E_o^{**} = N_B \frac{\hbar\Delta\omega}{Z} (\exp(-E_1/kT) - \exp(-E_4/kT)) \qquad \text{(B-8)}$$

In the high temperature approximation,

$$Z \simeq \mathrm{Tr}\ 1 = 2I + 1 = 4$$

and

$$E_o^{**} \simeq \frac{N_B \hbar\Delta\omega(E_4 - E_1)}{4kT} \qquad \text{(B-9)}$$

Extension to the other laboratory frame transitions is trivial. From Eqs. (B-8) and (B-9) it is apparent that $E_o^{**} = 0$ for $\Delta\omega = 0$, which could have been ascertained directly from Eq. (V-14), using Eq. (B-5). As in the case of a pure Zeeman laboratory frame hamiltonian, E_o^{**} changes sign as $\Delta\omega$ is swept through zero.

REFERENCES

1. F. Jona and G. Shirane, Ferroelectric Crystals (Pergamon Press, Oxford, London, New York, Paris, 1962).

2. L. D. Landau and E. M. Lifshitz, Statistical Physics (Pergamon Press, London-Paris 1958) Vol. 5.

3. H. Thomas, Proceedings from Meeting on Theory of Condensed Matter, Trieste, 1967 (Vienna IAEA, 1968) p. 357.

4. W. Cochran, Adv. in Physics 18, 157 (1969).

5. E. J. Samuelsen, E. Andersen and J. Feder, eds., Structural Phase Transitions and Soft Modes, in Proceedings of NATO Advanced Study Institute, Geilo, Norway, 1971 (Universitetsforlaget, Oslo, 1971).

6. J. des Cloiseaux, Proceedings of the International Course on the Theory of Condensed Matter, Trieste, 1967 (International Atomic Energy Agency).

7. Landolt Börnstein Tables, New Series, Ferro- and Antiferroelectric Substances, K. H. Hellwege, ed. (Springer Verlag, Berlin, Heidelberg and New York, 1969) Vol. 3, p. 29.

8. R. Blinc and S. Zumer, Phys. Rev. Letters 21, 1004 (1968).

9. D. Stehlik and P. E. Nordal, Proceedings of the XVI Congress AMPERE, Bucharest, 1970, p. 355.

10. A. G. Redfield, Phys. Rev. 98, 1787 (1955).

11. D. A. McArthur, E. L. Hahn and R. E. Walstedt, Phys. Rev. 188, 609 (1969).

12. D. A. McArthur, Nuclear Double Resonance Dynamics (Ph. D. Thesis), UCRL-17468, July 1967.

13. C. J. Gabriel, G. W. Leppelmeier and E. L. Hahn, Bull. Am. Phys. Soc. 9, 733 (1964).

14. J. Jeener, Advances in Magnetic Resonance, Vol. 3, p. 205 (1968).

15. M. Goldman, Spin Temperatures and Nuclear Magnetic Resonance in Solids (Oxford University Press, London and New York 1970).

16. A. Abragam and W. G. Proctor, Phys. Rev. 109, 1441 (1958).

17. J. G. Powles, Contemporary Physics 4, 338 (1962-63).

18. A. Abragam, The Principles of Nuclear Magnetism (Oxford-at-the-Clarendon Press, Oxford, England, 1961).

19. N. Bloembergen, E. M. Purcell and R. V. Pound, Phys. Rev. 73, 679 (1948).

20. W. I. Goldburg, Phys. Rev. 122, 831 (1961).

21. C. P. Slichter and W. C. Holton, Phys. Rev. 122, 1701 (1961).

22. A. G. Anderson and S. R. Hartmann, Phys. Rev. 128, 2023 (1962).

23. C. P. Slichter, Principles of Magnetic Resonance (Harper and Row, New York, 1963).

24. A. G. Anderson and S. R. Hartmann, Magnetic Resonance and Relaxation, J. Smidt, ed. (North-Holland Publishing Co., Amsterdam, 1963).

25. B. N. Provotoroff, Soviet Physics JETP 15, 611 (1962).

26. J. Philippot, Phys. Rev. 133A, 471 (1964).

27. J. Jeener, H. Eisendraht and R. Van Steenwinkel, Phys. Rev. 133A, 478 (1964).

28. W. K. Rhim, A. Pines and J. S. Waugh, Phys. Rev. 3, 684 (1971) and Phys. Rev. Letters 25, 218 (1970).

29. A. Abragam, op. cit., p. 35.

30. M. Schwab, Nuclear Magnetic and Nuclear Quadrupole Double Resonance in Solids (Ph. D. Thesis), UCRL-18278, July 1968.

31. D. C. Ailion, Advances in Magnetic Resonance, Vol. 5, p. 177 (1971).

32. C. P. Slichter and D. Ailion, Phys. Rev. 135A, 1099 (1964).

33. A. Abragam, op. cit., p. 272.

34. G. W. Leppelmeier and E. L. Hahn, Phys. Rev. 142, 179 (1966).

35. S. R. Hartmann and E. L. Hahn, Phys. Rev. 128, 2042 (1962).

36. M. Schwab and E. L. Hahn, J. Chem. Phys. 52, 3152 (1970).

37. D. V. Lang and P. R. Moran, Phys. Rev. B1, 53 (1970).

38. R. E. Slusher and E. L. Hahn, Phys. Rev. 166, 332 (1968).

39. R. M. Wilcox, J. Math. Phys. 8, 962 (1967).

40. P. M. Parker, J. Chem. Phys. 24, 1096 (1956).

41. E. G. Wikner, W. E. Blumberg and E. L. Hahn, Phys. Rev. 118, 631 (1960).

42. J. Van Kranendonk, Physica 20, 781 (1954).

43. K. Yosida and T. Moriya, J. Phys. Soc. (Japan) 11, 33 (1956).

44. J. Kondo and J. Yamashita, J. Phys. Chem. Solids 10, 245 (1959).

45. A. Abragam, op. cit., p. 279.

46. G. W. Leppelmeier (Ph. D. Thesis), University of California, Berkeley.

47. J. J. Lowe and C. E. Tarr, A Fast Recovery Probe and Receiver for Pulsed NMR Spectroscopy. Report on research sponsored by the Air Force Office of Scientific Research, Office of Aerospace Research, U. S. A. F. under A. F. O. S. R. grant No. 196-66.

48. Y. Tsutsumi, M. Kunitomo, T. Terao and T. Hashi, J. Phys. Soc. (Japan) 26, 16 (1969).

49. R. Blinc, Advances in Magnetic Resonance, Vol. 3, p. 141 (1968).

50. V. H. Schmidt and E. A. Uehling, Phys. Rev. 126, 447 (1962).

51. R. Blinc and J. Pirs, J. Chem. Phys. 54, 1535 (1971).

52. M. O'Keefe and C. T. Perrino, J. Phys. Chem. Solids 28, 211, 1086 (1967).

53. R. Blinc, V. Dimic, D. Kolar, G. Lahajnar, J. Stepisnik, S. Zumer and N. Vene, J. Chem. Phys. 49, 4996 (1968).

54. R. Blinc, private communication.

55. Y. Tsutsumi, J. Phys. Soc. (Japan) 25, 1576 (1968).

56. M. Kunitomo, T. Terao, Y. Tsutsumi and T. Hashi, J. Phys. Soc. (Japan) 22, 945 (1967).

57. L. C. Brown and P. M. Parker, Phys. Rev. 100, 1764 (1955).

58. M. Kunitomo, T. Terao and T. Hashi, Physics Letters 31A, 14 (1970).

59. R. Blinc and M. Mali, Phys. Rev. 179, 552 (1969).

60. L. C. Gupta and V. U. S. Rao, Physics Letters 28A, 187 (1968).

61. R. Blinc, E. M. Peterson and D. E. O'Reilly, Phys. Rev. B1, 1953 (1970).

62. J. C. Slater, J. Chem. Phys. 9, 16 (1941).

63. R. Blinc and M. Mali, Solid State Communication 7, 1413 (1969).

64. W. Cochran, Phys. Rev. Letters. 3, 412 (1959); Advances in Physics, Vol. 9, p. 387 (1960).

65. P. W. Anderson, Izv. Akad. Nauk SSSR, 290 (1960)

66. V. L. Ginzburg, Soviet Physics-Solid State 2, 1824 (1961).

67. P. G. de Gennes, Solid State Communication 1, 132 (1963).

68. R. Brout, K. A. Muller and H. Thomas, Solid State Communication 4, 507 (1966).

69. K. K. Kobayashi, J. Phys. Soc. (Japan) 24, 497 (1967).

70. E. J. Samuelsen, E. Andersen and J. Feder, eds., op cit. Of specific pertinence in the present context are the chapters starting on pages 97 and 371 (by R. Blinc and F. Borsa, respectively).

71. R. Blinc and B. Zeks, Advances in Physics 21, 693 (1972).

72. G. Bonera, F. Borsa and A. Rigamonti, Phys. Rev. B2, 2784 (1970).

73. I. P. Kaminow and T. C. Damen, Phys. Rev. Letters 20, 1105 (1968).

74. A. Abragam, op. cit., Chapter IX, Section IV.

75. M. Suzuki and R. Kubo, J. Phys. Soc. (Japan) 24, 51 (1968).

76. K. Tani, J. Phys. Soc. (Japan) 26, 93 (1969).

77. R. Blinc, S. Zumer and G. Lahajnar, Phys. Rev. B1, 4456 (1970).

78. E. J. Samuelsen, E. Andersen and J. Feder, eds., op. cit., p. 118.

79. R. Blinc, J. Phys. Chem. Solids 13, 204 (1960).

80. Y. Tmry, T. Pelah and E. Wiener, J. Chem. Phys. 43, 2332 (1965).

81. F. Jona and G. Shirane, op. cit., p. 93.

82. M. Tokunaga and T. Matsubara, Progr. Theor. Phys. 36, 857 (1966).

83. W. Cochran, Advances in Physics 10, 401 (1961).

84. E. M. Brody and H. Z. Cummins, Phys. Rev. Letters 21, 1263 (1968).

85. A. Abragam, op. cit., Chapter IX, Section II.

86. F. Jona and G. Shirane, op. cit., p. 67.

87. R. Blinc, M. Mali, J. Slak, J. Stepisnik and S. Zumer, J. Chem. Phys. 56, 3566 (1972).

88. G. Bonera, F. Borsa and A. Rigamonti, op. cit., see "note added in proof".

89. R. Blinc, J. Stepisnik, M. Jamsek-Vilfan and S. Zumer, J. Chem. Phys. 54, 187 (1971).

90. R. Blinc, M. Mali, J. Pirs and S. Zumer, J. Chem. Phys. 58, 2262 (1973).

91. J. L. Bjorkstam and E. A. Uehling, Phys. Rev. 114, 961 (1959).

92. H. B. Silsbee, E. A. Uehling and V. H. Schmidt, Phys. Rev. 133, A165 (1964).

93. T. Chiba, J. Chem. Phys. 41, 1352 (1964).

94. J. L. Bjorkstam. Phys. Rev. 153, 599 (1967).

95. V. H. Schmidt, Phys. Rev. 164, 749 (1967).

96. E. P. Jones and S. R. Hartmann, Phys. Rev. Letters 22, 867 (1969).

97. Y. Hsieh, J. C. Koo and E. L. Hahn, Chem. Phys. Letters 13, 563 (1972).

98. J. West, Z. Kirst. 74, 306 (1930).

TECHNICAL INFORMATION DIVISION
LAWRENCE BERKELEY LABORATORY
UNIVERSITY OF CALIFORNIA
BERKELEY, CALIFORNIA 94720